

# Modeling of evaporation processes in glass melting furnaces

**Citation for published version (APA):**

van Limpt, J. A. C. (2007). *Modeling of evaporation processes in glass melting furnaces*. [Phd Thesis 2 (Research NOT TU/e / Graduation TU/e), Chemical Engineering and Chemistry]. Technische Universiteit Eindhoven. <https://doi.org/10.6100/IR630685>

**DOI:**

[10.6100/IR630685](https://doi.org/10.6100/IR630685)

**Document status and date:**

Published: 01/01/2007

**Document Version:**

Publisher's PDF, also known as Version of Record (includes final page, issue and volume numbers)

**Please check the document version of this publication:**

- A submitted manuscript is the version of the article upon submission and before peer-review. There can be important differences between the submitted version and the official published version of record. People interested in the research are advised to contact the author for the final version of the publication, or visit the DOI to the publisher's website.
- The final author version and the galley proof are versions of the publication after peer review.
- The final published version features the final layout of the paper including the volume, issue and page numbers.

[Link to publication](#)

**General rights**

Copyright and moral rights for the publications made accessible in the public portal are retained by the authors and/or other copyright owners and it is a condition of accessing publications that users recognise and abide by the legal requirements associated with these rights.

- Users may download and print one copy of any publication from the public portal for the purpose of private study or research.
- You may not further distribute the material or use it for any profit-making activity or commercial gain
- You may freely distribute the URL identifying the publication in the public portal.

If the publication is distributed under the terms of Article 25fa of the Dutch Copyright Act, indicated by the "Taverne" license above, please follow below link for the End User Agreement:

[www.tue.nl/taverne](http://www.tue.nl/taverne)

**Take down policy**

If you believe that this document breaches copyright please contact us at:

[openaccess@tue.nl](mailto:openaccess@tue.nl)

providing details and we will investigate your claim.

# **Modeling of evaporation processes in glass melting furnaces**

PROEFSCHRIFT

ter verkrijging van de graad van doctor aan de Technische Universiteit Eindhoven, op  
gezag van de Rector Magnificus, prof.dr.ir. C.J. van Duijn, voor een commissie  
aangewezen door het College voor Promoties in het openbaar te verdedigen op  
maandag 26 november 2007 om 16.00 uur

door

**Johannes Alphonsius Christianus van Limpt**

geboren te Reusel

Dit proefschrift is goedgekeurd door de promotoren:

prof.dr.ir. R.G.C. Beerkens

en

prof.dr.ir. J.C. Schouten

A catalogue record is available from the Eindhoven University of Technology Library

ISBN: 978-90-386-1147-1

Printed by Eindhoven University Press, Eindhoven, The Netherlands

Cover design: Paul Verspaget, Grafische Vormgeving – Communicatie, Nuenen, The Netherlands



Samenstelling promotiecommissie:

Kerncommissie:

Eerste promotor: prof.dr.ir. R.G.C. Beerkens Technische Universiteit  
Eindhoven

Tweede promotor: prof.dr.ir. J.C. Schouten Technische Universiteit  
Eindhoven

prof.dr.ir. Th.H. van der Meer Universiteit Twente

prof.dr.rer.nat. R. Conradt Rheinisch-Westfälischen Technischen  
Hochschule, Aachen, Germany

prof.dr.ir. A.A. van Steenhoven Technische Universiteit Eindhoven

Lid aangevulde commissie:

prof.dr.ir. A.C.P.M. Backx Technische Universiteit Eindhoven

## Summary

### Modeling of evaporation processes in glass melting furnaces

The majority of glass furnaces worldwide, apply fossil fuel combustion to transfer heat directly by radiation from the combustion processes to the melting batch and glass melt. During these high temperature melting processes, some glass components, such as: sodium, potassium, boron and lead species will evaporate from the glass melt.

There are three main motives to study evaporation processes in glass furnaces. In the first place evaporation of volatile components from the glass melt surface is one of the main causes of particulate and heavy metal emissions of industrial glass furnaces. Secondly, incongruent evaporation of glass melt components might cause depletion of volatile glass compounds at the surface layer of the melt. This process may be a source for glass failures and inhomogeneities in the glass product. Thirdly, volatilization of glass melt components may lead to the formation of aggressive vapors, such as alkali or lead vapors, reacting with the superstructure silica based refractory materials or refractories in the flue gas system.

The evaporation rates depend on the process conditions in the glass furnace, like:

- Glass melt composition (at the surface);
- Temperature of the glass melt surface;
- Composition of the atmosphere. Especially the water vapor (air-fuel versus oxy-fuel) and the carbon monoxide contents just above the melt are important;
- Exposure time of a glass melt volume to the combustion atmosphere and
- Local gas velocities and turbulence intensity just above the glass melt surface.

For different glass types, the interaction between furnace atmosphere and the glass melt surface as well as the different evaporation reactions were summarized and discussed qualitatively, by many investigators. However, a universal and accurate mathematical evaporation model to predict evaporation rates of volatile glass components in industrial glass melt furnaces as well as laboratory glass melt furnaces quantitatively, was hardly available so far.

## Objective

The main goal of this study is the development of a general applicable evaporation model, for different types of glass furnaces and different glass compositions. This model should be based on validated mass transfer relations and simulation of the thermodynamic properties of multi-component silicate melts. With this evaporation model the evaporation rates of volatile species from different types of glass melts can be predicted. The model is meant to investigate quantitatively the impact of different process parameters on the evaporation rates of different volatile glass species and depletion of these glass components in the surface layer of the melt. The investigations in this study primarily focus on evaporation from multi-component silicate glass melts used for the industrial production of glass articles.

## Approach

In this study an evaporation model has been developed and validated by laboratory evaporation tests. For the evaporation model developed here, 5 different steps were required:

- I. Identification of the main volatile species and dominant evaporation reactions at prevalent conditions for the investigated glass melts.
- II. Modeling of the mass transport of volatile glass components in the glass melt. The second diffusion law of Fick in combination with known interdiffusion coefficients (from experiments, models or literature) of volatile glass compounds, to describe the diffusion mass transport in a static melt. Additional to this, Computational Fluid Dynamics (CFD) are applied to describe both, the convective and diffusive transport of volatile species from the bulk to the surface of the melt.
- III. Modeling of mass transport in the gas phase, describing the transport of volatile species from the glass melt surface into the gaseous atmosphere for laminar and turbulent gas flows.
- IV. Thermodynamic Associated Species Model (ASM) to calculate the chemical activities of volatile glass components in the melt and at the surface of the melt.
- V. Calculation of the evaporation rates. From the evaporation reaction, its chemical equilibrium constant and the chemical activities of the volatile glass components at the surface of the melt, the saturation pressure of the gaseous reaction products can be determined. The local evaporation rates of individual species, are calculated from the local mass transfer relations or local Nernst boundary layer thickness in the gas phase, the local saturation vapor pressures of the volatile species and the vapor pressures of these species in the bulk gas flow. The local Nernst boundary layer thickness of the

gas phase above the melt can be determined from the velocity profiles in the gas phase derived from CFD modeling, even for turbulent flows in combustion chambers. Laboratory-scale transpiration evaporation experiments have been used to: A) validate the evaporation modeling results and B) to study evaporation kinetics for sodium-silicate melts, multi-component alkali-lime-silicate melts and alkali-free borosilicate melts. In the transpiration set-up the furnace atmosphere composition, temperature level and gas velocity are controlled. Evaporation rates were measured for sodium, potassium, boron, chloride and sulfur species released from different well defined glass types, with known compositions. As will be shown later on in this summary, a procedure has been developed to derive chemical activities from the evaporation rates, measured during transpiration experiments. The validation of the evaporation model exists of a comparison between the experimentally and from thermodynamic modeling (ASM) derived chemical activities of volatile glass components.

### **Mass transport relations for the gas phase**

Mass transfer relations and procedures were derived to describe the mass transport of volatile glass components or their volatile reaction products from liquids or melts into the gaseous atmosphere. These mass transfer relations and procedures are developed for the applied laboratory transpiration experiments as well as for industrial glass furnaces. CFD modeling appears to be a useful tool to predict the mass transport of volatile species into a carrier gas for a complex geometrical configuration of a transpiration test set-up. Such CFD models are applied to describe and to understand the fluid dynamics in the gas phase and distribution of volatile species in this phase. Water is used as model liquid to investigate these mass transfer processes in transpiration evaporation tests. Results of the CFD-modeling for water evaporation tests at room temperature have been validated by transpiration experiments. Excellent agreement was found between model results and experiments, as the differences between the experimental measured evaporation rates and the CFD modeling results are less than 2 %. The results of CFD modeling and the results of simple water transpiration evaporation experiments at room temperature are used to obtain relatively simple mass transport relations for a fixed geometry of the transpiration test set-up. It has been shown in this study that these Sherwood relation are applicable for other evaporating liquids and temperatures as well when using the same equipment.



### **Chemical activities of volatile glass compounds in multi-component silicate melts**

The developed evaporation model requires chemical activity values of volatile components in the glass melt, especially at the glass melt surface. But, there are hardly experimental techniques available or sufficiently accurate to measure these equilibrium vapor pressures of glass melt species or chemical activities at high temperatures. It has been shown that equilibrium vapor pressures and chemical activities of volatile glass components can be derived from the mass transfer relations, determined for the used transpiration set-up and the measured evaporation rates of volatile species. The method developed here, offers a new approach to measure chemical activities of volatile components in the molten glass, such as  $\text{Na}_2\text{O}$ ,  $\text{K}_2\text{O}$  and  $\text{B}_2\text{O}_3$ , with a maximum error range of 10 to 30 %.

The experimentally derived thermodynamic properties of glass components are used to validate and to optimize thermodynamic models applied for multi-component silicate glass melts. Because of the different molecular structures and chemistry of soda-lime-silicate glass melts and borosilicate glass melts, the adjustments of the thermodynamic models for both glass types differ from each other.

The chemical activities of  $\text{Na}_2\text{O}$  in binary sodium-silicate melts and ternary soda-lime-silicate melts, have been determined experimentally by laboratory evaporation tests in the transpiration set-up and have also been estimated by the thermodynamic Associated Species Model for multi-component glass melts. Between the measured and modeled chemical activities a good linear correlation has been obtained for  $\text{Na}_2\text{O}$  in ternary soda-lime-silicate and binary sodium-disilicate melts:  $a_{\text{Na}_2\text{O}(\text{model})} = (0.98 \pm 0.04) \cdot a_{\text{Na}_2\text{O}(\text{measured})}$ .

The transpiration evaporation experiments have also been used to measure chemical activities of  $\text{Na}_2\text{O}$  and  $\text{K}_2\text{O}$  in other multi-component soda-lime-silicate glass compositions. For these multi-component glass melt, the measured and modeled chemical activities deviate maximum about 30 %.

The laboratory transpiration evaporation set-up has also been used to measure the boron evaporation rates from alkali-free borosilicate glass melts and to derive chemical activities of  $\text{B}_2\text{O}_3$  in these melts at the surface. The measured chemical activities of  $\text{B}_2\text{O}_3$  in alkali-lean borosilicate glass melts deviate 1 to 3 decades from results of existing thermodynamic models. This deviation is probably caused by lack of accurate thermodynamic data (especially for stoichiometric calcium-borate compounds with a molar ratios  $\text{CaO}/\text{B}_2\text{O}_3 > 3$ ) of associated species or neglecting important associated species in the model.

An approach to improve the existing Associated Thermodynamic Model (ASM) is presented and demonstrated for a selected range of alkali-free borosilicate glass melts, only existing of  $\text{SiO}_2$ ,  $\text{CaO}$ ,  $\text{Al}_2\text{O}_3$  and  $\text{B}_2\text{O}_3$ . In this adapted model, immiscibility is not taken into account.

Both, the results of thermodynamic modeling with the adapted ASM for these borosilicate compositions, as well as measuring results show a strong decrease in chemical activity of  $\text{B}_2\text{O}_3$  for concentrations below  $\pm 2.5$  mass-% in these borosilicate melts. This might be a result of a change in the molecular structure of the melt.

In order to extend the existing universal evaporation model for a wider range of glass compositions, such as lead glass or LCD glass, and other volatile species (e.g. Pb, Sb, Cl, F), the thermodynamic Associated Species Model has to be optimized for these new glass compositions. This can be done in two different ways:

1. In the thermodynamic Associated Species Model, the thermodynamic data of additional associated species have to be included to be able to describe the complete system;
2. In some glass melts, phase segregation occurs or associated species do not ideally mix. For these systems the Associated Species Model approach has to be modified to account for positive excess Gibbs free energy of mixing. Borosilicate and glass-ceramics compositions are suspected as not ideally mixed melts.

Validation of these models by transpiration evaporation measurements, as described in this thesis, is strongly recommended.

The thermodynamic Associated Species Model cannot only be used to predict chemical activities, but can also be applied in models describing refractory corrosion or to calculate solubilities of certain components in the multi-component silicate melts or to model crystallization processes during cooling of the melt.

### **Transport of volatile compounds in the melt**

As a result of surface depletion of volatile glass components, the chemical composition of the glass melt surface sometimes deviates from the bulk composition. Results of experimental studies have been used to describe phenomena like surface depletion and free convection in the melt qualitatively, depending on local differences in evaporation rate or presence of surfactants (surface tension gradients or bubble formation).

It is demonstrated by CFD modeling that, besides the effect of glass melt convection due to surface tension gradients or bubbles ascending in the melt, convection may take place as a result of non-uniform evaporation rates of volatile glass melt species along the glass melt surfaces. Because of the non-uniform evaporation rates, concentration and density differences in the melt are induced. Convection of the melt promotes the transport of material from the bulk to the surface of the melt and will stabilize evaporation rates of (minor) components in the melt like chlorine, sulfur and fluorine. In static melts surface depletion of these components takes place as time proceeds.

At the surface of the melt surface tension gradients might appear, as a result of concentration differences at the surface of the melt. These surface tension gradients might cause convective Marangoni flows. The Marangoni convection increases the mass transfer of (volatile) glass compounds compared to mass transfer by only diffusion in a static melt. Possible surface active components in a glass melt, such as  $\text{Na}_2\text{SO}_4$ ,  $\text{K}_2\text{SO}_4$ ,  $\text{NaCl}$ ,  $\text{KCl}$  and  $\text{B}_2\text{O}_3$  might cause convective Marangoni flows.

### **Evaporation tests for industrially produced alkali-lime silicate glasses**

For multi-component based alkali-lime-silicate melts, containing chloride and sulfur, these chlorides and sulfates promote the release of alkali species, such as  $\text{Na}_2\text{SO}_4$ ,  $\text{NaCl}$ ,  $\text{KCl}$  or possibly  $\text{K}_2\text{SO}_4$ . In a static melt, the evaporation rates of these species decreases in progress of time, as a result of the relatively slow diffusion transport. However, temperature gradients, differences in surface tension and bubbles in the melt can strongly affect the (local) convection in the melt and the evaporation rates of these minor species. The investigations showed that the main evaporation species from soda-lime-silicate float glass melts and alkali-lime-silicate tableware melts are:  $\text{NaOH}$ ,  $\text{KOH}$ ,  $\text{Na}_2\text{SO}_4$ ,  $\text{KCl}$  and at reducing conditions  $\text{Na}$  and  $\text{K}$ .

The evaporation rates of minor components, present in low concentration levels, are often limited by the slow transport of volatile components to the surface of the melt. This leads to distinct surface depletion of these elements. At the surface of the melt the concentration of these volatile compounds might eventually decrease to zero. Probably CFD (Computational Fluid Dynamics) modeling, taking into account the convection at surface near areas, can be applied to describe the transport of these minor compounds in the melt phase in case of non static melts. Phenomena like Marangoni flows and ascending fining bubbles seem to be important for convection in several industrial glass melting processes.

**Evaporation modeling for industrial glass furnaces**

The evaporation model developed in this study has been used to estimate the evaporation rates of volatile sodium and boron species in industrial glass furnaces. The modeling results were compared to the results of industrial evaporation measurements. To model evaporation processes in industrial glass melt furnaces a combustion modeling procedure is required to calculate the mass transport of volatile species from glass melts into combustion chambers of industrial glass furnaces. In the combustion chamber of an industrial glass furnace, the gas flows are turbulent. For the modeling of the gas flow patterns in case of turbulent conditions, the standard 'k- $\epsilon$  turbulence model' is used in CFD (Computational Fluid Dynamics) based computer simulations. However, the applied k- $\epsilon$  model is only valid for fully turbulent flows. In order to correctly calculate momentum-, mass- and energy fluxes near the (melt) surfaces without the necessity to use very fine grids, empirically derived relations for velocities, temperatures and mass fractions as function of the distance from the glass melt surface, are used. This method has been demonstrated for modeling of evaporation processes in industrial glass furnaces and is used to calculate the evaporation rates of sodium and boron.

**Concluding remark**

Thus, a general applicable evaporation model for a large range of glass compositions has been developed to predict the evaporation rates of the main volatile glass components. The model has been validated by laboratory evaporation experiments as well as industrial evaporation rate measurements. The results agree well with the beforehand defined objectives of this study.



# Contents

<b>Summary</b>	<b>5</b>
<b>1. Introduction</b>	<b>19</b>
1.1 Motivation of this study	21
1.2 Literature review on evaporation studies of glass melts	24
1.2.1 Evaporation of sodium species	28
1.2.2 Evaporation of potassium species	30
1.2.3 Evaporation of chloride species	31
1.2.4 Evaporation of boron species from glass melts	33
1.2.5 Evaporation of fluoride species from glass melts and glass forming batch	34
1.2.6 Evaporation of selenium species in glass furnaces	36
1.3 Objectives	38
1.4 Approach	40
1.5 Outline of the thesis	42
References	44
<b>2. Theory on glass melt evaporation kinetics</b>	<b>51</b>
2.1 Mass transfer evaporation model	57
2.1.1 Mass transport in a static melt layer	59
2.1.2 Mass transport in the gas phase	60
2.2 Mass transport in the melt	63
2.2.1 Marangoni flows	64
2.2.2 Transport of boron species in borosilicate melts	65
2.3 Mass transport in the gas phase	68
2.3.1 Relations for describing mass transfer in transpiration experiments	69
2.3.2 Empirical derivation of mass transfer relations for transpiration experiments	71
2.3.3 Determination of the Nernst boundary layer thickness in industrial glass furnaces	75

2.4	Important properties of alkali-lime silicate melts and borosilicate melts required for evaporation modeling	84
2.4.1	Molecular structure of borosilicate glass melts	84
2.4.2	Phase segregation in glass melts	85
2.5	Modeling of thermodynamic properties of silicate glasses and melts	89
2.5.1	Thermochemical Associated Species Model	90
2.5.2	Thermochemical modeling of soda-lime-silicate melts and float glass melts	93
2.5.3	Thermochemical modeling of $\text{SiO}_2\text{-CaO-Al}_2\text{O}_3\text{-B}_2\text{O}_3$ melts	94
2.6	Properties of volatile species	99
2.6.1	Determination of diffusion coefficient of species in gas phase ( $D_{g,i}$ )	99
2.6.2	Equilibrium constants	101
2.6.3	Diffusion coefficients of volatile species in glass melts	102
2.6.4	Other properties	106
2.7	Concluding remarks to chapter 2	107
	Appendix I: Equations of change in fluid dynamics	111
	Appendix II: Transition of velocity, temperature and mass fraction data in dimensionless values	112
	References	114
<b>3.</b>	<b>Experimental procedures for evaporation studies</b>	<b>121</b>
3.1	Transpiration evaporation experiments for model liquids	123
3.2	Transpiration set-up for glass melt evaporation tests	127
3.2.1	Set-up for glass melts	127
3.2.2	Procedure for evaporation experiments	127
3.3	Chemical analysis of glass and concentration profile analysis in glass	131
3.3.1	XRF and NAA analysis	131
3.3.2	SEM and XPS analysis	131
3.4	Fining tests facility	134
	References	136

<b>4. Experimental and modeling results for laboratory glass melt evaporation tests</b>	<b>139</b>
4.1 Validation of mass transfer relations for transpiration experiments	145
4.2 Sample preparation and homogeneity	150
4.3 Identification of main evaporation reactions	151
4.3.1 Evaporation of sodium species from sodium-disilicate melts	152
4.3.2 Evaporation of sodium species from soda-lime-silicate melts	158
4.3.3 Evaporation of boron species from alkali-lean borosilicate glass melts	158
4.4 Experimentally derived chemical activities of Na <sub>2</sub> O, K <sub>2</sub> O and B <sub>2</sub> O <sub>3</sub> in multi-component silicate melts	163
4.4.1 Measured and modeled chemical activities of Na <sub>2</sub> O in silicate melts	163
4.4.2 Measured chemical activities of K <sub>2</sub> O in multi-component silicate melts	170
4.4.3 Measured chemical activities of B <sub>2</sub> O <sub>3</sub> in alkali-lean borosilicate glass melts	171
4.5 Transport of volatile species in glass melts	173
4.5.1 Transport of Na <sub>2</sub> O in glass melts with and melts without sulfur	173
4.5.2 Transport of boron in alkali-lean borosilicate glass melts	178
4.6 Measuring errors	180
4.7 Evaporation processes of multi-component alkali-lime silicate compositions used in glass industry	184
4.8 Additional parameters influencing the evaporation during heating of melting glass forming raw materials and glass melts	184
4.9 Concluding remarks chapter 4	192
4.9.1 Validation of relations for mass transfer through gas phase boundary layers in transpiration evaporation tests	192
4.9.2 Identification of the most important evaporating species	192
4.9.3 Derivation of chemical activities of volatile species at the surface of a glass melt	193



4.9.4	Description of the transport of volatile components in the melt and description of depletion phenomena	194
4.9.5	Influence of minor components in the melt on the evaporation of sodium and potassium from alkali-lime-silicate melts	194
4.9.6	Concluding remark	195
Appendix I	Glass sample preparation for transpiration experiments	196
Appendix II	Impact of sulfur and chlorides on sodium and potassium evaporation rates	202
References		223
<b>5.</b>	<b>Evaporation modeling for industrial glass furnaces</b>	<b>225</b>
5.1	Sodium evaporation in industrial fossil-fuel fired glass furnaces	227
5.2	Reduction of superstructure corrosion and emissions	231
5.2.1	Modeling of evaporation of sodium species from soda-lime-silicate glass melts in industrial furnaces	232
5.2.2	Reactions between silica and sodium vapors	233
5.2.3	Kinetics of silica attack by alkali vapors	235
5.2.4	Modeling results of evaporation kinetics for sodium evaporation from soda-lime-silicate glass melt in industrial glass furnaces	237
5.2.5	Modeling results of silica attack	243
5.3	Boron evaporation from industrial E-glass melts	246
5.4	Conclusions chapter 5	250
References		252
<b>6.</b>	<b>Conclusions and outlook</b>	<b>255</b>
6.1	Identification of volatile species and evaporation reactions	255
6.2	Mass transport relations for the gas phase (boundary layer approach)	255
6.3	Chemical activities of volatile glass compounds in multi-component silicate melts	256
6.4	Transport of volatile compounds in the melt	256

## Contents

6.5	Evaporation tests for industrially produced alkali-lime silicate glasses	259
6.6	Evaporation modeling for industrial glass furnaces	259
6.7	Concluding remarks and outlook	260
	<b>Samenvatting</b>	<b>263</b>
	<b>Dankwoord / Acknowledgements</b>	<b>271</b>
	<b>Curriculum Vitae</b>	<b>273</b>



# 1. Introduction

Most glass furnaces apply fossil fuel firing to transfer heat directly from the combustion processes above the melting batch and glass melt. Evaporation processes and subsequent condensation processes during the cooling of the flue gases are major causes of pollutant emissions from glass furnaces. Important sources of emissions from glass furnaces are:

- Combustion process, which is often the major cause of NO<sub>x</sub> formation;
- Evaporation from the melting batch blanket;
- Carry-over of (fine) batch particles from the batch blanket;
- Evaporation of volatile glass components from the surface of the glass melt.

The investigations in this study primarily focus on evaporation from multi-component silicate glass melts used for the industrial production of glass articles. Evaporation processes during melting of model glass compositions and industrial glasses have been studied and the results are compared with literature. The vapor species of main concern are alkali, boron, chloride and fluoride species. These species or compounds containing these species are often volatile and the most important sources of emissions. In paragraph 1.1 the motivation for this study is given and in paragraph 1.2 the literature review on evaporation studies of glass melts is presented. The objective and approach of the study are described in the paragraphs 1.3 and 1.4. Paragraph 1.5 finally shows the outline of this thesis.

**Nomenclature**

a	chemical activity [-]
G	molar Gibbs energy free [ $\text{J}\cdot\text{mole}^{-1}$ ]
K	equilibrium constant [ $\text{Pa}^{(q-m)}$ ]
p	partial vapor pressure [Pa]
T	absolute temperature [K]

Subscripts and superscripts

<sup>0</sup>	standard state (pure liquid or solid at 1 bar, at prevalent temperature)
*	saturated gaseous atmosphere
g	gas phase
l	liquid state
m	melt phase
s	solid state

## 1.1 Motivation of this study

Since 1950, Dietzel and Merker [1] and Kruithof et al. [2] have investigated the relation between glass quality (presence of certain in-homogeneities) and evaporation processes. Since 1960, the evaporation of different volatile glass species like lead [3][4] boron [5][6][7], sodium [8][9], and fluorine species [5][10] from silicate glass melts have been studied extensively. For different glass types the interaction between furnace atmosphere and the glass melt surface as well as the different evaporation reactions have been summarized and discussed by Conrardt and Scholze [9]. Other investigators like Schaeffer and Sanders [8][11] described phenomena like glass melt surface depletion of volatile compounds.

Evaporation often causes formation of vapors (e.g. alkali or lead vapors), reacting with superstructure silica-based refractory materials [12][13][14][15].

Since 2000, Beerkens and van Limpt [16][17][18] applied evaporation models to calculate and estimate the evaporation rates of volatile species in industrial glass furnaces. The evaporation models are based on: mass transport relations in a glass melt, assumed to be static (diffusion) liquid, as well as relations for mass transfer in the gas phase [25]. These models use chemical activity and vapor pressure data derived from thermodynamic models [18][19][20][21][22][23][24]. The gaseous volatile species just above the melt are assumed to be in equilibrium with the glass composition at the surface of the melt.

The evaporation rates depend on the process conditions in the glass furnace, such as:

- Glass melt composition (at the surface);
- Temperature of the glass melt surface;
- Composition of the atmosphere. Especially the water vapor (air-fuel firing versus oxy-fuel firing) and the carbon monoxide partial vapor pressure just above the melt are important;
- Exposure time of a melt layer to the combustion atmosphere;
- Local gas velocities and gas phase turbulence intensity just above the glass melt surface.

The evaporation models have been demonstrated and described in this thesis for laboratory transpiration evaporation experiments carried out for sodium-silicate melts, alkali-lime-silicate melts and alkali-lean borosilicate melts. These types of glass melts are important for industrial glass production. Evaporation rates determined by transpiration evaporation

experiments and known mass transfer relations have also been used to validate thermodynamic (sub-) models for glass melts as will be discussed in chapter 4.4. Furthermore, the transport of volatile compounds in the melt as well as the impact of fining agents like sulfur and chlorides on depletion as well as the evaporation of sodium and potassium have been discussed (see chapter 4.7).

The validated evaporation model that describes quantitatively sodium evaporation from sodium containing silicate melts will be applied for industrial glass furnaces, to find process conditions that minimize sodium evaporation rates. Process settings resulting in lower evaporation rates will finally contribute to lower emissions (particulate, heavy metals), less refractory corrosion [12][13][14][15] and less glass failures like cords [2].

### Sources of emissions

Evaporation processes from the glass melt surface is the major cause of dust (particulate) emissions in the glass industry. During cooling processes of the flue gases, fine dust particles are formed by reaction and condensation processes [26]. For most of the soda-lime glass melting processes, sodium sulfate is used as fining agent. The dissociation of this sodium-sulfate leads to sulfur-oxide concentrations, which are much higher than the molar sodium concentrations in the combustion chamber and in the flue gases. During the cooling of the flue gases the sulfur-oxide reacts with almost all the sodium components, mainly present as NaOH vapor, to form sodium-sulfate [26]. The sodium-sulfate condensates below 1100 °C and below 884 °C these droplets crystallize to form sodium-sulfate particulates, with typical sizes of 0.02 till 0.5 μm [27] [28].

This chapter gives a short overview of the most important compounds emitted from soda-lime glass furnaces and borosilicate glass furnaces. Of course, in all types of fossil fuel fired glass furnaces, and furnaces using nitrates in the batch, NO<sub>x</sub> will be emitted as well.

Soda-lime glass melt furnaces (this glass type is used for container glass, float glass, tableware and lighting glass production):

- Sodium sulfate particulate matter, i.e. a condensation product of volatile NaOH and SO<sub>2</sub> [26] in the flue gases. The most important reaction is:



- Lead oxide particulate matter from glass furnaces using external recycling cullet or from lead silicate glass melting processes [3][4][9],
- Carry-over of batch particles. A well-known examples is decrepitation of dolomite, which leads to particulate emissions of MgO and CaO. The deliberated CO<sub>2</sub> from the decomposition of dolomite (or even limestone) will be directly released from open pore structured grains, but in case of dense grains with crystal defects, this CO<sub>2</sub> can build up a very high pressure inside the grains above the carbonate decomposition temperatures. These grains will burst and form very small fragments which are carried away by the combustion gases [29][30]. Fine (dry) sand or fine aluminum oxide raw materials or fine cullet powder might also be entrained by the combustion gases at high gas velocities.
- Gaseous HCl (see paragraph 1.2.3),
- Gaseous HF (see paragraph 1.2.5),
- Gaseous SO<sub>2</sub> (and at low flue gas temperatures also SO<sub>3</sub>) [9][26][31][32][32],
- Gaseous selenium compounds (see paragraph 1.2.6).

Borosilicate glass melt furnaces (E-glass<sup>1</sup>, insulation wool):

- Sodium-borate particulate matter (NaBO<sub>2</sub> and Na<sub>2</sub>B<sub>4</sub>O<sub>7</sub>) (see paragraph 1.2.4),
- Potassium-borate particulate matter (KBO<sub>2</sub> and K<sub>2</sub>B<sub>4</sub>O<sub>7</sub>) (see paragraph 1.2.4),
- Boric acid (HBO<sub>2</sub> and H<sub>3</sub>BO<sub>3</sub>), which is mainly a vapor species in flue gases from alkali-lean E-glass furnaces, above 200 °C (see paragraph 1.2.4),
- Sodium and potassium sulfate particulate matter,
- Gaseous fluoride components (like HF) from E-glass furnaces (see paragraph 1.2.5),
- SiO<sub>2</sub> particles from batch carry-over or caused by SiF<sub>4</sub> evaporation and subsequent reactions in the flue gases (see paragraph 1.2.5),
- Gaseous SO<sub>2</sub> (and at low flue gas temperatures also SO<sub>3</sub>).

At temperatures above 1200 °C, sodium metaborate, potassium metaborate and metaboric acid are the most important volatile boron components in the flue gases. During cooling of the flue gases all kinds of borates can be formed like potassium borates and sodium borates.

---

<sup>1</sup> E-glass is an alkali-lean borosilicate glass applied for production of textile glass fibers, or reinforcement fibers and for plastic and as fibers for printed circuit boards. The glass mainly exists of SiO<sub>2</sub>, CaO, Al<sub>2</sub>O<sub>3</sub> and B<sub>2</sub>O<sub>3</sub>.



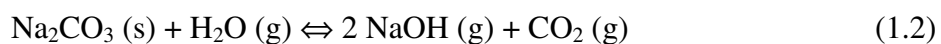
Below 800 °C very fine particulate material is formed [26] by condensation processes or reactions (e.g.  $2\text{NaBO}_2(\text{g}) + \text{SO}_2(\text{g}) + \text{H}_2\text{O}(\text{g}) + \frac{1}{2}\text{O}_2 \Leftrightarrow 2\text{HBO}_2(\text{g,l}) + \text{Na}_2\text{SO}_4(\text{l})$ ).

## 1.2 Literature review on evaporation studies of glass melts

In this study, the evaporation processes from soda-(lime)-silicate glass melts and borosilicate glass melts have been investigated. In fossil fuel fired glass furnaces there is direct contact between the gases in the combustion chamber and the surface of the melt. The developed evaporation model can be used to predict the evaporation rates of volatile glass components evaporating from the surface of the melt. However, in a glass melting furnace different types of evaporation processes can be distinguished.

An example has been used to present the most relevant evaporation processes in soda-lime silicate glass furnaces:

- a) Direct volatilization of raw material components from the surface of the batch blanket (batch = mixture of raw materials forming upon fusion and melting a molten glass, e.g.: sand, soda, limestone, dolomite, borates etc.). Vapor pressures of these components are rather low up to 1200 °C, and above 1000 °C, the single components have reacted to form silicates and therefore the vapor pressures of most batch components above the reacting batch blankets will be relatively low [29][33].
- b) Reactive evaporation by chemical reactions at the batch blanket surface with gas components in the furnace atmosphere. Thermodynamics and literature data [9] [31] [34][35][36][38] show that the water vapor in the atmosphere may cause reactions of soda in the batch to form NaOH:

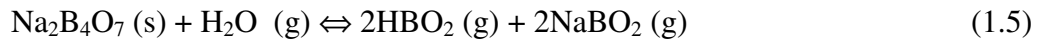
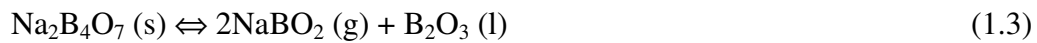


Similar reactions might take place for potassium carbonates forming gaseous KOH. Thermodynamic calculations shows that for furnaces atmospheres with respectively 20 vol.-% and 60 vol.-% water vapor (typical water vapor pressures for the case of respectively air-gas firing and oxygen-gas firing), this volatilization process will be important for batch blankets at temperatures exceeding 900 °C ( $p_{\text{NaOH}} > 10 \text{ Pa}$ ). However, above temperatures of 900 – 1000 °C the main part of the soda has probably reacted with other raw materials like silica to form sodium-silicate and

sodium-calcium-silicate melts [37]. The chemical activity of the sodium oxide in these melts will drop after reaction with silica or calcium-silicates.

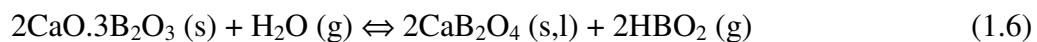
- c) Volatilization of sodium compounds from the melt phase into gas bubbles during the fining process. The bubbles contain mainly  $\text{SO}_2$ ,  $\text{CO}_2$ ,  $\text{H}_2\text{O}$  and some pure sodium,  $\text{Na}_2\text{SO}_4$  and/or  $\text{NaOH}$ . A balance on the total evolution of the volume of bubbles and their  $\text{Na}_2\text{SO}_4$  and  $\text{NaOH}$  contents show however, a minor importance of this source in the total release of sodium components.
- d) Volatilization of  $\text{NaCl}$  present as an impurity in synthetic soda. This salt has a relatively high vapor pressure above  $800\text{ }^\circ\text{C}$  and might have significant influence on the total sodium release. Nowadays, the chloride concentrations in raw materials like soda have been reduced considerably by the raw material producers in Europe and  $\text{NaCl}$  evaporation hardly contributes to the total sodium evaporation [39]. In some cases  $\text{NaCl}$  is used as fining agent and gaseous  $\text{NaCl}$  might be released at this stage.
- e) Volatilization of  $\text{Na}_2\text{SO}_4$  from the surface of a melt containing both, sodium and sulfur. Because of the relative high chemical activities of  $\text{Na}_2\text{SO}_4$  in the melt, the evaporation of  $\text{Na}_2\text{SO}_4$  might be significant. Conradt et al. [9] investigated sodium sulfate volatilization from a static soda-lime-silicate glass melt containing sulfate on laboratory scale. In their experiments direct sodium sulfate evaporation during evaporation tests of several hours is limited, because of  $\text{Na}_2\text{SO}_4$  surface depletion. (Because of chloride and fluoride depletion at the surface of a static melt, the evaporation rates of these species will also decrease as time proceed.)
- f) Reactive evaporation from the glass melt surface. Sodium oxide in the melt reacts with water vapor at the surface of the melt to form gaseous sodium hydroxide. Above temperatures of  $1200$  to  $1300\text{ }^\circ\text{C}$ , the evaporation of  $\text{NaOH}$  is considered as the major source of particulate emissions in fossil fuel-fired soda-lime-silicate glass furnaces [9][16][17][25][34].
- g) In case of the use of recycling cullet that is polluted with lead containing glass pieces. Lead compounds may evaporate directly from the soda-lime-silicate melt.

In most borosilicate glass furnaces, boron, sodium and potassium are the main volatile species. These components may evaporate from the batch blanket as well as from the glass melt. For batches containing borax (e.g.  $\text{Na}_2\text{B}_4\text{O}_7 \cdot 5\text{H}_2\text{O}$ ), the evaporation reactions 1.2 till 1.4 govern the volatilization process from the batch, according to Fernandes and Cable [40][41]. Here, the formation of  $\text{NaOH}$  seems to be of minor importance.



At 1000 °C the vapor pressures of pure NaBO<sub>2</sub> and pure Na<sub>2</sub>B<sub>4</sub>O<sub>7</sub> have been calculated from thermodynamic data presented in reference [26]. The equilibrium vapor pressures of these compounds are in the range from 20 to 40 Pa. In a humid atmosphere with p<sub>H<sub>2</sub>O</sub> = 0.15 bar, the equilibrium vapor pressures of NaOH and HBO<sub>2</sub> in equilibrium with Na<sub>2</sub>B<sub>4</sub>O<sub>7</sub> are about 5 to 10 Pa. Above 1000 °C, reactions between sand, borax and other raw materials take place and the evaporation rates of pure sodium borates (reactions 1.2 till 1.4) will become much lower. For sodium borosilicate glass melts at 1500 °C and p<sub>H<sub>2</sub>O</sub> = 0.15 bar, the equilibrium vapor pressures of NaBO<sub>2</sub> and HBO<sub>2</sub> above the melt are about 10 to 100 times higher. This means that boron species volatilization from batch blankets is of minor importance compared to evaporation from the glass melt at higher temperatures.

Frischat and Herr [42] measured the evaporation rate of metaboric acid from colemanite in humid atmospheres up to temperatures of 1200 °C (reaction 1.6). At 1000 °C colemanite appeared to give less volatile losses than ulexite (Na<sub>2</sub>O·2B<sub>2</sub>O<sub>3</sub>·5H<sub>2</sub>O) and tincalconite (Na<sub>2</sub>O·2B<sub>2</sub>O<sub>3</sub>·5H<sub>2</sub>O). In dry atmospheres and temperatures not exceeding 1100 °C the volatilization losses of borax, colemanite and ulexite are very low.



Considering the evaporation from borosilicate glass melts, the following observations were reported:

- Boron depletion in surface layers has been observed by Oldfield et al. [6] and Conradt et al. [9] after evaporation experiments. The depletion appeared to increase with the water vapor pressure in the atmosphere and the viscosity of the melt. Ehrig [7] performed evaporation experiments with different soda-borosilicate glass melts at temperatures up to 1600 °C and water vapor pressures between 0 and 0.5 bar. He

assumed that for a melt at 1500 °C, with the composition:  $\text{SiO}_2 : \text{B}_2\text{O}_3 : \text{Na}_2\text{O} = 71 : 24 : 5$  mass-%, the  $\text{SiO}_2$ -rich surface layer (due to sodium and boron evaporation) disappeared as a result of eddy-like convective currents in the melt.

- $\text{KBO}_2$  and  $\text{NaBO}_2$  appear to be the most important volatile components during alkali-borosilicate melting [5][6][7][9][40][41][43][44]. These compounds will evaporate according to the reactions 1.7 and 1.8. Alkali borates and boric acid as well as  $\text{SO}_2$  from the sulfate fining process, are the major volatile species from E-glass melts. In case fluorspar ( $\text{CaF}_2$ ) is used as melting flux agent, significant releases of fluoride species have been observed as well. According to reaction 1.9, boron species evaporate under influence of water vapor in the atmosphere. According to Oldfield and Wright [6],  $\text{Na}_2\text{B}_4\text{O}_7$  may be an important volatilization product if the molar ratio  $\text{B}_2\text{O}_3:\text{Na}_2\text{O}$  in the melt exceeds 2.
- For glass melts with a molar ratio  $\text{Na}_2\text{O}:\text{B}_2\text{O}_3 < 1$ , water vapor has a significant impact on the evaporation of boron, by formation of meta-boric acid (reaction 1.9) [36][44]. For molar ratios  $\text{Na}_2\text{O}:\text{B}_2\text{O}_3 > 1$  the evaporation of  $\text{NaBO}_2$  (reaction 1.7) becomes much more important.
- From E-glass melts with less than 1 mol-% alkali-oxides and generally more than 3 mol-%  $\text{B}_2\text{O}_3$ , metaboric acid is the main volatile component. Despite these low alkali levels, some volatilization of potassium metaborates and sodium metaborates has to be taken into account for such melts.



In the paragraphs 1.2.1 till 1.2.6, evaporation mechanisms for different glass components reported in literature are discussed.

### 1.2.1 Evaporation of sodium species

At the laboratory of the National Bureau of Standards much work has been done by Sanders, Schaeffer and co-workers on the evaporation of sodium compounds from soda-lime-silicate melts in the period 1970 - 1980 [8][11] [31][34][45][46]. They mainly studied the evaporation processes using the so-called transpiration method. In this method, a carrier gas is passed over a sample boat containing a silicate melt. In such experiments the evaporated species are picked up by the carrier gas. This carrier gas, containing the volatiles, has been extracted and analyzed. As carrier gas they used mixtures of N<sub>2</sub>, O<sub>2</sub> and water vapor.

Schaeffer [8] has shown that evaporation of sodium from a static soda-lime-silicate melt causes depletion of sodium at the surface. According to Sanders et al. [11] the evaporation of sodium from a static melt can be controlled by a 'surface membrane', having a composition which is different from that of the bulk composition. This surface composition is relatively constant and appeared to be independent of time and bulk sodium concentration. The sodium diffusion in the melt however appears to be strongly dependent on the sodium and presumably also on the water concentration in the melt [46].

The water vapor concentration or partial vapor pressure of water in the atmosphere mainly determines the sodium vaporization rate. At dry oxidized conditions, the sodium vaporization is negligible. Sulfur oxides in the combustion space are known to increase the volatilization of sodium compounds [47].

The formation of sodium hydroxide vapor by reaction of sodium oxide at the glass melt surface with water vapor [8][9][11][18][34][35] is the most important example of evaporation during the melting of soda-(lime)-silicate glasses (see reaction 1.10). According to equation 1.11, the vapor pressure of NaOH is proportional to  $p_{H_2O}^{1/2}$  at equilibrium conditions.  $K_{NaOH}$  is only temperature dependent.



$$K_{NaOH} = \frac{(p_{NaOH}^*)^2}{a_{Na_2O} \cdot p_{H_2O}} \quad (1.11a)$$

$$p_{NaOH}^* = \sqrt{a_{Na_2O} \cdot p_{H_2O} \cdot K_{NaOH}} \quad (1.11b)$$

Furthermore, the evaporation of elementary Na from the melt is proportional to  $p_{O_2}^{1/4}$  [45] as a result of the reduction of  $Na_2O$  at the melt surface:



$$K_{Na} = \frac{(p_{Na}^*)^2 \cdot (p_{O_2})^{0.5}}{a_{Na_2O}} \quad (1.13a)$$

$$p_{Na}^* = \sqrt{a_{Na_2O} \cdot (p_{O_2})^{0.5} \cdot K_{Na}} \quad (1.13b)$$

$Na_2O$  at the surface of the melt might be reduced also by reducing gases in the atmosphere like CO [16]. However, in the experimental study described in this paper, no reducing gas components have been used, and the impact of reducing atmospheres on evaporation of glass species has not been studied experimentally here.

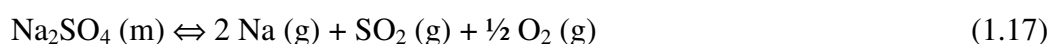
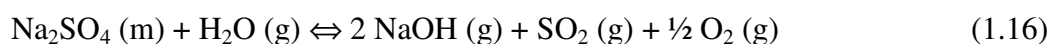
### ***Impact of sulfates in the glass melt on the evaporation of sodium species***

The impact of sodium sulfate ( $Na_2SO_4$ ) addition to the batch or melt, on evaporation of sodium or potassium species (even when keeping the total  $Na_2O$  content in the glass melt the same) from an industrial float glass (a sodium-calcium-magnesium silicate with additional compounds) furnace producing 600 metric tonnes of molten glass per day, has been investigated by Gebhardt [32]. The emission of particulate matter (dust) increases linearly with the amount of  $Na_2SO_4$  in the batch. Extrapolated to zero input sodium sulfate, still more than 5 kg/h dust is formed in the flue gases of this furnace. This is mainly a result of NaOH evaporation, plus subsequent flue gas reactions of NaOH with  $SO_2$  and  $O_2$  to form  $Na_2SO_4$  below 1100 °C [26] plus some carry-over of batch compounds. Matousek [48] also found higher evaporation losses for sodium with increasing sulfate content in the melt.

Conradt and Scholze [9] investigated the impact of sulfate content in the glass (melt) on the sodium evaporation rates from soda-lime-silicate glass melts ( $SiO_2:Na_2O:CaO = 74:16:10$  mass-%). In their transpiration evaporation experiments at 1400 °C they applied three different water vapor pressures of respectively 0, 0.1 and 0.2 bar. For every water vapor level they measured the sodium evaporation rate for three different  $SO_2$  vapor pressures of respectively 0, 0.1 and 1 mbar. In glass melts with sulfur concentrations (expressed as  $SO_3$

concentration), between 0.07 and 0.97 mass-%, higher sodium releases have been measured compared to SO<sub>3</sub> free glass melts with the same sodium content. It was concluded that for industrial practice-relevant SO<sub>2</sub> vapor pressures (< 500 Pa) from sulfate containing soda-lime-silicate melts, the increased sodium release (compared to sulfur free melts) was mainly a result of evaporation reaction 1.14. For soda-lime silicate melts without sulfur, but exposed to an atmosphere with p<sub>SO<sub>2</sub></sub> > 1000 Pa, it was shown that the evaporation losses increased, probably as a result of reaction 1.15 [9][31].

At a temperature of 1400 °C and a constant water vapor pressure, the measured sodium evaporation rates from a soda-lime-silicate melt with about 0.22 mass-% SO<sub>3</sub>, appeared to be hardly influenced by the SO<sub>2</sub> vapor pressures in the atmosphere, which has been varied between 0 and 100 Pa. According to Conradt and Scholze [9], the dissociation reactions 1.16 and 1.17 hardly contribute to the total sodium evaporation rate under oxidized conditions.



### 1.2.2 Evaporation of potassium species

From a potassium-lead-silicate melt (SiO<sub>2</sub>:PbO:K<sub>2</sub>O = 60:25:15 mass-%) the potassium evaporation rates during transpiration evaporation experiments have been measured by Conradt et al. [9]. From these melts potassium species evaporate in a similar way as sodium species from a soda-lime-silicate melt. The evaporation rate of potassium hydroxide is proportional to the square root of the water vapor pressure in water vapor containing atmospheres (see reaction 1.18). At reducing conditions evaporation reaction 1.19 will also contribute to the evaporation of potassium. Thermodynamic calculations with Factsage [49] confirm the importance of these evaporation reactions.



Potassium hydroxide and elementary potassium are the main volatile potassium species but other compounds like  $\text{K}_2\text{SO}_4$ , might evaporate from glass melts and the glass forming batch as well.

### 1.2.3 Evaporation of chloride species

In commercially produced soda-lime-silicate glass melts, such as container glass melts and float glass melts, chlorides are present due to contaminations or impurities of the applied raw materials or recycled glass cullet. Several authors have summarized the typical chloride sources for soda-lime-silica type glass batch components [32][33][39]. Soda and cullet are the main sources of chloride contaminations in most batches for production of soda-lime-silica glass.

Based on a chloride mass balance of an industrial amber glass furnace and thermodynamic calculations, Conradt et al. [50] showed that in that particular case about 40 % of the evaporated chloride species were released from the blank melt, 60 % volatilizes from the melting batch. At high, not specified temperatures, NaCl is assumed to be the major volatile chloride species (reaction 1.20). Below 1000 °C, chloride species may evaporate under influence of water vapor and  $\text{SO}_2$  (reactions 1.24 and 1.28).

Pelton [51] developed the software package Factsage, involving a Gibbs energy minimization routine that enables the estimation of solubilities of halides (like chlorides) in oxide and silicate melts and their chemical activities. The principles of their thermodynamic model will be discussed in paragraph 2.5. For all calculations, values of the Gibbs free energy  $G^0$  for the pure halides were taken from the well known Factsage database [49]. Solubilities of chlorides in a borosilicate glass composition ( $\text{SiO}_2 = 56.8$  mass-%,  $\text{B}_2\text{O}_3 = 5.0$  mass-%,  $\text{Na}_2\text{O} = 20.0$  mass-%,  $\text{Al}_2\text{O}_3 = 12.0$  mass-%,  $\text{CaO} = 4.0$  mass-%, other components 2.2 mass-%) in equilibrium with liquid NaCl, were measured by Li [52] over the range 1300 to 1400 °C and for an unspecified temperature range by Crichton et al. [53]. The predicted solubilities by Pelton et al. of chloride deviate about 10 to 40 % from the experimental values.

According to the results of thermodynamic modeling calculations [49][51] for  $\text{SiO}_2$ -CaO- $\text{K}_2\text{O}$ - $\text{Na}_2\text{O}$  melts plus small amounts of chlorides, the chemical activities of NaCl and KCl in



the melt are significant (0.5 to 1). The chemical activities of NaCl and KCl in these melts are of the same order of magnitude. At the surface of the melt, NaCl and KCl will probably evaporate. The evaporation/release of chlorides from a melt and the equilibrium conditions are given by equations 1.20 to 1.29.

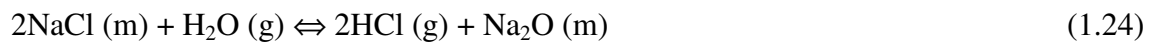
In industrially prepared glass melts, chlorides are sometimes deliberately applied as flux or fining agent. Emerging NaCl or KCl vapor bubbles in the case of ‘chloride’ fining also influence the mixing of the melt and have probably impact on the release of species like NaCl, KCl or HCl or even NaOH and KOH (suppressing depletion of sodium and potassium at the surface). The impact of the presence of chlorides in the melt on the evaporation of different glass components from the glass melt surface as well as chloride fining will be discussed in paragraph 4.7.



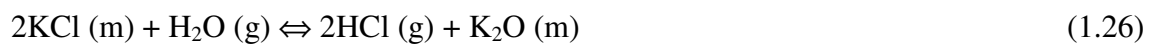
$$K_{\text{NaCl}} = \frac{p_{\text{NaCl}}^*}{a_{\text{NaCl}}} \quad (1.21)$$



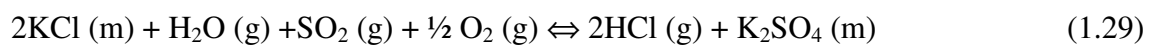
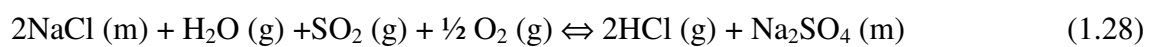
$$K_{\text{KCl}} = \frac{p_{\text{KCl}}^*}{a_{\text{KCl}}} \quad (1.23)$$



$$K_{\text{HCl},1} = \frac{(p_{\text{HCl}}^*)^2 \cdot a_{\text{Na}_2\text{O}}}{(a_{\text{NaCl}})^2 \cdot p_{\text{H}_2\text{O}}} \quad (1.25)$$



$$K_{\text{HCl},2} = \frac{(p_{\text{HCl}}^*)^2 \cdot a_{\text{K}_2\text{O}}}{(a_{\text{KCl}})^2 \cdot p_{\text{H}_2\text{O}}} \quad (1.27)$$



### 1.2.4 Evaporation of boron species from glass melts

Literature data on boron species evaporation rates of different borosilicate melts and thermodynamic data of components in alkali-free borosilicate melts are rare. For alkali-free  $\text{SiO}_2\text{-CaO-Al}_2\text{O}_3\text{-B}_2\text{O}_3$  melts (the basic composition of E-glass), the total evaporation rate of boron species depends mainly on the partial water vapor pressure in the furnace atmosphere and appears to be proportional to  $p_{\text{H}_2\text{O}}^{1/2}$  [36][44][54][55][56].  $\text{B}_2\text{O}_3$  at the glass melt surface reacts with the water vapor from the atmosphere according to reaction 1.30 (according to thermodynamic modeling the  $\text{H}_3\text{BO}_3$  partial vapor pressures are much lower at temperatures  $> 1200$  °C compared to  $p_{\text{HBO}_2}$ ).



The partial equilibrium vapor pressure of  $\text{HBO}_2$  ( $p_{\text{HBO}_2}^*$ ) just above the melt depends on the equilibrium constant  $K_{\text{HBO}_2}$ , the chemical activity of  $\text{B}_2\text{O}_3$  at the glass melt surface and the partial water vapor pressure  $p_{\text{H}_2\text{O}}$  in the atmosphere (equation 1.31). The equilibrium constant of this evaporation reaction can be derived from literature on thermodynamic data [57][58].

$$p_{\text{HBO}_2}^* = \sqrt{K_{\text{HBO}_2} \cdot a_{\text{B}_2\text{O}_3} \cdot p_{\text{H}_2\text{O}}} \quad (1.31)$$

In a fully dry atmosphere, only evaporation of  $\text{B}_2\text{O}_3$  is expected [6][59].

Mass spectrometric analysis has been used to identify the volatile boron species in equilibrium with different boron containing melts [60][61][62][63]. From alkali-borosilicate melts, compounds like  $\text{NaBO}_2$  and  $\text{KBO}_2$  will evaporate, without reaction with furnace atmosphere gases, according to the reactions 1.32 and 1.33 [41][64][65]. The water vapor contents in the atmosphere will not influence the evaporation of these species. However, for glass systems with molar ratio  $(\text{Na}_2\text{O}+\text{K}_2\text{O}+\text{Li}_2\text{O})/\text{B}_2\text{O}_3 \ll 1$  in humid atmospheres, boron is mainly released as meta-boric acid (reaction 1.30) [44]. According to Oldfield and Wright [6],  $\text{Na}_2\text{B}_4\text{O}_7$  might be an important volatilization product if the molar ratio at the glass melt surface fulfills:  $X_{\text{B}_2\text{O}_3}/X_{\text{Na}_2\text{O}} > 2$ .





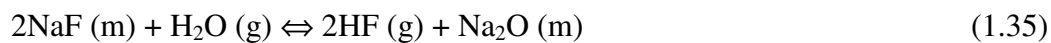
In some cases, in industrial practice,  $\text{CaF}_2$  is added as flux agent to raw material batches for melting borosilicate glass types such as E-glass (a  $\text{B}_2\text{O}_3$ - $\text{CaO}$ - $\text{Al}_2\text{O}_3$ - $\text{SiO}_2$  based glass type) or fluorides are present as impurity in raw materials such as clay. According to thermodynamic simulations using the software package Factsage [49] boron might partly be released as gaseous OBF from fluoride containing melts (reaction 1.35).



### 1.2.5 Evaporation of fluoride species from glass melts and glass forming batch

The use of fluorspar ( $\text{CaF}_2$ ) as melting flux in glass melting processes has been decreased strongly, only contaminations in natural raw materials and cullet have become the major sources for fluoride emissions. Kircher [33] mentioned that batch materials like phonolith, basalt and calumite contain relatively high amounts of fluoride (about 100 – 2000 mg/kg). For float glass production, Carduck et al. [67] mentioned that dolomite is the primary source of fluoride (100 – 300 mg/kg).

Fluoride in soda-lime silicate melts exposed to water vapor containing atmospheres, evaporates mainly as HF (reaction 1.35) and secondarily as NaF (reaction 1.36) as shown by Scholze et al. [10]. Fluor evaporates from the sodium rich glass melt by reaction with water according to:



Fluorides can also evaporate from sodium containing silicate melts without the presence of water, according to:



According to Scholze et al. [10], most of the fluorine in fossil-fuel fired soda-lime-silicate glass melts evaporates in the form of HF. The evaporation of other fluoride species is less than 10 % of the total fluoride release. TNO laboratory evaporation experiments [66] show that from these kinds of glass melts, the fluoride is mainly released as HF from the melting raw materials between 1000 and 1400 °C.

Based on the results of laboratory evaporation tests, Pentzel and Höhne [68][69] detected another volatile fluoride component above E-glass melts. From the balance of mass loss, fluorine and B<sub>2</sub>O<sub>3</sub> losses it has been concluded that fluoride mainly in the form of SiF<sub>4</sub> can be found above E-glass melts in dry and humid atmospheres and temperatures between 1250 and 1350 °C.

Concerning fluoride evaporation from soda-lime silicate-melts and batches Scholze et al. [10] have drawn some general conclusions:

- a) The fluoride release from the reacting batch blanket is relatively high. Increasing water vapor pressures and decreasing particle sizes of the batch materials both promote the fluoride release.
- b) Materials like cullet, melting at relatively low temperatures, result in a decreased fluoride release caused by a less porous batch blanket during fusion of the batch.
- c) The main fluorine evaporation mechanism from the melt is the reaction of chemical dissolved fluoride in the silicate melt with water vapor from the furnace atmosphere to form HF.
- d) The volatilization rate of fluoride from the melt is determined by the transport in the melt.
- e) The fluoride emission is linear proportional to the fluorine contents in the silicate melt.

For E-glass melts Pentzel and Höhne [68][69] concluded:

- a) The fluoride emission from an E-glass forming batch blanket increases linear with the temperature. The fluoride emission is the highest when the batch blanket is still porous. Thereafter the fluoride volatilization drops rapidly.
- b) In a humid atmosphere with  $p_{\text{H}_2\text{O}} = 0.1$  bar, the fluoride release increases 10 to 40 % compared to evaporation of fluorides in a dry atmosphere.
- c) The fluoride emission is linear proportional to the fluorine contents in the silicate melt.

- d) The release of fluoride is not affected by the release of boron (hardly any evaporation of boron-fluorides).

From the investigations of Pentzel and Höhne, it may be concluded that fluoride evaporation in E-glass melting furnaces is mainly limited by the transport of fluoride in the melt (fluoride depletion at the surface of the melt) and by the temperature of the batch blanket before melting.

Similar as the experimental results of Pentzel and Höhne, TNO laboratory evaporation studies [66] showed that the fluoride release from the E-glass forming batch blanket increases strongly with temperature up to about 1200 °C. At higher temperatures the fluoride release from the melting batch decreases. It was also measured that for temperatures up to 1200 °C, the fluoride release increases strongly with water vapor pressure in the atmosphere. In a humid atmosphere with  $p_{\text{H}_2\text{O}} = 0.55$  bar, the cumulative fluoride release from a melting batch between 800 and 1200 °C, was about 5 times higher than the fluoride release in a dry atmosphere in the same temperature range.

In two oil-fired industrial E-glass furnaces the local compositions of the atmosphere in the combustion chamber above the glass melt have been measured by TNO as well [66]. The molar ratio of the volatile fluoride (F) species and volatile silicon (Si) species in the combustion chamber above the glass melt, varies between 20 and 25 in an air-oil fired furnace ( $p_{\text{H}_2\text{O}} = 0.15$  bar) and between 40 and 60 in an oxygen-oil fired furnace ( $p_{\text{H}_2\text{O}} = 0.35$  bar). In these industrial furnaces the cannot only be attributed to the evaporation of  $\text{SiF}_4$  only. The higher molar F:Si ratio in the oxygen-oil fired furnace is probably a result of additional HF evaporation.

### 1.2.6 Evaporation of selenium species in glass furnaces

Selenium is applied as decoloring agent for flint container glass (Se addition in the batch is about 20 mg/kg) or for the coloring of bronze glass (Se addition in the batch is about 150 to 400 mg/kg). A recent paper of Technical Committee 13 of the International Commission on Glass (ICG) [70] shows that in industrial flint container glass furnaces up to 95 % of all added selenium to the batch may evaporate and that selenium mainly evaporates as  $\text{SeO}_2$  according to the reactions 1.38 to 1.40.





Gebhardt [32] showed that pure  $\text{SeO}_2$  reaches a high saturation pressure at relative low temperatures. Around 200 °C the partial vapor pressure of  $\text{SeO}_2$  reaches a value of 1 bar. Thus, gaseous  $\text{SeO}_2$  formed in batch materials starts to evaporate almost instantaneously after charging the batch into a glass furnace operating at much higher temperatures.

Shelestak and Arbab [71] showed that the selenium retention in bronze glass depends on the redox of the batch. They showed that there is a relatively large region for glass redox ratios (expressed as the molar ratio between ferrous iron and the total iron in the glass:  $[\text{Fe}^{2+}]/[\text{Fe}_{\text{total}}]$ ) from about 0.35 to 0.60 where the selenium retention is minimum. For more oxidizing conditions ( $0.2 < [\text{Fe}^{2+}]/[\text{Fe}_{\text{total}}] < 0.35$ ) or more reducing conditions ( $[\text{Fe}^{2+}]/[\text{Fe}_{\text{total}}] > 0.60$ ) the selenium retention rates are significantly higher. The different selenium retention levels relate to the different valence states of selenium in the glass ( $\text{Se}^{6+}$ ,  $\text{Se}^{4+}$ ,  $\text{Se}$  and  $\text{Se}^{2-}$ ).  $\text{Se}^{6+}$  and  $\text{Se}^{2-}$  seem to be more stable in the melt than  $\text{Se}$  or  $\text{Se}^{4+}$ .

### 1.3 Objectives

In order to predict the evaporation rates of different glass melt components (e.g. Na, B, K, F, Cl, Se and Sb species) in industrial glass melt furnaces, as a function of industrial process parameters like: glass composition, temperature, furnace atmosphere composition, gas velocity above the melt or gas flow pattern above the glass melt surface and exposure time (the time that the melt layer is exposed to the combustion atmosphere), new general applicable, evaporation simulation models have to be developed in this project. It is important to validate such models and to determine data required in these models such as chemical activities and mass transfer coefficients.

This study includes extensive evaporation experiments using the so-called transpiration method and the development of a mass transfer model in combination with a thermodynamic model to describe evaporation kinetics of volatile glass components from multi-component glass melts.

The obtained descriptive models should be able to predict the evaporation rates of volatile glass components most relevant for dust emissions of glass furnaces and for corrosion of glass furnace refractory materials. Refractory corrosion could be a consequence of contact between the refractory materials and the furnace atmosphere or exhaust gases containing volatile glass species. These models are applied to find optimum process conditions of glass furnaces with respect to minimize emission and material losses and to limit superstructure<sup>2</sup> refractory corrosion. This model should also be able to predict the depletion of the concentrations of volatile components at glass melt surfaces.

The study emphasizes on the mass transfer in the gas and glass melt phase and envisages the explanation of the concentration profiles of volatile species in the melt and the time dependent evaporation rates.

It will be shown that the experimental results, e.g. measured evaporation rates, from these investigations can be used to derive chemical activities of volatile glass species at the surface of the glass melt exposed to a (reactive) gas atmosphere.

The 4 main objectives of this study are:

1. Application and adjustments of a thermodynamic model to derive chemical activity of volatile components in glass melt as well as validation of the developed thermodynamic model. Since Van Limpt [9] derived mass transfer relations for

---

<sup>2</sup> The superstructure is the refractory lining of the combustion space chamber of a glass furnace above the melt.

transpiration experiments, it became possible to measure chemical activities of volatile compounds at the glass melt surface indirectly by calculating equilibrium vapor pressures from measured evaporation rates and known mass transfer relations. This will be demonstrated in this thesis for sodium-disilicate melts as well as for alkali-lime-silicate melts. For validation of the thermodynamic model (described in paragraph 2.5), the measured chemical activities will be compared with results of thermodynamic modeling.

2. Extension of the thermodynamic models for a wider range of glass compositions. Experimental results of evaporation tests will be used to adapt the thermodynamic model for alkali-lean borosilicate glass melts. The modified model will be applied to derive chemical activities of volatile boron compounds in the melt.
3. Further development of mass transport models for the gas phase as well as the melt. The diffusive and convective transport of volatile species in the melt should be described qualitatively and quantitatively. Computational Fluid Dynamics (CFD) calculations will be applied to model the transport of species in the melt as well as in the gas phase. Convection in the melt will counter-act depletion of volatile glass components at the glass melt surface.
4. Application of the validated mass transfer model and thermodynamic model for evaporation processes in industrial glass furnaces. Such models are meant to estimate evaporation rates of alkali and boron species from glass melts in industrial glass furnaces.



## 1.4 Approach

The final goal of this study is the development of a general evaporation model, applicable for different types of glass furnaces and different glass compositions. The envisaged model is meant to investigate the impact of different process parameters on the evaporation rates of different volatile species and depletion of these components in the surface layer of the melt.

The evaporation model consists of different sub-models, which describe the transport of volatile species in the melt as well as in the gas phase. Three sub-models underlie the evaporation model developed in this study:

1. Mass transport models to describe the transport of volatile glass components in the glass melt. The second diffusion law of Fick in combination with known interdiffusion coefficients (from experiments, models or literature) of volatile glass compounds describing the diffusion mass transport in a static melt and/or Computational Fluid Dynamics will both be used to describe the transport of volatile species from the bulk to the surface of the melt (paragraph 2.2).
2. Mass transport relations, describing the transport of volatile species from the glass melt surface into the gas phase (paragraph 2.3)
3. Thermochemical associated species model to calculate the chemical activities of volatile glass components in the melt and at the surface of the melt at the prevalent surface composition (see paragraph 2.5).

This first principle evaporation model should be applicable for industrial glass furnaces as well as for laboratory evaporation tests. The mass transport relation for the gas phase mass transfer (or Nernst boundary layer thickness) has to be known for the specific situation. From precisely controlled laboratory transpiration experiments with water and acetone as well as CFD modeling of this transpiration set-up, mass transport and Sherwood relations for the gas phase mass transfer process are obtained [25].

With the derived Sherwood relation, the mass transfer coefficient of volatile species into the atmosphere can be calculated, independent of the kind of liquid (or melt), for different glass compositions and different gas temperatures. For this calculation the diffusion coefficient of the volatile species is known. Two steps are required to determine chemical activities or equilibrium vapor pressures of glass melt volatile species from the measured evaporation rates:

### 1. Identification of the evaporation reactions

Depending on the gas composition above the melt, a volatile glass component like  $\text{Na}_2\text{O}$  might evaporate in different forms (e.g. gaseous  $\text{NaOH}$  or gaseous  $\text{Na}$ ). The gas composition above the melt is chosen in such a way that the evaporation of a specific volatile glass component is the result of one known dominating evaporation reaction.

### 2. Validation of the thermochemical sub-model

The saturation pressure of the gaseous volatile species just above the melt can be determined from the mass transport relation (equation 2.28) and the measured evaporation rates. Subsequently, the chemical activity of the volatile glass component at the glass surface can be obtained from the identified evaporation reaction equation and the corresponding equilibrium constant derived from thermodynamic data [57][58]. The measured chemical activities are compared with the chemical activities derived from a thermochemical sub-model developed in this study as described in paragraph 2.5.

Laboratory tests are carried out to validate the models, to derive mass transfer relations and to estimate chemical activities from the derived mass transfer relations and the measured evaporation rates. The evaporation tests are also performed to investigate the effect of minor constituents in the multi-component silicate melts on evaporation rates of alkali or boron species due to formation of additional vapor species or the impact on convective flows in the melt (see chapter 4).

To minimize the evaporation rates of volatile species in industrial glass furnaces, the developed evaporation model can be applied to simulate industrial glass melt processes [72]. The modeling results can be used to optimize the furnace design (e.g. geometry, burner settings, burner configuration, etc) in order to reduce emissions, and to reduce refractory corrosion problems in the superstructure of the furnace.

The outline of this thesis is presented in the next paragraph, a survey of the experimental work is given in chapter 3.

## 1.5 Outline of the thesis

After this general introduction, including the objective and motivation of this study as well as a literature review on evaporation studies performed for glass melts, the theoretical aspects of the developed evaporation model are described in chapter 2. After the explanation of the general principles of the evaporation model in paragraph 2.1, the mass transport processes of volatile glass components in the melt as well as the mass transfer of evaporated products in the gas phase are discussed in the paragraphs 2.2 and 2.3. In paragraph 2.3 mass transfer relations for the transport of gaseous volatile species into the atmosphere are presented for the used laboratory transpiration set-up as well as industrial glass furnaces. The, for evaporation processes relevant properties of alkali-lime-silicate melts and borosilicate melts, are shown in paragraph 2.4. Thermodynamic sub-models are used to determine the influence of the glass composition on the vapor pressures of reaction products of volatile glass compounds and thus on the evaporation rates of these compounds. These thermodynamic sub-models are explained and discussed in paragraph 2.5. Paragraph 2.6 finally, presents a review of the material properties or input data, required for the evaporation model.

The applied experimental approaches in this study are described in chapter 3. In paragraph 3.1 the transpiration evaporation equipment is discussed that has been used to study the mass transport of volatile species evaporating from model liquids at temperatures below 50 °C. For evaporation experiments with glass melts, another ‘high-temperature’ transpiration set-up has been developed. The specifications of this set-up are given in paragraph 3.2. In paragraph 3.3 the applied chemical analytical techniques to analyze glass samples and to analyze gas sampling solutions are described.

In chapter 4, the experimental results of this study are presented. Most evaporation laboratory evaporation tests are performed in the transpiration equipment. Since mass transfer relations in the gas phase were derived for this set-up, it is possible to measure indirectly thermodynamic properties, like chemical activities, of volatile species in glass melts. In paragraph 4.1 the derived mass transfer relations for a transpiration set-up are validated experimentally with model liquids like water and acetone and in paragraph 4.4 the measured chemical activities of  $\text{Na}_2\text{O}$ ,  $\text{K}_2\text{O}$  and  $\text{B}_2\text{O}_3$  were compared with the results of thermodynamic modeling. In the intermediate paragraph 4.2 the glass sample preparation for the transpiration experiments is discussed and in paragraph 4.3 the expected evaporation

reactions for the performed evaporation tests in this study with different glass compositions and experimental conditions are described.

In melts with hardly any convection, the evaporation rates might be limited by the diffusive transport of volatile species in the melt from the bulk to the surface. Transport mechanisms of volatile species in the melt are discussed in paragraph 4.5.

In paragraph 4.6 the range of the measuring errors in the experimentally derived chemical activities are estimated.

The paragraphs 4.1 till 4.6 focus on model glass melts while in the last two paragraphs (4.7 and 4.8) the measured evaporation rates from multi-component, industrial glass melts produced are presented and discussed. The effect of minor constituents in the glass melt on evaporation of alkali and convection in the melt are described.

The developed evaporation model has been applied to predict evaporation rates of volatile compounds in industrial glass furnaces. For this industrial validation, the procedure to determine the gas phase Nernst boundary layer thickness in industrial glass furnaces has been used (paragraph 2.3.3). In chapter 5 the modeling results (total calculated rates of evaporation from molten glass in glass melting furnaces) are compared with the measured evaporation rates in industrial glass furnaces.

In chapter 6 the conclusions of this study are summarized and recommendations for further improvements of the evaporation model are presented.

## References

- [1] A. Dietzel, L. Merker, 'Entstehung von Inhomogenitäten in der Glasschmelze durch Verdampfung einzelner Glasbestandteile. 1', *Glastech. Ber.* **30** [4], 134 – 138 (1957)
- [2] A.M. Kruithof, C.M. La Grouw, J. de Groot, 'Volatilization of glass', Proceedings, Symposium sur la Fusion du Verre (Brussels, Belgium, October 6-10, 1958), Union Scientifique Continentale du Verre, 515 –527 (1958)
- [3] R. Terai, T. Ueno, 'Volatilization of components from glasses containing high lead oxide at high temperature', *J. Ceram. Assoc. JPN.* **74**, 283 -295 (1966)
- [4] J. Matousek, J. Hlavac, 'A study of the volatilisation of lead glass', *Glass Technol.* **12** [4], 103-106 (1971)
- [5] D.F. Barlow, 'Volatilization of fluorides, borates and arsenic from glass', Proceedings, 7<sup>th</sup> International Congress on Glass (Brussels, Belgium), Vol. 1, [1], 2 – 19 (1965)
- [6] L.F. Oldfield, R.D. Wright, 'The volatilization of constituents from borosilicate glass at elevated temperatures', *Advances in Glass Technology, VI International Congress on Glass* (Washington, USA, July 8-14, 1962), 35 – 51 (1962)
- [7] R. Ehrig, 'Zum Problem der Oberflächenverdampfung aus Alkalibor-silikatglas-schmelzen', *Silikattechnik.* **24** [8-9], 296-298 (1973)
- [8] H.A. Schaeffer, D.M. Sanders, 'Verdampfungsvorgänge an einem Na<sub>2</sub>O-CaO-SiO<sub>2</sub>-Glas, Dampfdruck- und Konzentrationsprofilmessungen', *Glastech. Ber.* **49** [5], 95-102 (1976)
- [9] R. Conradt, H. Scholze, 'Zur Verdampfung aus Glasschmelzen', *Glastech. Ber.* **59** [2], 34-52 (1986)
- [10] H. Scholze, G. Tünker, R. Conradt, 'Verdampfung von Fluor aus Glasschmelzen und beim Einschmelzprozeß', *Glastech. Ber.* **56** [6-7], 131-137 (1983)
- [11] D.M. Sanders, H.A. Schaeffer, 'Reactive Vaporization of Soda-Lime-Silica Glass Melts', *J.Am.Ceram.Soc.* **59** [3-4], 96 -101 (1976)
- [12] R.G.C. Beerkens, O.S. Verheijen, 'Reactions of alkali vapours with silica based refractory in glass furnaces, thermodynamics and mass transfer', *Phys. Chem. Glasses* **46** [6], 583-594 (2005)
- [13] H.T. Godard, L.H. Kotacska, J.F. Wosinski, S.M. Winder, A. Gupta, K.R. Selkregg, S. Gould, 'Refractory corrosion behaviour under air-fuel and oxy-fuel environments', *Proc. 57<sup>th</sup> Conf. on Glass Problems. Ohio State University Columbus 8-9 Oct. 1996. Ceram. Eng. Sci. Proc.* **17** [1], 180-207 (1996)

- [14] A.J. Faber, O.S. Verheijen, 'Refractory corrosion under oxy-fuel firing conditions', *Ceram. Eng. Sci. Proc.* **18** [1], 109-119 (1997)
- [15] J.A.C. van Limpt, R.G.C. Beerkens, 'Reduction of superstructure corrosion and emissions by modern furnace design and optimized operation', *Proceedings XX. ATIV Conference Modern Technologies and Techniques for Glass Manufacturing, Parma Italy*, 73-89, 14-16 September 2005
- [16] R.G.C. Beerkens, J.A.C. van Limpt, 'Evaporation in industrial glass melt furnaces', *Journal of Glass Science and Technology* **74** [(9)], 245-257 (2001)
- [17] R.G.C. Beerkens, 'Modelling the Kinetics of Volatilization from Glass Melts', *J.Am.Ceram.Soc.* **84** [9], 1952-60 (2001)
- [18] H. van Limpt, R. Beerkens, O. Verheijen, 'Models and experiments for sodium evaporation from sodium containing silicate melts', *J.Am.Ceram.Soc.* **89** [11], 3446-3455 (2006)
- [19] C.W. Bale, P. Chartrand, S.A. Degterov, G. Eriksson, K. Hack, 'FactSage Thermochemical Software and Databases', *Calphad, Vol.*, **26** [2], 189-228 (2002)
- [20] A.D. Pelton, P. Wu, 'Thermodynamic modeling in glass-forming melts', *J. Non.-Cryst. Solids*, **253**, 178-191 (1999)
- [21] J.W. Hastie, D.W. Bonnell, 'A predictive phase-equilibrium model for multicomponent oxide mixtures. 2. Oxides of Na-K-Ca-Mg-Al-Si', *High Temp. Sci.*, **19** [3], 275-306 (1985)
- [22] T. M. Besmann, K.E. Spear, 'Thermochemical modeling of oxide glasses', *J.Am. Cer. Soc.*, **85** [12], 2887-2894 (2002)
- [23] B.A. Shakhmatkin, N.M. Vedishcheva, M.M. Shultz, A.C. Wright, 'The thermodynamic properties of oxide glasses and glass-forming liquids and their chemical structure', *J. Non-Crystalline Solids*, **177**, 249-256 (1994)
- [24] R. Conradt, 'A Simplified Procedure to Estimate Thermodynamic Activities in Multicomponent Oxide Melts', *Molten Salt Chemistry and Technology* ed. by H. Wendt, *Trans Tech Publication Zürich, Switzerland*, **5-6**, 155-162 (1998)
- [25] H. van Limpt, R. Beerkens, A. Lankhorst, A. Habraken, 'Mass transfer relations for transpiration evaporation experiments', *Int. J. of Heat and Mass Transfer* **48**, 4265-4281 (2005)
- [26] R.G.C. Beerkens, 'Deposits and condensation from flue gases in glass furnaces', *Thesis Technical University Eindhoven* (1986)
- [27] J.D. Stockham, 'The composition of glass furnace emissions', *J. Air. Poll. Ass.* **21** [11], 713-715 (1971)

- [28] A. Kasper, E. Carduck, M. Manges, H. Stadelmann, J. Klinkers, 'Particulate emissions in the flue gas of flat glass production after electrostatic precipitators', *Glass Sci. Technol.*, **77** [4], 177-185 (2004)
- [29] R.G.C. Beerkens, J.A.C. van Limpt, 'Impact of glass furnace operation on evaporation from glass melts', Proceedings of 61<sup>st</sup> Conference on glass problems, Ohio State of University, October 2000.
- [30] R.H.E.M. Martens, F.A.G. van Dijk, R.G.C. Beerkens, 'Batch carry-over in glass furnaces', Proceedings 78. Glastechnische Tagung, Nürnberg, 247-252 (2004)
- [31] D.M. Sanders, M.E. Wilke, S. Hurwitz, W.K. Haller, 'Role of water vapor and sulfur compounds in sodium vaporization during glass melting', *J.Am.Ceram.Soc.* **64** [7], 399 – 404, (1981)
- [32] F. Gebhardt, 'Emissionen von Glasschmelzwannen und deren Minderung durch schmelztechnische Maßnahmen', *Glstech. Ber.* **59** [12], 344-349 (1986)
- [33] U. Kircher, 'Emissionen von Glasschmelzöfen – Heutiger Stand', *Glstech. Ber.* **58** [12], 321 – 330, (1985)
- [34] D.M. Sanders, W.C. Haller, 'Effect of water vapor on sodium vaporization from two silica based glasses', *J.Am.Ceram.Soc.* **60**, 138-141, (1977)
- [35] K.P. Hanke, H. Scholze, 'Einfluss der Ofenatmosphäre auf die Verdampfung aus Glasschmelzen', *Glstech. Ber.* **50**, 271-275, (1977)
- [36] J.T. Wenzel, D.M. Sanders, 'Sodium and boron vaporization from a boric oxide and a borosilicate glass melt', *Physics and Chemistry of Glasses* **23**, 47-52, (1982)
- [37] O. Verheijen, 'Thermal and chemical behavior of glass forming batches' Thesis Eindhoven University of Technology (2003)
- [38] R. Conradt, H. Scholze, G.G. Waldecker, 'Verdampfungsuntersuchungen an binären und ternären Systemen – Ihre Bedeutung für die praktische Glasschmelze', *Glstech. Ber.* 56K [1] Sonderland LVI K, proceedings XIII – ICG Congress Hamburg, 88-93, (1983)
- [39] A.P.M. Ter Beek, E.J.M.C. Thole, 'Chloride emission from glass-melting furnaces', *Glstech. Ber.* **65** [11], 315-320, (1992)
- [40] M.H.V. Fernandes, M. Cable, 'The effect of water on the volatilization of sodium borate melts', Proceedings 16<sup>th</sup> Int. Congress on Glass, Vol. 6, 161 -166 (1992)
- [41] M.H.V. Fernandes, M. Cable, 'Reactive vaporisation of sodium tetraborate with water vapor', *Glass Technol.* **34** [1], 26 – 32, (1993)

- [42] G.H. Frischat, K. Herr, 'Verhalten von  $B_2O_3$ -Rohstoffen beim Erschmelzen von Glas', *Glastech. Ber.* **50** [5], 89-93, (1977)
- [43] G.A. Kolykov, 'Selective volatility of components of the system  $Na_2O-B_2O_3-SiO_2$ . A method for the investigation of the nature of the glassy state' in 'Structure of Glass, Vol.-1 (Translation of the Proceedings of the Conference on the Structure of Glass, Leningrad 1953, 184-192), Consultants Bureau Inc., New York (1958)
- [44] R. Terai, K. Egushi, 'Einfluß des Wasserdampfes auf die Verflüchtigungsgeschwindigkeit boroxidhaltiger Gläser', *Bull. Govt. Ind. Res. Inst. Osaka* **28** [1], 1-5, (1977)
- [45] D.M. Sanders, W.K. Haller, 'Influence of  $pO_2$  on vaporization of sodium-disilicate at 1345 °C', *J. Am. Ceram. Soc.* **62** [7-8], 424-425, (1979)
- [46] S. Murai, J. Wenzel, D. Sanders, 'Vaporization in an unstirred soda-lime-silicate glass melt', *Phys. Chem. Glasses* **21** [4], 150-155, (1980)
- [47] R. Brückner, 'Zur Kinetik des Stoffaustausches an der Grenzflächen zwischen Silikatglas- und Salz-schmelzen und des Stofftransportes in Silikatglasschmelzen unter besonderer Berücksichtigung des Verhaltens von  $Na_2SO_4$  und seinen Zersetzungsprodukten. Teil I: Grenzflächenenergetische Ausgleichsprozesse bei Stoffaustauschvorgängen' *Glastech. Ber.* **34** [9], 438 – 455 (1961), Teil II, 'Der Substanztausch zwischen Silicatglas- und Salzschnmelzen' *Glastech. Ber.* **34** [11], 515-528 (1961), Teil III, 'Thermische und chemische Zersetzung von  $Na_2SO_4$  und der Substanztausch zwischen Silikatglasschmelzen und  $SO_2$ -haltigen Atmosphären', *Glastech. Ber.* **35** [2], 93-105 (1962)
- [48] J. Matousek, 'Evaporation of silicate glasses containing  $Na_2SO_4$ ', *Riv. Stn. Sper. Vetro* **9** [5], 159 – 163 (1979)
- [49] C.W. Bale, P. Chartrand, S.A. Degterov, G. Eriksson, K. Hack, 'FactSage Thermochemical Software and Databases', *Calphad*, Vol.**26** [2] 189-228 (2002)
- [50] R. Conrad, 'Zur Chlorverdampfung bei der Glasschmelze', *Glastech. Ber.* **59** (4), N20 (1985)
- [51] A.D. Pelton, 'Thermodynamic calculations of chemical solubilities of gases in oxide melts and glasses', *Glastech. Ber.* **72** [7], 214-226 (1999)
- [52] H. Li, J.G. Darab, P.A. Smith, 'Effect of minor components on vitrification of low-level simulated nuclear waste glasses, Nuclear Materials Management. Proc. 36<sup>th</sup> Institute of Nuclear Materials Management Annual Meeting, Palm Desert, C.A. (1995). Pittsburgh, PA: INMM, 466-471 (1995)



- [53] S.N. Crichton, T.J. Barbieri, M. Tomozawa, 'Solubility limits for troublesome components in a simulated low-level nuclear waste glass', *Ceramic Transactions*, 61: Environmental issues and waste management technologies in the ceramic and nuclear industries, The Am. Ceram. Soc., 283-290 (1995)
- [54] A. Petzold, S.R. Ehrig, 'Chemische Aspekte bei Verdampfungsvorgängen aus Borosilicatglasschmelzen, Teil I, Sprechsaal **123** [11], 1114-1116 (1990)
- [55] S.R. Ehrig, A. Petzold, 'Chemische Aspekte bei Verdampfungsvorgängen aus Borosilicatglasschmelzen, Teil II, Sprechsaal **124** [2], 95-98, (1991)
- [56] C. Pentzel, D. Höhne, 'Chemische Aspekte bei Verdampfungsvorgängen aus Borosilicatglasschmelzen, Teil III, Sprechsaal **124** [5], 327-329, (1991)
- [57] I. Barin, 'Thermochemical data of pure substances', VCH Verlagsgesellschaft, ISBN-3-527-27812-5 (1989)
- [58] O. Knacke, O. Kubaschewski, K. Hesselman, 'Thermochemical properties of inorganic substances', Springer-Verlag / Verlag Stahleisen, ISBN 3-540-54014-8 (1973)
- [59] V.L. Stolyarova, G.A. Semenov, 'Mass spectrometric study of the vaporization of oxide systems', John Wiley & Sons, ISBN 0 471 93988 9 (1994)
- [60] D.J. Meschi, W.A. Chupka, J. Berkowitz, 'Heterogeneous reactions studied by mass spectrometry. Pt.1//reaction of  $B_2O_3$  (s) with  $H_2O$  (g), *J. Chem. Phys.* **33**, 530-533 (1960)
- [61] D. White, D. E. Mann, P.N. Walsh, 'Infrared emission spectrum of gaseous  $HBO_2$ ', *J. Chem. Phys.* **32**, 488 – 492 (1960)
- [62] S.P. Randall, J.L. Margrave, 'Vapour equilibria in the  $B_2O_3 - H_2O$  system at elevated temperatures', *J. Inorg. Nucl. Chem.* **16**, 29 -35 (1960)
- [63] G.W. Wilds, 'Volatilization from borosilicate glass melts of simulated Savannah River Waste', *Proceedings of the 15<sup>th</sup> DOE Nuclear Air Cleaning Conf.*, 95-110 (1979)
- [64] M. Cable, M.H.V. Fernandes, 'The volatilization of molten sodium metaborate', *Glass Technol.* 28 [3], 135-140, (1987)
- [65] R. Terai, E. Kosaka, 'Volatilization of low temperature glasses for high level radioactive wastes at elevated temperatures', *Bull. Gov. Int. Res. Inst. Osaka* **27** [3], 150-156 (1976)
- [66] J.A.C. van Limpt, A.J. Faber, 'Reduction of emissions by decreasing volatilization in glass furnaces, phase 2; Experimental simulation tests on volatilization in glass furnaces', TNO report HAM-RPT-98-408, TNO Institute of Applied Physics, Eindhoven (1998)
- [67] E. Carduck, A. Kasper, D. Küstner, 'Influence of raw materials and batch formula on the emissions of flat glass tank furnaces', *Glass Technology and Application. Technical sessions*,

Vol. 3a, Proceedings of XV International Congress on Glass, Leningrad, ed. O.V. Mazurin, Leningrad Nauka, 179 -184, (1989)

[68] C. Pentzel, D. Höhne, 'Emission von Fluor und Bor aus E-Glasschmelzen', paper presented at Technical Committee VI of the DGG on 20 October 1993 in Würzburg, Germany

[69] C. Pentzel, 'Mechanism of volatilisation of fluorides from E-glass melts', *Glastech. Ber.* **67** [8], 213-219, (1994)

[70] B. Scalet, S. Slade, A. Kasper, G. Van Marcke de Lummen, K. Gitzhofer, H. van Limpt, 'Selenium emissions from glass melting furnaces: formation, sampling and analysis. A position paper by the Technical Committee 13, 'Environment', of the International Commission on Glass (ICG)', *Glass Technology – European Journal of Glass Science and Technology Part A* **47** [2] 29-38, (2006)

[71] L.J. Shelestak, M. Arbab, 'Investigation of selenium retention in high redox glasses', *Glass. Sci. Technol.* **78** [6], 255-260, (2005)

[72] A. Lankhorst, A. Habraken, O. Op den Camp and Oscar Verheijen, 'Simulation of the impact of different combustion systems on the flow and temperature distribution in glass melting furnaces', HVG/NCNG Colloquium on Operation and Modelling of Glass Melting Furnaces, Aachen, 8 November 2005.



## 2. Theory on glass melt evaporation kinetics

From the literature review on evaporation studies of glass melts presented in paragraph 1.2 it has been shown that in industrial, fossil fuel-fired glass furnaces, most volatile glass compounds evaporate progressively from the surface of the melt at increased temperatures. For most volatile species in the melt, the evaporation reactions governing the evaporation processes are known from literature (see chapter 1). Some glass compounds (e.g. NaCl or Na<sub>2</sub>SO<sub>4</sub>) evaporate without reaction from the melt (or melting batch), but in most cases a glass compound reacts at the surface of the melt with a gaseous species in the atmosphere to form a new volatile species. The latter phenomenon is called ‘reactive evaporation’ and the most well known example of reactive evaporation is the evaporation reaction between sodium oxide in the melt and water vapor in the atmosphere to form gaseous sodium hydroxide (see paragraph 1.2.1).

The evaporation rates of the different volatile species and change of surface composition of the melt depend on the process conditions in the glass furnace, like:

- Glass melt composition (at the surface);
- Temperature of the glass melt surface;
- Composition of the atmosphere;
- Exposure time of a melt layer to the combustion atmosphere;
- Local gas velocities and turbulence intensity just above the glass melt surface;
- Mixing or convection of the melt. As a result of mixing or convection of the melt the transport of volatile components to the surface of the melt is promoted and less depletion of volatile species at the surface of the melt is expected, compared to static melts.

In this chapter, a general applicable evaporation simulation model, based on validated mass transfer relations and simulation of the thermodynamic properties of multi-component silicate melts will be described. The model can be used to predict the evaporation rates of volatile species from different types of glass melts. Mass transfer boundary-layer models, thermodynamic models and Computational Fluid Dynamics (CFD) modeling are applied to describe evaporation kinetics quantitatively.

Laboratory scale transpiration evaporation experiments (see chapter 3) are used to study evaporation kinetics as well as to validate evaporation models.

The most important developments of the evaporation model by this study are:

- Derivation of mass transfer relations of volatile species from the surface of the melt into the atmosphere, for laboratory transpiration evaporation tests. Because of these mass transfer relations it became possible to determine chemical properties (such as chemical activities) of glass melts experimentally, from the measured evaporation rates. This procedure will be described in paragraph 4.4.
- Description of the mass transport of volatile compounds in the melt. The diffusive and convective transport in the melt as well as the influence of the local composition differences of the melt on the occurrence of surface tension gradient driven 'Marangoni' flows will be discussed in paragraph 2.2.
- The development of a procedure to determine the mass transport of volatile species from the surface of the melt into the combustion chamber of industrial glass furnaces using results of CFD combustion modeling (see paragraph 2.3.3).
- Application of thermodynamic models for glass melts in the evaporation model developed in this study, and further optimization of these thermodynamic models by using the results of laboratory evaporation tests. The thermodynamic model is used to derive chemical activities of glass components in the melt. Because of the different molecular structures and chemistry of soda-lime-silicate glass melts and borosilicate glass melts, the adjustments of the thermodynamic models for both glass types differ from each other. In this chapter, the relation between glass structure and evaporation processes from borosilicate glass melts will be discussed as well.

In paragraph 2.1, the applied evaporation model describing the evaporation rate of volatile species or rate of formation of volatile reaction products from glass melts is presented. In the paragraphs 2.2 and 2.3 detailed information is given on the relevant mass transport relations for transfer of volatile or evaporated species in the melt phase and in the gas phase. Conradt and Scholze [1] showed that the evaporation processes from glass melts are mainly limited by the mass transfer of volatile components (in the melt and/or gas phase) and depend hardly on reaction kinetics limitations. In their transpiration evaporation experiments, with a PbO-SiO<sub>2</sub> melt at 1000 °C, different carrier gases (air, He and Ar) were used. The differences between the measured evaporation rates could be explained from the different mass transfer coefficients ( $h_i$ ) in the gas phase, which are proportional to the diffusion coefficient in the gas phase.

Laboratory evaporation studies of TNO [2] confirmed this minor effect of reaction kinetic limitations on the mass transfer of volatile species. In this study, laboratory transpiration experiments were applied to measure the boron evaporation rates ( $Q_{B_2O_3}$ ) from the surface of an alkali borosilicate melt for 4 different gas velocities ( $v$ ) varying between 1.4 and 2.8 m/s. Other parameters that influence the evaporation rates, such as temperature and gas composition were kept constant. As shown by Beerkens [3], the evaporation rates are about proportional to  $v^{0.8}$  for turbulent gas flows above the vessel in the tube. For the 4 evaporation tests, the measured average ratio between the boron evaporation rates ( $Q_{B_2O_3}$ ) and  $v^{0.8}$  was about constant (standard deviation 10 %). The results of these experiments also indicate that the evaporation rates are mainly governed by mass transfer into the gas phase. Besides the mass transfer relations in the gas phase or the melt, the evaporation rates from glass melts also depend on the molecular structure and composition of the glass melt determining the chemical activities of glass melt components. The molecular structure and to this structure related thermodynamic properties of glass melts are described in the paragraphs 2.4 and 2.5. In paragraph 2.6 the data of glass melt properties and some other parameters, required for the mathematical evaporation model are presented. Finally, the concluding remarks are given in paragraph 2.7.

**Nomenclature**

a	chemical activity in melt, relative to pure non-mixed liquid compounds at same temperature [-]
b	valence of an ion [-]
$c_{\mu}$	turbulence model constant [-]
C	concentration in melt or gas phase [ $\text{mole}\cdot\text{m}^{-3}$ ]
$C_1, C_2, C_3$	constants in equation 2.19 [-]
$C_4$	constant in equation 2.34 [ $\text{J}\cdot\text{mole}^{-1}$ ]
$C_p$	heat capacity [ $\text{J}\cdot\text{kg}^{-1}\cdot\text{K}^{-1}$ ]
d	inner diameter of transpiration experiment tube [m]
D	interdiffusion coefficient [ $\text{m}^2\cdot\text{s}^{-1}$ ]
$D^T$	tracer diffusion coefficient [ $\text{m}^2\cdot\text{s}^{-1}$ ]
$D^I$	intrinsic diffusion coefficient [ $\text{m}^2\cdot\text{s}^{-1}$ ]
E	integral constant [-]
G	molar Gibbs free energy [ $\text{J}\cdot\text{mole}^{-1}$ ]
I	transport of momentum [ $\text{kg}\cdot\text{m}^2\cdot\text{s}^{-1}$ ]
g	gravitational acceleration [ $9.8 \text{ m}\cdot\text{s}^{-2}$ ]
H	height of the boat [m]
h	mass transfer coefficient [ $\text{m}\cdot\text{s}^{-1}$ ]
k	turbulent kinetic energy [ $\text{m}^2\cdot\text{s}^{-2}$ ]
K, K(T)	equilibrium constant [ $\text{Pa}^{(q-m)}$ ]
L	length of a boat or characteristic length [m]
$L_g$	distance from the leading edge [m]
m	stoichiometry factor in equilibrium reaction [-]
n	stoichiometry factor in equilibrium reaction [-]
p	vapor pressure [Pa]
$P_M$	correction term wall functions for mass [-]
$P_T$	correction term wall functions for heat [-]
Pe	Péclet number [-]
Pr	Prandtl number [-]
$Pr_t$	turbulent Prandtl number [-]
q	stoichiometry factor in equilibrium reaction [-]
Q	molar flux density [ $\text{mole}\cdot\text{m}^{-2}\cdot\text{s}^{-1}$ ]

R	universal gas constant [ $8.31432 \text{ J}\cdot\text{mole}^{-1}\cdot\text{K}^{-1}$ ]
r	number of different volatile gas species formed from one compound in the glass [-]
$Re_L$	Reynolds number for flat plates ( $=\rho\cdot v\cdot L_g/\mu$ ) [-]
$Re_d$	Reynolds number for tubes ( $=\rho\cdot v\cdot d/\mu$ ) [-]
$Re_t$	turbulent Reynolds number [-]
Sc	Schmidt number ( $=\mu/\{\rho\cdot D\}$ ) [-]
$Sc_t$	turbulent Schmidt number [-]
$Sh_L$	Sherwood number for flat plates ( $=h\cdot L_g/D$ ) [-]
$Sh_d$	Sherwood number for tubes ( $=h\cdot d/D$ ) [-]
T	absolute temperature [K]
$T^+$	dimensionless notation for temperature [-]
t	time [s]
$u_\tau$	friction velocity [ $\text{m}\cdot\text{s}^{-1}$ ]
$U^+$	dimensionless velocity [-]
v	velocity of gas or melt [ $\text{m}\cdot\text{s}^{-1}$ ]
$v'$	turbulent part of gas velocity [ $\text{m}\cdot\text{s}^{-1}$ ]
W	width of boat [m]
x	distance in gas flow direction [m]
X	mole fraction [-]
$X^+$	dimensionless mass fraction [-]
y	distance perpendicular to glass melt surface [m] (vertical direction)
$y^+$	dimensionless distance from a grid point to the wall [-]
$y_m^+$	dimensionless distance from surface of a liquid to the transition point between laminar and the logarithmic sub-layer for momentum transport [-]
z	horizontal distance perpendicular to gas flow direction [m]

### Subscripts and superscripts

<sup>0</sup>	standard state (pure liquid or solid at 1 bar, at prevalent temperature)
*	saturated gaseous atmosphere or saturation (equilibrium) value
avg	average
bulk	parent glass or main gas stream
g	gas phase
h	hydraulic



i	component i in gas phase
in	inner part
j	(evaporating) component of the melt
k	reactive component k in gas phase
m	melt phase
n	normalized conditions of combustion gases or flue gases (at temperature of 293.15 K and pressure of 101325 Pa)
o	outer part
p	first grid point near wall or surface
surface	surface of a liquid / melt
w	wall or surface

### Greek and other symbols

$\lambda$	heat conductivity [ $\text{W}\cdot\text{m}^{-1}\cdot\text{K}^{-1}$ ]
$\mu$	dynamic viscosity of fluid phase or molecular viscosity [ $\text{Pa}\cdot\text{s}$ ]
$\mu_t$	turbulent viscosity [ $\text{Pa}\cdot\text{s}$ ]
$\delta_N$	Nernst boundary layer thickness [m]
$\rho$	density [ $\text{kg}\cdot\text{m}^{-3}$ ]
$\Phi$	thermodynamic factor [-]
$\theta_w''$	wall or surface heat flux [ $\text{W}\cdot\text{m}^{-2}$ ]
$\phi_w''$	local wall or surface mass flux [ $\text{kg}\cdot\text{m}^2\cdot\text{s}^{-1}$ ]
$\sigma$	surface tension [ $\text{N}\cdot\text{m}^{-1}$ ]
$\gamma$	chemical activity coefficient [-]
$\Delta$	difference between two different values
$\nabla$	vector differential operator [-]
$\kappa$	Von Karman constant [-]
$\varepsilon$	turbulent dissipation rate [ $\text{m}^2\cdot\text{s}^{-3}$ ]
$\tau$	shear stress [ $\text{kg}\cdot\text{m}\cdot\text{s}^{-2}$ ]
$\alpha_{1,2}$	constants in equation 2.17 [-]
$\chi$	mass fraction [-]
$\bar{\omega}$	time-mean of a certain variable $\omega$ (applied for different variables like v, T)

## 2.1 Mass transfer evaporation model

The evaporation model for glass melts, developed in this study and described in this chapter, calculates the evaporation kinetics of volatile species from static glass melts in direct contact with flowing gas phases [4][5]. The model is based on Fick's diffusion law for the melt and quasi-steady gas phase mass transfer relations, taking into account changing melt/gas phase boundary concentrations in both gas and glass melt phase.

Beerkens and Van Limpt [6][3] described a model to predict the evaporation rates of volatile species from a glass melt. The evaporation process from glass melts in industrial glass furnaces can be described as a process of diffusion of a volatile component in an almost static glass melt layer moving along a glass surface. This layer is exposed during certain time to a gas flow (or combustion atmosphere). However, especially in regions with strong convection loops (e.g. bubbling zone) this assumption of a static melt is not justified and the convective mass transfer in the melt has to be accounted for as well.

The length  $L_g$  of the gas flow along the glass surface, starting from the leading edge (where the gas stream first touches the melt surface), is typically a few meters. At the glass melt surface, the glass component  $j$  reacts or evaporates, forming volatile component  $i$ . This component  $i$  diffuses through a gaseous Nernst boundary layer (typically 0.5-5 cm thickness) in the gas phase above the melt. The Nernst boundary layer thickness ( $\delta_N$ ) is defined in equation 2.1.

$$\delta_N = \frac{\Delta C_i}{\left(\frac{\partial C_i}{\partial y}\right)_{y=0}} \quad (2.1)$$

In this equation  $Q_i$  is the molar evaporation rate of  $i$ .  $\Delta C_i$  represents the difference between the molar concentration of species  $i$  in the gas phase near the surface ( $C_i^*$ ) and concentration of that species in the main gas stream ( $C_i^{\text{bulk}}$ ), just outside the gas boundary layer. Figure 2.1 illustrates this process. In cases of static melts and high evaporation rates, depletion of volatile component  $j$  at the surface layer of the melt will take place. The degree of depletion depends on exposure time, diffusion rate in the melt and the evaporation rate.

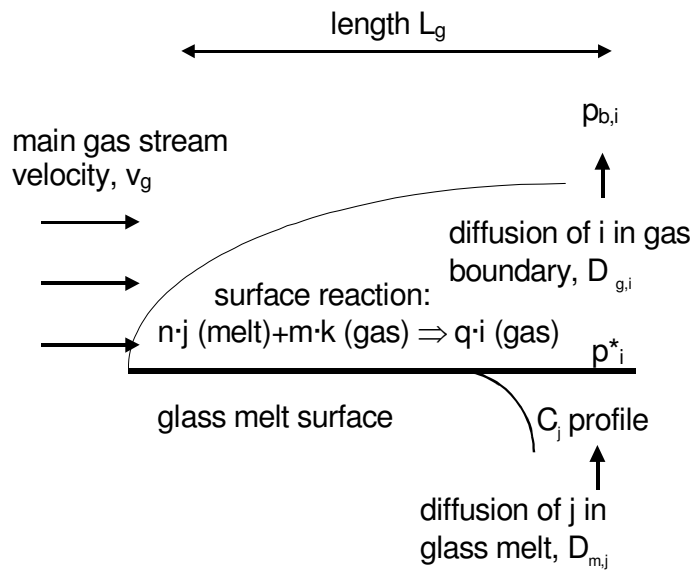
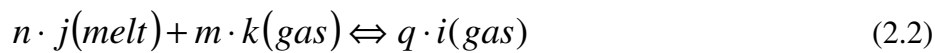


Figure 2.1: Schematic presentation of the evaporation process for a component  $j$  reacting at the glass melt surface with gaseous species  $k$  to form gaseous species  $i$ .

Evaporation of a component  $j$  from the melt, reacting with a gas species  $k$  and forming gaseous species  $i$  according to:



leads to loss of component  $j$  from the surface of the melt. It is assumed that the local partial vapor pressure (just above the melt) of evaporation product  $i$ , is in equilibrium with  $k$  and  $j$ . The saturation pressure of component  $i$  ( $p_i^*$ ) depends on the chemical activity of component  $j$  at the glass melt surface and partial pressure of reacting gas component  $k$ :

$$p_i^{*q} = K(T) \cdot a_j^n \cdot p_k^m \quad (2.3)$$

An example is the loss of  $\text{Na}_2\text{O}$  ( $j$ ) from the soda-lime-silica glass melt surface by a reaction with water vapor ( $k$  is water vapor) forming  $\text{NaOH}$  gas species ( $i$ ).

### 2.1.1 Mass transport in a static melt layer

The diffusion of an evaporating glass melt component (j) to the surface of the static glass melt (m) can be described by the second diffusion law of Fick, describing the concentration profile of  $C_j$  in the melt:

$$\frac{\partial C_j}{\partial t} = D_{m,j} \cdot \frac{\partial^2 C_j}{\partial y^2} \quad (2.4)$$

Equation 2.4 is only valid if no chemical reaction of j takes place. The interdiffusion coefficient value ( $D_{m,j}$ ) [7], is temperature and composition dependent, and therefore will also be position dependent. However, in most cases composition differences between the glass melt surface and the interior of the melt are often only moderate, so that  $D_{m,j}$  is often assumed to be constant during the time of the evaporation process and within the diffusion distance. This assumption may lead to some inaccuracy in the derivation of the diffusion rates [8][9], depending on the concentration profile.

The boundary and initial conditions, assuming an infinitely deep melt (depth of melt is much larger than the thickness of the layer with a non uniform concentration profile) are:

$$\text{at } t = 0 \quad -\infty < y < 0 \quad C_j = C_j^{\text{bulk}} \quad (2.5a)$$

$$\text{at } t > 0 \quad y \rightarrow -\infty \quad C_j = C_j^{\text{bulk}} \quad (2.5b)$$

$$\text{at } t > 0 \quad y = 0 \text{ (surface)} \quad C_j = C_j^{\text{surface}}(t) \quad (2.5c)$$

For the transpiration evaporation tests with shallow melt layers, as described in chapter 3, the assumption of an infinite deep melt is not valid and the boundary conditions 2.5a and 2.5b have to be modified into the equations 2.5d and 2.5e. The glass surface is located at  $y = 0$  and the bottom of the glass melt is located at  $y = y^{\text{bottom}}$ .

$$\text{at } t = 0 \quad y^{\text{bottom}} < y < 0 \quad C_j = C_j^{\text{bulk}} \quad (2.5d)$$

$$\text{at } t > 0 \quad y = y^{\text{bottom}} \quad \partial C_j / \partial y = 0 \quad (2.5e)$$

The time dependent surface concentration  $C_j^{\text{surface}}(t)$  depends on the evaporation losses at the surface of the melt and the diffusive transport of component j in the melt. Equations 2.4 and 2.5 are only valid for static melts. In paragraph 2.2, mass transport in the melt by convection plus diffusion is discussed.

At the glass melt surface, at  $y = 0$ , the loss of component  $j$  from the melt is given by Fick's law:

$$Q_{m,j} = -D_{m,j} \cdot \left( \frac{\partial C_j}{\partial y} \right)_{y=0} \quad (2.6a)$$

The concentration profile in the melt and the slope  $(\partial C_j / \partial y)_{y=0}$ , can be determined by the mathematical solution of equation 2.4 and boundary conditions 2.5. Among others, Beerkens [3] and Cable [10] presented an equation to calculate the concentration of volatile species  $j$  at the interface melt-gas, which has been derived from Crank [11]. However, this equation can only be applied for the assumption of a semi-infinite melt and constant ratio between surface concentration of component  $j$  and  $p_i^*$ .

In most studies presented in literature [8][9][10] and in case of the evaporation models applied in this study, the diffusion coefficient in the melt is often assumed to be constant during the mass transfer processes in the melt at isothermal conditions.

### 2.1.2 Mass transport in the gas phase

Similar as for the melt phase, the molar flux of a volatile species  $i$  can be determined from Fick's law for the gas phase:

$$Q_{g,i} = -D_{g,i} \cdot \left( \frac{\partial C_i}{\partial y} \right)_{y=0} \quad (2.6b)$$

Lewis and Whitman [12] described the theory of film models for mass transfer in fluids. This theory describes the mass transfer in a fictive mass transfer boundary layer  $\delta_N$  (here the concentration of gas species are position dependent). In this approach the assumptions are:

- The mass transfer in the gaseous phase takes place through this boundary layer;
- The one-dimensional mass transfer in this layer only takes place by diffusion;
- The concentration profile is stationary, which means that it is time independent.

Based on these assumptions the equation of continuity in the boundary layer is:

$$\frac{d^2 C_i}{dy^2} = 0 \quad (2.7a)$$

The boundary conditions for the Nernst boundary layer are:

- At  $y = 0$  (surface) :  $C_i = C_i^*$  (equilibrium concentration)
- At  $y = \delta$  :  $C_i = C_i^{bulk}$  (2.7b)

Here  $C_i$  is the molar concentration of component  $i$  in the gas phase in moles/m<sup>3</sup>. From the equations (2.6b) and (2.7) one can derive:

$$Q_{g,i} = \frac{D_{g,i}}{\delta_{N,i}} \cdot (C_i^* - C_i^{bulk}) = \frac{D_{g,i} \cdot \Delta C_i}{\delta_{N,i}} \quad (2.8)$$

The mass transfer coefficient for gaseous species  $i$  in the gas phase is:

$$h_{g,i} = \frac{D_{g,i}}{\delta_{N,i}} \quad (2.9)$$

Application of the ideal gas law and assuming isothermal conditions in the boundary layer, combined with the equations 2.8 and 2.9 give for mass transfer of species  $i$  into the gas phase:

$$Q_{g,i} = \frac{h_{g,i}}{R \cdot T} \cdot (p_i(t)^* - p_i^{bulk}) \quad (2.10)$$

When  $r$  different volatile components  $i$  are formed by different reactions from one glass component  $j$  (e.g. if Na<sub>2</sub>O in the melt evaporates as gaseous NaOH and gaseous Na:  $r = 2$ ), then the loss component  $j$  from the melt  $Q_{m,j}$  can be derived from:

$$\sum_{i=1}^r \frac{n_i}{q_i} \cdot Q_{g,i} = Q_{m,j} \quad (2.11)$$

In this equation  $n$  and  $q$  are the stoichiometric factors given in the general applicable equilibrium reaction 2.2.

For different geometrical designs, the local mass transfer coefficient  $h_{g,i}$  for mass transport through the boundary layer at the gas phase side can be estimated by Sherwood (Sh) relations (valid for given geometrical conditions and flow regimes) [13] and the relation:

$$h_{g,i} = \frac{Sh_{d,g,i} \cdot D_{g,i}}{d} \quad (\text{for transpiration experiments with tubes with an inner diameter } d) \quad (2.12a)$$

$$h_{g,i}(x) = \frac{Sh_{x,g,i} \cdot D_{g,i}}{x} \quad (\text{for industrial glass furnaces at } x \text{ meter downstream from the leading edge}) \quad (2.12b)$$

For gases, most Sherwood mass transfer relations show an analogy to Nusselt heat transfer relations [13][14]. The Sherwood number (Sh) depends in the same way on the diffusion coefficient  $D_{g,i}$  and the Schmidt number (Sc) as the Nusselt number (Nu) depends on the thermal diffusivity ( $=\lambda/(\rho \cdot C_p)$ ) and the Prandtl number (Pr).

For different geometries (e.g. flow through straight tubes, gas flows along flat plates) the Nusselt heat transfer relations can be obtained from the VDI-Wärmeatlas [15]. Figure 2.2 shows the transpiration set-up schematically used to study evaporation processes from glass melts exposed to gas flows. The set-up exists of a horizontal tube, with a boat (vessel) placed in a section with uniform temperature. The tube is flushed with a gas flow and the boat is (partly) filled with a liquid or melt. The value of the mass transfer coefficient,  $h_{g,i}$  depends on the gas velocity, the dimensions and geometry of the tube in our experimental set-up, the position of the boat filled with the melt and the filling level of the boat. For these cases Sherwood relations are not available from literature.

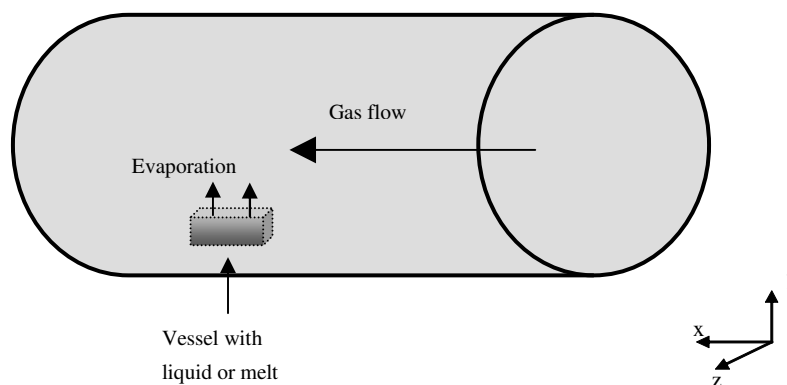


Figure 2.2: Schematic presentation of a transpiration evaporation set-up. In the horizontal tube, a boat (vessel) filled with a liquid or melt is placed in a section with uniform temperature. The melt is exposed to a gas flow rate. The gas flow rate as well as the gas composition are controlled.

In paragraph 2.3, different approaches will be shown to determine the mass transfer coefficient in the gas phase for transpiration experiments as well as for industrial glass furnaces.

## 2.2 Mass transport in the melt

Flow within the melt, created by the imposed glass pull or forced bubbling leads to forced convection. Free convection is caused by density differences present within the melt (e.g. due to temperature differences or concentration gradients) or surface tension gradients at the surface of the melt. Surface tension gradients and vertical density gradients may occur together and may lead to convection rolls. Convection flows might have an impact on the transport of volatile species in the melt and the local surface composition (refreshing the volatile species depleted top layer), which is assumed to be in equilibrium with the local atmosphere directly above the melt

The 3-dimensional flows in a glass melt can be derived from the moment equations or Navier-Stokes equations and the mass conservation equation, which are presented in appendix I.

Equation 2.40 in appendix I shows the effect of convection and diffusion on local concentration changes of compound  $j$  in a melt. The Péclet number ( $Pe$ ) in equation 2.13 is a dimensionless number expressing the ratio between convective transport and diffusive transport over a characteristic length  $L$ . Roughly, for  $Pe > 1$  transport of  $j$  in the melt is mainly a result of convection.

$$Pe_j = \frac{v \cdot L}{D_j} \quad (2.13)$$

In equation 2.13 'L' is a characteristic length to be defined (e.g. for our experimental studies the length of the glass melt sample boat). To simulate the mass transport in the melt, CFD (=Computational Fluid Dynamics) simulations were used, which discretize the equations of change (see appendix I) for discrete volume cells that compose the domain of interest and solves these equations with appropriate boundary conditions:

At the side walls and bottom of the boat:

$$v_x = v_y = v_z = 0$$



At the glass surface:

$$v_y = 0$$

$$\partial v_x / \partial y = \partial v_z / \partial y = 0 \text{ (no shear stress)}$$

$$Q_j(x, z, t) = \text{dependent on time, } x \text{ and } z \quad (2.14)$$

In this study, the software package GTM-X is used, which is developed by TNO [16] [17] to simulate numerically the convection and diffusion processes in glass melts. Details on the numerical methods used in GTM-X are discussed by Batchelor [18], Ferziger and Perić [19] and Patankar [20]. GTM-X will be used to simulate convection in a melt as a result of non-uniform evaporation from a surface of a melt (see paragraph 4.5.1)

### 2.2.1 Marangoni flows

In the surface layer of a glass melt, local convective flows may be caused by the Marangoni effect. In a nearly static glass melt the composition of the top layer might differ from the bulk composition as a result of depletion of volatile species. Due to convective Marangoni flows the local composition of the glass melt surface might change. The local composition of the glass surface may affect the evaporation rates of volatile species in the melt (see paragraph 2.1).

The Marangoni flow is the phenomenon that a liquid flows along a gas-liquid or liquid-liquid interface, from areas with low surface tension to areas with higher surface tensions [21] [22]. Local, in-stationary flows in the surface layer of a fluid can be a result of differences of surface tension or interfacial tension (interface between liquids or liquids and solids). The surface tension depends on the liquid composition. For glass melts certain compounds can decrease or increase surface tension. The surface tension of glass melts depend hardly on temperature. The Marangoni effect can occur in liquid-gas systems and liquid-liquid systems and can be a result of concentration and/or temperature gradients. In case of concentration gradients, the effect is called the solutal Marangoni effect. Concentration gradients at the surface of a liquid can be the direct result of non-uniform mass transfer between phases or non-homogeneous glass.

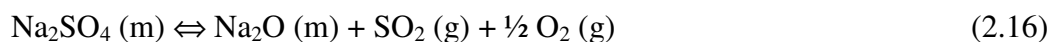
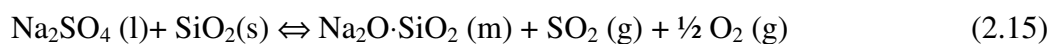
The driving force for Marangoni flows is the surface tension difference, mostly determined by the derivative of the surface tension to the concentration ( $\partial\sigma/\partial C$ ) or local concentration differences of surface active glass compounds at the surface of the melt ( $\Delta C_j^{\text{surface}}$ ) [21]. The derivative of the surface tension to temperature  $\partial\sigma/\partial T$  might be another driving force for Marangoni flows [23]. Marangoni flows close to the interface generally increase the transport

of matter to and from the interface. The Marangoni convection in a liquid therefore increases the mass transfer coefficient with respect to pure diffusive mass transfer in a static melt.

For glass melts studied here, local concentration differences at the surface of a melt might be a result of local differences in evaporation rates. For a chemical reacting mixture of raw materials and glass melt phases there might be random disturbances or heterogeneities that can cause Marangoni flows.

The Marangoni flows at the surface of a melt during the melting of batch and glass might be a result of:

- Formation of a sulfate gall (mainly  $\text{Na}_2\text{SO}_4$ ) not mixing with other phases (such gall layers show a relatively low surface tension, low density) at the surface of the melt [22][24]. Due to the local chemical reactions 2.15 and 2.16, between the gall and the surface of the melt, the composition of the glass melt surface might become non-uniform. At the surface of the melt surface tension gradients appear, which cause Marangoni flows;



- Local different evaporation rates might also lead to local differences in surface composition and surface tension gradients. Local differences in temperature, gas velocity or gas composition (e.g. reducing flame parts) may be responsible for non-uniform evaporation rates.
- Local temperature differences at the glass melt surface. This is probably a minor effect.

In a the investigated glass melts, components like  $\text{B}_2\text{O}_3$ ,  $\text{K}_2\text{O}$ ,  $\text{SO}_3$  and  $\text{Na}_2\text{O}$  are volatile and may decrease surface tension [24][25][26]. In these melts Marangoni flows may appear as a result of non-uniform evaporation from the surface of the melt.

### 2.2.2 Transport of boron species in borosilicate melts

In a static melt, existing of one single melting phase or solution, the transport of volatile species can be described by the 2<sup>nd</sup> law of Fick (equation 2.4). Flow within the melt, created by the imposed glass pull or forced bubbling leads to forced convection. Free

convection, as previously explained, can be caused by density differences within the melt (e.g. due to temperature differences or concentration gradients) or surface tension gradients at the surface of the melt. Convection flows might have influence on the transport of volatile species in the melt and the local glass melt surface composition, which is assumed to be in equilibrium with the atmosphere. Without convection, depletion of volatile glass melt species at the glass melt surface has to be accounted for. Computational Fluid Dynamics calculation schemes (solving equations shown in appendix I) can be applied to model the convection patterns (due to temperature differences or due to forced convection) in glass melts in tanks or crucibles and to describe the transport of the volatile glass compounds. In a melt existing of 2 or more melt phases (phase segregation in liquid state) with different densities, convection flows are expected as well until equilibrium or full segregation is established.

Oldfield and Wright performed evaporation tests with borosilicate glass melts in a dry static atmosphere during periods up to 70 hours at temperatures between 1200 and 1500 °C [27]. The measured evaporation rates were decreasing in time and the results were attributed to the formation of a silica rich surface layer depleted in volatile species. Conradt and Scholze [1] showed that the evaporation losses decrease in time during their transpiration evaporation tests with ternary soda-borosilicate glass melts ( $\text{SiO}_2 : \text{B}_2\text{O}_3 : \text{Na}_2\text{O} = 66 : 18 : 16$  mass-%) at temperatures between 1000 and 1200 °C exposed to furnace atmospheres with partial water vapor pressures between 0 and 0.4 bar. The samples from these transpiration evaporation tests showed the presence of a visual surface layer separated from the bulk melt.

Ehrig et al. [28] performed transpiration evaporation experiments with different soda-borosilicate glass melts at temperatures up to 1600 °C and water vapor pressures between 0 and 0.5 bar. They showed that for a melt at 1500 °C, with the composition:  $\text{SiO}_2 : \text{B}_2\text{O}_3 : \text{Na}_2\text{O} = 71 : 24 : 5$  mass-%, the  $\text{SiO}_2$ -rich surface layer disappeared as a result of eddy-like convective currents in the melt. According to Conradt, the existence and appearance of these eddies in the tests of Ehrig in contrast to surface depletion observed by Conradt can be explained by the much lower viscosity (0.3 Pa.s for Ehrig's experiment at 1500 °C versus 8 Pa.s for Conradt's experiment at 1200 °C) in Ehrig's glass melt evaporation experiments.

However, the observed eddies during Ehrig's evaporation experiments might be a result of phase segregation in the melt or just local concentration differences at the glass melt surface as well. Phase segregation in a melt may lead to local concentration differences of surface active compounds at the surface of the melt. As a result of these surface tension differences Marangoni flows might be induced. Phase segregation in borosilicate melts has been studied by Vogel [29][30] and will be discussed in paragraph 2.4.

In his thesis, Delorme [31] describes the results of transpiration evaporation tests with different alkali-borosilicate glass melts for temperatures between 1060 °C and 1200 °C. It was found that the boron evaporation rates are controlled by both the diffusion in the melt and transport in the gas phase. From his experiments he derived interdiffusion coefficients of boron in the order of magnitude  $10^{-12}$  to  $10^{-11}$  m<sup>2</sup>/s. Based on the viscosities of these melts ( $0.6 < {}^{10}\log\left(\frac{\mu_{melt}}{Pa.s}\right) < 1.9$ ) and the statistically derived correlation of Hermans [7] (equation 2.17), between diffusion on one side and viscosity and charge of the diffusing ion on the other side, the diffusion coefficients of boron in the borosilicate melts are estimated.

$$\log\left(\frac{D_{m,j}^T}{m^2 \cdot s}\right) = \alpha_1 + b \cdot \alpha_2 \cdot \log\left(\frac{\mu_{melt}}{Pa.s}\right) \quad (2.17)$$

For cations in silicate melts Hermans found  $\alpha_1 \approx -9.8$ ,  $\alpha_2 \approx -0.21$  and b is the valence of the cation. For the boron cation (B<sup>3+</sup>), b= 3. As will be discussed in paragraph 2.6.3, it is assumed that the apparent interdiffusion coefficient (D), intrinsic diffusion coefficient (D<sup>I</sup>) and tracer coefficient (D<sup>T</sup>) are about equal for most cations except Si<sup>4+</sup> ( $D \approx D^I \approx D^T$ ). Si<sup>4+</sup> cations are the main cations in the melt and act as a network former. Because of relaxation flows, the apparent interdiffusion coefficients of Si<sup>4+</sup> can be about 5 to 10 times higher than the tracer diffusion coefficient. Boron in the melt can be present as a network-former as well and the assumption:  $D \approx D^I \approx D^T$  might lead to a systematic error in the estimated interdiffusion coefficient of boron ( $D \gg D^I$ ).

The interdiffusion coefficient of boron in alkali-lean borosilicate glass melts is determined on values between  $1.0 \cdot 10^{-11}$  and  $6.6 \cdot 10^{-11}$  m<sup>2</sup>/s for temperatures between 1400 and 1500 °C. For our evaporation tests with alkali-lean borosilicate glass melts (originally with about 5 mass-% B<sub>2</sub>O<sub>3</sub>), this would mean that the boron evaporation rates would decrease 60 to 80 % within a period of 30 till 60 minutes after starting the evaporation test. Our evaporation tests did not show this strong decrease of evaporation rates during this measuring period, thus there should be convection or the real interdiffusion coefficients are much higher.

### 2.3 Mass transport in the gas phase

For relatively simple geometries mass transfer relations for the transport of species through boundary layers in the fluid phases can be derived from literature or can be empirically derived from laboratory experiments. For more complex geometries, Computation Fluid Dynamics (CFD) calculations can be applied to determine the local mass transfer coefficients. CFD calculations can be used to calculate the concentration distribution of volatile species in the atmosphere (see paragraph 2.3.1). From the calculated concentration distribution, the local thickness of the Nernst boundary layer (equation 2.1) and local mass transfer coefficient (equation 2.9) of a volatile species can be derived. In paragraph 2.3.2, the derivation of an empirical mass transfer relation for the gas phase Nernst boundary layer thickness (or Sherwood relation) is discussed for the experimental set-up used in this study. For industrial glass furnaces an approach to determine the mass transport rates in the gas phase is proposed in paragraph 2.3.3.

For the laboratory evaporation experiments in this study, the so-called transpiration set-up is used, described in detail in chapter 3. In this set-up, a controlled gas volume flow along a liquid/melt surface is applied to study evaporation of volatile compounds from the surface of the liquid/melt into the atmosphere. In order to model the mass transport of volatile species from the surface of the melt/liquid into the atmosphere, mass transfer relations are required. This paragraph shows two different methods to derive these mass transfer relations, by models or empirically (paragraphs 2.3.1 and 2.3.2).

Transpiration evaporation tests with model liquids (water / acetone) and glass melts have been carried out in a heated horizontal tube. Figure 2.2 shows the set-up schematically. In the horizontal tube, a boat (vessel) filled with a liquid or melt is placed in a section with uniform temperature. The melt is exposed to a controlled gas flow rate. The gas flow rate as well as the gas composition can be adjusted. The evaporation rates of a volatile species can be measured in two ways:

- 1) gravimetrically (if only one species evaporate and no components are absorbed by the melt) and
- 2) by measuring the vapor pressure (concentration) of the volatile compound in the gas outlet flow, the gas volume flow rate and the duration of the experiment.

### 2.3.1 Relations for describing mass transfer in transpiration experiments

The software package GTM-X is used to perform CFD simulations of the flow dynamics and mass transfer in the tube furnace used in the transpiration experiments. GTM-X is a CFD-model developed by TNO and dedicated to simulate mass and heat transfer in glass melt processes and combustion processes in industrial glass furnaces. GTM-X is a software package capable of both steady state and time-transient simulations [4]. The code is block structured. For the modeling of a glass furnace for example, the different blocks could be domains such as the melt, the combustion chamber and the batch blanket. Every block is divided in many small grid cells.

Per block, different sets of models can be selected (e.g. there is no need to solve for flow in refractories or for turbulence in the glass bath), allowing selection of the equations (such as mass, energy, momentum and species conservation equations) that have to be solved for on each cell in a certain block. Per block, the body-fitted grid is created and within each block the level of grid refinement can be specified, enabling the use of many grid cells and accurate discretization where it is really needed. Details on the physical models and numerical methods that have been used in GTM-X can be found in Batchelor [18], Ferziger and Perić [19] and Patankar [20].

#### *CFD calculations for mass transfer in a transpiration experiments*

The stationary gas flow pattern and the volatile species concentration distribution in the tube of the transpiration set-up are calculated in all three dimensions at each position. The gas flow rate and the Reynolds number in the tube are low ensuring that the flow remains in the laminar flow regime in the tube. Although, disturbances in this laminar flow are expected in the vicinity of the vessel obstructing the gas flow. The governing equations for stationary laminar flow with mass transport of species in three dimensions can be found in e.g. Bird, Stewart and Lightfoot [13] as well as in the appendix I of this chapter.

It is assumed that there is no significant heat exchange of the tube with the ambient and that the gas flow is in thermal equilibrium within the tube. As a consequence of the evaporation process from the melt or liquid, evaporation enthalpy is withdrawn from the heat contents of the liquid in the boat and consequently the temperature of the liquid will drop. Especially for liquids with a high molar heat of evaporation (like water) in combination with high evaporation rates, this may have large impact on the for evaporation processes important surface temperature. For our preliminary evaporation tests with water, the process conditions

are chosen in such a way that the evaporation rates are relatively low so that the temperature difference between the surface of the water and the atmosphere is less than 1 K.

For evaporation transpiration tests with glass melts at temperature between 1400 and 1500 °C, it is estimated that the heat of evaporation is in the order of magnitude of 20 to 100 W/m<sup>2</sup>. For the vessel with a glass melt in our transpiration set-up, and Fourier's law of heat conduction [13] it is estimated that the temperature difference between the bottom and surface of the melt is maximum about 0.5 K.

For the CFD modeling of mass transport in the tube, the surface temperature of the liquid in the boat and the gas temperature are assumed to be equal. Thus, the temperature of the whole system is assumed to be uniform and no energy conservation equations need to be solved. The 5 transport equations, shown in appendix I, are computed iteratively for the mesh given by Figure 2.3 and the boundary conditions presented below. These computations are based on the finite volume method according to Patankar [20].

### *Boundary conditions*

The boundary conditions of the experimental transpiration system are:

- At the inlet of the tube ( $x = 0$ ) the concentration of the gaseous volatile species from the glass melt,  $C_i = 0$  and a fully developed laminar gas flow velocity profile is assumed, with an average  $v_x$ -velocity according to the applied gas mass flow;

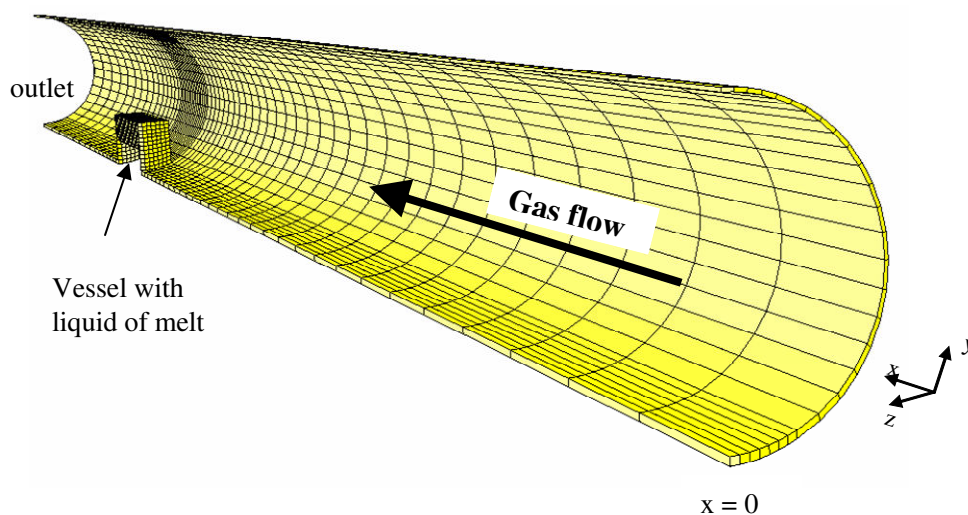


Figure 2.3: Geometry of the tube and the grid point distribution projected on the tube wall and on the liquid-filled container. The figure shows the cross-section of the transpiration set-up in the length-direction.

- On the evaporating surface of the liquid in the container, at the liquid-gas interface just in the gas phase, the vapor pressure is in equilibrium with surface composition of the liquid:  $C_i = C_i^*$ ;
- On all solid boundaries (tube and container walls), the three velocity components are set to zero (no slip) and for the volatile species, a zero mass flux at these walls is assumed (no condensation, evaporation, absorption or desorption);
- On the outflow boundary of the gas flow, the concentration gradient of the volatile species in the gas phase is zero in all directions. The velocity in the y-direction as well as the z-direction are set to zero.

### *Geometry and grid point distribution*

Throughout the computational flow domain (gas phase) within the tube, a mesh or grid of volume cells has been constructed (see Figure 2.3). For each of these volume cells, the in appendix I defined set of differential equations has been discretized. Three velocity components, pressure and the concentration of the volatile species are calculated in each cell or node. A total number of  $1.6 \cdot 10^5$  grid nodes have been used in this case.

### *Results*

As a result of the CFD modeling the concentration of volatile species  $i$  in the outlet of the tube will be calculated. From the boundary conditions, it follows that the concentration of this species at the outlet area of the tube is uniform. The total evaporation flux ( $Q_i$ ) of the volatile species  $i$  is calculated from the product of the concentration  $C_i$  at the outlet and the gas volume flow in the tube divided by the surface area of the liquid in the boat.

By applying equation 2.1, it is also possible to calculate the local thickness of the Nernst boundary layer from the obtained concentration profile of volatile species  $i$  above the surface of the liquid in the boat.

### **2.3.2 Empirical derivation of mass transfer relations for transpiration experiments**

For gases, known Nusselt relations to determine heat transfer, can be used to derive analogous Sherwood relations for mass transfer in the same geometrical configuration. For this conversion, the Prandtl number (Pr) in the Nusselt relations has to be replaced by the Schmidt number (Sc) [13][14].



For different rather simple geometries (e.g. tubes, flat plate), Nusselt heat transfer relations can be obtained from the VDI-Wärmeatlas [15]. One of the major questions is whether existing Nusselt heat transfer relations (and Sherwood mass transfer relations) can be used to describe the mass transport of volatile species during transpiration experiments with more complicated shapes and geometrical configurations and with flow obstacles. Possible existing Sherwood/Nusselt relations that can be used or should be modified for describing transfer processes in transpiration experiments are:

- Relations for mass transfer at the inside surface of a tube or
- Relations for mass transport between two concentric cylinders.

Van Limpt et al. [4] investigated the applicability of these mass transfer relations for evaporation tests in a transpiration set-up, schematically shown in Figure 2.2. It was concluded that these Sherwood relations for mass transfer inside a tube cannot be applied for transpiration set-ups. Because of the obstruction of the gas flows by the boat and the complex gas flow above the liquid (due to the rim of the boat), modified Sherwood relations are required for this set-up. The filling level of the boat will also have an influence on the gas flow just above the melt.

For all laboratory transpiration evaporation experiments, the Reynolds number ( $Re_d = \rho \cdot v \cdot d / \mu$ ) for the undisturbed tube flow is lower than 1000 and this means that laminar flow conditions can be assumed since the critical Reynolds number for gas flows in tubes is about 2500 [32]. Above the critical Reynolds number, transition from laminar to turbulent flow conditions can be expected. However, the flow may show eddies if the flow is not well-developed downstream a rim or near the inlet of the tube.

In this study, new empirical mass transport relations for transpiration set-ups were derived from own investigations. CFD models are also used to predict the mass transport in the gas phase for rather complex geometries and shapes, like transpiration set-ups with rectangular, partly filled boats in horizontal cylindrical tubes. CFD modeling and relatively simple water evaporation experiments have both been performed to find or test mass transfer relations, describing the kinetics of evaporation in transpiration experiments and to validate these relations. Mass transfer relations are also required to derive vapor pressures or diffusion coefficients (see paragraph 4.4). The latter parameters are required to predict evaporation kinetics in industrial glass furnaces

In most transpiration experiments, a boat with a liquid or melt is placed in the tube. In that case, Sherwood relations derived for mass transfer between the surfaces of two concentric tubes with laminar flow [15][33][34], might improve the prediction of the mass transfer rates for the evaporation tests. Now the boat in the tube is considered to be shaped cylindrically and placed at the centerline of the tube (see Figure 2.4a).

The surface of this inner tube is partly covered by a liquid or a melt. This introduces an additional assumption since most boats, and certainly the surface of a liquid, are not cylindrically shaped but rectangular. The rim of the boat will also disturb the gas flow pattern. Often the boat is not placed at the centerline and the length of the boat is much shorter than the length  $L$  of the tube.

The gas is assumed to flow between the inner and the outer cylinder (or boat). In this situation  $d_o$  is the inner diameter of the outer tube and  $d_{in}$  the outer diameter of the inner tube.

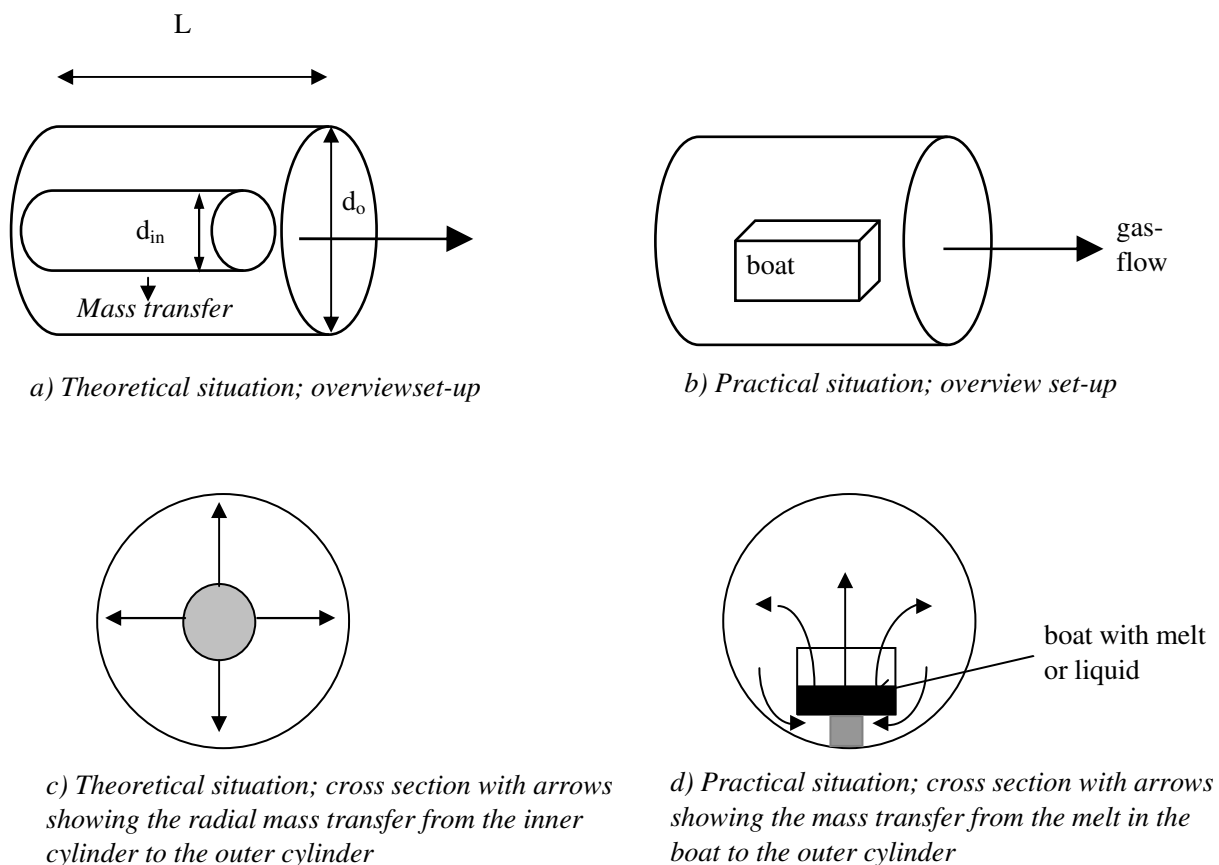


Figure 2.4: Schematic presentations of mass transfer between two concentric cylinders from the surface of the inner tube to the inner surface of the outer tube (a+c) and schematic presentations of mass transfer from a boat filled with a melt or liquid into the gas atmosphere in the tube (b+c)

The hydraulic diameter of the system is defined as  $d_h = d_o - d_{in}$  and the Reynolds number is now:  $Re_d = \rho \cdot v_{avg} \cdot d_h / \mu$ .

For this specific situation of 2 concentric tubes, the available Nusselt relations [15][33][34] have been converted into Sherwood relations as described previously in this paragraph. For the theoretical case of Figure 2.4a + c, the Sherwood equations 2.18a till 2.18e can be used to estimate the Sherwood number. It is assumed that radial mass transfer takes places between the inner cylinder and the outer cylinder. The temperatures are assumed to be uniform and constant.

In case of two concentric cylinders, with a fully developed laminar gas flow in the space between the cylinders and constant concentrations of the volatile species  $i$  at the surfaces of both cylinders, only  $Sh_1$  (equation 2.18a) can be used to calculate the Sherwood number [33][34].

$$Sh_1 = 3.66 + 1.2 \cdot \left( \frac{d_{in}}{d_o} \right)^{0.5} \quad (2.18a)$$

This situation represents the end conditions in the system of two long concentric cylinders.

For situations with a varying concentration profile of component  $i$  (in axial direction) and a fully developed laminar gas flow, the average Sherwood number increases, with increasing values of  $Re_d \cdot Sc \cdot d_h / L$ . Here is  $L$  the length of the tube. In this case the equations 2.18b and 2.18c [33] can be used to calculate  $Sh$ .

$$Sh_2 = f_g \cdot \sqrt[3]{\frac{Re_d \cdot Sc \cdot d_h}{L}} \quad (2.18b)$$

$$f_g = 1.615 \cdot \left\{ 1 + 0.14 \cdot \left( \frac{d_{in}}{d_o} \right)^{1/3} \right\} \quad (2.18c)$$

Near the inlet of the two concentric cylinders a non uniform gas flow profile as well as a concentration profile of the volatile component  $i$  are developing. The Sherwood number can be calculated from equation 2.18d [15].

$$Sh_3 = \left\{ \frac{2}{1 + 22 \cdot Sc} \right\}^{1/6} \cdot \left( \frac{Re_d \cdot Sc \cdot d_h}{L} \right)^{0.5} \quad (2.18d)$$

Now the average Sherwood number over a length  $L$  for the complete system of two concentric cylinders with radial transport of component  $i$  from the surface of the inner cylinder to the surface of the outer cylinder can be calculated from equation 2.18e [34].

$$Sh_{avg} = \left( Sh_1^3 + Sh_2^3 + Sh_3^3 \right)^{1/3} \quad (2.18e)$$

The Sherwood relations for two concentric cylinders (equation 2.18a to 2.18e) were applied to predict the radial mass transfer for boats with different lengths of respectively 5, 10 and 20 cm. In all cases the boats were completely filled with water. The measured and calculated water vapor pressures were compared [4]. To calculate the water vapor pressures, mass transfer equation 2.18e and the equations 2.10 and 2.12 were used. The calculated water vapor pressures differ maximum about 5 to 10 % from the measured vapor pressure.

However, equation 2.18 cannot be applied directly for a transpiration set-up with partly filled vessels / boats. The rim of the boat will change the gas flow pattern above the liquid surface and the mass transfer from the surface of the liquid into the atmosphere. For this specific situation the empirical Sherwood relation 2.19 is defined.

$$Sh_{transpiration} = \left( C_1 + C_2 \cdot Re_d \cdot Sc + \left( \frac{2}{1 + 22 \cdot Sc} \right)^{0.5} \cdot C_3 \cdot (Re_d \cdot Sc)^{1.5} \right)^{1/3} \quad (2.19a)$$

$$h_{g,i} = \frac{Sh_{transpiration} \cdot D_{g,i}}{d} \quad (2.19b)$$

The Sherwood number for the transpiration set-up ( $Sh_{transpiration}$ ) depends in a similar way on  $Re$  and  $Sc$  as the Sherwood relation for two concentric cylinders (equations 2.18b and 2.18d). A fitting procedure based on the general equation given by equation 2.19 is used to describe the relation between  $Sh$ ,  $Re$  and  $Sc$ . In equation  $Re_d$  is defined as:  $Re_d = \rho \cdot v \cdot d / \mu$ , with  $d$  the inner diameter of the tube. The constants  $C_1$ ,  $C_2$  and  $C_3$  only depends on the geometry of the tube and the boat and were derived by a procedure of fitting experimental data with calculated data using this Sherwood relation. For transpiration experiments the mass flux  $Q_i$  can be now calculated from the equations 2.10, 2.12 and 2.19.

In paragraph 4.1 transpiration experiments with water and acetone are discussed to validate the applicability of this empirical relation and to derive values for  $C_1$ ,  $C_2$  and  $C_3$ . Equation 2.19a is only for a fixed geometry of the transpiration set-up, a fixed position of the vessel and a fixed filling level of the boat.

### **2.3.3 Determination of the Nernst boundary layer thickness in industrial glass furnaces**

Contrary to the almost laminar gas flows in the transpiration set-up, turbulent gas flows prevail in the combustion chamber of a glass furnace. For the gas flow, in the combustion space the surface of the melt can be regarded as a flat surface. Examining Figure 2.5, the gas boundary layer over a flat plate will be considered qualitatively [35]. At the point where the gases touches the plate (the leading edge), the undisturbed gas flow velocity is  $v_0$ . A laminar gas boundary layer is formed at the leading edge and grows in thickness with increasing distance from the leading edge. A transition region is reached where the flow changes from laminar to turbulent, with a consequent increasing boundary layer thickness. The turbulence becomes suppressed when approaching the surface of the plate. Near the surface a viscous sub layer (or laminar sub layer) is defined where viscous effects (shear stress between the horizontal gas sub layers) predominate. The turbulent sub layer, also called inertial sub layer or logarithmic sub layer, is the outer part of the boundary layer between the viscous sub layer and the free flow region.

The specific characteristics of turbulent gas flows are used to develop mathematical models for turbulence. According to Rietema [32] these 3 characteristics are:

1. On a macroscopic scale, the turbulent movements/flows are chaotic and unpredictable. There is no relation between the turbulent movements at different positions and time.
2. Apart from the mean velocity of the fluid, the turbulent movements do not have a preferential direction.
3. On a microscope scale there is coherence between the turbulent movements.

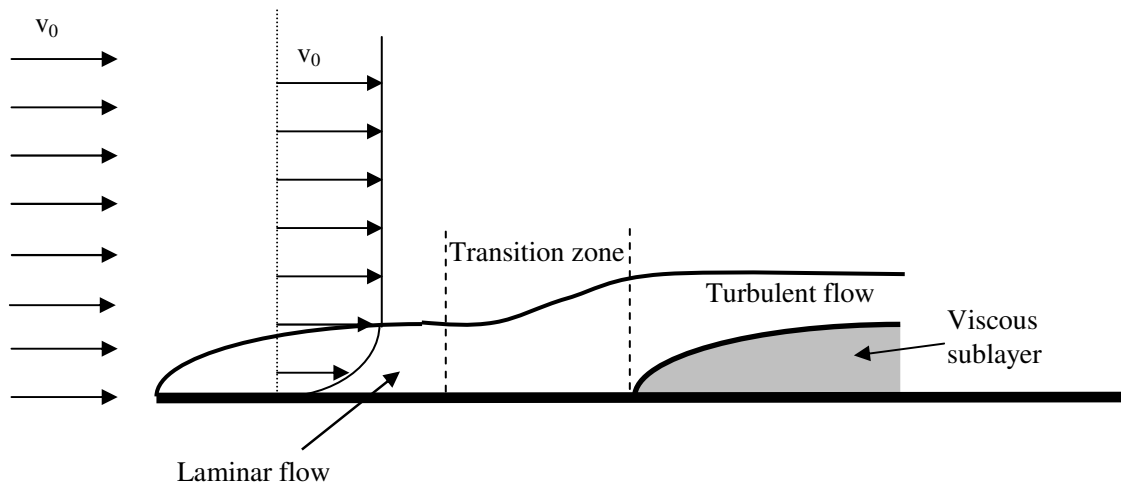


Figure 2.5: Details of the turbulent boundary layer flow over a flat plate.

The first two characteristics are analogous to the thermal molecular movements as described by kinetic gas theory [36]. On a microscopic scale the coherence between the turbulent movements is a result of viscosity (and shear stress) of the fluid. Because of the viscosity, the turbulent movements will be reduced and mechanical energy is dissipated. This is called kinetic energy dissipation.

For modeling of turbulent flows modified expressions for shear stress ( $\tau$ ) and molecular (or dynamic) viscosity ( $\mu$ ) have to be applied as well as for the turbulent kinetic energy ( $k$ ) and the turbulent dissipation rate ( $\epsilon$ ). For a simple turbulent flow an example will be given in which the modified expressions for shear stress and molecular viscosity are discussed [14][32].

### Example:

Assume a one-dimensional flow in the x-direction  $v_x$ , which is assumed to be a superposition of a time-mean velocity  $\bar{v}_x$  and a fluctuating part  $v_x'$ . In this example, the average velocities

$\bar{v}_y$  and  $\bar{v}_z$  in the other directions y and z are nil. Thus:

$$v_x = \bar{v}_x + v_x' \quad (2.20a)$$

$$v_y = v_y' \quad (2.20b)$$

$$v_z = v_z' \quad (2.20c)$$

When a gas flows with a velocity  $v_x$  through an area  $A$ , normal to the  $x$ -direction, the transport of momentum in the  $x$ -direction ( $I_{x,x}$ ) is:

$$I_{x,x} = (\rho \cdot v_x) \cdot v_x \cdot A \quad (2.21a)$$

Figure 2.6 shows schematically the transport of momentum in the  $y$ -direction ( $dI_{x,y}$ ), due to the gas flow in the  $x$ -direction, through a surface with an area  $dx \cdot dz$ , normal to the  $y$ -axis is:

$$dI_{x,y} = \rho \cdot v_x \cdot v_y \cdot dx \cdot dz \quad (2.21b)$$

However, because of turbulence, the momentum transport fluctuates in time and the time-mean transport of momentum  $\overline{dI_y}$  is given by:

$$\overline{dI_y} = \rho \cdot \overline{v'_x \cdot v'_y} \cdot dx \cdot dz \quad (2.21c)$$

The time-mean shear stress  $\overline{\tau_{yx}}$  due to both molecular and turbulent effects can now be written as:

$$\overline{\tau_{yx}} = -\mu \frac{d\overline{v_x}}{dy} + \rho \overline{v'_x \cdot v'_y} \quad (2.22a)$$

The first term of equation 2.22a may be considered as the laminar part and the second term as the turbulent part. By defining the turbulent (or eddy) viscosity  $\mu_t$  this equation yields:

$$\overline{\tau_{yx}} = -(\mu + \mu_t) \frac{d\overline{v_x}}{dy} \quad (2.22b)$$

With

$$\mu_t = \frac{\rho \overline{v'_x \cdot v'_y}}{\frac{d\overline{v_x}}{dy}} \quad (2.22c)$$

Please note that the equations 2.20 till 2.22 are only valid for this specific situation with a one-dimensional flow in the  $x$ -direction.

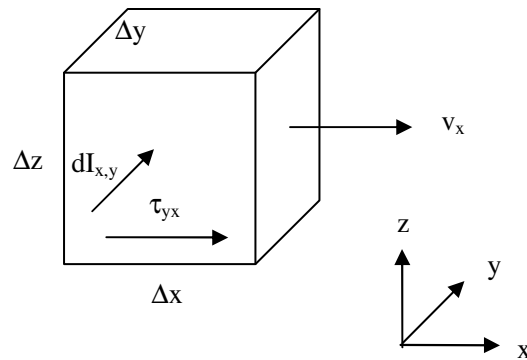


Figure 2.6: Schematic presentation of transport of momentum in the  $y$ -direction ( $dI_{x,y}$ ) through a surface with area  $\Delta x \cdot \Delta z$ , due to a gas flow (with velocity  $v_x$ ) in the  $x$ -direction.

The differential equations expressing the conservation of momentum and energy for turbulent flows include the unknown turbulent viscosity ( $\mu_t$ ). In order to obtain values for the eddy (or turbulent) viscosity throughout the flow domain, in the  $k$ - $\epsilon$  model [37][38] two additional differential equations have to be solved, one for the turbulent kinetic energy ( $k$ ) and one for the turbulent dissipation rate ( $\epsilon$ ). In this model the turbulent viscosity  $\mu_t$  is assumed to be proportional to  $k^2$  and  $\epsilon^{-1}$ .

### CFD modeling

In order to predict the mass transfer of volatile species from the surface of a liquid into a turbulent gas flow, the thickness of the Nernst boundary layer in the viscous sub layer has to be derived. Based on results of CFD calculations and the analogy between momentum, heat and mass transfer, a procedure has been developed to estimate the Nernst boundary layer thickness of the gas phase in the combustion chamber of industrial glass furnaces, just above the surface of the melt.

In this paragraph the method for estimating the local value of the Nernst boundary layer thickness from information of the CFD results is presented.

For CFD modeling the combustion space is divided in a large number of grid cells. In order to correctly determine the mass transfer of volatile species into the gas phase, for the first grid point  $p$  in this mesh in the gas phase domain above the glass melt surface, one should



determine whether this point  $p$  is located in the viscous sub layer or in the turbulent inertial sub layer.

For turbulence modeling of the gas velocity and energy transfer in combustion spaces by CFD codes such as GTM-X, usually the  $k$ - $\epsilon$  turbulence model is used [37][38]. However, the  $k$ - $\epsilon$  model only applies to fully turbulent flows.

As mentioned earlier, viscous effects play an important role in near-wall regions such as above the glass melt surface. The high turbulent Reynolds number approximations on which the  $k$ - $\epsilon$  models are based, as well as the empirically obtained values for the  $k$ - $\epsilon$  model constants are no longer valid in these regions. In order to correctly calculate momentum-, mass- and energy fluxes near the (melt) surfaces without the necessity to use very fine grids, wall-functions for velocities, temperature, mass fractions and turbulence quantities are normally used instead of straightforward boundary conditions. For the descriptions of the wall functions for heat transport and mass transport, usually analogies with momentum transport are used.

#### *Determination of Nernst boundary layer thickness*

The definitions of the used dimensionless normalized velocity ( $U^+$ ), dimensionless normalized temperature ( $T^+$ ) and dimensionless normalized mass fraction ( $X^+$ ) in this chapter, are given in appendix II.

Figure 2.7 shows a turbulent dimensionless normalized velocity profile ( $U^+$ ) near a wall (e.g. glass melt surface) [37] as a function of the dimensionless distance normal to the wall ( $y^+$ ). These dimensionless parameters are defined in such a way that a general applicable relation was obtained between  $y^+$  and  $U^+$ . Please note that the scaling of the x-axis is <sup>10</sup>logarithmic. The transition point  $y_m^+$  at point  $x$  subdivides the boundary layer in a viscous sub layer ( $y^+ < y_m^+$ ) and in an inertial sub layer ( $y^+ \geq y_m^+$ ). The transition point  $y_m^+$  depends on  $y$  and  $z$ . The dots in the figure represent the exact solutions obtained from Direct Numerical

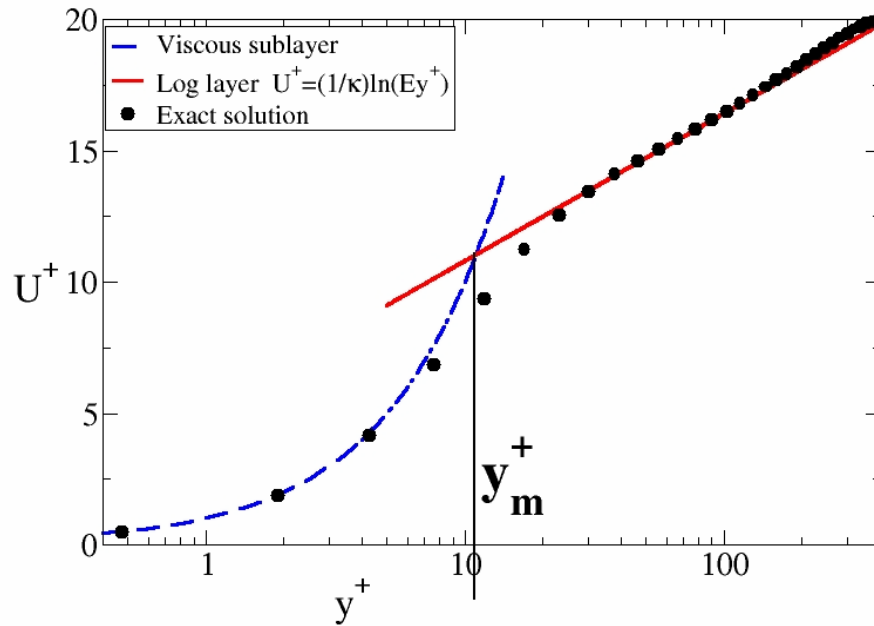


Figure 2.7: General profile of turbulent wall-parallel dimensionless velocity near a wall or surface. Given are the results of a DNS (Direct Numerical Simulation) simulation, which can be considered as the exact solution (black dots). The curves are fitted with equation 2.23.  $U^+$  is a dimensionless velocity and  $y^+$  the dimensionless distance perpendicular to the wall/surface. The wall or surface is positioned at  $y^+ = 0$ . Please note the logarithmic x-axis.

Simulations (DNS). For these simulations an extremely fine grid, with grid points in the viscous sub layer as well as in the turbulent inertial sub layer, has been used so that even the smallest turbulent fluctuations can be predicted. This is commonly accepted as an exact solution of the turbulent momentum differential equation.

According to Launder and Spalding [37] the dimensionless normalized velocity profile can be fitted by:

$$U^+ = y^+ \quad y^+ < y_m^+ \quad (2.23a)$$

$$U^+ = \frac{1}{\kappa} \ln(E \cdot y^+) \quad y^+ \geq y_m^+ \quad (2.23b)$$

With  $y^+$  defined as:

$$y^+ = \frac{y \rho u_\tau}{\mu} \quad (2.23c)$$

$$u_\tau = c_\mu^{0.25} \cdot k^{0.5} \quad (2.23d)$$

In these equation  $u_\tau$  is the friction velocity which can be derived from the k- $\epsilon$  turbulence model. The friction velocity is a function of a turbulence model constant  $c_\mu$  and the turbulent kinetic energy k. According Launder and Spalding  $c_\mu$  is about 0.09 [37]. The friction velocity  $u_\tau$  is derived iteratively during the CFD simulations.  $\kappa$  is the Von Karman constant ( $\kappa = 0.41$ ) and E is the integral constant of the logarithmic law of the wall ( $E = 8.432$ ), both constants being fitting parameters. The momentum transition point lies at  $y_m^+ = 11.062$ .

For heat transfer, using the analogy between heat and momentum transfer, we obtain (see Khalil [39]) for the dimensionless normalized temperature profile ( $T^+$ ) as a function of the distance to the surface of the melt:

$$T^+ = Pr \cdot y^+ \quad y^+ < y_m^+ \quad (2.24a)$$

$$T^+ = Pr_t \left[ \frac{1}{\kappa} \ln(E \cdot y^+) + P_T \right] \quad y^+ \geq y_m^+ \quad (2.24b)$$

Pr is the laminar Prandtl number and  $Pr_t$  is the turbulent Prandtl number for temperature (generally  $Pr_t = 0.9$ , see Launder and Spalding [37]). The correction term  $P_T$ , given by Khalil [39] and Carvalho [40], is generally accepted as correction on the standard wall function for heat transfer in CFD modeling. This correction term, derived by fitting of equation 2.24 to describe the relation between  $T^+$  and  $y^+$ , depends on the laminar Prandtl number (Pr) and the turbulent Prandtl number ( $Pr_t$ ). Khalil and Carvalho give the equation of  $P_T$  depending on Pr and  $Pr_t$ .

For mass transfer, the analogy between mass, heat and momentum transfer has been used to determine the dimensionless normalized mass fraction  $X^+$  as a function of the distance to the surface of the melt of a volatile species in the gas phase:

$$X^+ = Sc \cdot y^+ \quad y^+ < y_m^+ \quad (2.25a)$$

$$X^+ = Sc_t \left[ \frac{1}{\kappa} \ln(E \cdot y^+) + P_M \right] \quad y^+ \geq y_m^+ \quad (2.25b)$$

$Sc$  is the laminar Schmidt number and  $Sc_t$  is the turbulent Schmidt number.  $P_M$  is a correction term, analogous to the correction term for heat transfer ( $P_T$ ). To calculate the value of  $P_M$ , the Prandtl number in the expression for the correction term  $P_T$ , has to be replaced by the Schmidt number.

### Procedure Nernst-boundary layer thickness determination

Since the dimensionless mass fraction (of a volatile species in the gas phase) has been defined, the Nernst boundary layer thickness can be calculated with the following procedure. In the following equations, subscript 'p' denotes values on the first grid point p in our mesh (this point can be inside or outside the laminar sub layer) in the gas phase near the glass melt surface; subscript 'w' is used for values of properties on the glass melt surface itself.

1. Determine the value of  $y^+$  of the first grid point close to the glass melt surface,  $y_p^+$ , at a certain location in the combustion space according to equation 2.26. In this equation  $y_p$  is the real distance of the first grid point to the surface of the melt,  $\rho$  the density of the gas,  $C_\mu$  the turbulence model constant,  $k$  the turbulent kinetic energy and  $\mu$  the molecular viscosity of the gas.

$$y_p^+ = \frac{\rho_p C_\mu^{0.25} k_p^{0.5} y_p}{\mu_p} \quad (2.26)$$

2. The transition point  $y_m^+$  from the laminar to logarithmic sub layer, for mass transfer, is defined by the intersection point of both parts of the profile given by equation 2.27.

$$y_m^+ = \frac{Sc_t}{Sc} \cdot \left[ \frac{1}{\kappa} \ln(E \cdot y_m^+) + P_M \right] \quad (2.27)$$

3. Depending on whether the calculated value of  $y_p^+$  of the first grid point near the wall is smaller or larger than the boundary layer transition point  $y_m^+$ , determine the mass transfer coefficient  $h_w$  [m/s].  $C_i$  is the concentration of a volatile species  $i$  in the gas phase in mole/m<sup>3</sup> and  $C_i^*$  is the equilibrium concentration of species  $i$  in the gas phase near the surface of the melt in mole/m<sup>3</sup>.

$$h_w = \frac{D_p}{y_p} \cdot \left( \frac{C_i^* - C_{i,p}}{C_i^* - C_i^{bulk}} \right) \quad \text{if } y_p^+ < y_m^+ \quad (2.28a)$$

$$h_w = \frac{u_\tau}{Sc_i \cdot \left( \frac{1}{\kappa} \ln(E \cdot y_p^+) + P_M \right)} \cdot \left( \frac{C_i^* - C_{i,p}}{C_i^* - C_i^{bulk}} \right) \quad \text{if } y_p^+ \geq y_m^+ \quad (2.28b)$$

For  $y_p^+ < y_m^+$ , a linear relation between the concentration  $C_i$  of a volatile species in the atmosphere and the distance  $y$  normal to the surface is assumed and for  $y_p^+ \geq y_m^+$  a logarithmic profile is assumed.

4. Determine the Nernst boundary layer thickness  $\delta_N$  (e.g. for NaOH or Na) from the mass transfer coefficient, using:

$$\delta_N = \frac{D_p}{h_w} \quad (2.29)$$

## 2.4 Important properties of alkali-lime silicate melts and borosilicate melts required for evaporation modeling

The evaporation model requires data for the chemical activity of volatile glass compounds in the multi-component silicate melt as input parameter in order to calculate equilibrium vapor pressures. Chemical activities can be derived or estimated from thermodynamic models as will be described in paragraph 2.5. For alkali-lime-silicate melts, thermodynamic models have been applied and the results of these models are partly validated by results of laboratory evaporation experiments [5]. In these alkali-lime-silicate melts, silicon is the main network former, which is normally tetrahedrally bonded and present as  $\text{SiO}_4$  units [29][41]. In borosilicate glass melts the boron will be present as a second network former (see paragraph 2.4.1). Boron is a volatile species in glass melt processes. The chemical activity of  $\text{B}_2\text{O}_3$  in the molten glass will strongly depend with on the molecular structure of the glass melt and the affinity of  $\text{B}_2\text{O}_3$  to the  $\text{SiO}_2$  network. Therefore, paragraph 2.4.1 focuses on the molecular structure of glass melts.

### 2.4.1 Molecular structure of borosilicate glass melts

Generally Si atoms are normally tetrahedrally bonded, boron in borate melts or glasses can exist in tetrahedral and trigonal coordination [42]. According to Wright et al. [43][44][45], the addition of a network modifier to a glass or melt containing  $B_2O_3$  leads initially to a conversion of  $BO_3$  triangular structural units into  $BO_4$  tetrahedra, rather than the formation of non-bridging oxygen atoms bonded to boron. In the case of silicate systems the addition of alkali will cause formation of non-bridging oxygen atoms.

To study the glass structure, Wright et al. [43][44][45] applied molecular dynamics computer simulations in combination with advanced NMR<sup>1</sup> and Raman<sup>2</sup> techniques. Wright et al. [46] applied thermodynamic models to describe the structure of sodium borosilicate glasses. The main limitations in the modeling is the lack of knowledge concerning the structure of relevant crystalline compounds, especially at high temperatures.

Vedishcheva et al. [47][48][49] propose a thermodynamic approach to obtain information on the structure and thermodynamic properties of mainly sodium borosilicate glasses. It has been shown that the calculated distributions of the basis structural units ( $BO_4$  tetrahedra,  $BO_3$  triangles and  $SiO_4$  tetrahedra) for alkali borate glasses / melts and alkali silicate melts are in good agreement with results of experimental studies. For their calculations they applied a thermodynamic Associated Species Model, assuming the melt as an ideal mixture of oxides and associated species (see chapter 2.5). Vedishcheva et al. compared their modeling results with experimental results in literature.

Li et al. [50] improved the stabilization of boron oxide in the melt by adding rare earth elements. The emissions of boron from E-glass borosilicate melts, composed of  $Al_2O_3$ ,  $B_2O_3$ ,  $CaO$  and  $SiO_2$ , were reduced by addition of lanthanum. They showed that the ratio  $BO_3/BO_4$  in the melt increases as the  $La_2O_3$  concentration increases. NMR and Raman spectroscopy showed increasing orthoborate ( $BO_3^{3-}$ ) concentrations as  $La_2O_3$  concentrations increase. Presumably this leads to lower  $B_2O_3$  evaporation losses. In the next paragraph the relation between glass composition, phase segregation and boron evaporation will be discussed in more detail.

---

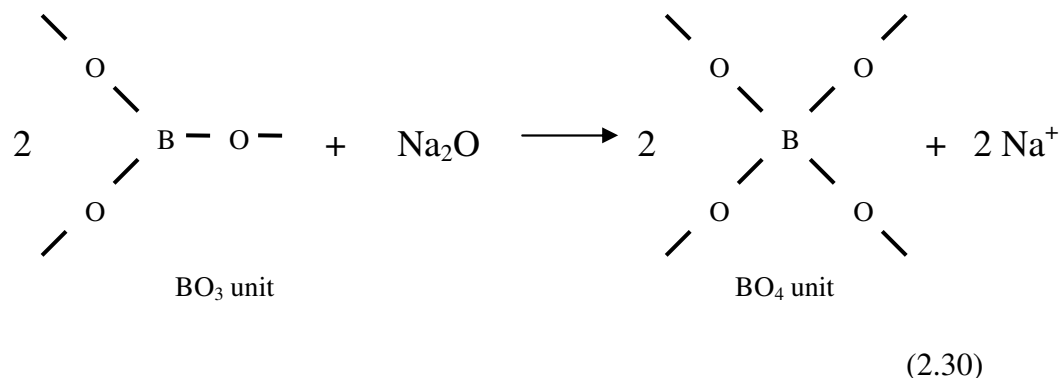
<sup>1</sup> NMR (Nuclear Magnetic Resonance) spectroscopy is a technique that can provide detailed information on the structure of molecules in a material. Nuclear magnetic resonance is a physical phenomenon based upon the absorption of electromagnetic waves by nuclei (often isotopes) of atoms. The molecular environment of these nuclei influences the absorption of these electromagnetic waves [51].

<sup>2</sup> Raman spectroscopy is a spectroscopic technique used in condensed matter physics and chemistry to study vibrational, rotational, and other low-frequency modes in a system [51][52]. The vibrational information is very specific for the chemical bonds in molecules.

### 2.4.2 Phase segregation in glass melts

In our thermodynamic modeling studies (see paragraph 2.5.1) it is assumed that most glass melts can be considered as one phase. This melt phase is assumed to be an ideal mixture of oxides and associated species.<sup>3</sup> For soda-lime-silicate melts, this assumption seems to be valid in most cases as shown later on in paragraph 4.3. For borosilicate glass melts this assumption might not be valid.

The chemistry, structure of glass (melts) and crystallization in glass melts has been reported in detail by Vogel [29][30]. Also for binary and ternary borosilicate glasses, the correlation between molecular glass structure, glass properties and phase separation has been discussed by Vogel. The addition of Na<sub>2</sub>O to a pure borate (B<sub>2</sub>O<sub>3</sub>) melt leads initially to a conversion of structural BO<sub>3</sub> units into BO<sub>4</sub> tetrahedrons. Schematically this reaction is given by [52]:



The sodium acts as a network modifier for Na<sub>2</sub>O concentrations of 16 mol-% and higher. Triangular BO<sub>3</sub> groups with non-bridging oxygen atoms are formed. The presence of different structural borate units may explain the ‘curious’ relation found between the borate glass composition and the measured expansion coefficients of sodium-borate melts and the observed phase segregation after cooling of the glass. As a result of phase segregation, phases in the form of droplets might be formed and dispersed in a second phase. These droplets comprise a phase with a structure of mainly BO<sub>4</sub> tetrahedra with free charges. The Na-ions in the melt are not arranged uniformly in the material, but they are swarmed around the negatively charged BO<sub>4</sub> tetrahedra. These free charges lead to higher inner wards directed

<sup>3</sup> Associated species are compounds with stoichiometric compositions. For instance the binary Na<sub>2</sub>O (N)-SiO<sub>2</sub> (S)-system is considered as a mixture of single oxides and stoichiometric compounds N, S, N<sub>2</sub>S, N<sub>3</sub>S<sub>2</sub>, NS, NS<sub>2</sub> and N<sub>3</sub>S<sub>8</sub>. A complete overview of all stoichiometric compounds applied in this study is given in Table 2.1.

forces and consequently to higher surface tensions. In a sodium-borate glass, probably three different melt phases are present:

1. A boron rich melt phase with mainly  $\text{BO}_3$  units;
2. A silica rich melt phase with mainly  $\text{SiO}_4$  units;
3. A sodium-borate melt phase with mainly  $\text{BO}_4$  units surrounded by  $\text{Na}^+$  ions.

Up to 16 mol-%  $\text{Na}_2\text{O}$ , the phase segregation tendency increases, above this concentration less phase segregation is observed [29][30].

A ternary  $\text{Na}_2\text{O}-\text{B}_2\text{O}_3-\text{SiO}_2$  system, exists probably of silica rich phases and boron-rich phases [30]. Vogel [29] shows schematically the different glass phases for a  $\text{Na}_2\text{O}-\text{B}_2\text{O}_3-\text{SiO}_2$  system, as shown in Figure 2.8. In systems with low  $\text{SiO}_2$  contents, the melt might probably be considered as phase of  $\text{BO}_3$  units with droplets of a  $\text{SiO}_2$  rich glass phase (with  $\text{SiO}_4$  units) and droplets of a sodium-borate phase (figure a). As the  $\text{SiO}_2$  contents increases the number of ‘ $\text{SiO}_2$ -rich islands’ increases and finally they will merge together to form one  $\text{SiO}_2$  melt phase (figure c). In ternary borosilicate systems with Ba, Pb and Ca, immiscibility gaps have been observed also. Here, silica rich and Ba-, Pb or Ca- rich borosilicate phases are probably present [29][30]. Similar as a  $\text{Na}_2\text{O}-\text{B}_2\text{O}_3-\text{SiO}_2$  system, a  $\text{CaO}-\text{B}_2\text{O}_3-\text{SiO}_2$  system might exist of  $\text{SiO}_2$  rich,  $\text{B}_2\text{O}_3$  rich and calcium-borate melt phases. The binary  $\text{B}_2\text{O}_3 - \text{CaO}$  phase diagram [53] shows a liquid miscibility gap for  $1 < C_{\text{CaO}} < 30$  mole-% and temperatures above  $1000^\circ\text{C}$ . For molar ratios  $\text{CaO}/\text{B}_2\text{O}_3 > 2$  the phase diagram is not known.

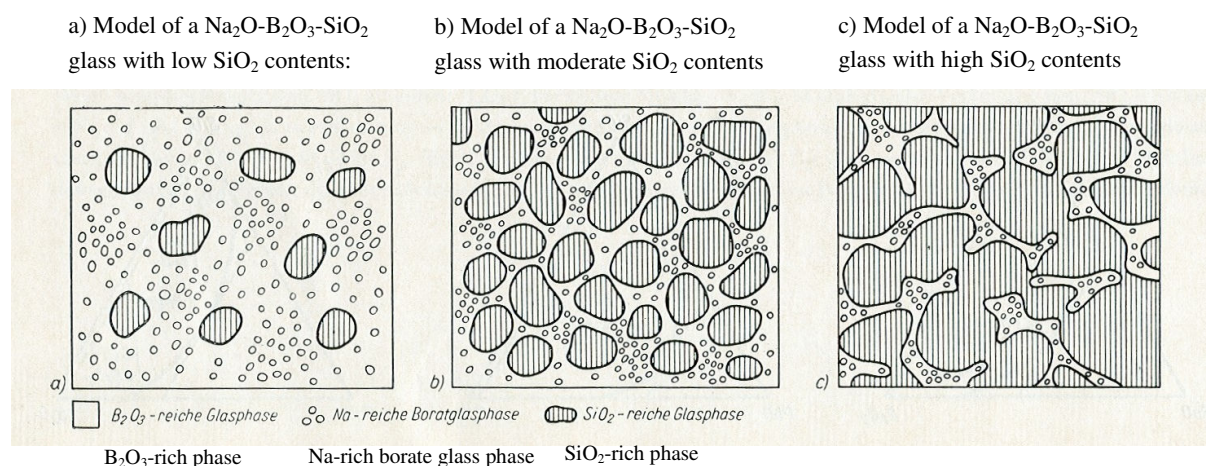


Figure 2.8: Schematic presentation of phase segregation in a sodium-borosilicate glass. The originally picture is published by Vogel [29]



Especially the latter region is of importance for calcium borate phases expected to be present in the investigated borosilicate glass melts (i.e. nearly all calcium is bonded in borate phases). Also the ternary  $B_2O_3$ -CaO-SiO<sub>2</sub> phase diagram shows the presence of liquid miscibility gaps for the investigated glass melt compositions and temperatures [53] in this study.

The results of leaching experiments with E-glass types ( $B_2O_3$ -CaO-SiO<sub>2</sub>-Al<sub>2</sub>O<sub>3</sub>) also suggest the presence of different phases in the product. Elmer [54] performed leaching experiments with E-glass (SiO<sub>2</sub> = 52.8 mass-%, B<sub>2</sub>O<sub>3</sub> = 10.8 mass-%, Al<sub>2</sub>O<sub>3</sub> = 14.4 mass-%, CaO = 16.7 mass-%, MgO = 4.5 mass-%) in a 1.5 N HNO<sub>3</sub> solution at 95 °C. For times ranging up to 30 minutes, he measured relatively high weight changes that are probably a result of the removal of constituents (structures) in the sample that react fast with the HNO<sub>3</sub>. For times ranging from 30 to 500 minutes, the measured weight changes are much lower and represent the removal of ions that are trapped in the stable lattice or remain in the porous structure obtained after initial leaching. As a function of time the chemical compositions of the specimens that had been leached were measured. Based on these results, one could suggest that this E-glass consists of two main phases:

1. a SiO<sub>2</sub> rich glass phase (SiO<sub>2</sub> ≈ 99.2 mass-%, Al<sub>2</sub>O<sub>3</sub> ≈ 0.4 mass-%, B<sub>2</sub>O<sub>3</sub> ≈ 0.1 mass-%, CaO ≈ 0.3 mass-%) and a
2. second glass phase with almost no SiO<sub>2</sub> (Al<sub>2</sub>O<sub>3</sub> ≈ 36 mass-%, B<sub>2</sub>O<sub>3</sub> ≈ 23 mass-%, CaO ≈ 36 mass-%, MgO ≈ 4 mass-%).

Das and co-workers [55] investigated the acid corrosion of E-glass fibers. In this case an E-glass was exposed to 0.5 N H<sub>2</sub>SO<sub>4</sub> and again the residual porous glass product consists mainly of SiO<sub>2</sub>.

#### *Melt properties and boron evaporation*

The observations of Li et al. [50], described in paragraph 2.4.1, showed that the boron evaporation rates from alkali-lean types of borosilicate glass melt decreases as the La<sub>2</sub>O<sub>3</sub> concentration in the melt increases. Simultaneously BO<sub>4</sub> units are converted into BO<sub>3</sub> units. In these BO<sub>3</sub> units the distance between the O<sup>2-</sup> anions and B<sup>3+</sup> cations is about 1.36 Å, for BO<sub>4</sub> units this distance is 1.50 Å. Therefore the field strength<sup>4</sup> (i.e. a measure for the strength of the bond between ions) in a BO<sub>3</sub> unit is higher than in a BO<sub>4</sub> unit (1.63 in a BO<sub>3</sub> unit versus 1.34 in a BO<sub>4</sub> unit) [30]. In the BO<sub>3</sub> melt phase the chemical activity of B<sub>2</sub>O<sub>3</sub> is lower

---

<sup>4</sup> According Vogel [29] the field-strength between cations and anions in BO<sub>3</sub> units and BO<sub>4</sub> units is defined as the ratio between the valency of boron (3) and the quadrate of the distance between the B<sup>3+</sup> ion and O<sup>2-</sup> ion in Å.

than in a  $\text{BO}_4$  melt phase and the boron evaporation rates will decrease as the fraction  $\text{BO}_3$  increases.

Based on the previously described glass structure of borosilicate glasses, one could suggest that the formation of silica rich melt phases, as shown in Figure 2.8c, might limit the transport of boron ions to the surface of the melt. The diffusion distance of boron ions become longer.

Because of the presence of 3 different phases in sodium borosilicate melts (and probably also in calcium borosilicate melts), the bulk of the melt might be covered by a thin melt phase layer with a low surface tension. In silica rich borosilicate melts, the bulk of the melt might be covered with a silica rich melt phase layer with a relatively low surface tension compared to the sodium borate or calcium borate phase. The transport of boron through such a layer will be hindered.

As will be discussed in chapter 4, the boron concentration profile measurements in glass samples after evaporation tests, could not confirm this hypothesis. Of course, in a cooled glass sample the situation might be different as in a hot melt. Furthermore, it is impossible to measure very thin glass layers in the order of magnitude of nanometers with the applied SEM-WDX technique (see chapter 3).

Thus, the evaporation rates of boron from borosilicate melts might depend on:

1. The transport of the boron ions in the melt constituting of a mixture of different melt phases;
2. The structure of the boron oxide in the melt ( $\text{BO}_3$  units and  $\text{BO}_4$  units);
3. Formation of a surface layer of non-volatile boron species.

The thermodynamic properties required for the mathematical evaporation model, such as chemical activity and saturation pressure of volatile species, depend on the structure of the glass melt or the occurrence of phase segregation. Since the structure of borosilicate glass melts seems to deviate from the structure of soda-lime-silicate melts, the applied thermodynamic models for both glass types will be different as shown in paragraph 2.5.

## **2.5 Modeling of thermodynamic properties of silicate glasses and melts**

Because of strong interactions between the different constituents in multi-component silicates or borates, the derivation of the thermodynamic properties of silicate or borate glass melts from their chemical composition is a complex task. The structural units (e.g.  $\text{BO}_4$

tetrahedra,  $\text{BO}_3$  triangles and  $\text{SiO}_4$  tetrahedra) in the network of the melt or glass will have an important effect on the interaction and bonding between the ions or single atoms in this material and the chemical activities coefficients of the single oxides (e.g.  $\text{Na}_2\text{O}$ ,  $\text{CaO}$ ,  $\text{SiO}_2$ ,  $\text{B}_2\text{O}_3$  etc.) in the material or melt. The activity coefficients may be orders of magnitude smaller than unity.

Two different approaches are successfully applied to model the thermodynamic properties of multi-component oxide systems:

1. Quasi-chemical models to describe the short-range order in these oxide systems and
2. Different types of Associated Species Models (ASM).

Bale et al. [56] and Pelton et al. [57] developed the quasi-chemical Factsage model, based on the short-range order (bondings between neighboring units/atoms) in these oxide multi-component systems. The model involves the determination of the interactions, or bonding, between second-nearest-neighbor ions and the distribution of these bondings<sup>5</sup>. The energy change in establishing those bonds and distribution (entropy) of these bonds is expressed with a mathematical equation having composition and temperature dependent terms. Factsage is partly based on semi-empirical equations and contains adjustable parameters to adapt the model to existing phase diagrams or other properties such as eutectic composition, melting point et cetera. Accurate results are generally obtained for systems, for which the model parameters are adjusted to existing comprehensive phase diagrams.

The original Associated Species Model was first elaborated by Hastie, Bonnell et al. [58]. In the evaporation model in this prevalent study, the Associated Species Model is the basis of a modified model to calculate the chemical activities of volatiles species in alkali-lime-silicate melts [5]. This thermodynamic model will be described in paragraph 2.5.1.

### 2.5.1 Thermochemical Associated Species Model

The chemical activity of volatile components in the glass are used to calculate the saturation pressures of gaseous volatile species [5], using equation 2.3. These data are required for our evaporation model (see paragraph 2.1). Thermodynamic models have been developed to calculate the chemical activity of species in multi-component silicate melts from the chemical composition of the glass and temperature.

---

<sup>5</sup> In his thesis, Steiner [62] discussed the quasi-chemical approach. A regular solution model assumes random mixed atoms even though the enthalpy of mixing is not zero. The configurational entropy should vary with temperature, which is better treated with the quasi-chemical model, where a non-random distribution of the atoms is realized. It also incorporates a mass balance. The modified quasi-chemical model as developed by Pelton et al.[56][57] incorporates modifications to the short range ordering of the quasi-chemical model.

In this thesis the standard Gibbs free energy of formation of a substance, represents the free energy change associated with the formation of the substance from components in their most stable form (e.g. O<sub>2</sub>, Na, K, B) as they exist under the standard conditions of P = 1 atm and T = 298 K. In the thermochemical Associated Species Model (ASM) the Gibbs energy data of the associated species are taken from the pure phases in the liquid state. In case of evaporation modeling, ASM is only applied for liquid melts.

The chemical activity  $a_j$ , relative to the pure liquid substance at the same temperature, of a glass melt component j is equal to the product of the activity coefficient  $\gamma_j$  of that specific species and its molar fraction ( $X_j$ ) in a phase:

$$a_j = \gamma_j \cdot X_j. \quad (2.31)$$

To describe the thermodynamic behavior of a single phase glass melt, expressions for the activity coefficients of all species i in the glass melt as function of glass melt composition and temperature are required:

$$\gamma_i = f(X_1, \dots, X_i, \dots, X_n, T). \quad (2.32)$$

Such relations can be very complex and are difficult to assess for multi-component glass melt compositions. Alternatively, a mathematical model, describing the thermodynamic behavior of glass melts, almost similar to the approach proposed by Shakmatkin et al. [59] is used. With this thermodynamic model, chemical activities of glass melt components (end-member oxides and associated species) for a large variety of glass melt compositions can be calculated as function of temperature.

In this thermodynamic model, the glass melt is assumed to be an ideal mixture of single end-member oxides and associated species (stoichiometric compounds with known or estimated thermodynamic properties). For instance the binary Na<sub>2</sub>O (N)-SiO<sub>2</sub> (S)-system is considered as a mixture of end-member oxides and associated species N, S, N<sub>2</sub>S, N<sub>3</sub>S<sub>2</sub>, NS, NS<sub>2</sub> and N<sub>3</sub>S<sub>8</sub>, see also reference [60]. The different oxides and associated species applied for thermodynamic modeling in this study are listed in Table 2.1. The chemical activity (relative to the pure non-mixed liquid compounds) of each of these different compounds N (Na<sub>2</sub>O), S (SiO<sub>2</sub>) and the associated species: N<sub>2</sub>S, N<sub>3</sub>S<sub>2</sub>, NS, NS<sub>2</sub> and N<sub>3</sub>S<sub>8</sub> etc., equals the concentration (given as molar fraction) of these compounds in the mixed melt, assuming ideal mixing of the liquid associated species and the liquid single end-member oxides. Also for multi-component

systems, such as float glass melts, the activity of the single oxides ( $a_{\text{SiO}_2}$ ,  $a_{\text{Na}_2\text{O}}$ ,  $a_{\text{CaO}}$ ,  $a_{\text{MgO}}$ , etc.) in a mixture of associated species (including binary, ternary and quaternary stoichiometric compositions or associated species) can be estimated by this approach. The composition of the mixture of all these associated species is calculated by minimization of the Gibbs free energy of the total system under constraint of conservation of mass for each chemical element [61]. For this minimization procedure, a numerical algorithm is developed, calculating the molar equilibrium concentrations of the associated species in the mixture, assuming the mixture to behave ideally. The algorithm and the thermodynamic Associated Species Model (ASM) are described in the thesis of Steiner [62]. The above described procedure is only applicable for multi-component melts with ideally mixing of all oxides plus associated species.

Later Besmann and Spear [63] used another somewhat modified thermodynamic associated species model, that accurately reproduces the phase equilibria of more complex multi-compounds systems, such as:  $\text{Na}_2\text{O}-\text{Al}_2\text{O}_3-\text{B}_2\text{O}_3-\text{SiO}_2$ . Their model reproduces important melting points and liquidus lines and surfaces for this system. As will be shown later in this paragraph, their modified method was also applied to  $\text{CaO}-\text{SiO}_2$  systems to demonstrate the treatment and application of this type of model for systems showing immiscible liquid phases. The model reproduces the phase diagram of  $\text{CaO}-\text{SiO}_2$  system very well. Besmann et al. presented two modification applied in their Associated Species Model:

- 1) Possibility to add associated species that do not exist as separate isolated compound;
- 2) Treatment of immiscibilities in solution phases.

*Table 2.1: Overview of all oxides and associated species used for the thermodynamic Associated Species Model, for soda-lime-silicate and alkali-lean borosilicate compositions described in paragraph 2.5.*

	<b>Oxides and associated species</b>
<b>Oxides</b>	$\text{CaO}$ , $\text{Al}_2\text{O}_3$ , $\text{Na}_2\text{O}$ , $\text{MgO}$ , $\text{SiO}_2$ , $\text{K}_2\text{O}$ , $\text{B}_2\text{O}_3$
<b>Binary oxide species</b>	$\text{Al}_6\text{Si}_2\text{O}_{13}$ , $\text{Ca}_2\text{SiO}_4$ , $\text{Ca}_3\text{Si}_2\text{O}_7$ , $\text{CaSiO}_3$ , $\text{CaAl}_2\text{O}_4$ , $\text{CaAl}_4\text{O}_7$ , $\text{Na}_4\text{SiO}_4$ , $\text{Na}_2\text{SiO}_3$ , $\text{Na}_6\text{Si}_8\text{O}_{19}$ , $\text{Na}_6\text{Si}_2\text{O}_7$ , $\text{Na}_2\text{Si}_2\text{O}_5$ , $\text{Al}_2\text{MgO}_4$ , $\text{MgSiO}_3$ , $\text{Mg}_2\text{SiO}_4$ , $\text{Al}_{12}\text{Na}_2\text{O}_{19}$ , $\text{Al}_9\text{NaO}_{14}$ , $\text{AlNaO}_2$ , $\text{Al}_{12}\text{K}_2\text{O}_{19}$ , $\text{Al}_9\text{KO}_{14}$ , $\text{AlKO}_2$ , $\text{SiK}_2\text{O}_3$ , $\text{Si}_2\text{K}_2\text{O}_5$ , $\text{Si}_4\text{K}_2\text{O}_9$ , $\text{Ca}_3\text{SiO}_5$ , $\text{CaB}_2\text{O}_4$ , $\text{CaB}_4\text{O}_7$ , $\text{Ca}_2\text{B}_2\text{O}_5$ , $\text{Ca}_3\text{B}_2\text{O}_6$ , $\text{Ca}_5\text{B}_2\text{O}_8$ , $\text{Al}_4\text{B}_2\text{O}_9$ , $\text{Al}_{18}\text{B}_4\text{O}_{33}$ , $\text{NaBO}_2$ , $\text{NaB}_3\text{O}_5$ , $\text{NaB}_5\text{O}_8$ , $\text{NaB}_9\text{O}_{14}$ , $\text{Na}_2\text{B}_4\text{O}_7$ , $\text{Na}_2\text{B}_8\text{O}_{13}$ , $\text{Na}_4\text{B}_2\text{O}_5$ , $\text{KBO}_2$ , $\text{K}_2\text{B}_4\text{O}_7$ , $\text{K}_2\text{B}_6\text{O}_{10}$ , $\text{K}_2\text{B}_8\text{O}_{13}$ , $\text{Al}_2\text{Si}_2\text{O}_7$ , $\text{Al}_2\text{SiO}_5$ , $\text{Ca}_3\text{Al}_2\text{O}_6$ , $\text{CaAl}_{12}\text{O}_{19}$
<b>Ternary oxide species</b>	$\text{Ca}_2\text{Na}_2\text{Si}_3\text{O}_9$ , $\text{Ca}_3\text{Na}_2\text{Si}_6\text{O}_{16}$ , $\text{CaNa}_2\text{Si}_5\text{O}_{12}$ , $\text{CaNa}_4\text{Si}_3\text{O}_9$ , $\text{AlNaSi}_2\text{O}_6$ , $\text{AlNaSi}_3\text{O}_8$ , $\text{AlNaSiO}_4$ , $\text{Na}_2\text{MgSi}_4\text{O}_{10}$ , $\text{Na}_2\text{Mg}_2\text{Si}_6\text{O}_{15}$ , $\text{CaAl}_2\text{Si}_2\text{O}_8$ , $\text{Ca}_2\text{Al}_2\text{SiO}_7$ , $\text{Al}_2\text{Mg}_3\text{Si}_3\text{O}_{12}$ , $\text{Al}_4\text{Mg}_2\text{Si}_5\text{O}_{18}$ , $\text{CaMgSiO}_4$ , $\text{CaMgSi}_2\text{O}_6$ , $\text{Ca}_2\text{MgSi}_2\text{O}_7$ , $\text{Ca}_3\text{MgSi}_2\text{O}_8$ , $\text{AlSi}_2\text{KO}_6$ , $\text{AlSi}_3\text{KO}_8$ , $\text{AlSiKO}_4$ , $\text{Al}_6\text{Si}_2\text{B}_2\text{O}_{16}$ , $\text{Ca}_3\text{Al}_2\text{Si}_3\text{O}_{12}$ , $\text{CaAl}_2\text{SiO}_6$

*Modification 1:*

In the Associated Species Model the Gibbs free energy of a mixture is determined by assuming ideal mixing of single oxides and associated species. The model uses thermodynamic data of single oxides and a selection of known associated species with available thermodynamic data on species expected from their presence in phase diagrams. However, in some cases it appears that the Gibbs free energy determined for the equilibrium of this ideal mixture of associated species and single oxides, is too high. This means that the model is not correct and that other rather stable associated species exist in this mixture and have to be included in the model.

*Modification 2*

Systems with immiscible phases show positive interaction energies between some of the oxides and associated species. A mixture of oxides and associated species at equilibrium may have a higher Gibbs free energy than the constituting oxides and associated species together, assuming ideal mixing. For these systems, the modified associated species model requires the inclusion of excess Gibbs free energy terms of mixing, determined by a fitting procedure. The Gibbs free excess energy terms depend on temperature and molar fractions of the species with positive interaction energy. Initially the Gibbs free energy is calculated assuming an ideal mixture of oxides and associated species. In order to represent the immiscible phases correctly, the total Gibbs free energy of such system is calculated as summation of Gibbs free energy of an assumed ideal mixture plus excess Gibbs free energy terms. For this new value of Gibbs free energy the molar composition (molar fractions of the single oxides and associated species) is calculated.

The model was demonstrated for the CaO-SiO<sub>2</sub> system [63] to estimate the compositions of the phases in the liquid-liquid immiscibility region in the phase diagram. The liquid-liquid immiscibility region requires the inclusion of non-ideal interaction terms or excess free energy values, determined by trial and error (to fit the phase diagram), between CaSiO<sub>3</sub> (l) and SiO<sub>2</sub> (l).

**2.5.2 Thermochemical modeling of soda-lime-silicate melts and float glass melts**

In our study, the described thermochemical model in paragraph 2.5.1 is applied for binary sodium-silicate melts, ternary soda-lime-silicate melts and industrial produced multi-component float glass compositions, that consist basically of SiO<sub>2</sub>, Na<sub>2</sub>O, CaO, MgO, Al<sub>2</sub>O<sub>3</sub> and K<sub>2</sub>O. Components like Fe<sub>2</sub>O<sub>3</sub> and SO<sub>3</sub> are not taken into account in our model. The

accuracy of the model depends very much on the validity of the model assumptions and the accuracy of the available thermodynamic data (Gibbs free energy value of formation of all the associated species and single oxides used in the Gibbs free energy minimization routine). For example, in the CaO-SiO<sub>2</sub> phase diagram, a two liquid region can be observed for SiO<sub>2</sub> > 70 mass-%, and for temperatures above the liquidus temperature [64]. In this region the assumption of an ideal mixture of oxides and associates species is not true. This two-liquid region is characterized by an immiscibility gap [65] and the ASM approach without adjustments is not applicable.

Several sources report experimentally derived chemical activities of Na<sub>2</sub>O in a binary Na<sub>2</sub>O-SiO<sub>2</sub> system [53][56][66][67]. Differences between the reported chemical activities of Na<sub>2</sub>O in these sodium-disilicate melts for the same compositions, when comparing different literature sources, are up to a factor 3. For the case of evaporation of NaOH from such melts, according to equation 2.10 this would result in a difference up to  $\sqrt{3}$  in the calculated value of  $p_{\text{NaOH}}^*$ . Thus, it is very important to find accurate measurements or models to derive chemical activities of Na<sub>2</sub>O in silicate melts.

### 2.5.3 Thermochemical modeling of SiO<sub>2</sub>-CaO-Al<sub>2</sub>O<sub>3</sub>-B<sub>2</sub>O<sub>3</sub> melts

The borosilicate glass melts, investigated in this study, contain basically 54 – 60 mass-% SiO<sub>2</sub>, 22 – 25 mass-% CaO, about 14 mass-% Al<sub>2</sub>O<sub>3</sub> and 2 – 8 mass-% B<sub>2</sub>O<sub>3</sub> and are comparable with industrial E-glass melts, but here we studied mainly compositions without sulfur, alkali-oxides and impurities. The molar ratio CaO/B<sub>2</sub>O<sub>3</sub> varies between 3 and 10 in the investigated compositions. For thermodynamic modeling of these kinds of glass melts, accurate thermodynamic data of each oxide and relevant associated species are required. Figure 2.9 shows the calculated chemical activities of B<sub>2</sub>O<sub>3</sub> in alkali-free borosilicate melts as a function of the B<sub>2</sub>O<sub>3</sub> concentration at T = 1450 °C. Three different thermodynamic models have been used: 1) Factsage [56], 2) Associated Species Model described in paragraph 2.5.1 and 3) an adapted Associated Species Model with extra associated species taken into account. The latter model will be described in this paragraph. The differences between the calculated chemical activities appear to be 1 up to more than 3 orders of magnitude.

Furthermore, the standard Gibbs energy ( $G^0$ ) of pure B<sub>2</sub>O<sub>3</sub> in a molten, liquid state were derived from two different databases and compared. For this comparison Factsage [56] and a database of Besmann and Spear et al. [63][68][69] were used. Figure 2.10 shows the standard Gibbs energy value of pure B<sub>2</sub>O<sub>3</sub>(l) as a function of temperature obtained from

different literature sources. The differences are only about 2 %, but this might have an enormous effect on the calculated chemical activities. Example: For a glass melt  $\text{SiO}_2:\text{CaO}:\text{Al}_2\text{O}_3:\text{B}_2\text{O}_3 = 62 : 25 : 8 : 5$  mol-%, the chemical activities of  $\text{B}_2\text{O}_3$  have been calculated by using both standard Gibbs energy databases for pure  $\text{B}_2\text{O}_3(\text{l})$ . For the calculations the previously described Associated Species Model has been used (paragraph 2.5.1). The difference between both calculated activity values for  $\text{B}_2\text{O}_3$  in this glass melt, appeared to be approximately a factor 5.

As shown in paragraph 2.4.1, there are liquid miscibility gaps in the binary  $\text{B}_2\text{O}_3 - \text{CaO}$  phase diagram and the ternary  $\text{B}_2\text{O}_3\text{-CaO-SiO}_2$  phase diagram. The existence of associated species with unknown standard Gibbs energy, like  $5\text{CaO}\cdot\text{B}_2\text{O}_3\cdot\text{SiO}_2$  and  $11\text{CaO}\cdot\text{B}_2\text{O}_3\cdot 4\text{SiO}_2$ , are mentioned in the Slag Atlas [70]. The presence of such associated species should be taken into account in the model in cases they have relatively low Gibbs free energy levels (i.e. these compounds are rather stable). However, there are hardly thermodynamic data available for these compounds.

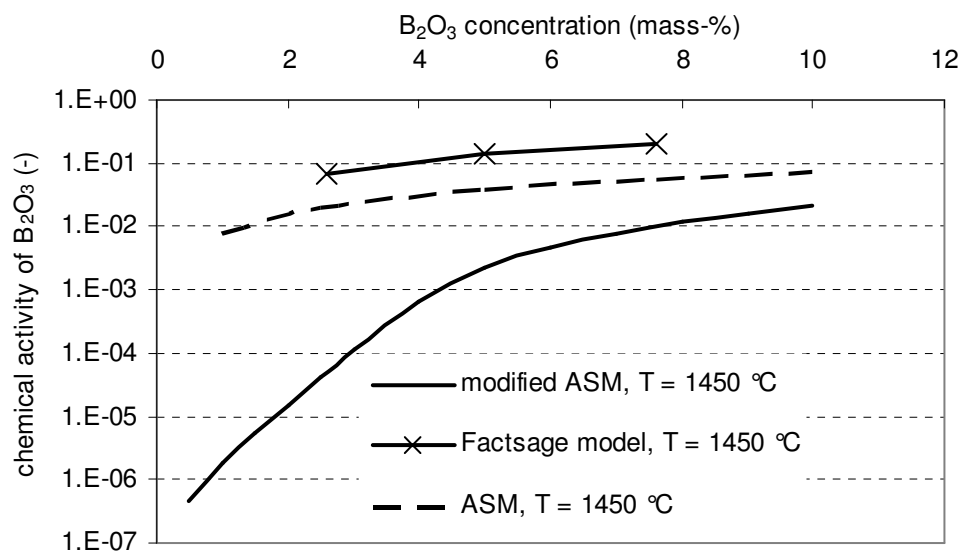


Figure 2.9: Chemical activities of  $\text{B}_2\text{O}_3(\text{l})$  in alkali-lean borosilicate glass melts (see paragraph 2.5.3) as a function of the concentration  $\text{B}_2\text{O}_3$  in the melt at  $T = 1450$  °C. Three different thermodynamic models were used: 1) Factsage [56], 2) Associated Species Model (see paragraph 2.5.1) and 3) Associated Species Model modified here for borosilicate glass melts (see paragraph 2.5.3). The latter model has been especially adapted for alkali-lean borosilicate glass melts.



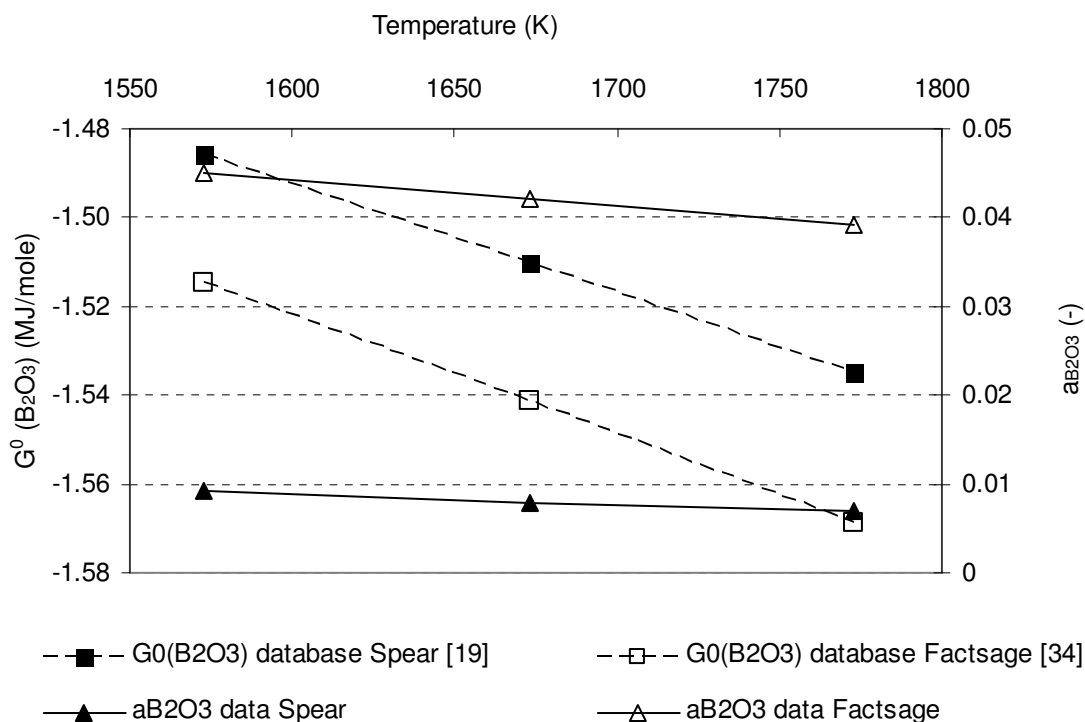


Figure 2.10: Standard Gibbs energy ( $G^0$ ) of  $B_2O_3$  (l) and calculated chemical activity of  $B_2O_3$  in a glass melt ( $SiO_2:CaO:Al_2O_3:B_2O_3 = 62 : 25 : 8 : 5$  mol-%) as a function of temperature. The thermodynamic modified associated species model described in paragraph 2.5.1 has been applied to calculate the chemical activities.

Thus, insufficient accurate thermodynamic data are available for  $SiO_2$ - $CaO$ - $Al_2O_3$ - $B_2O_3$  systems relevant for E-glass. As discussed previously in this chapter, Besmann and Spear [63] validated their thermodynamic databases for  $CaO$ - $SiO_2$ ,  $Na_2O$ - $Al_2O_3$  and  $Na_2O$ - $Al_2O_3$ - $B_2O_3$ - $SiO_2$  systems. These databases are also used in our modified Associated Species Model, described in this paragraph.

Databases like Factsage [56] contain thermodynamic data for the species:  $CaO$  (l),  $B_2O_3$  (l),  $CaO \cdot B_2O_3$  (l),  $CaO \cdot 2B_2O_3$  (l)  $2CaO \cdot B_2O_3$  (l) and  $3CaO \cdot B_2O_3$  (s). For associated species with a molar ratios  $CaO/B_2O_3 > 3$  no thermodynamic data of these compounds are available at all. In our modified Associated Species Model we optimized the database (by a fitting procedure) for the mentioned calcium-borate compounds by using experimentally, from laboratory evaporation tests derived, chemical activities of  $B_2O_3$  in  $SiO_2$ - $CaO$ - $Al_2O_3$ - $B_2O_3$  melts (see paragraph 4.4.3). In order to fit the experimental results with the modeling results, the fictive  $5CaO \cdot B_2O_3$ (l) compound is assumed to be a relevant associated species in E-glass. The introduction of the fictive species  $5CaO \cdot B_2O_3$ (l) is based on a method described by Besmann and Spear [63]. They introduced fictive associated species, not existing as condensed phase to

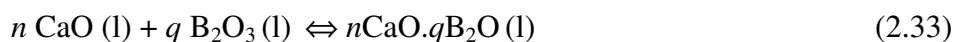
optimize the modeled phase equilibria. In the applied thermodynamic model, the  $5\text{CaO}\cdot\text{B}_2\text{O}_3(\text{l})$  species is introduced in order to optimize our model for alkali-free borosilicate melts. By introducing this new compound it became possible to accurately reproduce the experimentally derived chemical activities of  $\text{B}_2\text{O}_3$  in the investigated glass melt systems.

In developing a thermodynamic database for the relevant species, constituting the quaternary  $\text{SiO}_2\text{-CaO-Al}_2\text{O}_3\text{-B}_2\text{O}_3$  system, the initially used thermochemical associated species model has been modified in this study on three different points:

1. The condensed-phase data of the Na-Ca-Al-B-Si-O system of Besmann, Spear and co-workers has been applied [63][69] (see Table 2.1);
2. In order to describe glass compositions with a molar ratio  $\text{CaO}/\text{B}_2\text{O}_3 > 3$ , the fictive species  $5\text{CaO}\cdot\text{B}_2\text{O}_3(\text{l})$  has been introduced. It is assumed that this species ideally mix with the oxides and associated species in the melt;
3. The condensed-phase database of Besmann, Spear and co-workers [63][69] contains only data for pure  $\text{CaO}(\text{l})$  and pure  $\text{B}_2\text{O}_3(\text{l})$  but not for other associated  $\text{CaO}\cdot\text{B}_2\text{O}_3$  species. The estimated standard Gibbs energy values of the liquid associated species:  $\text{CaO}\cdot\text{B}_2\text{O}_3$ ,  $\text{CaO}\cdot 2\text{B}_2\text{O}_3$ ,  $2\text{CaO}\cdot\text{B}_2\text{O}_3$ ,  $3\text{CaO}\cdot\text{B}_2\text{O}_3$  and  $5\text{CaO}\cdot\text{B}_2\text{O}_3$  have been added to the original database of Besmann et al.. The standard Gibbs energy values of these compounds were estimated by the application of fitting equations 2.34 for each compound. The condensed-phase database of Spear et al. [63] has been used to obtain the Gibbs functions of pure  $\text{CaO}(\text{l})$  and pure  $\text{B}_2\text{O}_3(\text{l})$ ,  $\Delta G_{\text{reaction}}^0$  for reaction 2.33 has been calculated from Factsage [56] for  $\text{CaO}\cdot\text{B}_2\text{O}_3$ ,  $\text{CaO}\cdot 2\text{B}_2\text{O}_3$ ,  $2\text{CaO}\cdot\text{B}_2\text{O}_3$ ,  $3\text{CaO}\cdot\text{B}_2\text{O}_3$ . The constant  $C_4$  in equation 2.34 is an empirically derived constant<sup>6</sup>. The value of  $C_4$  depends only on the stoichiometry factors  $n$  and  $q$  in equation 2.33. This constant  $C_4$  is derived by fitting of experimental data with modeling results. As an example, the Gibbs functions of  $\text{CaO}\cdot\text{B}_2\text{O}_3(\text{l})$  and  $2\text{CaO}\cdot\text{B}_2\text{O}_3(\text{l})$  derived by this method are presented and compared in Figure 2.11. The values of  $C_4$ , experimentally derived in this study, are given in Table 2.2.

---

<sup>6</sup> In this example the standard Gibbs free energy, used in the modified Associated Species Model, is calculated for the compound  $\text{CaO}\cdot\text{B}_2\text{O}_3(\text{l})$  at 1400 °C. According to Factsage [56] the standard Gibbs free energy of  $\text{CaO}(\text{l})$ ,  $\text{B}_2\text{O}_3(\text{l})$  and  $2\text{CaO}\cdot\text{B}_2\text{O}_3(\text{l})$  at 1400 °C are respectively: -739901 J/mole, -1541400 J/mole and -3202067 J/mole. The reaction energy  $\Delta G_{\text{reaction}}^0 = -3202067 - (2 * -739901 - 1541400) = -180865$  J/mole. According to the database of Spear, Besmann et al. [63]  $G_{\text{B}_2\text{O}_3(\text{l})}^0 = -1592000$  J/mole and  $G_{\text{CaO}(\text{l})}^0 = -735570$ , the empirical derived constant  $C_4$  is -144287 J/mole. According to equation 2.34,  $G_{2\text{CaO}\cdot\text{B}_2\text{O}_3(\text{l})}^0 = 2 * -735570 + 1 * -1592000 - 180865 - 144287 = -3388292$  J/mole.



$$G_{n\text{CaO} \cdot q\text{B}_2\text{O}_3}^0 = n \cdot G_{\text{CaO}}^0 + q \cdot G_{\text{B}_2\text{O}_3}^0 + \Delta G_{\text{reaction}}^0 + C_4 \quad (2.34)$$

In this adapted Associated Species Model, a new species has been introduced and the standard Gibbs energy values of different calcium-borate compounds were estimated. In this model it is assumed that all oxides and associated species mix ideally.

Table 2.2: Values for the constant  $C_4$  in equation 2.34. These values are required for the thermodynamic modified Associated Species Model described in paragraph 2.5.3.

Associated Species	Value for $C_4$ in equation 2.34 (J/mole)
$\text{CaB}_2\text{O}_4 \text{(l)}$	-45001
$\text{Ca}_2\text{B}_2\text{O}_5 \text{(l)}$	-144287
$\text{Ca}_3\text{B}_2\text{O}_6 \text{(l)}$	-243573
$\text{Ca}_5\text{B}_2\text{O}_8 \text{(l)}$	-442145

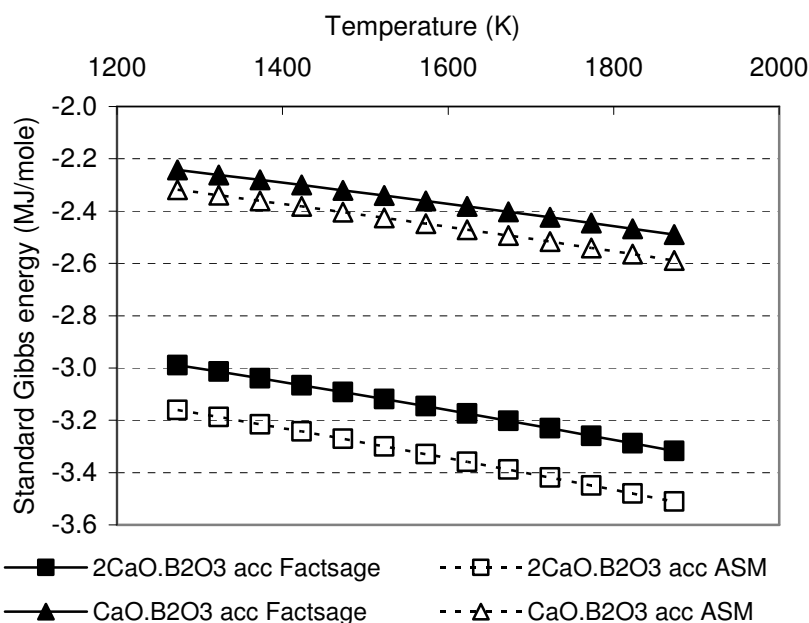


Figure 2.11: Standard Gibbs free energy of  $\text{CaO} \cdot \text{B}_2\text{O}_3 \text{(l)}$  and  $2\text{CaO} \cdot \text{B}_2\text{O}_3 \text{(l)}$  as a function of temperature. The figure shows the data derived from the Factsage database [56] and the data applied in our extended associated species model, described in paragraph 2.5.3.

The model presented here does not account for possible phase segregation in the borosilicate melt at high temperatures. As will be discussed in paragraph 4.5.2 there is no clear evidence for phase segregation in this type of glass. The investigated borosilicate glass samples in this study were also observed with a SEM (on micrometer scale) and with atomic force microscopy (AFM) on nanometer scale. In both cases no phase segregation was observed on the accessible scales.

In order to improve thermodynamic models for borosilicate glass melts, it is recommended to combine the results of thermodynamic modeling, glass structure measurements and simulations and chemical activity measurements (e.g. by transpiration evaporation tests) for a wider range of glass compositions.

## 2.6 Properties of volatile species

The evaporation model also requires input data of properties, such as diffusion coefficients (for species in the melt as well as in the gas phase) and equilibrium constants of the evaporation reactions, taking place at the surface of the melt. The derivation of these parameters and some other relevant material properties is presented in this paragraph.

### 2.6.1 Determination of diffusion coefficient of species in gas phase ( $D_{g,i}$ )

For the description and calculation of the mass transport of volatile species in the gas phase, information on the diffusion coefficient values of the volatile species in the gas stream is required (equations 2.8, 2.9 and 2.12) [5]. The values for  $D_{g,i}$  can be estimated by Chapman-Enskog relations given by Bird, Stewart and Lightfoot [13]. For these Chapman-Enskog relations, the intermolecular Lennard-Jones parameters (i.e. the collision diameter of gaseous molecules and collision integral for viscosity) are required. For light elements, noble gases and simple polyatomic substances, these parameters are given in tables [13][71], but for most other compounds these data are not given. For the calculation of the collision integrals of these molecules, values for the maximum attractive energy between two molecules are required. Hirschfelder et al. [71] present a procedure to estimate diffusion coefficients in multi-component gas mixtures, like combustion gases.

In case that values for these Lennard-Jones parameters are not known, they may be estimated from the properties of the fluid at the critical point, the liquid at the normal boiling point and the solid at the melting point [13].

In the thesis of Beerkens [72], values are given for the collision diameter of several volatile sodium, potassium, boron and lead species. Conradt and Scholze [1] also described an

empirical relation to estimate the diffusion coefficient of volatile species in gas atmospheres. Table 2.3 shows the calculated diffusion coefficients of gaseous NaOH in different gas atmospheres from different literature sources or methods. Comparing the calculated values of  $D_{\text{NaOH}}$ 's in air, with  $D_{\text{NaOH}}$  in combustion gases (existing mainly of  $\text{O}_2$ ,  $\text{N}_2$ ,  $\text{H}_2\text{O}$  and  $\text{CO}_2$ ) and with  $D_{\text{NaOH}}$  in a  $\text{N}_2/\text{H}_2\text{O}$  gas mixture, the differences are less than 6 %. But the reported  $D_{\text{NaOH}}$  values by Beerkens and Conradt et al. differ about 35 %. As will be discussed in paragraph 5.4 the accuracy of the experimentally derived chemical activities, depends strongly on the accuracy of  $D_{\text{NaOH}}$ . For the most important investigated gaseous volatile species the calculated diffusion coefficients are shown in Table 2.4.

Table 2.3: Calculated diffusion coefficients in  $\text{cm}^2/\text{s}$  of gaseous NaOH in gases at 1400 and 1500 °C

Temperature (°C)	$D_{\text{NaOH}}$ in air	$D_{\text{NaOH}}$ in combustion gases <sup>2)</sup>	$D_{\text{NaOH}}$ in $\text{N}_2/\text{H}_2\text{O}$ mixture (50/50)	$D_{\text{NaOH}}$ reported by Conradt [1] <sup>3)</sup>	$D_{\text{NaOH}}$ reported by Beerkens [72] <sup>1,2)</sup>
	D in $\text{cm}^2/\text{s}$			D in $\text{cm}^2/\text{s}$	
	Calculated from Chapman-Enskog relation <sup>1)</sup>				
1400	3.12	2.96	3.01	3.3	2.46
1500	3.45	3.27	3.33	3.7	2.73

<sup>1)</sup> The collision diameter of gaseous NaOH is 3.804 Å [72]

<sup>2)</sup> Composition of combustion gases:  $\text{H}_2\text{O}$  = 13 vol.-%,  $\text{O}_2$  = 4.4 vol.-%,  $\text{CO}_2$  = 9.0 vol.-% and  $\text{N}_2+\text{Ar}$  = 3.6 vol.-%

<sup>3)</sup> Valid for  $\text{N}_2/\text{H}_2\text{O}$  mixtures. The  $\text{H}_2\text{O}$  volume fraction varies between 0 and 0.5.

Table 2.4: Calculated diffusion coefficients in  $\text{cm}^2/\text{s}$  of gaseous volatile species in a gas mixture of 20 % water vapor and 80 % nitrogen at temperatures of 1400 °C, 1500 °C and 1600 °C. The diffusion coefficients are calculated from Chapman-Enskog relation as discussed in paragraph 2.6.1.

$D_i$ in $\text{cm}^2/\text{s}$	T = 1400 °C	T = 1500 °C	T = 1600 °C
$D_{\text{NaOH}}$	3.05	3.37	3.71
$D_{\text{Na}}$	3.18	3.52	3.88
$D_{\text{KOH}}$	2.52	2.79	3.07
$D_{\text{Na}_2\text{SO}_4}$	1.55	1.71	1.88
$D_{\text{K}_2\text{SO}_4}$	1.45	1.61	1.78
$D_{\text{HBO}_2}$	3.27	3.62	3.98

### 2.6.2 Equilibrium constants

As discussed in paragraph 2.1, the (reactive) evaporation rate of glass melt species from a glass melt into the combustion atmosphere above the glass melt is assumed to be governed by mass transfer processes in the glass melt and mass transfer from the glass melt surface into the combustion space. It is assumed that the reaction kinetics are fast compared to the transport processes, implying local chemical equilibrium conditions. The temperature dependent reaction equilibrium constant  $K$  for a reaction is generally given by

$$K = e^{\frac{-\Delta G^0}{RT}} \quad (2.35)$$

in which  $\Delta G^0$  is the standard Gibbs free energy change of the reaction,  $T$  is the temperature expressed in Kelvin, and  $R$  is the universal gas constant. The Gibbs free energy change by reaction can be described by

$$\Delta G^0 = \sum_{j=1}^{n1} \nu_j G_j^0 - \sum_{i=1}^{n2} \nu_i G_i^0 \quad (2.36)$$

in which  $n2$  is the number of reactants  $i$ ,  $n1$  is the number of reaction products  $j$ ,  $\nu$  is the reaction stoichiometric coefficient for a species, and  $G^0$  is the standard Gibbs free energy. For the evaporation reaction 2.1, the standard Gibbs free energy of reaction is given by

$$\Delta G^0 = q G_i^0 - m G_k^0 - n G_j^0 \quad (2.37)$$

which can be derived from thermodynamic tables for pure substances [73][74].

Equilibrium constants also can be obtained directly from databases like FactSage [56]. Conradt and Scholze [1] also supply equilibrium constants for chemical reactions of sodium, potassium, boron and lead compounds evaporating from the melt. Table 2.5 shows values of the equilibrium constants used in this study at different temperatures.

### 2.6.3 Diffusion coefficients of volatile species in glass melts

According to Hermans [7], the interdiffusion coefficient of a species in a melt or liquid, relative to a fixed frame of reference, is defined from Fick's law as the proportionality between the net mole flux and concentration gradient (eq 2.6) at a fixed position in the melt. The given interdiffusion coefficients of the oxides suggest that the oxides in the melt (e.g.  $\text{SiO}_2$ ,  $\text{Na}_2\text{O}$ ,  $\text{CaO}$ ) are the moving particles in the melt, which is not true.

Table 2.5: Equilibrium constants for different evaporation reactions from glass melts. The equilibrium constants were obtained from the thermodynamic database Factsage [56]. These equilibrium constants are derived for vapor pressures expressed in bar.

Evaporation reaction	Temperature (°C)						
	1000	1100	1200	1300	1400	1500	1600
$\text{Na}_2\text{O(l)} + \text{H}_2\text{O(g)} \rightleftharpoons 2\text{NaOH(g)}$	$7.76 \cdot 10^{-2}$	$2.70 \cdot 10^{-1}$	$7.76 \cdot 10^{-1}$	1.92	4.17	8.20	14.77
$\text{K}_2\text{O(l)} + \text{H}_2\text{O(g)} \rightleftharpoons 2\text{KOH(g)}$	$1.01 \cdot 10^3$	$1.831 \cdot 10^3$	$2.99 \cdot 10^3$	$4.49 \cdot 10^3$	$6.32 \cdot 10^3$	$8.42 \cdot 10^3$	$1.07 \cdot 10^4$
$\text{B}_2\text{O}_3\text{(l)} + \text{H}_2\text{O(g)} \rightleftharpoons 2\text{HBO}_2\text{(g)}$	$4.94 \cdot 10^{-6}$	$5.02 \cdot 10^{-5}$	$3.66 \cdot 10^{-4}$	$2.04 \cdot 10^{-3}$	$9.12 \cdot 10^{-3}$	$3.40 \cdot 10^{-2}$	$1.09 \cdot 10^{-1}$
$2\text{NaCl(l)} + \text{H}_2\text{O(g)} \rightleftharpoons 2\text{HCl(g)} + \text{Na}_2\text{O(l)}$	$2.25 \cdot 10^{-14}$	$5.25 \cdot 10^{-13}$	$7.95 \cdot 10^{-12}$	$8.47 \cdot 10^{-11}$	$6.78 \cdot 10^{-10}$	$4.28 \cdot 10^{-9}$	$2.21 \cdot 10^{-8}$
$2\text{KCl(l)} + \text{H}_2\text{O(g)} \rightleftharpoons 2\text{HCl(g)} + \text{K}_2\text{O(l)}$	$4.41 \cdot 10^{-18}$	$1.72 \cdot 10^{-16}$	$4.05 \cdot 10^{-15}$	$6.31 \cdot 10^{-14}$	$7.02 \cdot 10^{-13}$	$5.90 \cdot 10^{-12}$	$3.93 \cdot 10^{-11}$
$\text{KCl(l)} \rightleftharpoons \text{KCl(g)}$	$1.48 \cdot 10^{-2}$	$4.77 \cdot 10^{-2}$	$1.29 \cdot 10^{-1}$	$3.00 \cdot 10^{-1}$	$6.23 \cdot 10^{-1}$	1.18	2.04
$\text{NaCl(l)} \rightleftharpoons \text{NaCl(g)}$	$9.01 \cdot 10^{-3}$	$3.08 \cdot 10^{-2}$	$8.75 \cdot 10^{-2}$	$2.15 \cdot 10^{-1}$	$4.67 \cdot 10^{-1}$	$9.19 \cdot 10^{-1}$	1.67
$\text{Na}_2\text{SO}_4\text{(l)} \rightleftharpoons \text{Na}_2\text{SO}_4\text{(g)}$	$6.76 \cdot 10^{-7}$	$4.58 \cdot 10^{-6}$	$2.33 \cdot 10^{-5}$	$9.41 \cdot 10^{-5}$	$3.16 \cdot 10^{-4}$	$9.09 \cdot 10^{-4}$	$2.30 \cdot 10^{-3}$
$\text{K}_2\text{SO}_4\text{(l)} \rightleftharpoons \text{K}_2\text{SO}_4\text{(g)}$	$3.85 \cdot 10^{-6}$	$2.20 \cdot 10^{-5}$	$9.61 \cdot 10^{-5}$	$3.39 \cdot 10^{-4}$	$1.01 \cdot 10^{-3}$	$2.60 \cdot 10^{-3}$	$5.97 \cdot 10^{-3}$

In an electrolyte such as a silicate glass melt, ions are the main moving particles, but the interdiffusion coefficient is used to describe the results of diffusion experiments (e.g. diffusion couples [7]).

Several molecular scale diffusion models are based on the principle of moving ions in the melt [10][75][76][77]. The diffusion coefficient that is derived for average Brownian movement in absence of an activity gradient is called the tracer diffusion coefficient ( $D^T$ ). In case the chemical activity of a component  $j$  in the melt is not linear proportional to the molar concentration, the intrinsic diffusion coefficient should be applied ( $D^I$ ).  $D^I$  is the product of  $D^T$  and a thermodynamic factor  $\Phi$ . See for detailed information on this subject reference [7].

### ***Diffusion in soda-(lime)-silicate glass melts***

In the evaporation model for a binary sodium-silicate melt, the mass transport of sodium species in the melt is described, by assuming a binary system of  $\text{Na}_2\text{O}$  and  $\text{SiO}_2$  with constant interdiffusion coefficients. The model requires the interdiffusion coefficients for oxides (e.g.  $D_{\text{Na}_2\text{O}}$ ). Contrary to the tracer diffusion coefficients ( $D^T$ ), the inter-diffusion coefficients depend on the type of experiment. In his thesis Hermans [7], gives a statistic correlation between the viscosity, ion charge and the tracer diffusion coefficients of anions as well as cations (eq 2.17). To obtain these correlations, he used literature data on diffusion coefficients of silicate melts above the transformation temperature  $T_g$ . For cations, other than silicon, he used 993 data points and he assumed  $D \approx D^I \approx D^T$ . This assumption is only valid for diluted concentrations of mobile cations in the melt. Then the thermodynamic factor  $\Phi$  is

often approximately 1 ( $D^I \approx D^T$ ), and pressure relaxation and the condition of electrical neutrality play a limited role ( $D \approx D^I$ ).

He showed that for relative low concentrations of different, rather mobile components in silicate melts, this approximation gives small errors. The correlation coefficient of this linear relation (equation 2.17) fitting literature data, is only 0.64 and the residual standard deviation in  $^{10}\log\left(\frac{D}{m^2 \cdot s}\right) = 1.3$  (a factor 20 in the D values). Thus equation 2.17 gives only very rough estimates of diffusion coefficients.

For soda-lime-silicate melts, the results of his correlation are shown for the diffusion coefficients of sodium in the melt in Figure 2.12. For sodium-silicate glass melts [78][79] as well as soda-lime-silicate melts [3][7][80] the differences between the tracer diffusion coefficients of  $\text{Na}^+$  and interdiffusion coefficients of the sodium oxide are about 1 to 3 decades. In all cases, the reported tracer diffusion coefficients are much higher. This might be a result of massive relaxation flows (in opposite direction from the sodium diffusion) during the diffusion of mobile sodium cations. To release pressure differences in the melt (i.e. pressure relaxation), a net convective molar transport of matter can be expected relative to a fixed frame of references.

In a multi-component glass melt with other mobile ions, such as: calcium, magnesium or potassium, pressure relaxation will be neutralized for the most part by the diffusion of these ions in the opposite direction compared to the sodium ions. For this specific situation the interdiffusion coefficient and tracer diffusion coefficient are about similar.

Several other authors [8][10][81] reported values of  $\text{Na}_2\text{O}$  inter-diffusion coefficients or sodium tracer diffusion coefficients measured for soda-lime-silica melts and others [82][83] showed  $\text{Na}_2\text{O}$  concentrations profiles near the surface of the melt after a certain exposure time of a soda-silicate melt to a furnace atmosphere in evaporation experiments.

From these profiles the  $\text{Na}_2\text{O}$  interdiffusion coefficients can be estimated. Cable et al. [8][10] summarized the results of several sodium evaporation studies and concluded that the diffusivity values of  $\text{Na}_2\text{O}$  in soda-lime-silicate melts show considerable scatter and some anomalies in their dependency on composition and temperature. Cable also mentioned that convection might lead to errors in these experimentally derived interdiffusivity values.



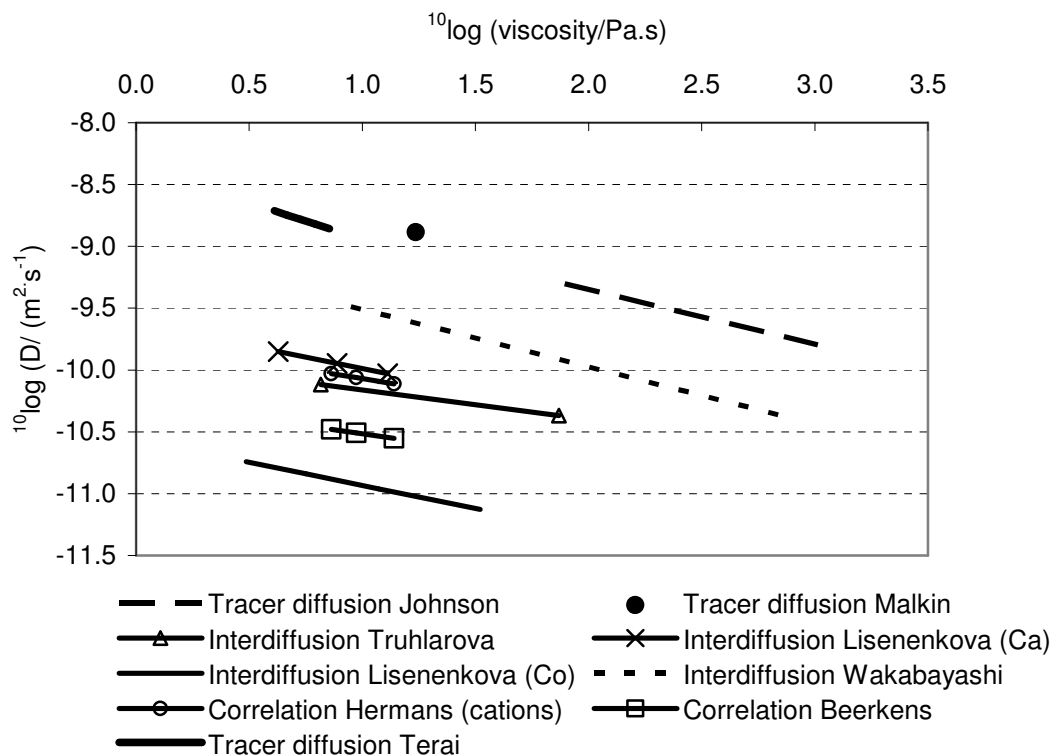


Figure 2.12: Reported interdiffusion coefficients and tracer diffusion coefficients ( $D_{Na+}^T$ ) in soda-lime-silicate melts. The interdiffusion coefficients were obtained from the handbook of glass data [79][80] and from Hermans' [7] correlation between viscosity and charge of the ion at one side and tracer diffusion coefficient at the other side. Beerkens [3] used an empirical relation between temperature and interdiffusion coefficient.

Growth and rise of gas bubbles, temperature gradients, change of density as a function of changing glass melt composition, as volatilization proceeds, and surface tension gradients at the surface of the melt can cause convection.

Only a few concentration profiles of individual glass components after evaporation tests or information about depletion of volatile glass components at the surface after evaporation have been published. Schaeffer and Sanders [82][83] found for soda-lime-silica melts at room temperature, after an evaporation test, that the  $\text{Na}_2\text{O}$  as well as  $\text{CaO}$  concentrations decreased near the surface, while the  $\text{CaO}$  concentration in the interior increased slightly. After an evaporation experiment at  $1335\text{ }^\circ\text{C}$  of 25.5 hours, the  $\text{CaO}$  concentration at the surface decreased from initially 10 mass.-% to about 7 mass.-% at the end. In the interior,  $\text{CaO}$  concentrations up to 11 mass.-% were found. Stirred, homogeneous glass samples were used at the start of their transpiration experiments. Calcium was not found to be a volatile component during the transpiration evaporation test. The observed  $\text{CaO}$  concentration profile might be a result of an increasing  $\text{CaO}$  chemical activity with decreasing  $\text{Na}_2\text{O}$  contents in

the melt. In a Na<sub>2</sub>O depleted surface layer the SiO<sub>2</sub> concentration is higher and according to thermodynamic calculations with our Associated Species Model (see paragraph 2.5) and Factsage [56] a higher chemical activity of CaO is expected in this silica rich surface layer, when the CaO concentration in the surface layer is similar to the CaO concentration in the bulk of the melt. As a result of the higher  $a_{\text{CaO}}$  in the surface layer CaO starts to diffuse from the surface layer to the bulk of the melt, until the chemical activities of CaO are equal all over the melt (uphill diffusion). The thermodynamic calculations show that this may lead to differences between the CaO concentrations at the surface and the CaO concentrations in the bulk of the melt of about 0.5 mol-%. Thus the calculations cannot explain the observed high CaO difference in the melt.

Kucuk et al. [84] investigated the potassium and sodium evaporation from potassium-lime-silicate melts as well as sodium-lime-silicate melts. They suggested, as a possible explanation for strong Na<sub>2</sub>O surface depletion, that calcium in the soda-lime-silica melt blocks the diffusion path of the sodium through the melt, preventing the continual replenishment of the sodium surface concentration during the sodium evaporation processes. This partly explains the low Na<sub>2</sub>O diffusivity and the observed Na<sub>2</sub>O surface depletion, but this does not explain the observed CaO concentration differences between bulk and surface of 1.5 to 2 mol-%.

Figure 2.12 shows different reported tracer diffusion coefficients and interdiffusion coefficients of Na<sub>2</sub>O in soda-lime-silicate melts. From sodium concentration gradients in glass samples obtained after transpiration evaporation experiments of Schaeffer and Sanders [82][83], Beerkens [3] derived an empirical relation for the interdiffusion coefficient of Na<sub>2</sub>O in soda-lime-silicate melts as a function of temperature:  $D_{\text{Na}_2\text{O}} = 8 \cdot 10^{-10} \cdot \exp(-5655/T)$ . In our investigations we used equation 2.17 to calculate the interdiffusion coefficients of volatile glass compounds.

#### 2.6.4 Other properties

For our evaporation model, other material properties are required, such as:

- Density of glass melt,
- Viscosity of the glass melt,
- Density and viscosity of the gas atmosphere.

The density and viscosity relations for a glass melt as function of the composition were derived from the International TNO Glass Course [41]. The viscosity has been calculated

from the so-called VFT (Vogel, Fulcher, Tammann) relation further developed and applied by Lakatos [85]. To calculate the density the method of Appen is applied [65].

The density and viscosity of the main gas species in the atmosphere ( $\text{N}_2$ ,  $\text{O}_2$  and  $\text{H}_2\text{O}$ ) are derived from a database of the Dutch Gasunie [86].

## 2.7 Concluding remarks to chapter 2

In this chapter a general applicable evaporation simulation model for multi-component glass melts, based on partly validated mass transfer relations (for laboratory transpiration tests) in combination with simulations of the thermodynamic properties of multi-component silicate melt has been presented. The model can be used to predict the evaporation rates of volatile species from different types of glass melts exposed to furnace atmospheres.

The here developed evaporation model for glass melts, mainly based on first principles, describes the evaporation kinetics from glass melts in direct contact with flowing gas phases. In a static melt, the transport of evaporating glass melt components is described by the 2<sup>nd</sup> diffusion law of Fick. However, convective flows in the melt have an impact on the transport of volatile compounds in the melt and the local surface composition, which is in equilibrium with the local atmosphere directly above the melt. Free convection in the melt might be a result of: 1) local differences in density due to local temperature differences or local composition differences and/or 2) Marangoni flows which are a result of local differences in surface tension. Surface tension differences and Marangoni flows are often a result of local differences in surface composition, during glass melting. These concentration differences might be a result of the presence of local sulfate gall layers on top of the melt, formed during melting of glass batches with sulfur. Due to the local dissociation reactions of this sulfate gall, concentration differences can be expected in the surface layer of the melt. The non-uniform evaporation of volatile species might also be a cause of Marangoni flows. Convective flows as a result of density differences (buoyancy) have been modeled with CFD. For the modeling of Marangoni flows in glass melts no tools have been developed yet.

Mass transfer boundary-layer models and Computational Fluid Dynamics (CFD) modeling have been used to calculate the mass transfer from the surface of the melt into the atmosphere. These models require data on Nernst boundary layer thickness or Sherwood relations, equilibrium vapor pressures and chemical activities of volatile species in the glass melt surface layer. To calculate chemical activities of volatile glass components in multi-component silicate melts as a function of the glass composition and temperature a thermochemical Associated Species Model (ASM) has been developed, extended and applied. Thermodynamic properties of glass melts showing phase segregation, require further modification in the associated species model applied here.

Laboratory scale transpiration evaporation experiments are used to study evaporation kinetics as well as to validate the evaporation models described in this chapter (see chapter 3).

The most important conclusions, concerning the developed evaporation models are:

- For laboratory transpiration evaporation tests, mass transfer relations for transport of volatile species from the surface of the melt into the atmosphere have been derived and tested with model liquids and glass melt. Because of these mass transfer relations it became possible to derive, chemical properties of glass melts, such as chemical activities and saturation vapor pressures, from the measured evaporation rates. In this study, mass transport relations for transpiration set-ups were derived from own investigations. CFD modeling and relatively simple water evaporation experiments have been performed to find these mass transfer relations. These Sherwood relations are used to describe quantitatively the kinetics of evaporation in transpiration experiments. Additional experiments have been performed to validate these relations. As will be shown in chapter 4, the measured (from transpiration experiments) and modeled chemical activities (from ASM) of volatile species in soda-(lime)-silicate melts deviate in most cases less than 10 %.
- The development of a method to derive local, Nernst gas phase boundary layer thickness, from CFD modeling. This method enables the calculation of mass transport of volatile species from the surface of the melt into the combustion chamber of an industrial glass furnace. Based on CFD calculations for turbulent gas flows in combination with wall-functions for velocities, temperatures and mass fractions, the concentration profiles of evaporating species from the melt into the gas phase layer above the melt can be determined. The local mass transfer of gaseous volatile species can now be derived from the calculated concentration gradient at the surface of the melt. For the description of these wall functions the analogy between momentum transport, heat transport and mass transport has been used. In an example to be presented in chapter 5, the calculated Nernst boundary layer thickness values for gas phase boundary layers above industrial glass melts are used to estimate the boron evaporation rates in an industrial E-glass furnace.
- With the thermodynamic Associated Species Model developed in this study, the required thermodynamic properties (chemical activity and saturation vapor pressure) of volatile glass compounds in multi-component soda-(lime)-silicate glass melts can

be estimated. In the thermodynamic model, the glass melt is assumed to be an ideal mixture of single oxides and associated species (stoichiometric compounds with known thermodynamic properties). The chemical activity (relative to the pure non-mixed liquid compounds) of each of these different compounds (e.g.  $\text{Na}_2\text{O}$  or  $\text{SiO}_2$ ) and the associated species equals the concentration (molar fraction) of these compounds in the melt. The composition of the mixture of all these associated species is calculated by minimization of the Gibbs free energy of the total system under constraint of conservation of mass for each chemical element. For this minimization procedure, a numerical algorithm is developed, calculating the equilibrium concentrations of the associated species in the mixture, assuming the mixture to behave ideally. This method is only applicable for single phase glass melts and ideal mixing of all associated species taken into account.

- In our study, the previously described thermochemical Associated Species Model (ASM) is applied for binary sodium-silicate melts, ternary soda-lime-silicate melts and industrial produced multi-component float glass compositions, which consists basically of the oxides:  $\text{SiO}_2$ ,  $\text{Na}_2\text{O}$ ,  $\text{CaO}$ ,  $\text{MgO}$ ,  $\text{Al}_2\text{O}_3$  and  $\text{K}_2\text{O}$ . The accuracy and reliability of the model depends very much on the validity of the model assumptions and the accuracy of the available thermodynamic data (Gibbs free energy). For glass melt systems with liquid miscibility gaps the ASM approach used here in its original form, is not applicable. Based on the binary  $\text{B}_2\text{O}_3 - \text{CaO}$  phase diagram and the ternary  $\text{B}_2\text{O}_3\text{-CaO-SiO}_2$  phase diagram liquid miscibility gaps are expected for these systems.

For possible relevant associated species with a molar ratios  $\text{CaO}/\text{B}_2\text{O}_3 > 3$  no thermodynamic data is available at all. These are probably the main reasons for the inaccurate thermodynamic modeling results for  $\text{SiO}_2\text{-CaO-Al}_2\text{O}_3\text{-B}_2\text{O}_3$  melts when using the original ASM approach with limited number of associated species and assuming no immiscibility. To improve the thermodynamic modeling of these kinds of melts, the associated species  $5\text{CaO.B}_2\text{O}_3(\text{l})$  has been introduced and thermodynamic data of other calcium-borate species were derived .

Chemical activities of  $\text{B}_2\text{O}_3$  in  $\text{SiO}_2\text{-CaO-Al}_2\text{O}_3\text{-B}_2\text{O}_3$  melts, derived from laboratory evaporation tests, are used to estimate the Gibbs energy values of liquid calcium-borates as a function of temperature. In order to fit the experimental results with the modeling results, the Gibbs energy values of a fictive  $5\text{CaO.B}_2\text{O}_3(\text{l})$  compound is used to accurately reproduce the experimentally derived chemical activities of  $\text{B}_2\text{O}_3$  in

glass melt systems with a molar  $\text{CaO}:\text{B}_2\text{O}_3$  ratio of about 5. In this modified thermodynamic model it is assumed that all oxides and associated species mix ideally. In the current model immiscibility is not taken into account.

Recommendations for further improvements and validation of the evaporation model described in this chapter are:

1. Industrial validation of the developed evaporation model. For the modeling of evaporation rates in industrial glass furnaces all modeling tools are now available:
  - a. CFD modeling, which can be used to estimate the mass transfer from the surface of the melt in the gas phase (see paragraph 2.3.3).
  - b. Specific CFD models, like GTM-X (see chapter 2.2) are applied to simulate numerically the convection and diffusion processes in glass melts. With these models, the heat transfer in melts, and thus glass melt surface temperatures, can be calculated as well.
  - c. The required chemical activities of volatile species at the surface of the melt can be obtained from the Associated Species Model (paragraph 2.5). The local evaporation rates calculated by the models for an industrial glass furnace should be compared with the measured evaporation rates in that specific furnace. This validation tests could be performed for different process conditions in the furnace.
2. Development of thermodynamic models to describe quantitatively compositions of the phases and chemical activities of phase separated silicate melts. Till now the ASM, developed in this study, is only applicable for single phase melts. For multi-phase melts, the thermodynamic model need to be adapted.
3. Study on the effect of free Marangoni convection in the molten glass on reduction of depletion of volatile species at the surface of a melt.

**Appendix I: Equations of change in fluid dynamics**

The 3-dimensional flows in a gas or liquid can be derived from the moment equations or Navier-Stokes equation (eq. 2.38) and the mass conservation equation (2.39). Notice the extra term for gravity in equation 2.38b [13].

$$\rho \left( \frac{\partial v_x}{\partial t} + v_x \frac{\partial v_x}{\partial x} + v_y \frac{\partial v_x}{\partial y} + v_z \frac{\partial v_x}{\partial z} \right) = -\frac{\partial p}{\partial x} + \mu \left( \frac{\partial^2 v_x}{\partial x^2} + \frac{\partial^2 v_x}{\partial y^2} + \frac{\partial^2 v_x}{\partial z^2} \right) \quad (2.38a)$$

$$\rho \left( \frac{\partial v_y}{\partial t} + v_x \frac{\partial v_y}{\partial x} + v_y \frac{\partial v_y}{\partial y} + v_z \frac{\partial v_y}{\partial z} \right) = -\frac{\partial p}{\partial y} + \mu \left( \frac{\partial^2 v_y}{\partial x^2} + \frac{\partial^2 v_y}{\partial y^2} + \frac{\partial^2 v_y}{\partial z^2} \right) + \rho g \quad (2.38b)$$

$$\rho \left( \frac{\partial v_z}{\partial t} + v_x \frac{\partial v_z}{\partial x} + v_y \frac{\partial v_z}{\partial y} + v_z \frac{\partial v_z}{\partial z} \right) = -\frac{\partial p}{\partial z} + \mu \left( \frac{\partial^2 v_z}{\partial x^2} + \frac{\partial^2 v_z}{\partial y^2} + \frac{\partial^2 v_z}{\partial z^2} \right) \quad (2.38c)$$

$$\frac{\partial \rho}{\partial t} = -\left( \nabla \cdot \rho \vec{v} \right) = -\left( \frac{\partial}{\partial x} \rho v_x + \frac{\partial}{\partial y} \rho v_y + \frac{\partial}{\partial z} \rho v_z \right) \quad (2.39)$$

For a stationary conditions  $\partial \rho / \partial t = 0$  and  $\partial v / \partial t = 0$ .

The change of the concentration of compound j in this medium is a result of convective and diffusive transport and reactions. In this equation,  $R_j$  is a reaction term taking into account the chemical formation of a compound j. For stationary conditions  $\frac{\partial C_j}{\partial t} = 0$ .

$$\frac{\partial C_j}{\partial t} = -\left( v_x \cdot \frac{\partial C_j}{\partial x} + v_y \cdot \frac{\partial C_j}{\partial y} + v_z \cdot \frac{\partial C_j}{\partial z} \right) + \frac{\partial}{\partial x} \left( D_j \frac{\partial C_j}{\partial x} \right) + \frac{\partial}{\partial y} \left( D_j \frac{\partial C_j}{\partial y} \right) + \frac{\partial}{\partial z} \left( D_j \frac{\partial C_j}{\partial z} \right) + R_j \quad (2.40)$$

Thus, from known  $v_x, v_y, v_z, D_j$  values (solution of equations 2.38 and 2.39) and the boundary conditions plus initial conditions,  $C_j$  can be determined dependent on  $x, y, z$  and  $t$ .



## Appendix II: Transition of velocity, temperature and mass fraction data in dimensionless values.

In paragraph 2.3.3 the dimensionless normalized velocity in the x-direction ( $U_x^+$ ), dimensionless normalized temperature ( $T^+$ ) and dimensionless normalized mass fraction of a gaseous volatile species  $i$  in the atmosphere ( $X_i^+$ ) have been applied to calculate the Nernst boundary layer thickness in the gas phase above the melt in industrial glass furnaces. The index 'w' refers to the values on the wall/liquid surface and the index 'p' refers to values of the first grid point above the wall/liquid surface.

For more information about the definitions of these dimensionless parameters see Launder & Spalding [37].

Here, the normalized dimensionless absolute velocity  $U_x^+$  is defined as:

$$U_x^+ = \frac{v_{x,p}}{v_\tau} \quad (2.41)$$

Here,  $v_{x,p}$  is the gas velocity in the x-direction in the first grid point p near the surface/wall

and  $v_\tau$  is the so-called friction velocity, in the wall function method, defined as:

$$v_\tau = \sqrt{\frac{\tau_w}{\rho_p}} \quad (2.42)$$

The dimensionless normalized temperature  $T^+$  (in the first grid point p) is defined by:

$$T^+ = \frac{(T_w - T_p) \cdot \rho_p \cdot C_{p_p} \cdot v_\tau}{\theta_w''} = \frac{\rho_p \cdot C_{p_p} \cdot v_\tau}{h_w} \quad (2.43)$$

with  $\theta_w''$  the wall or surface heat flux [ $\text{W}/\text{m}^2$ ] and  $h_w$  the wall heat transfer coefficient [ $\text{W}/\text{m}^2/\text{K}$ ]. As boundary condition temperature  $T_w$  or heat flux  $\theta_w''$  is fixed.

The dimensionless normalized mass fraction  $X_i^+$  in a grid point p is given by:

$$X_i^+ = \frac{(\chi_w - \chi_p) \cdot \rho_p v_\tau}{\phi_w''} = \frac{v_\tau}{h_w} \quad (2.44)$$

with  $\phi_w''$  the local wall or surface mass flux [ $\text{kg}/\text{m}^2/\text{s}$ ],  $\chi$  the local mass fraction of i in the gas phase (-) and  $h_w$  the local wall mass transfer coefficient (m/s).

**References**

- [1] R. Conradt, H. Scholze, 'Zur Verdampfung aus Glasschmelzen', *Glastech. Ber.*, **59** [2] 34-52 (1986)
- [2] J.A.C. van Limpt, A.J. Faber, 'Reduction of emissions by decreasing volatilization in glass furnaces, phase 2; Experimental simulation tests on volatilization in glass furnaces', TNO report HAM-RPT-98-408, TNO Institute of Applied Physics, Eindhoven (1998)
- [3] R.G.C. Beerkens, 'Modelling the Kinetics of Volatilization from Glass Melts', *J.Am.Ceram.Soc.*, **84** [9] 1952-60 (2001)
- [4] H. van Limpt, R. Beerkens, A. Lankhorst, A. Habraken, 'Mass transfer relations for transpiration evaporation experiments', *Int. J. of Heat and Mass Transfer*, **48**, 4265-4281 (2005)
- [5] H. van Limpt, R. Beerkens, O. Verheijen, 'Models and experiments for sodium evaporation from sodium containing silicate melts', *J.Am.Ceram.Soc.*, **89** [11], 3446-3455 (2006)
- [6] R.G.C. Beerkens, J.A.C. van Limpt, 'Evaporation in industrial glass melt furnaces', *Journal of Glass Science and Technology*, **74** [(9)] 245-257 (2001)
- [7] J.M. Hermans, 'Diffusion in multicomponent silicate glass melts', Thesis Fakultät für Georessourcen und Materialtechnik der Rheinisch Westfälische Technische Hochschule Aachen, (2004)
- [8] M. Cable, C. Apak, M.A. Chaudhry, 'The kinetics of volatilization from lead glasses', *Glastech. Ber.*, **48** [1] 1-11 (1975)
- [9] J. Matousek, J. Hlavac, 'A study of the volatilisation of lead glass', *Glass Technol.*, **12** [4] 103-106 (1971)
- [10] M. Cable, M.A. Chaudhry, 'Volatilisation from soda-lime-silica melts at one atmosphere and reduced pressures', *Glass Technol.*, **16** [6] 125-134 (1975)
- [11] J. Crank, 'The Mathematics of Diffusion', 2<sup>nd</sup> ed., Oxford Science publications (1975), ISBN 0-19-853411-6
- [12] W.K. Lewis, W.G. Whitman, 'Principles of gas absorption', *Industrial and Engineering Chemistry*, **16**, 1215-1220, (1924)
- [13] R.B. Bird, W.E. Stewart, E.N. Lightfoot, 'Transport Phenomena', second ed., John Wiley & Sons, 77-78, 420, 525-528 (2002)
- [14] J.M. Smith, E. Stammers, L.P.B.M. Janssen, 'Fysische Transport Verschijnselen I', Delftse Uitgevers Maatschappij b.v., 2e druk, ISBN 90-6562-050-8, 146-148 (1981)

- [15] Verein Deutscher Ingenieure, 'VDI-Wärmeatlas', 6th edition, VDI-Verlag GmbH Düsseldorf (1991), ISBN 3-18-401084-8
- [16] A. Lankhorst, A. Habraken, O. Op den Camp and Oscar Verheijen, 'Simulation of the impact of different combustion systems on the flow and temperature distribution in glass melting furnaces', HVG/NCNG Colloquium on Operation and Modelling of Glass Melting Furnaces, Aachen, 8 November 2005.
- [17] L. Thielen, A.M. Lankhorst, B.D. Paarhuis and O.S. Verheijen 'Simulation of multi-physical phenomena in glass melting furnaces', presented at NAFEMS World Congress, May 2007, Vancouver, Canada
- [18] G.K. Batchelor, 'An Introduction to Fluid Dynamics', Cambridge University Press (1970)
- [19] J.H. Ferziger, M. Perić, 'Computational Methods for Fluid Dynamics', Springer (1999)
- [20] S.V. Patankar, 'Numerical Heat Transfer and Fluid Flow', Hemisphere Publishing Co., McGraw-Hill (1980)
- [21] T. Molenkamp, 'Marangoni Convection, Mass Transfer and Microgravity', Thesis University of Groningen (1998)
- [22] R. Brückner, 'Zur Kinetik des Stoffaustausches an der Grenzflächen zwischen Silikatglas- und Salz-schmelzen und des Stofftransportes in Silikatglasschmelzen unter besonderer Berücksichtigung des Verhaltens von  $\text{Na}_2\text{SO}_4$  und seinen Zersetzungsprodukten. Teil I: Grenzflächenenergetische Ausgleichsprozesse bei Stoffaustauschvorgängen' *Glastech. Ber.*, **34** [9], 438 – 455 (1961), Teil II, 'Der Substanztausch zwischen Silicatglas- und Salzschnelzen' *Glastech. Ber.*, **34** [11], 515-528 (1961), Teil III, 'Thermische und chemische Zersetzung von  $\text{Na}_2\text{SO}_4$  und der Substanztausch zwischen Silikatglasschnelzen und  $\text{SO}_2$ -haltigen Atmosphären', *Glastech. Ber.*, **35** [2], 93-105 (1962)
- [23] L.J. Austin, W.E. Ying, H. Sawistowski, 'Interfacial phenomena in binary liquid-liquid systems', *Chem. Eng. Sci.*, **21**, 1109-1110 (1966)
- [24] P. Laimböck, 'Foaming of glass melts', Thesis Eindhoven University of Technology, ISBN 90-386-0518-8 (1998)
- [25] A.A. Appen, 'Versuch zur Klassifizierung von Komponenten nach ihrem Einfluß auf die Oberflächenspannung von Silikatschnelzen', *Silikattechnik* **5**, 11-12 (1954)
- [26] A. Dietzel, E. Wegner, 'Einfluß von  $\text{SO}_3$  auf die Oberflächenspannung von Gläsern', *Atti III. Congr. Internat. Vetro, Venedig*, 354-363 (1953)

- [27] L.F. Oldfield, R.D. Wright, 'The volatilisation of constituents from borosilicate glass at elevated temperatures', *Glass Technol.*, **3** [2], 59 – 68 (1962)
- [28] S.R. Ehrig, A. Petzold, 'Chemische Aspekte bei Verdampfungsvorgängen aus Borosilicatglasschmelzen, Teil II', *Sprechsaal*, **124** [2], 95-98, (1991)
- [29] W. Vogel, 'Struktur und Kristallisation der Gläser', VEB Deutscher Verlag für Grundstoffindustrie, 2<sup>nd</sup> ed., Leipzig (1971)
- [30] W. Vogel, 'Glaschemie', VEB Deutscher Verlag für Grundstoffindustrie, Leipzig (1979)
- [31] L. Delorme, 'Mecanismes de volatilité des verres et des fontes borosilicates d'intérêt nucléaire – influence de la structure, Thèse de doctorat, Sciences Appliquées, Université d'Orléans (1998)
- [32] K. Rietema, *Fysische transport- en overdrachtsverschijnselen*, Uitgeverij Het Spectrum, Utrecht/Antwerpen (1976)
- [33] K. Stephan, 'Waermeuebergang und Druckabfall bei nicht ausgebildeter Laminarstroemung in Rohren und in ebenen Spalten', *Chemie Ingenieur Technik* 31, (1959) 773-778
- [34] H. Martin, *Vorlesung Wärmeübertragung II*, Univ. Karlsruhe (TH) (1990)
- [35] I.H. Shames, 'Mechanics of fluids', 2<sup>nd</sup> ed., McGraw-Hill International Book Company, ISBN 0-07-056385-3 (1982)
- [36] A.N. Borghouts, 'Warmteleer en Kinetische Gastheorie', 4<sup>e</sup> druk, Delftsche Uitgevers Maatschappij B.V. ,Delft, The Netherlands (1976)
- [37] B.E. Launder, D.B. Spalding, 'Mathematical models of turbulence'. Academic Press (1972)
- [38] A. Lankhorst, 'Laminar and turbulent natural convection in cavities, numerical modeling and experimental validation', PhD thesis, Technical Universtiy Delft, The Netherlands (1991)
- [39] E.E. Khalil, 'Modelling of furnaces and combustors', Abacus Press (1982)
- [40] M.G. Carvalho, 'Computer simulation of a glass furnace', PhD thesis, Imperial College, London (1983)
- [41] TNO International course on Glass Technology (2004), derived from NCNG course for glass technologists, TNO Eindhoven, The Netherlands (1997)
- [42] R.W. Cahn, P. Haasen, E.J. Kramer, 'Materials Science and Technology, Volume 9, Glasses and Amorphous Materials', VCH, Weinheim, New York, Basel, Cambridge (1991)

- [43] A.C. Wright, 'The structure of borosilicate glass', Proceedings TNO Glass Trend workshop: 'Borosilicate glasses and raw materials in the glass industry', Castellón Spain (2005)
- [44] A.C. Wright, J.L. Shaw, R.N. Sinclair, N.M. Vedishcheva, B.A. Shakmatkin, C.R. Scales, 'The use of crystallographic data in interpreting the correlation function for complex glasses', *J. Non-Cryst. Solids*, **345/346**, 24-33 (2004)
- [45] A.C. Wright, B.A. Shakmatkin, N.M. Vedishcheva, 'The Chemical Structure of Oxide Glasses: A Concept Consistent with Neutron Scattering Studies?', *Glass Phys. and Chem.*, **27** [2], 97 -113 (2001)
- [46] A.C. Wright, N.M. Vedishcheva, B.A. Shakmatkin, 'Thermodynamic modelling of the real-space correlation function for four sodium borosilicate glasses', Proc. Fifth Int. Conf. on Borate Glasses, Crystals and Melts, *Phys. Chem. Glasses: Eur.J.Glass.Sci. Technol. B.* **47** [4], 497-506, August (2006)
- [47] N.M. Vedishcheva, B.A. Shakmatkin, A.C. Wright, 'Modeling the structure and properties (densities) of sodium borosilicate glasses', Proceedings: TNO Glass Trend workshop May 2005: 'Borosilicate glasses and raw materials in the glass industry', Castellón Spain (2005)
- [48] N.M. Vedishcheva, B.A. Shakmatkin, A.C. Wright, 'The structure of sodium borosilicate glasses: thermodynamic modelling vs. experiment', *J. Non-Cryst. Solids*, **39**, 345-346 (2004)
- [49] N.M. Vedishcheva, B.A. Shakmatkin, A.C. Wright, 'Thermodynamic modelling of the structure and properties of glasses in the systems  $\text{Na}_2\text{O}-\text{B}_2\text{O}_3-\text{SiO}_2$  and  $\text{Na}_2\text{O}-\text{CaO}-\text{SiO}_2$ ', *Phys. Chem. Glasses*, **46**, 99 - 107 (2005)
- [50] H. Li, R. Hicks, C. Richards, J. Parker, 'Structural approach to boron emission reduction – Rare earth stabilization of boron in borosilicate melts', Proceedings Glass Trend workshop: 'Borosilicate glasses and raw materials in the glass industry', Castellón Spain, May (2005)
- [51] D.A. Skoog, 'Principles of Instrumental Analysis', 3th ed., Saunders College Publishing, Japan, ISBN 4-8337-0282-7 (1985)
- [52] D.L. Griscom, 'Borate glass structure' in 'Borate glasses – Structure, Properties, Applications', *Materials Science Research volume 12*, 11-138, Plenum Press, New York, ISBN 0-306-40016-2 (1978)
- [53] Verein Deutscher Eisenhüttenleute, VDEh Slag Atlas, 2nd edition. Verlag Stahleisen GmbH, Düsseldorf, ISBN 3-514-00457-9 (1995)

- [54] T.H. Elmer, 'Leaching of E-glass', *J. Am. Cer. Soc.*, **67** [12], 778-782 (1984)
- [55] B. Das, B.D. Tucker, J.C. Watson, 'Acid corrosion analysis of fibre glass', *J. of. Mat. Sci.*, **26**, 6606- 6612 (1991)
- [56] C.W. Bale, P. Chartrand, S.A. Degterov, G. Eriksson, K. Hack, 'FactSage Thermochemical Software and Databases', *Calphad*, Vol., **26** [2], 189-228 (2002)
- [57] A.D. Pelton, P. Wu, 'Thermodynamic modeling in glass-forming melts', *J. Non.-Cryst. Solids*, **253**, 178-191 (1999)
- [58] J.W. Hastie, D.W. Bonnell, 'A predictive phase-equilibrium model for multicomponent oxide mixtures. 2. Oxides of Na-K-Ca-Mg-Al-Si', *High Temp. Sci.*, **19** [3], 275-306 (1985)
- [59] B.A. Shakhmatkin, N.M. Vedishcheva, M.M. Shultz, A.C. Wright, 'The thermodynamic properties of oxide glasses and glass-forming liquids and their chemical structure', *J. Non-Crystalline Solids*, **177**, 249-256 (1994)
- [60] R. Conradt, 'A Simplified Procedure to Estimate Thermodynamic Activities in Multicomponent Oxide Melts', *Molten Salt Chemistry and Technology* ed. by H. Wendt, Trans Tech Publication Zürich, Switzerland, **5-6**, 155-162 (1998)
- [61] R.G.C. Beerkens, O.S. Verheijen, 'Reactions of alkali vapours with silica based refractory in glass furnaces, thermodynamics and mass transfer', *Phys. Chem. Glasses*, **46** [6], 583-594 (2005)
- [62] A. Steiner, 'Foam glass production from vitrified municipal waste fly ashes' thesis University of Eindhoven (2006)
- [63] T. M. Besmann, K.E. Spear, 'Thermochemical modeling of oxide glasses', *J. Am. Cer. Soc.*, **85** [12], 2887-2894 (2002)
- [64] E.M. Levin, C.R. Robbins, H.F. McMurdie, 'Phase Diagrams for Ceramists', American Ceramic Society, Columbus Ohio, USA (1964)
- [65] H. Scholze, 'Glas, Natur, Struktur und Eigenschaften', 3th edition, Springer Verlag, Berlin, ISBN 3-540-08403-7, (1988)
- [66] J. Richter, 'Konzentrationsverlauf thermodynamischer Funktionen bei Salzschnmelzen mit zwei Komponenten', *Z. Naturforsch.*, **24a**, 835-844 (1969)
- [67] R.J. Charles, 'Activities in  $\text{Li}_2\text{O}$ -,  $\text{Na}_2\text{O}$ -, and  $\text{K}_2\text{O}$ - $\text{SiO}_2$  solutions', *J. Am. Ceram. Soc.*, **50** [12], 631-641 (1967)
- [68] T.M. Besmann, N.S. Kulkarni, K.E. Spear, 'Thermochemical and Phase Equilibria Property Prediction For Oxide Glass Systems Based On The Modified Associate Species Approach', *High Temperature Corrosion and Materials Technology IV*, The Electrochemical Society, Pennington, NJ, 557-566 (2004).

- [69] K.E. Spear, T.M. Besmann, E.C. Beahm, 'Thermochemical modeling of glass: Application to high-level nuclear waste glass', *MRS bulletin*, **24** [4], 37 – 44 (1999)
- [70] Verein Deutscher Eisenhüttenleute, *VDEh Slag Atlas*, 2nd edition. Verlag Stahleisen GmbH, Düsseldorf, ISBN 3-514-00457-9
- [71] J.O. Hirschfelder, C.F. Curtiss, R.B. Bird, 'Molecular theory of gases and liquids', John Wiley & Sons, New York (1954)
- [72] R.G.C. Beerkens, 'Deposits and condensation from flue gases in glass furnaces', Thesis Technical University Eindhoven (1986)
- [73] I. Barin, 'Thermochemical data of pure substances', VCH Verlagsgesellschaft, ISBN-3-527-27812-5 (1989)
- [74] O. Knacke, O. Kubaschewski, K. Hesselmann, 'Thermochemical properties of inorganic substances', Springer-Verlag / Verlag Stahleisen, Berlin, ISBN 3-540-54014-8 (1973)
- [75] G.H. Frischat, 'Ionic diffusion in oxide glasses', Diffusion and defect monograph series, Trans Tech. Publications (1975)
- [76] Y. Liang, 'Models and experiments for multicomponent chemical diffusion in molten silicates', thesis University of Chicago, Illinois, USA, December 1994, printed by UMI Dissertation Services
- [77] T. Pfeiffer, 'Viscosities and electrical conductivities of oxidic glass-forming melts', *Solid State Ionics*, **105**, 277-287, (1998)
- [78] H. Barklage-Hilgefort, 'Korrosionsversuche im System SiO<sub>2</sub>-Na<sub>2</sub>O', Thesis Technical University Clausthal, Germany (1978)
- [79] O.V. Mazurin, M.V. Streltsina, T.P. Shvaiko-Shvaikovskaya, 'Physical Sciences Data 15, Handbook of Glass Data – Part A: silica glass and binary silicate melts', Elsevier Science Publishers B.V., Amsterdam, ISBN 0-444-42215-3 (1983)
- [80] O.V. Mazurin, M.V. Streltsina, T.P. Shvaiko-Shvaikovskaya, 'Physical Sciences Data 15, Handbook of Glass Data – Part C: ternary silicate glasses', Elsevier Science Publishers B.V., Amsterdam, ISBN 0-444-42889-5 (1987)
- [81] M. Kizilyalli, J. Corish, R. Metselaar, 'Definitions of terms for diffusion in the solid state', *Pure Appl. Chem.*, **71** [7], 1307-1325, (1999)
- [82] H.A. Schaeffer, D.M. Sanders, 'Verdampfungsvorgänge an einem Na<sub>2</sub>O-CaO-SiO<sub>2</sub>-Glas, Dampfdruck- und Konzentrationsprofilmessungen', *Glustech. Ber.*, **49** [5] 95-102 (1976)
- [83] D.M. Sanders, H.A. Schaeffer, 'Reactive Vaporization of Soda-Lime-Silica Glass Melts', *J.Am.Ceram.Soc.*, **59** [3-4] 96 -101 (1976)



- [84] A. Kucuk, A.G. Clare, L.E. Jones, 'Differences between surface and bulk properties of glass melts I. Compositional differences and influence of volatilization on composition and other physical properties', *Journal of Non-Crystalline Solids*, **261**, 28-38, (2000)
- [85] T. Lakatos, L.G. Johansson, B. Simmingsköld, 'Viscosity-Temperature relations in the glass system  $\text{SiO}_2\text{-Al}_2\text{O}_3\text{-Na}_2\text{O-K}_2\text{O-CaO-MgO}$  in the composition range of technical glasses', *Glass Technol.*, **13** [3], 88-95 (1972)
- [86] Gasunie, 'Physical properties of natural gases' published by N.V. Nederlandse Gasunie, Groningen, The Netherlands (1988)

### 3. Experimental procedures for evaporation studies

The applied experimental methods, developed and applied in this study, are described in this chapter. In paragraph 3.1, two different transpiration evaporation set-ups, used to study the mass transport of evaporation processes from model liquids at temperatures below 1000 °C, are described and discussed. For experimental investigations of evaporation from glass melts, another high-temperature transpiration set-up has been developed. The specifications of this set-up are given in paragraph 3.2. In paragraph 3.3 the applied analytical techniques are described. The glasses have been analyzed before and after evaporation experiments on changes in chemical composition. Furthermore, the analytical techniques to analyze the collected evaporation products are described in this paragraph.. A fining test facility to study the effect of fining bubble evolution on evaporation is discussed in paragraph 3.4.

Three different transpiration set-ups are applied for the evaporation tests:

- A. Transpiration set-up used at room temperature for water and acetone evaporation tests. This set-up is used to investigate the mass transfer of volatile species from the surface of the liquid into the atmosphere under different experimental conditions.
- B. Transpiration set-up used for water evaporation tests at higher temperatures up to 100 °C. The results of the experiments in this set-up are used to validation the derived mass transfer relations of gaseous volatile species.
- C. High temperature transpiration set-up for glass melt evaporation tests between 1000 and 1550 °C.

**Nomenclature**

d	inner diameter of tube used in tube-furnace [m]
D	diffusion coefficient [ $\text{m}^2 \cdot \text{s}^{-1}$ ]
H	height of the boat [m]
h	mass transfer coefficient [ $\text{m} \cdot \text{s}^{-1}$ ]
L	length of a boat [m]
p	partial vapor pressure (Pa)
Re	Reynolds number ( $=\rho \cdot v \cdot d / \mu$ ) [-]
Sc	Schmidt number ( $=\mu / \{\rho \cdot D\}$ ) [-]
Sh	Sherwood number = $(h \cdot d / D)$ [-]
T	absolute temperature [K]
t	time [s]
v	gas velocity [ $\text{m} \cdot \text{s}^{-1}$ ]
W	width of boat [m]
x	distance in gas flow direction [m]
y	distance perpendicular to glass melt surface [m] (vertical direction)
z	distance perpendicular to main gas flow direction [m] (horizontal direction)

Subscripts, superscripts and Greek symbols

$\mu$	dynamic viscosity of fluid phase or molecular viscosity [Pa·s]
$\rho$	density [ $\text{kg} \cdot \text{m}^{-3}$ ]
*	saturated conditions gaseous atmosphere
i	evaporating species in the gas phase
n	normalized conditions (at temperature of 293.15 K and pressure of 101325 Pa)

### 3.1 Transpiration evaporation experiments for model liquids

Transpiration evaporation experiments are often applied to study the nature of volatile species or kinetics of evaporation processes of liquids or melts into flowing gas phases [1]. The mass transport of volatile species in a transpiration experiment depends among others on the flow conditions of the carrier gas in the tube and on the geometrical configuration.

For a transpiration test set-up, detailed CFD modeling (for details see chapter 2) showed to be an excellent tool to predict the mass transport of volatile species into a carrier gas and to understand the fluid dynamics in the gas phase and distribution of the released volatile species in this phase. Relatively simple mass transfer relations for the transport of species from the surface of the melt into a gas flow were obtained for a fixed geometry of the transpiration test set-up. These relations proved to be applicable for all investigated volatile species and different liquids at different temperature levels, as will be shown in chapter 4.

#### Transpiration set-up for investigations on evaporation kinetics

Transpiration experiments using model liquids with known properties, like water, were performed in order to validate the applicability of existing mass transfer relations (paragraph 2.3.2) and validity of the results of CFD calculations (paragraph 2.3.1) for transpiration experiments. Furthermore, these experiments were also used to obtain quantitative relations between evaporation rates on one hand and different process parameters on the other hand. Process parameters that govern the evaporation rates are the gas flow rate, gas flow profile, shape and geometrical aspects of the tube and vessel/boat, the filling level of the liquid in the boat, the composition of the liquid, temperature and gas phase composition.

Two different laboratory set-ups for transpiration evaporation trials have been developed and tested and have been used to investigate mass transfer kinetics during evaporation processes. In the first set-up ('low temperature set-up A'), only experiments at room temperature have been performed while in the second set-up B (tube furnace) the temperature can be controlled up to 100 °C.

The 'low temperature set-up A' for water and acetone evaporation experiments at room temperature, exists of a transparent, vitreous silica, inert tube with a length of 0.73 m and an inner diameter of 0.06 m. Figure 3.1 shows schematically the equipment.

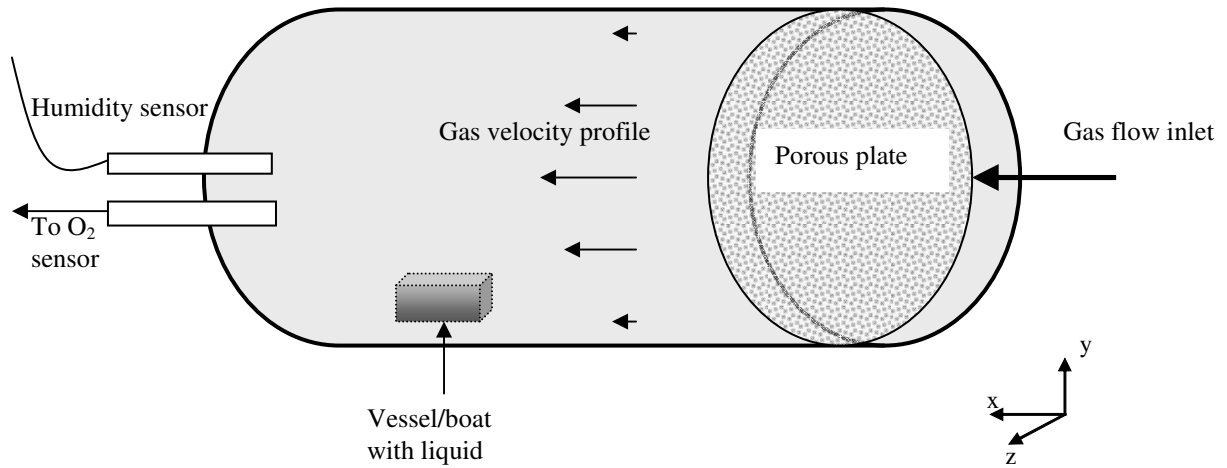


Figure 3.1: Schematic presentation of the laboratory test set-up for evaporation experiments at room temperature. The total length of the vitreous silica tube is 0.73 m and the inner diameter is 0.06 m. In the circular tube, different types/shapes of vessels/boats can be positioned. These boats are partly filled with a liquid. The porous plate is used to obtain an uniform laminar gas flow distribution. Sensors are used to monitor continuously the oxygen and water partial vapor pressures in the gases leaving the tube.

The tube is purged with a controlled gas volume flow of almost dry nitrogen ( $\text{H}_2\text{O} < 5$  ppm) and the gas stream flows along a rectangular boat, partly filled with water. At the outlet, a long tube (about 2 m) is connected to ensure that the nitrogen and water vapor are well mixed. In the outlet of the latter tube a combined humidity/temperature sensor is placed to measure the water vapor pressure and the gas temperature. The sensor, type: Vaisala HMP45A, is calibrated by the manufacturer. All results of this calibration are traceable in terms of dew point to NPL standards (National Physical Laboratory, United Kingdom) and NIST standards (National Institute of Standards and Technology, USA) and in terms of temperature to CMA standards (Finnish National Laboratory for Temperature). The maximum error in the measured water vapor pressure ( $\Delta p_{\text{H}_2\text{O}}$ ) at atmospheric conditions is about 20 Pa. To check on possible air leakages, the  $\text{O}_2$  concentration in the exit gases is measured. Just downstream the gas inlet, a porous plate is placed to obtain a fully developed laminar gas flow profile in the tube.

Different experiments were performed to derive systematically the effect of the geometrical configuration, shape of the boat, filling level of the boat and position of the

boat on the transport of water vapor into the atmosphere. The ‘low-temperature set-up A’ was used to determine the impact of: a) the position of the boat in the tube, b) gas flow rate, c) filling level of the boat and d) dimensions of the boat, on the evaporation rate of water.

During the experiments with water in this ‘low temperature set-up’, the nitrogen gas volume flow is controlled at values between  $8.3 \cdot 10^{-6}$  and  $1.75 \cdot 10^{-4}$  m<sub>n</sub><sup>3</sup>/s. This means that the Reynolds number for tube flow ( $Re = \rho \cdot v \cdot d / \mu$ ) for the tube without obstructions is in the range between 15 and 305. The narrow temperature range is 18 - 20 °C. In all cases the Reynolds number in the undisturbed gas flow is much lower than 2300, which is the critical Reynolds number. Below the critical Re laminar flow conditions are expected for undisturbed flows

Set-up B is a tube furnace with a total length of 1.24 m (hot zone is 1.00 m) and an inner diameter of 10.4 cm. The tube is made of a FeCrAl-alloy. Dry nitrogen is used as carrier gas flushes in the tube and the gas flows along a boat, partly filled with water. The gas outlet of the tube is covered with a flange with two small holes. In this second set-up, water evaporation experiments were carried out at room temperature and at a temperature of about 46 °C. The results of the experiments in this set-up are used to validate the derived mass transfer relations of gaseous volatile species.

To describe quantitatively the mass transport of water vapor or acetone from the liquid phase in the boat into the atmosphere, the following data on material properties are required:

1. The partial water vapor equilibrium pressure of water ( $p_{H_2O}^*$ ) and acetone ( $p_{acetone}^*$ ). These data are obtained from data in thermodynamic tables given in literature [2][3]. At 20 °C, the water vapor equilibrium pressure is 2336 Pa and the acetone vapor equilibrium pressure is 32400 Pa.
2. The diffusion coefficient,  $D_{H_2O}$  of water vapor in nitrogen as a function of temperature at atmospheric pressure. Some values of  $D_{H_2O}$  are reported for air as well as nitrogen [4]. The diffusion coefficients can also be estimated from a molecular dynamic approach. Relations for diffusion in binary gas mixtures at low level (nearly vacuum) to moderate (atmospheric) pressure levels have been described by Chapman and Enskog and are presented by Bird, Stewart and Lightfoot [5] and Reid, Prausnitz and Poling [4]. Fuller et al. [6][7][8] described a modified Chapman-Enskog relation for estimating diffusion coefficients in

binary gas systems with empirical constants based on experimental data. The authors reported an average error of about 4 % when using their equation. Based on Fuller's modified Chapman-Enskog relation the diffusion coefficient of water vapor in nitrogen at 20°C and 1 bar is estimated on  $2.54 \cdot 10^{-5} \text{ m}^2/\text{s}$ . Fuller's approach was applied to estimate the diffusion coefficient of acetone into nitrogen. At 20 °C the diffusion coefficient of acetone in nitrogen ( $D_{\text{acetone}}$ ) is about  $1.1 \cdot 10^{-5} \text{ m}^2/\text{s}$ .

3. For the calculation of the Sherwood number, the Reynolds number ( $Re = \rho \cdot v \cdot d / \mu$ ) of the undisturbed gas flow in the tube and the Schmidt number ( $Sc$ ) should be determined (see paragraph 2.3.2).

### 3.2 Transpiration set-up for glass melt evaporation tests

Several investigators such as: Conradt and Scholze [9], Cable and Fernandes [10], Schaeffer and Sanders [11][12] applied laboratory transpiration tests to simulate and study the kinetics of the evaporation processes of volatile species from glass melts. Such a transpiration set-up often exists of a horizontally positioned ceramic or noble metal tube. The tube is generally heated at the outside by electric heating elements. In the horizontal tube, a boat filled with a uniform melt is placed in a section with constant temperature. The melt is exposed to a controlled gas flow. The gas flow rate as well as the gas composition can be adjusted. The evaporation losses are determined, either by measuring the weight losses of the melt or by measuring the composition of the gas leaving the tube and gas volume flow.

The evaporation rates of the volatiles depend on the vapor pressures in equilibrium with the composition of the glass melt surface and the mass transfer coefficient in the gas phase. The vapor pressures are directly related to the chemical activities of the volatile compounds at the melt surface as described in chapter 1.

In case of non-congruent evaporation, which is the case for many volatile glass melt processes, the glass melt surface composition and evaporation rate also depends on the diffusion of volatile species in the melt and time

#### 3.2.1 Set-up for glass melts

The transpiration evaporation tests with glass melts have been carried out in a horizontal  $\text{Al}_2\text{O}_3$  tube furnace [13] (set-up C). Figure 3.2 shows the set-up schematically. The tube is heated by electrical heating elements. The maximum temperature is 1550 °C. In the horizontal tube, a vessel/boat partly filled with a melt is positioned in a section with uniform temperature. The melt is prepared from about 200 g chemically pure raw materials. These raw materials are mixed and melted in a laboratory furnace at 1400 °C during periods varying between 1 and 4 hours. The borosilicate batches are melted at 1550 °C during a period of 2 hours. Afterwards the glass is quenched, grained to sizes between 5 and 10 mm and mixed. The boat used for the transpiration experiments is filled with 25 gram of these glass grains. Prior to the evaporation tests, these cullet is re-melted in the boat during periods of 30 to 60 minutes at temperatures between 1400 °C and 1450 °C. This remelting takes place at conditions with very low evaporation losses.



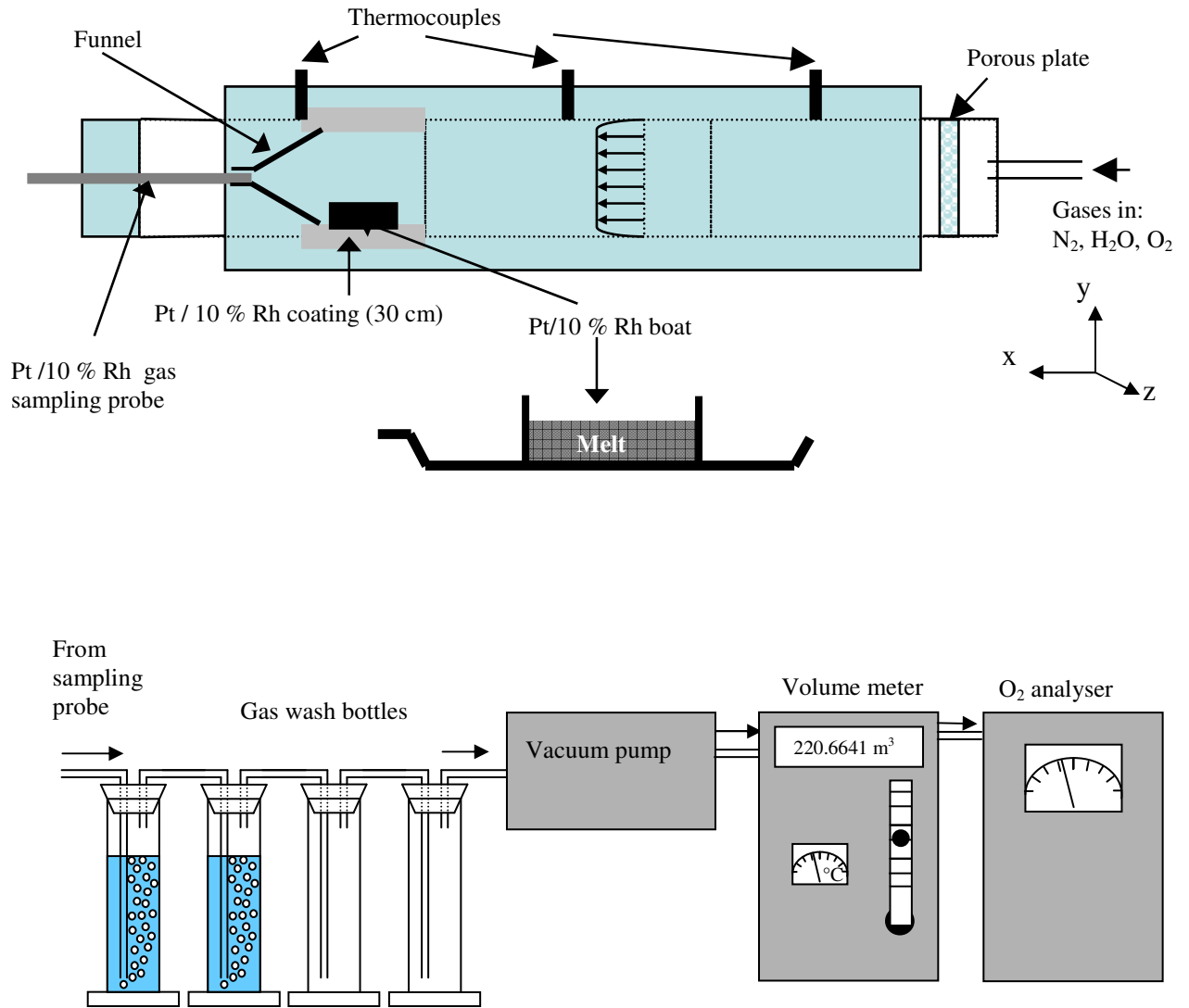


Figure 3.2: Scheme of the transpiration set-up for glass melt evaporation studies. The maximum achievable temperature is about 1550 °C.

During the transpiration experiment the melt is exposed to a controlled gas flow rate and controlled gas composition. Mass flow controllers control the gas flow rate and a humid atmosphere can be created by the injection of water in the preheated carrier gas. The injected amount of water vapor is controlled gravimetrically. After finishing the transpiration experiments the total weight loss of the glass in the boat has been determined in two ways:

1. gravimetrically by measuring the weight losses of the melt and

2. by multiplying the measured concentrations of all relevant volatile species in the gas phase (in  $\text{mg}/\text{m}_n^3$ ) with the controlled gas volume flow rate (in  $\text{m}_n^3/\text{s}$ ) and the duration of the experiment (in s).

The latter procedure is explained in more detail at the end of this paragraph. The evaporation rate of a species depends on the partial vapor pressures ( $p_i^*$  just above the melt and  $p_i$  in the carrier gas) of these species in the gas phase and the mass transfer coefficient ( $h_{g,i}$ ) in the gas phase. In case of non-congruent evaporation, as it is mostly the case, the evaporation rate depends on time and the inter-diffusion of the volatile species in the melt. Saturation vapor pressures are directly related to the chemical activities of the evaporating glass compounds at the melt surface.

The total length of the tube is 3 meter and the inner diameter is 0.10 m. Between 2.00 and 2.30 meter downstream of the gas inlet, the inner part of the tube has been coated with a platinum/rhodium layer (90/10 mass-%) to avoid any chemical reactions between the evaporated glass components and the ceramic tube downstream the boat. A platinum-rhodium boat ( $L \times W \times H = 0.050 \times 0.030 \times 0.015$  m) partly filled with a glass melt is placed in this coated part of the tube. Platinum-rhodium is almost inert under these conditions. During the experiments the gas flows were controlled at flow rates between  $9.0 \cdot 10^{-4}$  and  $1.8 \cdot 10^{-3} \text{ m}^3/\text{s}$ . This means that the average Reynolds number ( $Re = \rho \cdot v \cdot d / \mu$ ) for the gas flow in the tube, without obstructions, is between 42 and 77. In all cases  $Re \ll 2300$ , which is the transition Reynolds number from laminar to turbulent flow. Below this critical Reynolds number laminar flow conditions are expected after the flow is well-developed downstream the inlet. The temperature is controlled at values between 1300 and 1500 °C.

### 3.2.2 Procedure for evaporation experiments

All evaporation experiments are performed similarly: the platinum-rhodium boat filled with 25 gram of homogeneous multi-component silicate glass is placed in the furnace at room temperature. The furnace is heated with a temperature gradient of 2 °C/minute and meanwhile the furnace is flushed with a dry gas mixture of nitrogen and oxygen. In the oxidized, dry atmosphere the evaporation rates of most volatile glass compounds are low. At higher heating rates the  $\text{Al}_2\text{O}_3$  tube might crack due to stresses in the material. After reaching the temperature set point, water vapor, nitrogen and oxygen are mixed and this mixture is introduced as carrier gas. At that moment the

extractive sampling of vapors starts. A platinum-rhodium conically shaped tube (funnel) has been used to obtain a homogeneous gas mixture at the gas sampling point where a part of the carrier gas with evaporation products is extracted (see Figure 3.2). Because of the presence of this funnel it is impossible to place the boat with the melt directly in a preheated furnace.

After the sampling, the dosing of the water vapor stops and the furnace is cooled down (again 2 °C/minute). During a period of about 6 to 8 hours, 4 till 6 extractive gas samples were taken for each experiment. The duration of each sampling period varied between 5 and 60 minutes. The gas volume of each sample was measured with a calibrated gas volume meter. After each single gas extraction period, the platinum/rhodium extraction tube was removed from the set-up and was rinsed carefully with a 5 vol.-% HNO<sub>3</sub> solution. Both, the rinse liquid and the liquid in the gas wash bottles are collected, combined and mixed. The concentrations of different elements in the this liquid were analyzed chemically by Inductively Coupled Plasma Emission Spectroscopy (ICP-ES). From the measured concentrations of the volatile species in the liquid solution, the volume of the solution and the measured gas volume, the average concentration of the volatile species in the atmosphere can be calculated.

### 3.3 Chemical analysis of glass and concentration profile analysis in glass

After evaporation experiments, the glass melts were cooled down at 2 °C/minute to avoid cracking of the ceramic tube. The average compositions of the grained and well-mixed glass samples after the evaporation tests, have been analyzed by XRF (X-Ray Fluorescence), NAA (Neutron Absorption Analysis) or ICP-ES (Inductively Coupled Plasma Emission Spectrometry).

Scanning Electron Microscopy (SEM) in combination with a chemical micro-analysis technique was applied to measure concentrations profiles in alkali-lime-silicate glass samples. To measure B<sub>2</sub>O<sub>3</sub> concentrations gradients in the glass samples, Electron Micro Probe Analysis were applied. XPS (=X-ray Photoelectron Spectroscopy) technique [14] was applied to analyze the chemistry of the surface of a sample.

#### 3.3.1 XRF and NAA analysis

For a XRF analysis, the powdered samples are irradiated by an X-ray beam, which results in ejection of inner shell electrons from the sample atoms. Outer shell electrons take their place and the difference in energy level results in the emission of X-rays (secondary radiation) during transition of electrons from higher to lower energy levels. The wavelength of these X-rays is characteristic for the elements present in the sample. The intensity of the emission at a specific wavelength is related to the concentration of the elements [15]. XRF can be applied to determine the concentrations of elements with atom number between 9 (F) and 92 (U). The XRF technique is less suitable for accurate chemical analysis of boron. Therefore the Neutron Absorption Analysis were applied to measure boron concentration in glass samples accurately. With this technique the glass sample is bombarded by neutrons. The boron in the glass absorbs these neutrons and the intensity of the neutron flux is reduced. The change of intensity is measured and is a direct measure for the boron concentration in the glass sample [16].

#### 3.3.2 SEM and XPS analysis

SEM-EDX can be applied to measure the local concentrations of the most chemical elements in glass like Si, Ca, Na, K, Al and Mg. For local boron concentration measurements the application of SEM-WDX is required [17]. The principle of both analytical techniques is the same. The samples are bombarded with a beam of accelerated electrons. The electron beam is focused on the surface of a specimen using a

series of electromagnetic lenses. The incident beam excites an electron in an inner shell of an atom, prompting its ejection and resulting in the formation of an electron hole within the atom's electronic structure. An electron from an outer, higher-energy shell then fills the hole, and the excess energy of that electron is released in the form of an X-ray. The release of X-rays creates spectral lines that are highly specific to individual elements.

X-rays have characteristics of both particles and waves and can be described, and therefore measured, in terms of their energies or wavelengths. An electron microprobe is equipped with an energy-dispersive (ED) spectrometer, which electronically sorts and measures X-rays with respect to their energies. Electron microprobes may be equipped with several wavelength-dispersive (WD) spectrometers, which use diffraction to obtain a wavelength spectrum of the X-rays and to focus on X-rays within a very narrow wavelength-band.

When white light passes through a prism or diffraction grating, it divides into its constituent colors, each of which has its own wavelength. The same phenomenon occurs in WD spectrometers; the X-rays are dispersed with respect to their wavelengths by a crystal. In a particular arrangement of the sample, the crystal, and the detector, the atomic lattice of the crystal reflects just one wavelength of the incoming X-rays toward the detector. Consequently, a WD spectrometer is "tuned" to a single wavelength at a time, which means it can better resolve X-rays and obtain more accurate measurements.

In our investigations the Philips XL30 SEM-EDX was used to measure the local concentrations of Si, Ca, Na, K, Al<sub>3</sub> and Mg on micrometer level and to measure the vertical concentration profiles of these elements in the glass sample. Electron Micro Probe Analysis has been applied to measure boron concentration profiles in the glass samples. For this analysis, a Philips SEM XL40 with WDX600 has been applied. For calibration of both systems standard glasses with known glass compositions are used.

Some important remarks about SEM are:

- A source of electrons is used to excite the molecules in the area of the glass surface and photons (light) are emitted when electrons falling back to the ground energy level. The electron beam is focused on a small spot and light elements like sodium might preferably evaporate during the SEM measurement. This might result in too low concentration measured for this element after a certain time.

- Concentrations below about 0.5 mass-% cannot be measured accurately.
- The local evaporation rates during the transpiration tests are different. In that case a 3-dimensional concentration profile of the different glass species can be expected in the glass (melt). It is rather complicated to measure such profiles with SEM-EDX or SEM-WDX.
- During the rather slow cooling down process of the glass melt after the transpiration experiment, the diffusion processes in the melt may continue, but without further evaporation. During the cooling process the concentration profiles may be flattened a little bit. Profiles, measured by SEM-EDX scanning, can deviate from the concentration profile existing directly after the experiment at high temperature. As an example, CFD modeling has been applied to estimate the vertical Na<sub>2</sub>O concentration profiles in a soda-lime-silicate melt after an evaporation tests at 1500 °C. The CFD calculations take convective as well as the diffusive transport of Na<sub>2</sub>O into account. The results are shown in Figure 3.3. At  $t = 0$ , it is assumed that the sodium evaporation stopped and the melt in the furnace has been cooled down with a cooling rate of 120 °C/hour. The concentration profiles in vertical direction were calculated at the centerline for the melt at  $x = 5$  mm,  $x = 25$  mm and  $x = 45$  mm. After a period of 6 hours cooling the Na<sub>2</sub>O concentration near the surface increased in average about 0.4 mass-% according to the calculations. After 6 hours cooling, the gradient  $(\partial C_{\text{Na}_2\text{O}}/\partial y)_{y=0}$  becomes almost 0 at the surface of melt.

To analyze the chemistry of the surface of a material, the XPS (=X-ray Photoelectron Spectroscopy) technique [14] is applied. XPS is a quantitative spectroscopic technique that identifies the chemical compound. XPS spectra are obtained by irradiating a material with a beam of X-rays while simultaneously measuring the kinetic energy of electrons and number of electrons that escape from the top. About a thickness of 1 to 10 nm of the material is irradiated. XPS requires ultra-high vacuum conditions.

XPS detects all elements with an atomic number between 3 and 103. Detection limits for most of the elements are in the parts-per-thousand range.

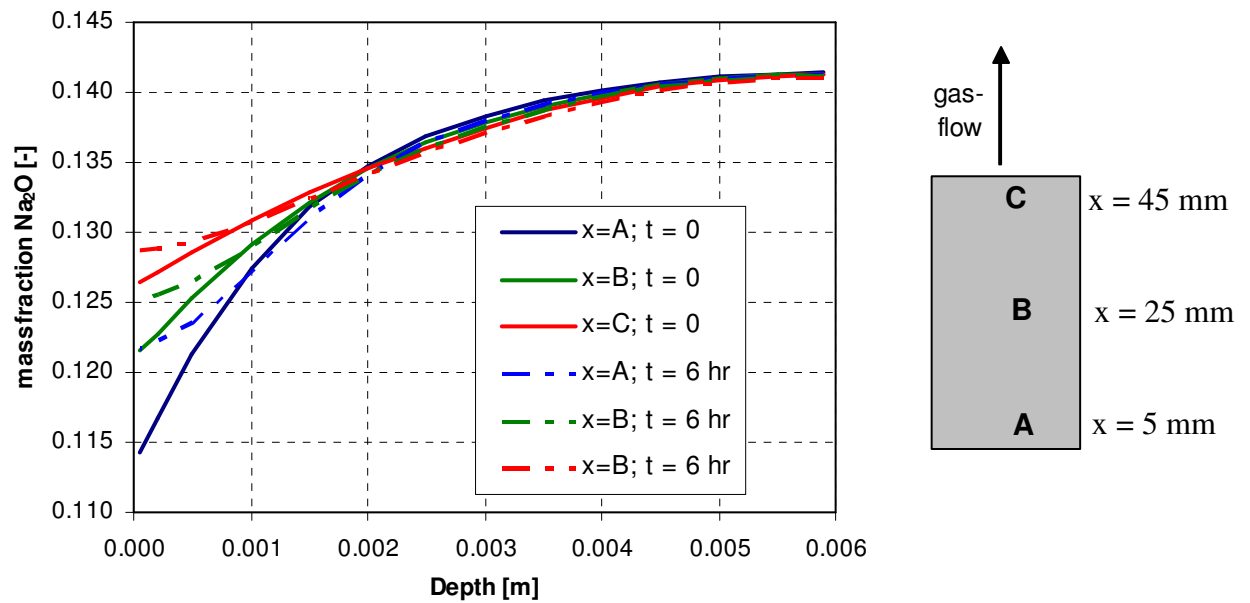


Figure 3.3: Vertical  $\text{Na}_2\text{O}$  concentration profiles in a soda-lime-silicate melt after an evaporation tests at  $1500\text{ }^\circ\text{C}$  according to CFD modeling (see paragraph 2.2). At  $t = 0$ , the sodium evaporation stopped and the melt in the furnace was cooled down during 6 hours with a cooling rate of  $120\text{ }^\circ\text{C}/\text{hour}$  to  $780\text{ }^\circ\text{C}$ . The profiles were calculated for the centerline of the melt at the positions A, B and C. The positions A and C are located 5 mm from the side wall and position B is located in the center. For these calculations  $D_{\text{Na}_2\text{O}} = 8 \cdot 10^{-10} \cdot \exp(-5655/T)$  (see paragraph 2.6.3).

### 3.4 Fining tests facility

The release of volatile glass components can be affected by ascending fining bubbles, which often contain gases such as  $\text{SO}_2$ , oxygen and/or chloride species/vapors. These fining bubbles may not only contain glass melt vapors or evaporation products, but will also cause convective mixing of the melt. Convection will result in less depletion of volatile components at the surface layer and consequently this causes higher evaporation rates. To control whether fining bubbles can be expected during the transpiration evaporation tests, the fining process of some glass samples have been visualized by using this fining test facility.

The fining test facility has been used to visualize the melting and fining processes in a glass melt by applying a video recording system<sup>1</sup> [18]. The set-up is schematically shown in Figure 3.4. For these tests, transparent vitreous silica crucibles were placed in a chamber / box furnace equipped with heating elements.

<sup>1</sup> Camera equipped with optical filters

The furnace front panel includes a thin vertical slit for an optical access to the crucible enabling video recordings of the transparent crucible filled with batch or melt. The atmosphere in above the melt in the crucible is flushed with a controlled gas flow. The composition of the released gases can be measured by applying an oxygen analyzer in combination with a Fourier Transform Infra-Red analyzer (FTIR). FTIR was applied to measure for instance the  $\text{H}_2\text{O}$ ,  $\text{HCl}$  and  $\text{SO}_2$  concentrations.

To collect the other released species, such as metal vapors or salt vapors, extractive gas sampling via gas wash bottles was used. After a certain period the sampling train is rinsed and all solutions are combined. Chemical analysis of the combined solution gives information on the total evaporation of different chemical elements from the glass melt.

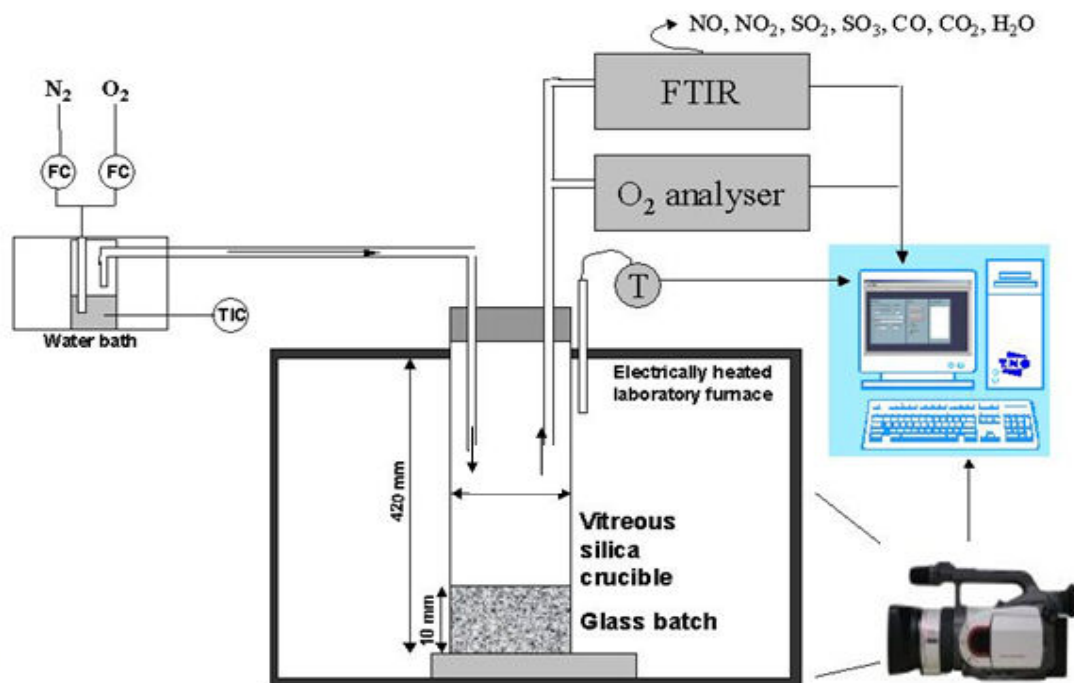


Figure 3.4: Laboratory set-up (fining test) used to visualize and observe the melting and fining process of glass melts. A video recording system is used to visualize the glass melting process in transparent vitreous silica crucibles continuously. Furthermore the gas composition can be measured with an oxygen analyzer ( $\text{O}_2$ ) in combination with a Fourier Transform Infra-Red analyzer (FTIR) to analyze components like  $\text{HCl}$ ,  $\text{SO}_2$ ,  $\text{H}_2\text{O}$ ,  $\text{CO}_2$  and  $\text{CO}$ .



**References**

- [1] H. van Limpt, R. Beerkens, A. Lankhorst, A. Habraken, 'Mass transfer relations for transpiration evaporation experiments', *Int. J. of Heat and Mass Transfer*, **48**, 4265-4281 (2005)
- [2] O. Knacke, O. Kubaschewski, K. Hesselman, 'Thermochemical properties of inorganic substances', Springer-Verlag / Verlag Stahleisen, ISBN 3-540-54014-8, 810-811 (1973)
- [3] I. Barin, 'Thermochemical data of pure substances', VCH Verlagsgesellschaft, ISBN-3-527-27812-5, 265-266, 649-650 (1989)
- [4] R.C. Reid, J.M. Prausnitz, B.E. Poling, 'The properties of gases and liquids' in McGraw-Hill Book Company, fourth edition, ISBN 0-07-051799-1(1987)
- [5] R.B. Bird, W.E. Stewart, E.N. Lightfoot, 'Transport Phenomena', second ed., John Wiley & Sons, 77-78, 420, 525-528 (2002)
- [6] E.N. Fuller, J.C. Giddings, 'A comparison of methods for predicting gaseous diffusion coefficients', *Journal of Gas Chromatography* **3**, 222 (1965)
- [7] E.N. Fuller, K. Ensley, J.C. Giddings, 'Diffusion of halogenated hydrocarbons in helium. The effect of structure on collision cross sections', *Journal of Physical Chemistry* **73** 3679-3685 (1969)
- [8] E.N. Fuller, P.D. Schettler, J.C. Giddings, 'A new method for prediction of binary gas-phase diffusion coefficients', *Industrial and Engineering Chemistry*, **58**, 18-27 (1966)
- [9] R. Conradt, H. Scholze, 'Zur Verdampfung aus Glasschmelzen', *Glastechnische Berichte*, **59** [2], 34-52 (1986)
- [10] M. Cable, M.H.V. Fernandes, 'Volatilisation of molten sodium metaborate with convection of the furnace atmosphere', *Physics and Chemistry of Glasses*, **39** [4], 228-35 (1998)
- [11] D.M. Sanders, H.A. Schaeffer, 'Reactive Vaporization of Soda-Lime-Silica Glass Melts', *J.Am.Cer.Soc.*, **59** [3-4], 96 -101 (1976)
- [12] H.A. Schaeffer, D.M. Sanders, 'Verdampfungsvorgänge an einem Na<sub>2</sub>O-CaO-SiO<sub>2</sub>-Glas, Dampfdruck- und Konzentrationsprofilmessungen', *Glastechnische Berichte*, **49** [5], 95-102 (1976)
- [13] H. van Limpt, R. Beerkens, O. Verheijen, 'Models and experiments for sodium evaporation from sodium containing silicate melts', *J.Am.Ceram.Soc.*, **89** [11], 3446-3455 (2006)

- [14] J.F.Moulder, W.F. Stickle, P.E. Sobol, and K.D. Bomben, 'Handbook of X-ray Photoelectron Spectroscopy', published by Perkin-Elmer Corp., Eden Prairie, Minn, USA (1992)
- [15] X-Ray Fluorescence Spectrometry, Vol. 152, editor: Ron Jenkins, published by Wiley, John & Sons, Incorporated, ISBN: 0471299421 (1999)
- [16] Personal communication with Mr. J.H.G. Smolders, Analytical chemist, Materials Analysis, Miplaza Philips Research Europe, High Tech Campus 11, Eindhoven, The Netherlands (2007)
- [17] S.J.B. Reed, 'Electron Microprobe Analysis', Publisher: Cambridge University Press; 2<sup>nd</sup> edition ISBN: 0521419565, (1993)
- [18] M. Rongen, A.J. Faber, R. Beerkens, R. Breeuwer, 'Physical fining techniques of glass melts', ESG-Conference, Sunderland, UK, September 10th - 14th (2006)



## 4. Experimental and modeling results for laboratory glass melt evaporation tests

A general applicable simulation model to calculate evaporation rates from glass melts, based on validated mass transfer relations for the applied experimental transpiration set-up, has been developed to predict the evaporation rates of volatile species from different types of glass melts (see chapter 2). Within this model, the thermodynamic properties of volatile compounds in multi-component glass melts are derived by an Associated Species Model. In this chapter, the results of evaporation tests are discussed and the evaporation processes in these experiments are modeled. The objectives of these tests and simulations are:

- 1) Validation of mass transfer relations for the transport of species in the gas phase, during transpiration evaporation tests.
- 2) Identification of the most important evaporating species from model glass melts and (industrial) multi-components glass melts, exposed to different furnace atmospheres.
- 3) Derivation of chemical activities of volatile species at the surface of a glass melt. Transpiration tests have been applied to determine the saturation vapor pressures of evaporating components just above the melt. The saturation vapor pressure can be determined from the measured evaporation rates and known mass transfer relations. The chemical activity of a volatile glass species in the glass melt surface layer is derived from the saturation vapor pressure and known reaction equilibrium constant.
- 4) Semi-quantitative description of the transport of volatile components in the melt and description of depletion phenomena.
- 5) Description of the influence of minor components in the melt on the evaporation of sodium and potassium from alkali-lime-silicate melts.

In paragraph 4.1, the experimental results of transpiration evaporation tests with water and acetone as evaporating liquids are used to validate the derived mass transfer relations for the transpiration set-up described in paragraph 2.3. In paragraph 4.4, the chemical activities of  $\text{Na}_2\text{O}$ ,  $\text{K}_2\text{O}$  and  $\text{B}_2\text{O}_3$  measured by evaporation experiments, are compared with the results of thermodynamic modeling. In the intermediate paragraph 4.2, the preparation of the glass samples that are used for transpiration experiments, is discussed. In paragraph 4.3, the different evaporation reactions are identified and experimental evidence for these reactions is shown.

In melts with hardly any convection, the evaporation rates might be limited by the diffusive transport of volatile species from the bulk to the surface of the melt. Transport of volatile species in the melt is discussed in paragraph 4.5. In paragraph 4.6 the measuring errors in the experimentally derived chemical activities are estimated.

The paragraphs 4.1 till 4.6 focus on glass melts with 2 to 4 components (model glass compositions), while in the last two paragraphs (4.7 and 4.8) the evaporation rates from more complex industrial glass melt compositions are presented and discussed. In paragraph 4.9 the main conclusions of this chapter are given.

Three different transpiration set-ups have been used in this study, which are described in chapter 3. For all of these set-ups equation 2.19 can be applied to calculate the average Sherwood number. The values of the constants  $C_1$ ,  $C_2$  and  $C_3$  in this equations are different for these set-ups and are given in Table 4.1.

For all transpiration evaporation experiments in this study, with different liquids and glass melts, the vapor pressures of the volatile gaseous species in the carrier gas are much lower than the saturation vapor pressures of these species just above the surface of the melt (in an unsaturated carrier gas:  $p_i^{\text{bulk}} \ll p_i^*$ ). Other authors like Schaeffer and Sanders [1][2] used very low gas flows in their transpiration experiments in order to obtain an atmosphere which is fully saturated with evaporated species. In their evaporation experiments the gas flow rate is about 25 to 30 times lower as in our transpiration tests.

The chemical compositions of the applied glass types are given in Table 4.2 and Table 4.3.

Table 4.1: Short description of the applied transpiration set-ups in this study and described in chapter 3. The table also shows the values of the constants  $C_1$ ,  $C_2$  and  $C_3$  which are required to calculate the average Sherwood number (equation 2.19) in the different set-ups.

Transpiration set-up	Short description	Constants in equation 2.19		
		$C_1$ (-)	$C_2$ (-)	$C_3$ (-)
<b>A</b>	Set-up used at room temperature for water and acetone evaporation tests.	43.0	0.454	$5.1 \cdot 10^{-3}$
<b>B</b>	Set-up used for water evaporation tests up to 100 °C.	196.6	0	0.40
<b>C</b>	Set-up used for glass melt evaporation tests.	255.9	0	0.40

Table 4.2: Measured average chemical composition (XRF) of different float glass and tableware glass compositions with and without  $SO_3$ . The compositions have been measured for glass samples obtained from transpiration evaporation tests. Between brackets the theoretical concentrations for some components are given, calculated from the raw material batch composition. During the preparation of the glass samples and the heating of the glass in the tube furnace, species like Na, K, S, Sb and Cl partly evaporate.

Component	<u>Float glass</u> without $SO_3$ (mass-%)	<u>Float glass</u> with $SO_3$ (mass-%)	<u>Tableware</u> <u>glass A</u> (mass-%)	<u>Tableware glass</u> <u>B</u> <sup>1)</sup> (mass-%)	<u>Tableware</u> <u>glass C</u> (mass-%)
SiO <sub>2</sub>	72.85	72.16	70.1	(67.2)	70.4
Na <sub>2</sub> O	13.98	14.18	10.5	(10.0)	10.4
CaO	7.46	7.88	8.00	(8.00)	8.25
MgO	4.52	4.32	< 0.01	(0)	< 0.01
Al <sub>2</sub> O <sub>3</sub>	0.86	0.85	1.09	(0.97)	1.06
K <sub>2</sub> O	0.22	0.20	4.98	(5.03)	4.67
Fe <sub>2</sub> O <sub>3</sub>	0.095	0.087	< 0.01	(0)	< 0.01
SO <sub>3</sub>	< 0.01	0.25	0.01	(0)	0.13 (0.40)
Cl	< 0.01	< 0.01	< 0.01	(0.42)	0.03 (0.44)
Sb <sub>2</sub> O <sub>3</sub>	< 0.01	< 0.01	0.22 (0.30)	(0)	0.06 (0.10)
BaO	< 0.01	< 0.01	5.07	(8.41)	4.98

1) Theoretical composition calculated from batch composition, not taken into account evaporation losses

Table 4.3: Initial glass compositions of the used borosilicate glass samples for the transpiration evaporation tests. The composition has been measured with XRF and NAA analysis.

	<b>Glass 1</b> (mass-%)	<b>Glass 2</b> (mass-%)	<b>Glass 3</b> (mass-%)
<b>B<sub>2</sub>O<sub>3</sub></b>	2.6	5.0	7.6
<b>Na<sub>2</sub>O</b>	0.10	0.10	0.15
<b>Al<sub>2</sub>O<sub>3</sub></b>	14.1	13.7	13.8
<b>SiO<sub>2</sub></b>	59.7	58.8	54.1
<b>CaO</b>	23.5	22.4	24.3

### Nomenclature

a	chemical activity in melt [-]
A	area [m <sup>2</sup> ]
C	concentration in melt or gas phase [mole·m <sup>-3</sup> ] or [mass-%]
C <sub>1</sub> , C <sub>2</sub> , C <sub>3</sub>	constants in equation 2.19 [-]
C <sub>5</sub>	constant in equation 4.2 [mole·s <sup>0.8</sup> ·kg <sup>-0.5</sup> ·m <sup>-2.3</sup> ]
d	inner diameter of transpiration experiment tube [m]
D	diffusion coefficient [m <sup>2</sup> ·s <sup>-1</sup> ]
H	height of the boat [m]
H <sub>rim</sub>	height of rim above liquid surface [cm]
h	mass transfer coefficient [m·s <sup>-1</sup> ]
L	length of a boat or characteristic length [m]
m <sub>H<sub>2</sub>O</sub>	mass of water [g]
p	partial vapor pressure [Pa]
Pe	Péclet number (=v·L/D) [-]
Q	molar flux density [mole·m <sup>-2</sup> ·s <sup>-1</sup> ]
Re	Average Reynolds number (=ρ·v·d/ μ) [-]
Sh	Average Sherwood number (=h·d/D) [-]
T	absolute temperature [K]
t	time [s]
v	velocity of gas or melt [m·s <sup>-1</sup> ]
V	volume [m <sup>3</sup> ]
W	width of boat [m]
x	distance in gas flow direction [m]
y	distance perpendicular to glass melt surface [m] (vertical direction)
z	distance perpendicular to gas flow direction in horizontal direction [m]

### Subscripts and superscripts

*	saturated gaseous atmosphere
bulk	parent glass or main gas stream
g	gas phase
h	hydraulic
i	component i in gas phase



i      inner part  
j      (evaporating) component in melt  
m      melt phase  
o      outer part  
surface surface of a liquid

Greek and other symbols

$\mu$       dynamic viscosity of fluid phase or molecular viscosity [Pa·s]  
 $\delta_N$       Nernst boundary layer thickness [m]  
 $\Delta$       difference between two different experimental values  
 $\phi$       actual gas flow at prevalent temperature and pressure [ $\text{m}^3 \cdot \text{s}^{-1}$ ]

#### 4.1 Validation of mass transfer relations for transpiration experiments

In paragraph 2.3, the mass transport of volatile species from a liquid surface into the atmosphere is discussed. For the transpiration experiments, CFD modeling results and empirical mass transfer relations have been used to describe the mass transfer rate of volatile species from the surface of a liquid / melt into the gas phase. In their paper, Van Limpt et al. [3] discuss in detail the relation between different geometrical aspects of boats in the tube and from literature available Sherwood relations.

In set-up A (see Table 4.1) evaporation experiments with model liquids were performed to derive empirical Sherwood relations, describing the mass transfer of volatile species into the atmosphere. The derived mass transfer relations are only applicable in case of laminar gas flow conditions in the tube (between the gas inlet and the position of the boat). First of all, the gas flow conditions were investigated experimentally.

##### Impact of filling level of the boat on the water evaporation rate

Water evaporation tests were performed in a rectangular boat of 0.047 x 0.022 x 0.018 m (L x W x H). The initial water level in the boat was varied for the different experiments. By decreasing the amount of water, the height of the rim above the liquid of the boat increases (see Figure 4.1):

$$H_{rim}(cm) = 1.8 - 0.1 \cdot m_{H_2O} \quad (4.1)$$

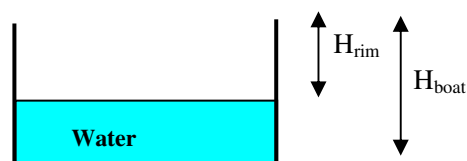


Figure 4.1: Rectangular boat used for water transpiration tests with different amounts of water in the boat. Because of different amounts of water, the height of the rim ( $H_{rim}$ ) differs. The picture shows the boat filled with 19 gram of water. The water surface layer exceeds the height of the sidewalls by about 0.1 cm (surface tension).

In this formula  $H_{\text{rim}}$  is the height of the rim above the water surface in cm and  $m_{\text{H}_2\text{O}}$  is the mass of the water in the boat in gram. It is assumed that the density of the water is  $1.0 \text{ kg/m}^3$ . The measured water evaporation rates increased when increasing the water level. For low amounts of water  $\leq 2.5$  gram ( $1.55 \leq H_{\text{rim}} < 1.8$  cm), the measured evaporation rates are about the same for the same gas flow rates. However, in case the boat is almost completely filled, an increase of the amount of water in the boat from 18 to 19 grams shows a significant impact on the evaporation rate. In case of 19 gram water in the boat, the water surface bellies out due to the high surface tension of water and the height of the water surface exceeds the height of the side walls by about 0.1 cm.

As can be seen in Figure 4.2, for all filling levels nearly linear relations were found between the reciprocal gas velocity and the measured water vapor pressures.

### Validation of empirical mass transport relations

The empirical Sherwood relation (eq. 2.19) for transpiration experiments has been discussed in paragraph 2.3.2. This equation involves the parameters  $Re$  and  $Sc$  to predict Sherwood numbers for different volatile species, gas compositions, temperature levels and gas flows.

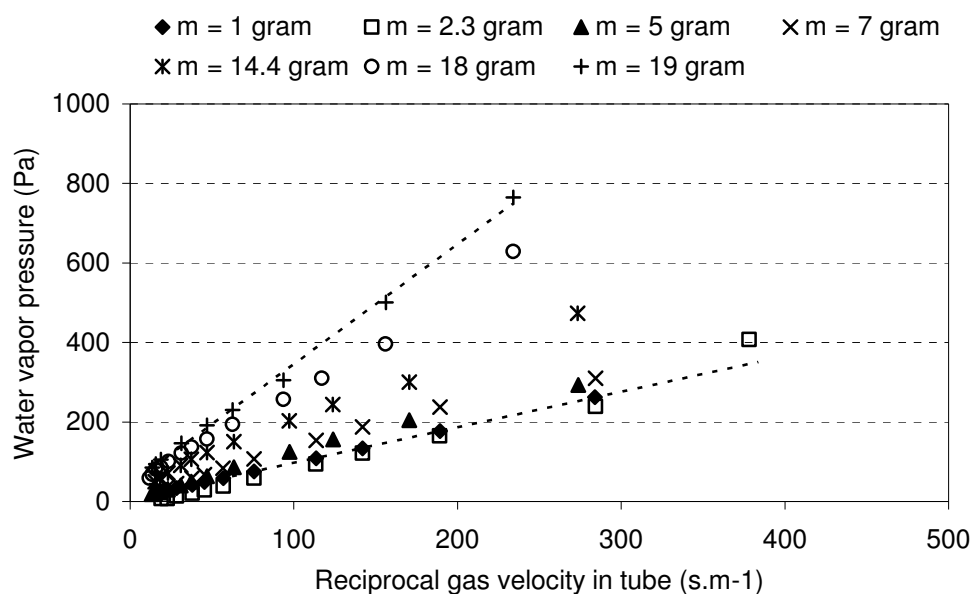


Figure 4.2: Measured water vapor pressure in carrier gas at the exit of the tube as a function of the reciprocal gas flow rate and the amount of water in the boat.

In first instance independent evaporation experiments with acetone under a nitrogen atmosphere were performed using transpiration set-up A (the ‘low-temperature set-up’) and secondly water evaporation experiments at higher temperatures (about 46 °C) were carried out in transpiration set-up B. Both set-ups are described in chapter 3. In the tube furnace the maximum Reynolds-number ( $=\rho \cdot v \cdot d / \mu$ ) in the undisturbed flow is about 1000 ensuring laminar flow conditions.

*Water and acetone transpiration experiments for boats partly filled with a liquid*

The experiments in set-up A were carried out with water and acetone at room temperature and the filling levels in the boat are always the same. For all experiments the same carrier gas has been used ( $N_2$ ). The nitrogen gas flow rate has been controlled at a value within the range  $1.0 \cdot 10^{-5}$  and  $2.0 \cdot 10^{-4} \text{ m}_n^3/\text{s}$  (n refers to standard conditions at 273.15 K and 101325 Pa) and the height of the rim above the liquid surface was 1.1 cm. Based on the water evaporation experiments, the values for the constants  $C_1$ ,  $C_2$  and  $C_3$  in equation 2.19 were obtained.

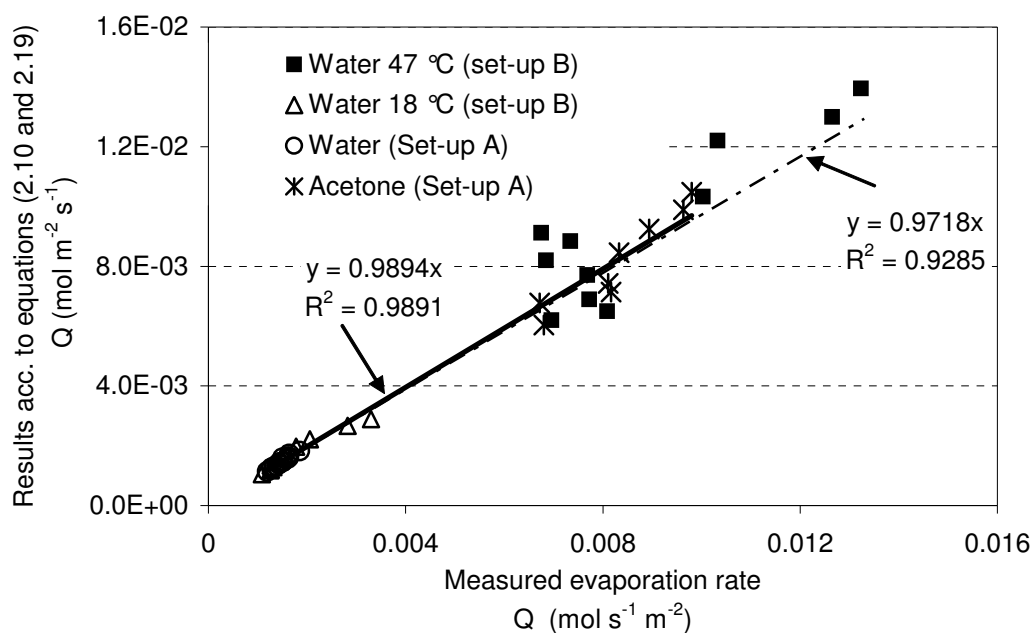


Figure 4.3: Predicted evaporation rates versus measured evaporation rates of water and acetone using equation (2.19) to predict the average Sherwood number. For the water and acetone evaporation tests performed in the set-up A (see chapter 3) the values for the constants are:  $C_1 = 43.0$ ,  $C_2 = 0.454$  and  $C_3 = 5.1 \cdot 10^{-3}$ . For the water evaporation tests in set-up B with another geometry (see chapter 3), the measurements at room temperature were used to obtain numerical values for the constants:  $C_1 = 196.6$ ,  $C_2 = 0$  and  $C_3 = 0.397$ . The tube furnace has been flushed with dry  $N_2$  and the Reynolds number of the undisturbed gas flow are in the range between 7 and 1026.

For the same geometrical configuration these values should be constant and should not depend on gas flow, temperature and type of liquid. The equations 2.10 and 2.12a have been used to predict the evaporation rates of acetone. Figure 4.3 shows the predicted evaporation rates, according to equation (3.5), versus the measured evaporation rates.

In these calculations the bulk concentration,  $C_i^{\text{bulk}}$ , is assumed to be the average concentration of component  $i$  in the outlet of the tube:  $C_i^{\text{bulk}} = Q_i \cdot A / \phi_{\text{avg}}$ . The concentration  $C_i^{\text{bulk}}$  is required to calculate the vapor pressure  $p_i^{\text{bulk}}$  in equation 2.10.

Here  $A$ , is the area of the surface of the liquid in the boat (in  $\text{m}^2$ ) and  $\phi_{\text{avg}}$  is the actual average gas flow rate in the tube (in  $\text{m}^3/\text{s}$ ). According to the least squares method the average deviation between the predicted and measured water vapor evaporation rates is 0.9 %. For transpiration experiments with acetone this error is 2.6 % using  $C_1=43.0$ ,  $C_2=0.454$ ,  $C_3=5.1 \cdot 10^{-3}$ .

In Figure 4.4 the experimental results from the transpiration tests with water, the results of the CFD modeling and the obtained results from equation (2.19) were plotted versus the Reynolds number in the tube (all for set-up A).

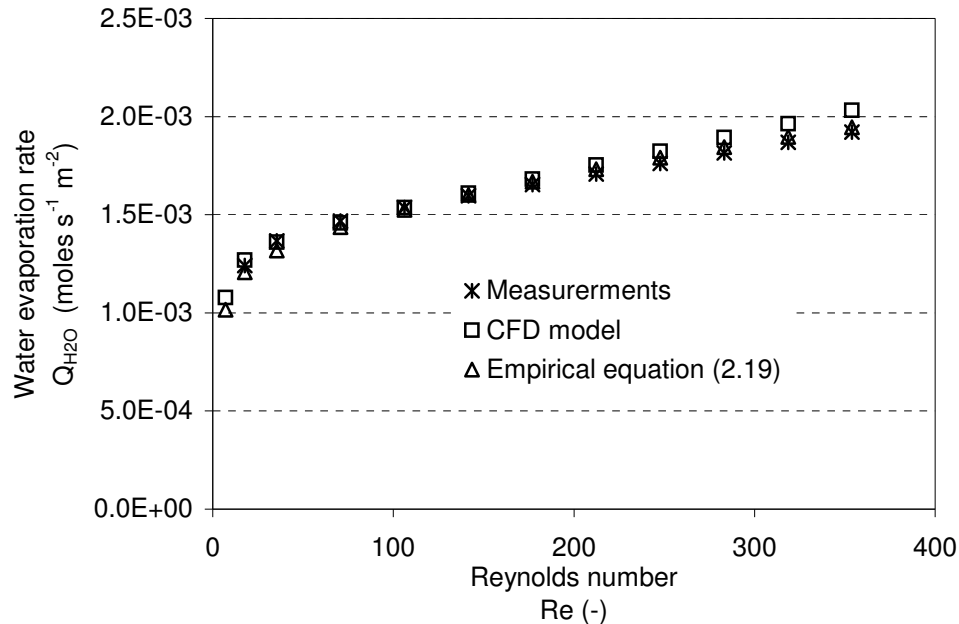


Figure 4.4: Measured and predicted water evaporation rates from a rectangular boat ( $L \times W \times H = 4.7 \times 2.2 \times 1.8$  cm) filled with 7 g water. The tests were done in the 'low-temperature set-up A' at room temperature. The values for the constants in equation 2.19 are:  $C_1 = 43.0$ ,  $C_2 = 0.454$  and  $C_3 = 5.1 \cdot 10^{-3}$ .

Accurate measurements were not possible for  $Re < 17$  and therefore in this range only the results of the CFD models are compared with the results from the application of the empirical relation 2.19. However, even in the range:  $7 < Re < 17$ , these results deviate less than about 6 %. In the range:  $17 < Re < 354$ , the average deviation between the 3 approaches is even less than 0.5 %.

Additional water transpiration experiments have been performed in transpiration set-up B (see Table 4.1) to test the applicability of equation 2.19 also for another experimental set-up and other process conditions. Again, the same rectangular  $Al_2O_3$  boats were used and filled with 7 gram of water. The tube was flushed with dry nitrogen and experiments were carried out at room temperature (about 18 till 19 °C) and at a temperature of about  $47 \pm 1$  °C. The Reynolds numbers ( $Re_d$ ) of the laminar undisturbed gas flow was controlled at a value in the range between 4 and 1026. The evaporation losses have been determined by measuring the weight losses of the boats after the transpiration experiment. The results are shown in Figure 4.3. The experimental results at room temperature and equation 2.19 were used to derive the values of  $C_1$ ,  $C_2$  and  $C_3$  for this set-up and to predict the water evaporation rates at 47 °C. The average deviation in the predicted water evaporation rates compared to the experimentally found evaporation rates at 47 °C is about 4.8 %.

This paragraph shows that the empirically derived Sherwood relation (eq. 2.19) for transpiration evaporation tests can be applied to predict the mass transfer of volatile species from the surface of a liquid into the atmosphere. Once the Sherwood relation for a transpiration set-up is known, the chemical activities of volatile glass components can be derived from the measured evaporation rates as will be shown in paragraph 4.4.

## 4.2 Sample preparation and homogeneity

The incongruent evaporation of volatile species like sodium and potassium species from glass melt surfaces depends among others on the transport of these compounds in the melt (see chapter 2). The composition of the surface of the melt depends on the evaporation rates, diffusion and convection in the melt, the presence of surface active compounds in the melt and/or phase segregation. The evaporation rates will also depend on the initial homogeneity of the glass sample in the boat which is directly a consequence of the sample preparation as described in paragraph 3.2. In this paragraph the homogeneity of the glass melt before the test and the sample preparation are discussed.

The homogeneity of the pre-melted glass in the boat, before the start of the transpiration (evaporation) test, will influence the local evaporation rates of volatile compounds and transport in the melt. The glass samples for the transpiration experiments are prepared from well-mixed pre-melted cullet pieces (in first stage molten from raw material mixtures) with sizes of 5 to 10 mm. Too small pieces of cullet might lead to air inclusions (blisters) in the glass and this might influence the evaporation process. Too large pieces can influence the homogeneity.

During the sample preparation in a nearly static and nearly dry atmosphere (air), no significant evaporation losses of the main glass components: Si, Ca, Al, Na and B are expected (see chapter 1).

During melting of the raw materials different melt phases will be formed as function of temperature and time. For soda-lime-silicate glass batches, Verheijen [4] showed that at temperatures around 900 °C, the first sodium-silicate melts are formed. At higher temperatures components like CaO and MgO dissolve in the silicate melt phases. Even around 1400 °C residual crystalline quartz and cristobalite particles might still be present at short melting times.

During the heating of the batches, the carbonates (e.g. soda-ash, limestone, and dolomite) dissociate around 600-900 °C and CO<sub>2</sub> bubbles are formed. During the melting of most flint soda-lime-silicate raw material batches with sodium sulfate, SO<sub>2</sub> is released as result of a reaction between SiO<sub>2</sub> and Na<sub>2</sub>SO<sub>4</sub> around 1100 °C and fining reactions due to decomposition of sulfates at higher temperatures. During the fining process SO<sub>2</sub> bubbles are formed, which may enhance the growth of the gas bubbles in the melt. The ascending gas

bubbles in the melt will promote the mixing of the different melt phases and thus the homogeneity of the melt.

In appendix I of this chapter the sample preparation of soda-lime-silicate batches with and without sulfate is discussed extensively.

Based on the results presented in appendix I it is concluded that the composition of glasses melted from raw materials without sulfate appeared to be less homogeneous than glasses prepared from raw materials with sulfates. During the melting processes of raw materials with sulfate, Marangoni flows (see paragraph 2.2.1) and fining bubbles improve the mixing and homogeneity of the melt.

It appeared that before the start of the evaporation tests, the surface of the fresh sulfate-free glass samples show a silica rich surface layer with relative low concentrations of CaO and Na<sub>2</sub>O. In order to prepare homogeneous glass sample compositions for the purpose of transpiration evaporation experiments, fine cullet could be applied or the melt should be mixed intensively in vertical direction. However, melts prepared from fine cullet contain more fine air blisters, especially before fining (removal of bubbles at high temperatures). In paragraph 4.5 the impact of deviations in surface concentration on the evaporation of volatile species will be discussed.

### **4.3 Identification of main evaporation reactions**

In chapter 1 different evaporation reactions for several species in the glass melt are shown. For sodium and boron in the glass the main evaporation reactions may change by modifying the composition of the gas phase or the composition of the glass melt. In the paragraphs 4.3.1 and 4.3.2, the evaporation reactions of sodium species for binary sodium-disilicate melts and for soda-lime silicate melts are discussed. In paragraph 4.3.3, the major boron evaporation reactions for alkali-lean borosilicate glass melts are shown.

All transpiration evaporation experiments with glass melts have been performed in transpiration set-up C (see Table 4.1).



### 4.3.1 Evaporation of sodium species from sodium-disilicate melts

The evaporation rates of all sodium species together (Na, NaOH, ...) from a sodium-disilicate melts [5] were measured at different conditions for:

- the temperature,
- the gas composition and
- the gas flow rate.

In industrial fossil fuel-fired glass furnaces the water vapor pressure in the furnace atmosphere varies roughly between 0.12 bar (air-fuel oil fired) and 0.60 bar (oxygen-gas fired). Sodium in the molten glass may evaporate at the surface by reaction with water vapor, forming NaOH or by reduction of Na<sub>2</sub>O at the glass melt surface, due to reactions with CO or with incompletely burnt hydrocarbons in the combustion space [6]. In this paragraph the impact of the atmospheric composition on the measured total rate of sodium evaporation is presented (e.g.  $Q_{\text{Na-total}} = Q_{\text{NaOH}} + Q_{\text{Na}} + Q_{\text{NaO}} + Q_{\text{Na}_2\text{O}}$ ). The NaO or Na<sub>2</sub>O evaporation rates and vapor pressures seem to be much lower than NaOH or Na vapor pressures in humid or reducing atmospheres. In this study, the composition of the atmosphere has been varied systematically in order to identify the different relevant evaporation reaction mechanisms of sodium.

The total sodium evaporation losses of a sodium-disilicate melt were measured by extractive sampling of the carrier gas (plus entrained evaporated species) through gas-wash bottles (see paragraph 3.2). The collected solutions were chemically analyzed by ICP-ES. From the total gas volume flow and the measured sodium concentration in the gases, the total sodium evaporation rates were calculated. The results of these measurements are compared to the gravimetrically determined weight-losses before and after the evaporation experiment and presented in this paragraph.

The results of the sodium evaporation tests (total sodium evaporation rates) and known mass transfer coefficients or Sherwood numbers were used to determine the chemical activities of Na<sub>2</sub>O in the surface layer of the melt. The results will be shown and discussed in paragraph 4.4.

***Impact of redox state of carrier gas***

According to the chemical reactions 1.10 and 1.12, given in chapter 1, sodium may evaporate from the melt surface as gaseous NaOH or gaseous Na. The saturation vapor pressure of NaOH is linear proportional to  $p_{\text{H}_2\text{O}}^{1/2}$  (equation 1.11) and the equilibrium vapor pressure of Na is linear proportional to  $p_{\text{O}_2}^{-1/4}$  (equation 1.13). The impact of the redox state of the carrier gas on the sodium evaporation rate was determined by a comparison of the results two different experiments:

1. Experiment with  $\text{N}_2/\text{H}_2\text{O}$  carrier gas and
2. Experiment with  $\text{Air}/\text{H}_2\text{O}$  carrier gas.

In experiment 1, the partial  $\text{O}_2$  pressure in the carrier gas was in all cases lower than 0.01 bar and in experiment 2 the partial  $\text{O}_2$  pressure has been set to about 0.16 bar. The water vapor pressure during both experiments is set to  $0.25 \pm 0.01$  bar and the temperatures have been varied between 1400 and 1460 °C. The gas volume flow rate (under normalized conditions, i.e.  $T = 293.15$  K and  $P = 101325$  Pa) in the tube is about  $1.6 \cdot 10^{-4} \text{ m}_n^3/\text{s}$ .

The total sodium evaporation rate (all gaseous sodium species together) has been determined by the method described in paragraph 3.2. The measured sodium evaporation rates for both experiments are nearly identical at 1450 – 1460 °C (about  $1.2 \cdot 10^{-4} \text{ mole}/\text{m}^2/\text{s}$ ). For the 1400 °C experiments, the differences are maximum about 10 % (about  $7 \cdot 10^{-5} \text{ mole}/\text{m}^2/\text{s}$ ). Based on thermodynamic modeling with ASM (see paragraph 2.5.1), it was found that for:

- a.  $1300 < T < 1450$  °C,
- b.  $p_{\text{H}_2\text{O}} = 0.27$  bar (atmosphere) and
- c.  $p_{\text{O}_2} \approx 0.01$  bar (atmosphere),

a maximum of 10 % of the total evaporated sodium species may evaporate as pure Na. Since NaOH seems to be the major volatile sodium species, an almost linear relation is expected between  $p_{\text{H}_2\text{O}}^{1/2}$  in the atmosphere and the NaOH saturation vapor pressure ( $p_{\text{NaOH}}^*$ ).

For a temperature of  $1416 \pm 5$  °C, and constant Sherwood number, the  $p_{\text{NaOH}}^*$  values have been obtained from both evaporation measurements using the transpiration evaporation set-up and by thermochemical modeling (see paragraph 2.5.1). To calculate  $p_{\text{NaOH}}^*$ , the measured total sodium evaporation rates in combination with the equations 2.10, 2.12 and 2.19 were used. The results are compared in Figure 4.5. For water vapor pressures  $> 0.10$  bar the measured and modeled saturation pressures ( $p_{\text{NaOH}}^*$ ) in Figure 4.5 deviate 1 to maximum 15

%. At dry gas conditions however, the measured evaporation rate of Na (g) in oxygen lean gas flows cannot be ignored. The evaporation rate of elemental sodium depends very much on the partial oxygen pressure just above the melt (see equation 1.13). Oxygen might also be released from a silicate melt by decomposition reactions. Assuming an equilibrium between the carrier gas (nitrogen) and the glass melt surface, the oxygen partial pressure can be estimated using thermodynamic models such as Factsage [7]. Between 1300 and 1450 °C the calculated oxygen partial equilibrium pressure (released from the melt) lies between 0.4 and 3 Pa.

From the reaction equilibrium constant, from the equilibrium oxygen pressure just above the surface of the melt and from the calculated chemical activity of Na<sub>2</sub>O in the melt (see paragraph 2.5.1), the saturation pressure of elemental sodium can be estimated as a function of temperature.

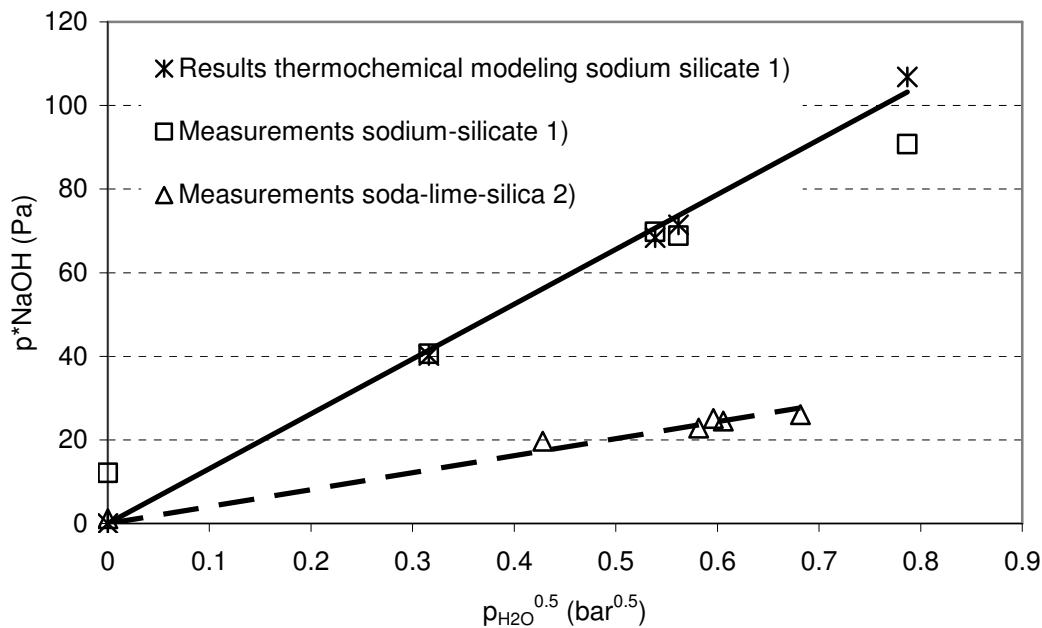


Figure 4.5: Saturation pressure of NaOH ( $p^*_{NaOH}$ ) for: 1) a sodium-disilicate glass melt at 1416 °C and 2) a soda-lime-silicate melt ( $SiO_2:Na_2O:CaO = 74:16:10$  mole-%) at 1463 °C as a function of the square root of the water vapor pressure in the furnace atmosphere. The figure contains measured data (assuming all sodium evaporates as NaOH) and calculations using the Associated Species Model (ASM) for  $a_{Na_2O}$  (only for sodium-disilicate) and using equation 2.10 for the evaporation rate.

From results of evaporation measurements at two different temperatures the saturation pressure of Na above a  $\text{Na}_2\text{O}\cdot 2\text{SiO}_2$  melt was also determined using pure nitrogen as carrier gas.

The results of the calculations based on the thermodynamic Associated Species Model (ASM) as well as the results derived from measurements are shown in Figure 4.6. The measured saturation pressures ( $p_{\text{Na}}^*$ ) are maximum 1 Pa (about 20 %) higher than the saturation pressures obtained from modeling. Figure 4.6 shows also the measured and modeled  $p_{\text{Na}}^*$  for a situation with  $p_{\text{O}_2} = 0.22$  bar and a temperature of 1462 °C. The calculated vapor pressures of species like NaO or  $\text{Na}_2\text{O}$  are at least a factor 100 lower.

Compared to a pure  $\text{N}_2$  atmosphere, the equilibrium partial pressure of oxygen is higher for evaporation experiments performed under an  $\text{N}_2/\text{H}_2\text{O}$  atmosphere.

For example, in an atmosphere with  $p_{\text{H}_2\text{O}} = 0.27$  bar and a temperature of 1400 °C, the partial equilibrium  $\text{O}_2$  pressure is about 10 times higher compared to conditions of pure nitrogen gas (based on thermodynamic calculations with Factsage). This is the result of the dissociation of water at high temperatures:  $\text{H}_2\text{O}(\text{g}) \rightleftharpoons \text{H}_2(\text{g}) + \frac{1}{2} \text{O}_2(\text{g})$ . Consequently the  $p_{\text{Na}}^*$  in the humid atmosphere is about 56 % lower ( $10^{-1/4}$ ) than the  $p_{\text{Na}}^*$  prevailing at dry conditions.

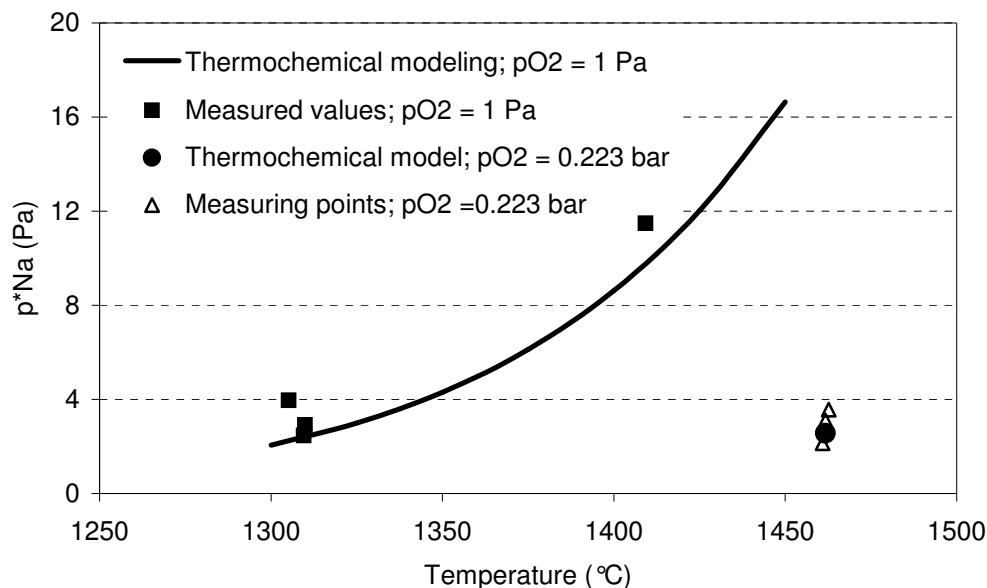


Figure 4.6: Calculated and measured saturation pressure of elemental sodium  $\text{Na}(\text{g})$  in equilibrium with a  $\text{Na}_2\text{O}\cdot 2\text{SiO}_2$  melt as a function of temperature.

Based on the experimental results and the estimations using thermochemical modeling (Associate Species Model and Factsage modeling), it was found that NaOH is the main evaporating sodium species from a sodium-disilicate melt exposed to a water vapor containing atmosphere ( $p_{\text{H}_2\text{O}} > 0.10$  bar). In a humid atmosphere at 1300 °C, with  $p_{\text{H}_2\text{O}} = 0.20$  bar and  $p_{\text{O}_2} = 100$  Pa,  $p_{\text{Na}}^*$  is more than 30 times lower than  $p_{\text{NaOH}}^*$ .

### ***Mass balances***

As already mentioned in paragraph 3.2, the total Na<sub>2</sub>O losses of the sodium-disilicate melt by evaporation processes were measured in two different ways:

1. Gravimetric determination of the weight loss of the melt at the end of the experiment (assuming only Na<sub>2</sub>O as volatile glass melt species) and
2. Extractive sampling of the carrier gases through gas-wash bottles and sodium analysis in the known volume of extracted gas during the complete experiment.

The gravimetric determination of the weight loss of the melt is a good measure for the total sodium evaporation losses during the total evaporation experiment in the transpiration set-up (including heating and cooling processes), assuming no significant absorption of water in the glass. Based on the results of Franz and Scholze [8] the maximum solubility of water in a sodium-disilicate melt is 1773 mg/kg at 1400 °C. The solubility of water in glass is nearly independent of the temperature and linear proportional to  $p_{\text{H}_2\text{O}}^{1/2}$  in the atmosphere. During an experiment at 1400 °C and  $p_{\text{H}_2\text{O}} = 0.50$  bar a maximum amount of about 31 mg of water can be absorbed by the 25 gram sodium silicate glass melt in the boat. The measured weight changes after the evaporation tests were between 70 and 190 mg. For the determination of the contribution of the water absorption on the total weight change of the glass melt, the water concentrations in the glass samples after the evaporation tests were measured using IR spectroscopy [9]. For partial water vapor pressures during the transpiration experiments of  $p_{\text{H}_2\text{O}} = 0.27$  bar and at temperatures: 1426 °C < T < 1454 °C, the measured water concentrations in the glass samples after cooling, were less than 150 mg/kg, thus maximum about 4 mg of water has been absorbed into the melt.

During heating and cooling, the furnace is flushed with dry nitrogen and only elemental Na and water can evaporate. Based on the results presented in Figure 4.6, the total amount of evaporated elemental sodium during the heating and cooling period has been estimated. From the measured sodium evaporation rate at the set-point temperature and the estimated sodium release during the heating and cooling periods, the total sodium release (expressed as Na<sub>2</sub>O) during one experiment can be calculated and compared with the gravimetric weight loss of

the glass sample. For 6 different experiments these mass balance checks were made and shown in Table 4.4. Between the gravimetrically ( $m_{\text{gravimetric}}$ ) and extractive ( $m_{\text{extractive}}$ ) measured weight losses a linear correlation was found:  $m_{\text{gravimetric}} = (1.02 \pm 0.04) \cdot m_{\text{extractive}}$  (i.e. a slope of 1.02 with a standard deviation of 0.04).

From the mass balances it is also concluded that the evaporation rates of silicon compounds are very low compared to the sodium release rates.

Table 4.4: Mass balances for 6 transpiration experiments with sodium-disilicate melts.

Temperature during experiment (°C)	Weight loss calculated from extractive sampling method ( $m_{\text{extractive}}$ ) (mg)	Weight loss gravimetrically ( $m_{\text{gravimetric}}$ ) (mg)	Ratio $m_{\text{extractive}} / m_{\text{gravimetric}}$ (-)
1416	112	125	0.90
1437	146	153	0.96
1439	166	170	0.98
1354	69	79	0.87
1454	188	188	1.00
1356	85	71	1.21

### 4.3.2 Evaporation of sodium species from soda-lime-silicate melts

Transpiration evaporation experiments were also performed with soda-lime-silicate melts [10] ( $\text{SiO}_2:\text{Na}_2\text{O}:\text{CaO} = 74:16:10$  mole-%). The glass melts are exposed to an oxidized atmosphere containing  $\text{O}_2$ ,  $\text{N}_2$  and  $\text{H}_2\text{O}$ . Thermodynamic calculations show that for the chosen gas composition NaOH is the main volatile species as a result of the dominating evaporation reaction 1.10. According to equation 1.11 a linear relation is expected between  $p_{\text{NaOH}}^*$  and  $p_{\text{H}_2\text{O}}^{1/2}$ .

For the soda-lime-silicate melt  $p_{\text{NaOH}}^*$  was derived experimentally for different water vapor pressures in the atmosphere at  $1463 \pm 2$  °C. The results are compared in Figure 4.5. For temperatures between 1300 °C and 1450 °C,  $p_{\text{H}_2\text{O}} = 0.27$  bar and  $p_{\text{O}_2} = 0.01$  bar it was calculated that maximum 2 % of the total evaporated sodium species may evaporate as pure Na.

During evaporation experiments from a static melt, the surface of the melt will become  $\text{Na}_2\text{O}$  depleted and the  $\text{Na}_2\text{O}$  bulk concentration will be higher than the  $\text{Na}_2\text{O}$  surface concentration. During the first 6 to 8 hours the measured NaOH evaporation rates (4 samples) change maximum 5 % only. Thus, the  $\text{Na}_2\text{O}$  surface concentration remains nearly constant during this period. Based on the measured sodium evaporation rates and  $\text{Na}_2\text{O}$  concentration profile measurements in the obtained glass samples (after the evaporation tests), the molar  $\text{Na}_2\text{O}$  surface fraction has been estimated to be  $0.157 \pm 0.003$  for these soda-lime-silicate melts [5].

### 4.3.3 Evaporation of boron species from alkali-lean borosilicate glass melts

The composition of the investigated alkali-free borosilicate glass melts is given in Table 4.3. Our evaporation tests and results of thermodynamic modeling show that  $\text{B}_2\text{O}_3$  in the melt is the major volatile species. The total  $\text{B}_2\text{O}_3$  losses of the alkali-free borosilicate melts can be determined in two different ways: 1) gravimetrically or 2) by measuring the boron release rates.

The gravimetric determination of the mass loss of the melt is a good measure for the total boron evaporation losses, assuming no evaporation of other compounds as well as no significant absorption of water in the glass. From transpiration evaporation tests with sodium-disilicate melts it has been shown that maximum about 4 mg water is absorbed by sodium-disilicate glass melts that have been exposed for 6 to 8 hours to a humid atmosphere with  $p_{\text{H}_2\text{O}} = 0.27$  bar and temperatures between 1427 and 1454 °C [10]. Based on a report of Faber et al. [11] it is concluded that the water solubility for sodium-disilicate melts and borosilicate

melts are quite similar. In most cases the measured mass changes after the evaporation tests vary between 200 and 800 mg, it is calculated that the maximum measuring error due to neglecting the mass increase caused by absorption of water in the melt, is 2 %.

Figure 4.7 shows the mass balances for different evaporation tests with the alkali-free borosilicate glass melts. The slope of the linear fit is almost 1.0, but the fit does not cross the origin. Probably small amounts of boron evaporate during the heating and the cooling of the glass sample in the tube furnace (in a dry oxidized atmosphere). During these stages the evaporated boron is not collected in washing bottles.

### ***Impact of process conditions on evaporation of boron species***

The total evaporation rate of boron (e.g.  $\text{HBO}_2$  and  $\text{B}_2\text{O}_3$ ) from alkali-free borosilicate melts (see Table 4.3) has been measured as a function of time, temperature and furnace atmosphere composition.

In typical industrial fossil fuel-fired E-glass furnaces, the partial water vapor pressure in the furnace atmosphere will be in the range between 0.12 bar (air-fuel oil fired) and 0.60 bar (oxygen – natural gas fired). In paragraph 1.2.4, the different relevant evaporation reactions are discussed.

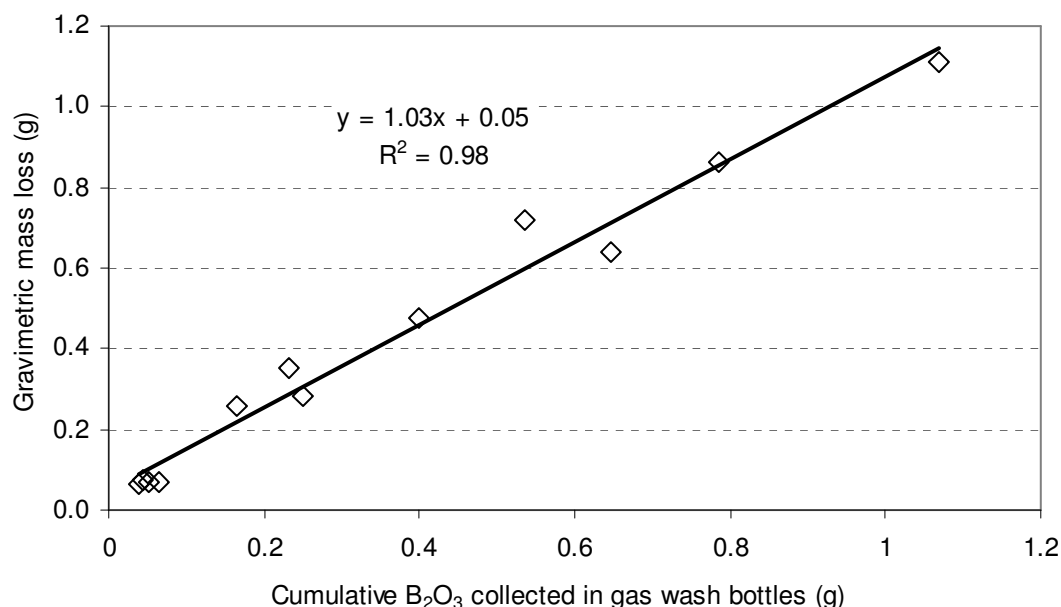


Figure 4.7: Boron mass balances of glass samples obtained from laboratory transpiration evaporation tests. The mass loss of the samples during the evaporation tests has been determined gravimetrically and the cumulative  $\text{B}_2\text{O}_3$  losses were derived from the measured amount of boron in the washing bottles.



In first instance, it has been verified that  $\text{HBO}_2$  is the main evaporating boron species as a result of a chemical reaction between  $\text{B}_2\text{O}_3$  in the melt and water vapor in the atmosphere (reaction 1.30) for these industrial atmospheres. As discussed in paragraph 1.2.4 a linear relation between the boron evaporation rate and  $p_{\text{H}_2\text{O}}^{0.5}$  is expected. For a melt with about 5 mass-%  $\text{B}_2\text{O}_3$  and a temperature of about 1450 °C, the boron evaporation rates were measured for 3 different water vapor pressures of 0, 0.14 and 0.31 bar. Figure 4.8 confirms the expected linear correlation between the measured boron evaporation rates and  $p_{\text{H}_2\text{O}}^{0.5}$ .

For pure liquid  $\text{B}_2\text{O}_3$  in equilibrium with a humid gas phase, the equilibrium vapor pressures of gaseous boron species were derived from thermodynamic calculations with Factsage [7]. For  $T = 1500$  °C,  $p_{\text{H}_2\text{O}} = 0.05$  bar and  $p_{\text{O}_2} = 0.01$  bar it is shown that  $\text{HBO}_2$  and  $\text{B}_2\text{O}_3$  are the main volatile boron species. About 90 % of the total boron species vapor pressure ( $p_{\text{B-total}}^* = p_{\text{HBO}_2}^* + 2 \cdot p_{\text{B}_2\text{O}_3}^*$ ) can be attributed to  $\text{HBO}_2$  vapor species. The vapor pressure  $p_{\text{B}_2\text{O}_3}$  is independent of  $p_{\text{O}_2}$  and  $p_{\text{H}_2\text{O}}$ .

In case that the boron species evaporation rate is partly controlled by diffusion of boron species in the melt, one could expect a boron-depleted surface layer and the boron evaporation rate will not only be controlled by the water vapor pressure and gas velocity, but also by the  $\text{B}_2\text{O}_3$  surface concentration changing in time. Especially, for high water vapor pressures (and high  $\text{HBO}_2$  vapor pressures) this effect might become important.

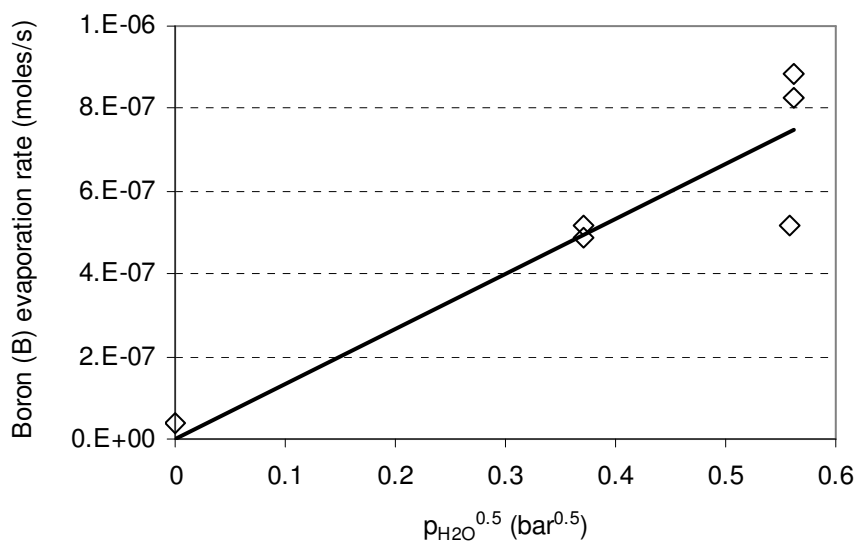


Figure 4.8: Measured total boron evaporation rates as a function of  $p_{\text{H}_2\text{O}}^{0.5}$  at  $T = 1450$  °C. The  $\text{B}_2\text{O}_3$  concentration in the alkali free borosilicate glass melts is between 4.6 mass-% and 5.0 mass-%.

As will be shown in paragraph 4.5, boron depletion at the surface of the melt compared to the average boron composition in the sample is not found for glass melts with about 5 mass-%  $B_2O_3$ . The average  $B_2O_3$  concentration in the melt at a certain time during a transpiration experiment can be calculated from the cumulative  $B_2O_3$  release until this time. It is expected that the  $B_2O_3$  surface concentrations in these experiments have values between 4.6 mass-% and 5.0 mass-%.

Besides the evaporation of  $HBO_2$ , small amounts of  $B_2O_3$  will evaporate as well. This explains the measured boron evaporation rates of about  $3.7 \cdot 10^{-8}$  mol/s at  $p_{H_2O} = 0$  bar. Before starting the evaporation test, the samples are heated from room temperature to the set-point temperature (1400 °C to 1500 °C) in a dry gas flow. During heating of the melt, the measurements show that about 15 mg  $B_2O_3$  has been released from the melt. This means that the average  $B_2O_3$  concentration in the melt drops during the heating process with about 0.06 mass-%.

In Figure 4.9 the measured total boron species evaporation rates are shown as a function of the temporarily  $B_2O_3$  concentration in the melt (averaged over the total sample), for  $p_{H_2O} \approx 0.3$  bar and 3 different temperature levels. The average  $B_2O_3$  concentration in the melt at a certain time was calculated from the initial  $B_2O_3$  concentration in the melt and the measured cumulative  $B_2O_3$  loss from the glass during experiment. For  $B_2O_3$  concentrations higher than 2.5 mass-%, the boron evaporation rates increase almost linearly with increasing  $B_2O_3$  concentration, but below an average  $B_2O_3$  concentration of about 2.5 mass-%, the boron release rate suddenly drops to values below  $2 \cdot 10^{-4}$  moles/m<sup>2</sup>/s.

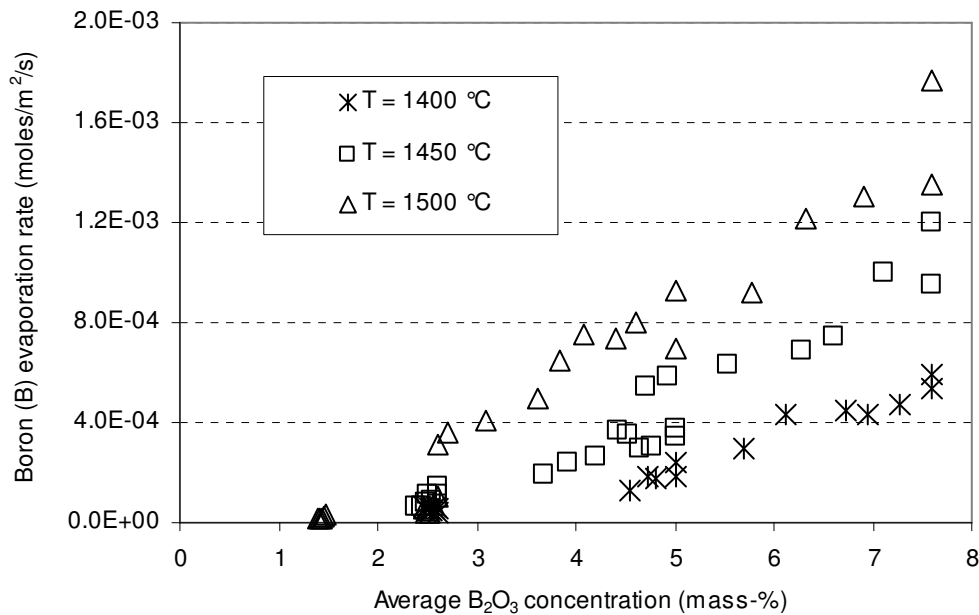


Figure 4.9: Measured total boron evaporation rates as a function of temperature and average  $B_2O_3$  concentration in the melt. The average  $B_2O_3$  concentration in the melt during the experiment has been determined from the initial  $B_2O_3$  concentration in the melt (see Table 4.3) and the measured  $B_2O_3$  loss (as a function of time).

Three possible explanations for this sudden drop of boron release are:

1.  $B_2O_3$  depletion at surface of the melt to very low  $B_2O_3$  surface concentrations;
2. Change of the molecular structure of the melt. Above a certain fraction  $B_2O_3$  in this type of melt, the molecular structure may change and the additional  $B_2O_3$  may be incorporated in a different way compared to the  $B_2O_3$  incorporation below this fraction. The coordination number of the extra boron atoms in the melt may change and boron becomes less tight bonded in the matrix leading to increased chemical activities of  $B_2O_3$  in the melt;
3. Phase segregation in the melt above a threshold concentration level  $B_2O_3$  in the silicate melt (see section 2.5).

The transport mechanisms of boron in the melt might be an important parameter that influences the boron evaporation rate. In the paragraph 4.5 this phenomenon will be discussed in more detail.

#### 4.4 Experimentally derived chemical activities of Na<sub>2</sub>O, K<sub>2</sub>O and B<sub>2</sub>O<sub>3</sub> in multi-component silicate melts

As discussed in paragraph 2.4, the developed evaporation model requires data for the chemical activity of volatile glass compounds in silicate melts as input parameter to calculate equilibrium vapor pressures of volatile species. This paragraph shows the experimentally derived chemical activities of Na<sub>2</sub>O, K<sub>2</sub>O and B<sub>2</sub>O<sub>3</sub> in sodium-silicate melts, alkali-lime silicate melts and alkali-lean borosilicate melts. Transpiration evaporation experiments were used to derive chemical activities of volatile species at the surface of the melt. Based on known Sherwood relations and known diffusion coefficients of volatile gaseous species in the gas phase, two steps are required to derive these chemical activities [10]:

##### A. Verification of the evaporation reactions

Depending on the gas composition above the melt, a volatile glass component like Na<sub>2</sub>O might evaporate in different forms (e.g. gaseous NaOH or gaseous Na). The gas composition above the melt is chosen in such a way that the evaporation of a specific volatile glass component is the result of one dominating evaporation reaction.

##### B. Determination of equilibrium pressures of evaporation species.

The saturation pressure of the gaseous volatile species just above the melt can now be determined from the mass transport relations (equations 2.10 and 2.12a given in chapter 2) and the measured evaporation rates. Subsequently, the chemical activity of the volatile glass component at the glass surface can be obtained from the evaporation reaction equation and the corresponding chemical equilibrium constant derived from the thermodynamic Factsage database [7]. The measured chemical activities can be compared with the chemical activities derived from the described Associates Species Model (paragraph 2.5).

The experimental set-up C is shown in chapter 3, figure 3.2 and the experimental procedure is described in paragraph 3.2.

#### 4.4.1 Measured and modeled chemical activities of Na<sub>2</sub>O in silicate melts

The Na<sub>2</sub>O activity values, calculated by the Associates Species Model for Alkali-lime-Silicate melts (abbreviated in this chapter as ASM-AS), are compared with experimental data derived from literature references [12]. For ternary SiO<sub>2</sub>-Na<sub>2</sub>O-CaO melts at 1400 °C the deviations between the modeled and experimentally derived activities are between 0 and 30 %.

Different models based on thermodynamic equilibrium conditions are available to derive chemical activities of sodium oxide in multi-component soda-lime-silicate melts. The modeled activities of  $\text{Na}_2\text{O}$  in float glass compositions for temperatures between 1300 °C and 1600 °C have been compared and shown in Figure 4.10. For this comparison models of Conradt [13][14], Factsage [7] and the here presented Associated Species Model for soda-lime-silicate melts (paragraph 2.5.2) were used. The maximum deviations comparing the different models decrease with increasing temperature from a factor 5 at 1300 °C to a factor 1.5 at 1600 °C. Furthermore the model shows the experimental results derived by Beerkens [15]. He measured  $a_{\text{Na}_2\text{O}}$  by means of a combination of sulfate decomposition measurements and electrochemical analysis.

Despite these differences, the deviations are acceptable, because of the large errors that can be made in activity measurements at high temperatures and because of the assumptions of the associated species model. In most cases the accuracy of the Associated Species Model appears to be sufficient to estimate evaporation rates from most glass melts as shown in this thesis. However, this level of accuracy may also explain differences found between modeled and measured evaporation rates for these type of glass melts.

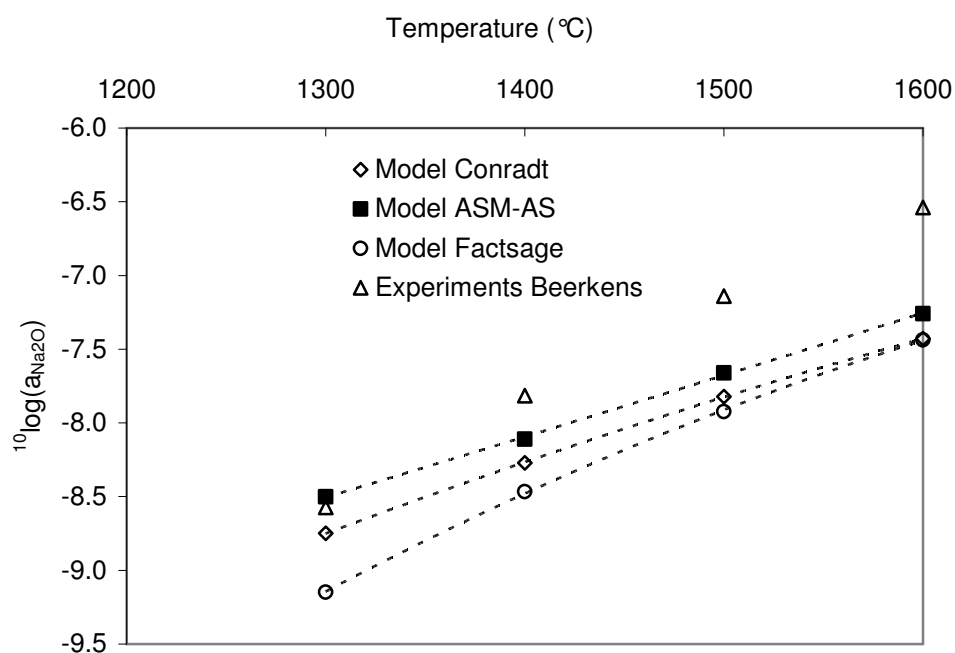


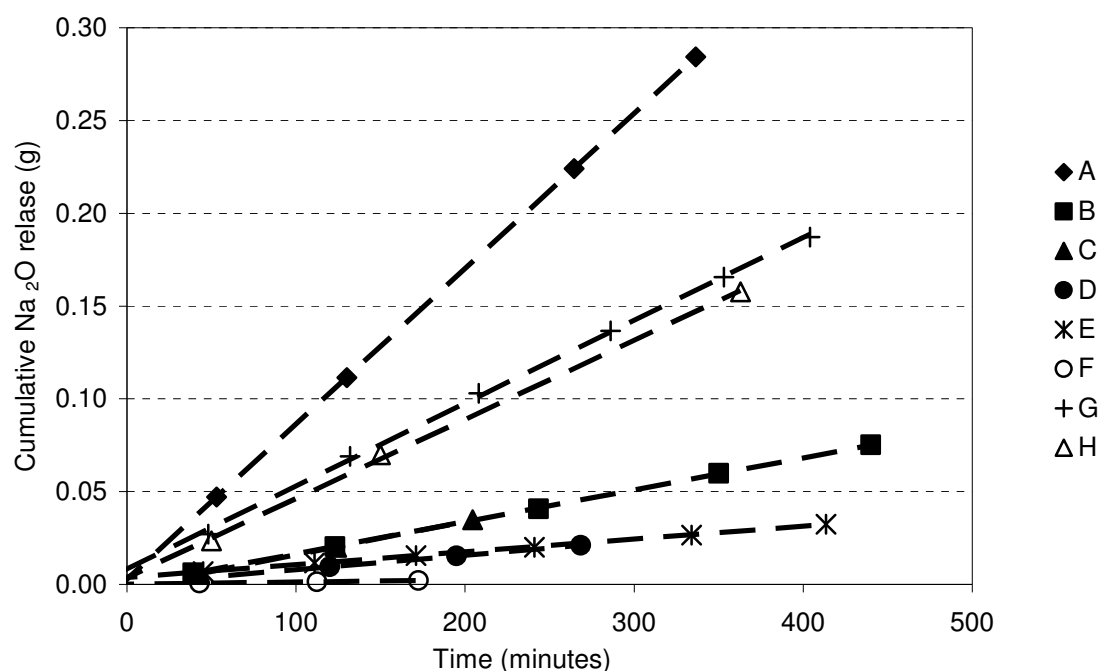
Figure 4.10: Comparison of  $\text{Na}_2\text{O}$  activity data for float glass at different temperatures. The experimental results were obtained from Beerkens [15]. The modeling results were derived from Conradt [13][14], Factsage [7] and the in this thesis presented ASM-AS model (see paragraph 2.5.2).

From sodium evaporation rates measured by this transpiration set-up, the chemical activity of  $\text{Na}_2\text{O}$  at the surface of the sodium-disilicate melt can be calculated using the equations 2.2, 2.3, 2.10, 2.11 and 2.12. The measured chemical activities of  $\text{Na}_2\text{O}$  are compared with the results of ASM-AS.

After heating up of the tube furnace until the set-point temperature, the tube is flushed with a nitrogen/water vapor gas mixture. As described in paragraph 3.2, gas samples were extracted as a function of time. During this period,  $\text{NaOH}$  evaporates from the static melt and the melt surface will become  $\text{Na}_2\text{O}$ -depleted. In a diffusion-controlled process, the  $\text{Na}_2\text{O}$  bulk concentration will be higher than the  $\text{Na}_2\text{O}$  surface concentration resulting in a boundary layer in the melt. Sanders and Schaeffer [16] concluded that in their transpiration experiments with soda-lime-silicate melts, the vaporization process is partly controlled by a surface membrane having a composition different from that of the bulk composition. The glass samples obtained from their transpiration experiments are characterized by a flat  $\text{Na}_2\text{O}$  concentration profile in the bulk glass at distances  $> 100 \mu\text{m}$  from the surface.

In our studies similar results were obtained after an evaporation test of 78 hours at  $1402 \text{ }^\circ\text{C}$  with a sodium-disilicate melt ( $p_{\text{H}_2\text{O}} = 0.48 \text{ bar}$ ). During our tests the  $\text{NaOH}$  evaporation rates were measured as a function of time and afterwards the vertical  $\text{Na}_2\text{O}$  concentration profile has been measured with Scanning Electron Microscopy (SEM-EDX). The glass sample with a thickness of  $7500 \mu\text{m}$  was characterized by a surface boundary layer thickness of about  $600 - 800 \mu\text{m}$  and a flat  $\text{Na}_2\text{O}$  concentration profile in the bulk glass. The average molar fraction  $\text{Na}_2\text{O}$  in the bulk is 0.308 and the molar fraction  $\text{Na}_2\text{O}$  at the surface is about  $0.293 \pm 0.005$ .

During the first 6 to 8 hours, after starting the experiment, the measured  $\text{NaOH}$  evaporation rates of the 4 samples deviate less than 5 % in time. Thus, during this period the  $\text{Na}_2\text{O}$  surface concentration is expected to remain nearly constant with time (see Figure 4.11). The measured partial vapor pressure of  $\text{NaOH}$  in the main gas stream ( $p_{\text{NaOH}}$ ) is more than 30 times lower than the calculated  $\text{NaOH}$  saturation vapor pressures ( $p_{\text{NaOH}}^*$ ). According to the equations 2.10 and 1.11, the  $\text{NaOH}$  evaporation rate is proportional to  $a_{\text{Na}_2\text{O}}^{1/2}$ . From the initially measured  $\text{NaOH}$  evaporation rates ( $Q_{\text{NaOH},t=0}$ ), the  $\text{NaOH}$  evaporation rate at  $t = 78$  hours ( $Q_{\text{NaOH},t=78}$ ) and the known  $\text{Na}_2\text{O}$  activity at the surface (calculated with ASM from the measured surface concentration) at  $t = 78$  hours ( $a_{\text{Na}_2\text{O},t=78}$ ), the constant  $\text{Na}_2\text{O}$  surface concentration during the first 6 to 8 hours ( $a_{\text{Na}_2\text{O},t=0}$ ) of the experiment can be calculated since  $Q_{\text{NaOH},t=0} / Q_{\text{NaOH},t=78} = (a_{\text{Na}_2\text{O},t=0} / a_{\text{Na}_2\text{O},t=78})^{1/2}$ .



Experiment	Temperature (°C)	Water vapor Pressure (bar)
A	1451	0.51
B	1306	0.52
C	1312	0.46
D	1295	0.29
E	1303	0.19
F	1308	0.00
G	1401	0.49
H	1424	0.46

Figure 4.11: Measured cumulative  $\text{Na}_2\text{O}$  release from sodium-disilicate melt during a transpiration experiment as a function of time. The figure shows the results of 8 different evaporation experiments A to H. For each experiment the temperature and water vapor pressure has been fixed at a constant value.

Using the Thermochemical Associated Species Model (paragraph 2.5) the initial molar  $\text{Na}_2\text{O}$  surface fraction at  $t = 0$  is calculated to be 0.328.

For soda-lime-silicate glass melts (float glass compositions without  $\text{SO}_3$ ) the  $\text{Na}_2\text{O}$  surface concentration at the glass surface was about 0.5 mole-% lower than the  $\text{Na}_2\text{O}$  concentration in the bulk of the melt after transpiration experiments of about 6 hours and temperatures between 1400 °C and 1500 °C ( $p_{\text{H}_2\text{O}} \approx 0.3$  bar). This is could be partly a result of sample

preparation (see paragraph 4.2) and partly of sodium depletion at the surface of the melt. Because of convection in the melt as a result of non-uniform evaporation of sodium (see paragraph 4.5), the sodium evaporation during the transpiration experiments will hardly contribute to significant surface depletion of sodium compounds (see paragraph 4.5). For both glass types, sodium-silicate as well as soda-lime-silicate melts, the  $\text{Na}_2\text{O}$  surface activity during the transpiration experiments appears to be about 10 to 15 % lower than the  $\text{Na}_2\text{O}$  surface activity in the bulk of the melt.

The observed differences between surface and bulk glass composition have to be taken into account for the thermodynamic modeling. For sodium-disilicate glass melts the molar  $\text{Na}_2\text{O}$  fraction at the surface is assumed to be  $0.330 \pm 0.005$  and for these soda-lime-silicate glass the molar  $\text{Na}_2\text{O}$  fraction at the surface is assumed to be  $0.157 \pm 0.003$ .

The measured cumulative  $\text{Na}_2\text{O}$  loss from the start of the experiment is given as a function of time in Figure 4.11. For all the experiments, a nearly linear relation was found between the cumulative  $\text{Na}_2\text{O}$  release and time, meaning that the  $\text{Na}_2\text{O}$  activity at the surface of the melt is remaining constant. During the experiments only about 0.5 to 3.5 % of the total amount of  $\text{Na}_2\text{O}$  present in the original melt is evaporated.

Figure 4.12 shows the (indirectly) measured and modeled chemical  $\text{Na}_2\text{O}$  activities as a function of temperature for sodium-disilicate melts. In the modeling approach, it is assumed that the  $\text{Na}_2\text{O}$  concentration at the surface of the melt is about 0.3 to 0.5 mole-% lower than the  $\text{Na}_2\text{O}$  bulk concentration.

Both the results of the modeling and the measurements show nearly the same temperature dependency. The measured  $\text{Na}_2\text{O}$  activity values above 1400 °C deviate 10 to 20 % from the ASM-AS modeling results. This is probably due to measuring errors (see paragraph 4.6) and deviating glass melt surface compositions.

Similar as for the sodium-disilicate melt the chemical activities of  $\text{Na}_2\text{O}$  have been measured in a soda-lime-silicate melt between temperatures of 1360 and 1465 °C. The model glass melt contains initially 74 mole-%  $\text{SiO}_2$ , 16 mole-%  $\text{Na}_2\text{O}$  and 10 mole-%  $\text{CaO}$ . The results are given in Figure 4.13. Except for one measuring point at 1456 °C the measuring and modeling results deviate less than 15 % from each other for the same temperature.



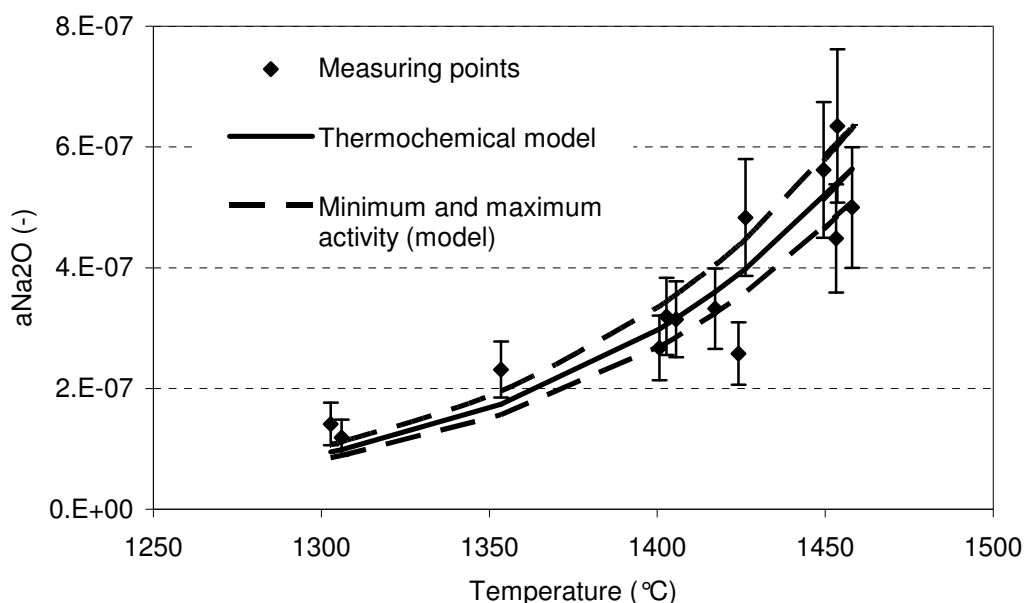


Figure 4.12: Chemical activity of  $\text{Na}_2\text{O}$  in sodium-disilicate ( $\text{Na}_2\text{O}\cdot 2\text{SiO}_2$ ) melt as a function of temperature. The graph shows the results of thermodynamic modeling (ASM) as well as results derived from the evaporation measurements performed with the transpiration set-up. Based on a molar  $\text{Na}_2\text{O}$  fraction of  $0.330 \pm 0.005$ , the minimum and maximum chemical activities were calculated from the model. Most measuring points are within or very close to the modeled range.

For a multi-component soda-lime silicate float glass composition without sulfates, the activities of  $\text{Na}_2\text{O}$  at the glass melt surface, have been measured in a similar way and the results are compared to the thermodynamic modeling results (using the Associated Species Model described in paragraph 2.5.1). The initial composition of the glass is given in Table 4.2 and the results are shown in Figure 4.14. Based on the mass balance (gravimetric weight loss of the glass melt versus the measured cumulative  $\text{Na}_2\text{O}$  release) the maximum error in the measured sodium evaporation rates was estimated.

It is assumed that the measured mass loss is a result of  $\text{Na}_2\text{O}$  evaporation only. The discrepancy between the total analyzed sodium that evaporated from the melt and sodium loss calculated from the weight loss fluctuates between 10 % for temperatures around 1500 °C to nearly 40 % for temperatures around 1350 °C. Around 1350 °C the sodium evaporation rates are low and the analytical errors are high. The errors in the measured sodium evaporation rates affect the accuracy of the experimentally derived chemical activities of  $\text{Na}_2\text{O}$  in the melt. In paragraph 4.6 the measuring errors in the experimentally derived chemical activities are discussed.

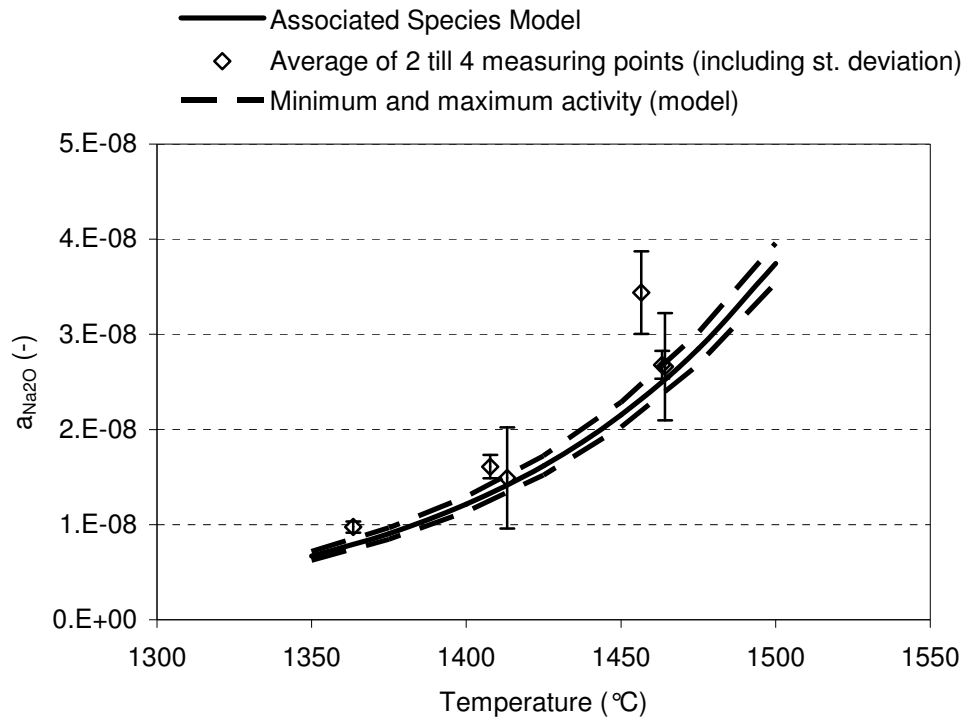


Figure 4.13: Chemical activity of  $\text{Na}_2\text{O}$ , measured for a soda-lime-silicate melt sample ( $\text{SiO}_2:\text{Na}_2\text{O}:\text{CaO} = 74:16:10$  mole-%) as function of temperature by transpiration test. The graph shows the results of thermodynamic modeling (ASM) as well as activity values (for surface of the melt) derived from the measurements performed with the transpiration evaporation set-up. The measuring points are average values of 2 to 4 separate measuring points also showing the standard deviations (shown as error bars). Based on a molar  $\text{Na}_2\text{O}$  fraction in the silicate melt of  $0.157 \pm 0.003$ , the minimum and maximum chemical activities have been calculated from the model.

For this multi-component glass melt the estimated measuring errors in the experimentally derived chemical activities of  $\text{Na}_2\text{O}$  are about 20 % at 1500 °C and even 50 to 100 % at 1350 °C. On average, the measured activities of  $\text{Na}_2\text{O}$  in the surface of a float glass melts are about 20 % higher than the modeled activities (Associated Species Model). The measuring errors in the experimentally derived chemical activities might explain the differences between the experimental results and the modeling results. However, the differences might also be a result of incomplete databases for associated species.

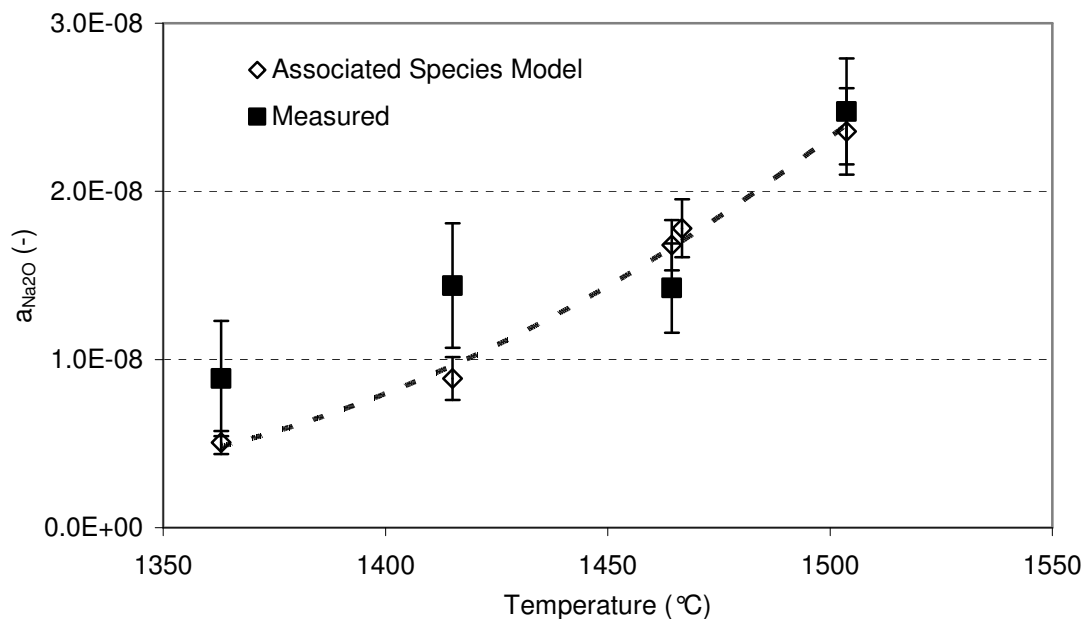


Figure 4.14: Measured and modeled chemical activity of  $\text{Na}_2\text{O}$  versus temperature in a typical float glass composition without sulfate (see Table 4.2). The measuring results have been derived from laboratory transpiration experiments and the modeling results from the thermodynamic Associated Species Model (paragraph 2.5).

#### 4.4.2 Measured chemical activities of $\text{K}_2\text{O}$ in multi-component silicate melts

For 2 different multi-component alkali-lime-silicate tableware glass compositions with  $\text{K}_2\text{O}$  as well as  $\text{Na}_2\text{O}$  (Table 4.2), the chemical activities of  $\text{K}_2\text{O}$  have been derived at different temperatures between 1400 °C and 1500 °C and compared with the results of the thermodynamic Associated Species Model (ASM-AS), assuming no depletion of  $\text{K}_2\text{O}$  and  $\text{Na}_2\text{O}$  at the glass melt surface. As shown in chapter 1, KOH is the main volatile K-species under the chosen oxidized and humid conditions. The two investigated melts contain initially respectively 4.8 mass-% and 7.8 mass-%  $\text{K}_2\text{O}$ . The measured activities (refers to surface glass composition) and modeled activities (using bulk glass composition data) of  $\text{K}_2\text{O}$  are shown in Figure 4.15.

For temperatures at about 1410 °C the measured potassium evaporation rates are relatively low compared to 1500 °C, and the relative standard deviation of the measured  $\text{K}_2\text{O}$  activities lies between 24 % and 31 %. For temperatures around 1510 °C these relative standard deviation are less: 7.5 % to 22.5 %.

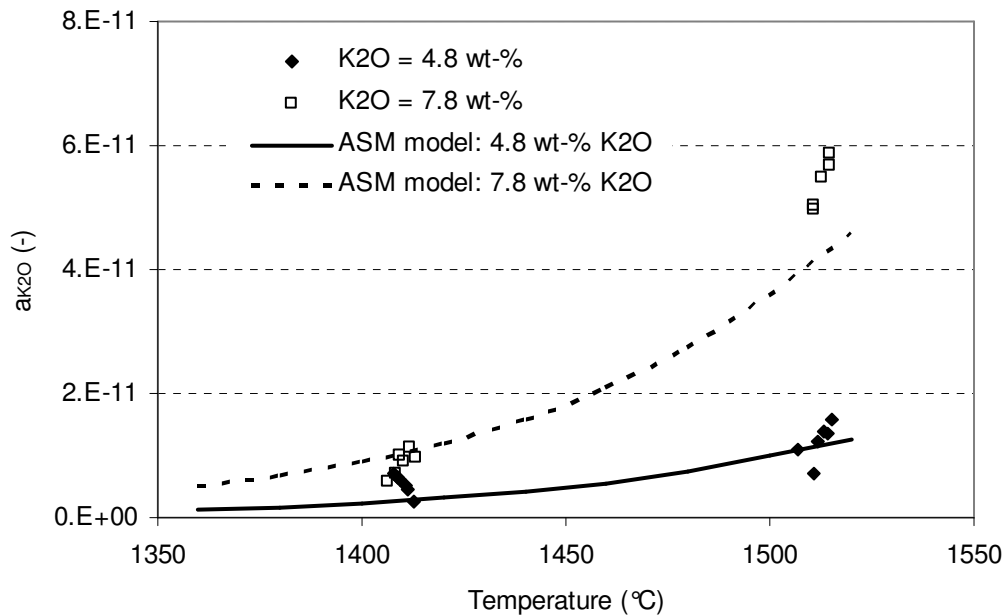


Figure 4.15: Chemical activity of  $K_2O$  versus temperature in a multi-compound alkali-lime-silicate glass compositions. The chemical compositions of the glass samples were given in Table 4.2. The measuring results for the glass melt surface (assuming only the reaction:  $K_2O + H_2O \rightleftharpoons 2 KOH(g)$ ) were derived from evaporation rates measured by laboratory transpiration experiments and the modeling results for the initial glass composition from a thermodynamic Associated Species Model (described in paragraph 2.5).

Except for the glass melt with 4.8 mass-%  $K_2O$  at 1410 °C, the measured and modeled activities of  $K_2O$  deviate between 6 and 29 %. For the glass melt with 4.8 mass-%  $K_2O$  at  $T=1410$  °C the measured  $a_{K_2O}$  is about 2 times higher than the modeled  $a_{K_2O}$ . High measuring errors in the determined potassium evaporation rates might explain the large difference between the modeled and measured  $K_2O$  activities for this specific situation.

#### 4.4.3 Measured chemical activities of $B_2O_3$ in alkali-lean borosilicate glass melts

Thermodynamic models as well as transpiration experiments are used to derive or at least estimate the chemical activities of  $B_2O_3$  in alkali-lean borosilicate melts of compositions such as shown Table 4.3. From the measuring results the chemical activities at the glass melt surface are derived and from the modeling results the chemical activities of the bulk glass are estimated. In case of surface depletion these bulk and surface compositions are different.

For the thermodynamic modeling the Associated Species Model for Boro-Silicate melts (abbreviated as ASM-BS) is used, described in paragraph 2.5.3. It is assumed that in water vapor containing atmospheres all boron evaporates as  $HBO_2$  according to reaction 1.30. The chemical activity of  $B_2O_3$  at the surface of the borosilicate melts can be calculated from the

boron evaporation rates using equation 1.31 and equation 2.10. The measured chemical activities of  $B_2O_3$  are compared with the results of a modified thermochemical model for borosilicate glass melts (see paragraph 2.5.3). Figure 4.16 shows the measured chemical activities of  $B_2O_3$  (relative to pure molten  $B_2O_3$ ) as a function of the concentration  $B_2O_3$  in the melt and temperature on a logarithmic scale. For  $C_{B_2O_3} > 2.5$  mass-%, the glass melts are nearly homogeneous (as shown by the concentration profiles measured by SEM-WDX described in paragraph 4.5) and therefore the average surface concentration can be set as the average concentration. From the measured cumulative boron losses, the average remaining  $B_2O_3$  concentration in the glass is calculated as function of time.

As already mentioned in paragraph 2.5.3, the experimental derived activities are used to optimize the modified Associated Species Model for alkali-lean borosilicate melts. For  $C_{B_2O_3} > 2.5$  mass-% the separate measuring points deviate maximum 1 decade from the modeled activities.

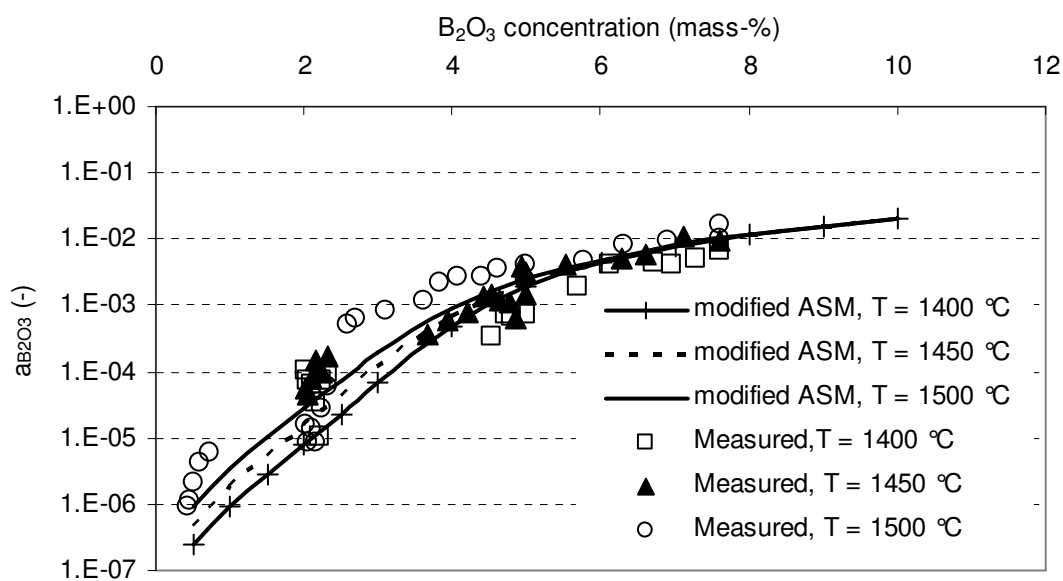


Figure 4.16: Chemical activity of  $B_2O_3$  in alkali-lean borosilicate glass melts as a function of the concentration  $B_2O_3$  in the melt and temperature. The initial glass compositions are given in Table 4.3. The measured chemical activities for the glass melt surface are obtained from transpiration evaporation tests. For the modeling of the  $B_2O_3$  activities (based on average  $B_2O_3$  concentration in the melt) the modified Associated Species Model, described in paragraph 2.5.2 is used.

For  $C_{B_2O_3} < 2.5$  mass-% the deviations are larger, because of the larger errors of the measured boron evaporation rates and the observed  $B_2O_3$  depletion at the surface for these low  $B_2O_3$  concentrations (see paragraph 4.5.2). Despite the adaptations of the model using measured  $a_{B_2O_3}$  values, the fitted model seems to be still not very precise for  $B_2O_3$  concentrations lower than 2.5 mass-%.

At this moment, the modified Associated Species Model for alkali-lean borosilicate glass melts (described in paragraph 2.5.3) can only be used to estimate  $a_{B_2O_3}$  for a small range of glass compositions and a small temperature range (1400 °C to 1500 °C). The concentration  $B_2O_3$  in these glasses is in the range of 1 to 10 mass-%, but the molar ratio between the other compounds ( $SiO_2$ ,  $CaO$  and  $Al_2O_3$ ) has not been changed.

The applied thermodynamic model for borosilicate glass melts does not account for possible phase segregation in the borosilicate melt at high temperatures. Indications for phase segregation in borosilicate glass melts are discussed in paragraph 2.4.2 but experimental evidence for phase segregation was not found in this study (see paragraph 4.5.2). In order to improve thermodynamic models for borosilicate glass melts, it is recommended to combine the results of thermodynamic modeling, glass structure measurements and molecular dynamic simulations plus chemical activity measurements (e.g. by transpiration evaporation tests) for a wider range of glass compositions. In case of phase segregation the ASM-BS model described in paragraph 2.5.3 is not applicable and the model should be modified using excess Gibbs free energy terms to describe phase segregation phenomena for these systems.

## 4.5 Transport of volatile species in glass melts

In this paragraph, the transport of sodium species in alkali-lime silicate melts (paragraph 4.5.1) and transport of boron in alkali-lean borosilicate glass melts (paragraph 4.5.2) are discussed. Phenomena like diffusion in combination with convection (e.g. Marangoni flows) in the melt influences mass transfer and release of volatile species during evaporation processes.

### 4.5.1 Transport of $Na_2O$ in glass melts with and melts without sulfur

In paragraph 4.4.1 it has been shown, that the measured sodium evaporation rates from the investigated soda-lime-silicate melts without sulfur and without chlorides are about constant (mutual differences are about 5 %) during a period of 6 to 8 hours, after starting the evaporation experiment. Thus, during this period the  $Na_2O$  surface concentration (chemical activity) is probably almost constant. According to calculations with the Thermochemical

Associated Species Model (see paragraph 2.5.1) and the measured surface concentrations (SEM-EDX) after cooling the glass melt it was found that the chemical activity of  $\text{Na}_2\text{O}$  at the surface is about 10 to 20 % lower than the  $\text{Na}_2\text{O}$  activity of the bulk glass composition.

As discussed in paragraph 4.2, the from coarse cullet prepared float glass samples without sulfur, appeared to be inhomogeneous in composition, even before the evaporation test started. Compared to the average composition, the surface layer of the melt is silica-rich and contains relatively low concentrations of  $\text{Na}_2\text{O}$  and  $\text{CaO}$ . Fresh glass melts just prepared from batches with sulfates are much more homogeneous compared to glasses prepared from batches without sulfates.

The measured  $\text{Na}_2\text{O}$  and  $\text{CaO}$  concentration profiles of float glass samples without sulfur are compared before and after a transpiration evaporation test (i.e. a raw material melt versus a melt prepared from cullet). A glass sample was prepared from raw materials, which have been melted during 1 hour at a temperature of  $1450\text{ }^\circ\text{C}$ . In this sample concentration profiles were measured. Afterwards, the sample was broken into cullet with sizes of 5 – 10 mm. The re-melted cullet has been used for a transpiration evaporation test ( $T = 1467\text{ }^\circ\text{C}$ ,  $p_{\text{H}_2\text{O}} = 0.33\text{ bar}$  and  $t = 380\text{ minutes}$ ). After this evaporation test, the  $\text{Na}_2\text{O}$  and  $\text{CaO}$  concentration profiles in this sample are measured again. Figure 4.17 shows for both glass samples almost similar  $\text{Na}_2\text{O}$  and  $\text{CaO}$  concentration profiles. The concentration profiles in the glass samples seem to be hardly influenced by the  $\text{NaOH}$  evaporation process. Apparently, glass phase with lower density seems to be separated from a bulk glass phase with higher density. In order to get a better understanding of these experimental observations, CFD models (see paragraph 2.2) are applied to simulate the convective and diffusive transport of volatile components in the melt during a transpiration experiment. Firstly, the relation between a temperature gradient over the length-direction ( $x$ -direction) of the boat and free convection in the melt has been simulated. The measured temperature difference ( $\Delta T$ ) in the gas flow direction of the boat is maximum 2 till 3 K, but for this simulation a scenario with  $\Delta T = 5\text{ K}$  has been simulated. For this situation, the free convection caused by density differences, would lead to maximum velocities in the melt of  $2 \cdot 10^{-7}\text{ m/s}$ . This corresponds to  $\text{Pe}_{\text{max}} = v_{x,\text{max}} \cdot L / D_{\text{Na}_2\text{O}} \approx 2$  (with  $L$  defined as the length of the boat) in the surface layer of the melt. In practice the temperature differences will be smaller and the Péclet number is estimated to be about 1. For this low Péclet number moderate convective transport is expected (see paragraph 2.2) and the glass melt surface might become  $\text{Na}_2\text{O}$  depleted.

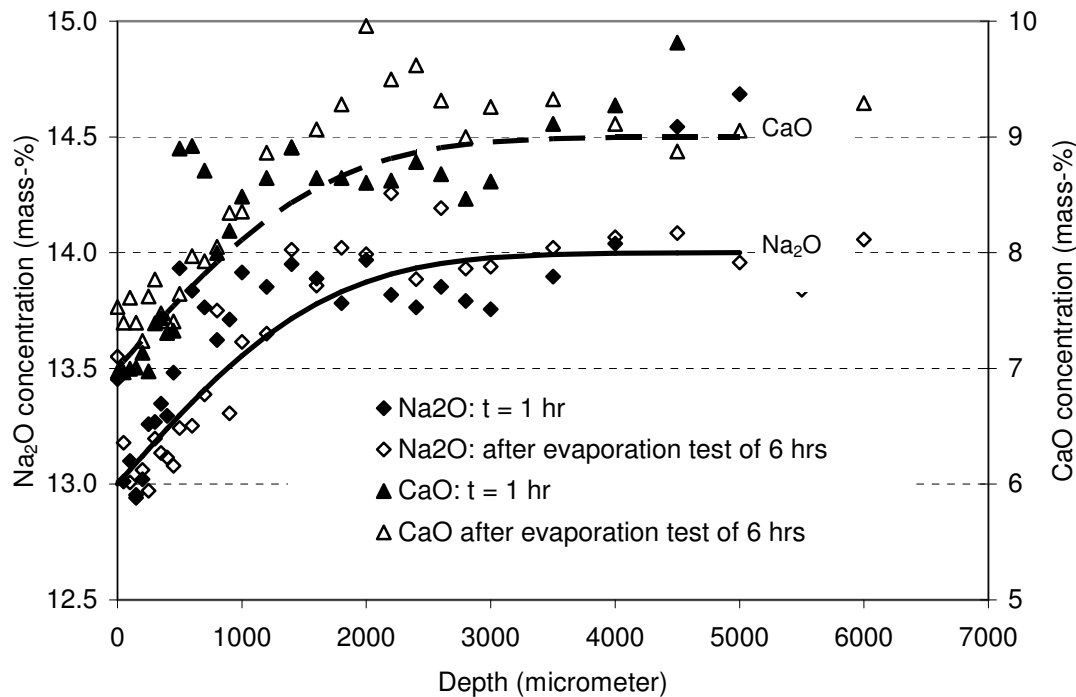


Figure 4.17: Measured  $\text{Na}_2\text{O}$  and  $\text{CaO}$  vertical concentration profiles in  $\text{SO}_3$ -free float glass samples. One sample has been melted from raw material batch during 1 hour at  $1450^\circ\text{C}$ , the other sample has been prepared from  $\text{SO}_3$ -free float glass cullet (pieces of 5 – 10 mm) and was used for a transpiration evaporation test at  $1467^\circ\text{C}$  during a period of 6 hours in a humid atmosphere ( $p_{\text{H}_2\text{O}} = 0.33$  bar).

As a result of different local mass-transfer coefficients in the gas phase [3] (which are a result of different distances from the leading edge of the flowing gases along the glass melt surface and the geometry of the vessel/boat), a non-uniform sodium evaporation profile is expected. Because of local differences in sodium evaporation rates, the local composition and local density of the surface of the melt will be different. The local differences in density might cause convective movements of the melt. From transpiration evaporation experiments and CFD simulations with water evaporation it has been shown that the local evaporation rates can be more than a factor 2 [3].

The CFD model has been used to simulate a non-uniform  $\text{NaOH}$  evaporation experiment for float glass melt without sulfur (Table 4.2). The following assumptions were made:

- $\text{NaOH}$  is the only evaporating species. The average  $\text{NaOH}$  evaporation rate is constant in time, but with a non-uniform evaporation rate distribution over the surface of the melt. Based on CFD modeling results of water evaporation tests in a transpiration set-up [3], the local mass transfer coefficients were derived. Based on



the results of this simulation, it is assumed that the local sodium evaporation rates at both ends of the boat differ about a factor 2.5.

- The initial composition of the melt is not homogeneous but vertical Na<sub>2</sub>O, CaO and SiO<sub>2</sub> concentration profiles are present as shown in Figure 4.17. The calculated densities (derived from the measured composition) of the melt at the surface and the bottom are respectively about 2140 kg/m<sup>3</sup> and about 2200 kg/m<sup>3</sup> at T = 1504 °C.
- The simulated process conditions are:
  - T = 1504 °C, p<sub>H<sub>2</sub>O</sub> = 0.33 bar, D<sub>Na<sub>2</sub>O</sub> = 7 · 10<sup>-11</sup> m<sup>2</sup>/s
  - Measured average evaporation rate: Q<sub>Na<sub>2</sub>O</sub> = 3.9 · 10<sup>-4</sup> moles/s/m<sup>2</sup>
  - Duration of the evaporation experiment is 520 minutes.

The results of the CFD modeling are shown in Figure 4.18. Figure 4.18A shows the calculated velocities in the melt in the x-direction after 520 minutes. Due to the differences in local sodium evaporation rates, the local composition of the glass surface is not uniform. In the surface layer of the melt, a net mass flow of glass melt from silica rich areas with low density to silica lean areas with high density is observed. In the deeper layers of the melt there is a net mass flow in the opposite direction. The melt at the surface is continuously refreshed by this convective flow.

The highest velocities are observed in the surface layer ( $1 < \delta_N < 1.5$  mm) of the melt, in the x-direction. However, the Na<sub>2</sub>O gradient does not disappear after the simulated evaporation process during 520 minutes (see Figure 4.18B). The maximum velocity in the surface layer of the melt is about 6 · 10<sup>-7</sup> m/s and in the surface layer Pe<sub>max</sub> ≈ 10. Since Pe is significant higher than 1, convective movements in the melt cannot be neglected in these experiments.

The absolute values of velocities in vertical direction (y) in the melt are a factor 3 lower and in the width-direction (z) the velocities are even about 20 times lower compared to the average absolute velocity in the x-direction.

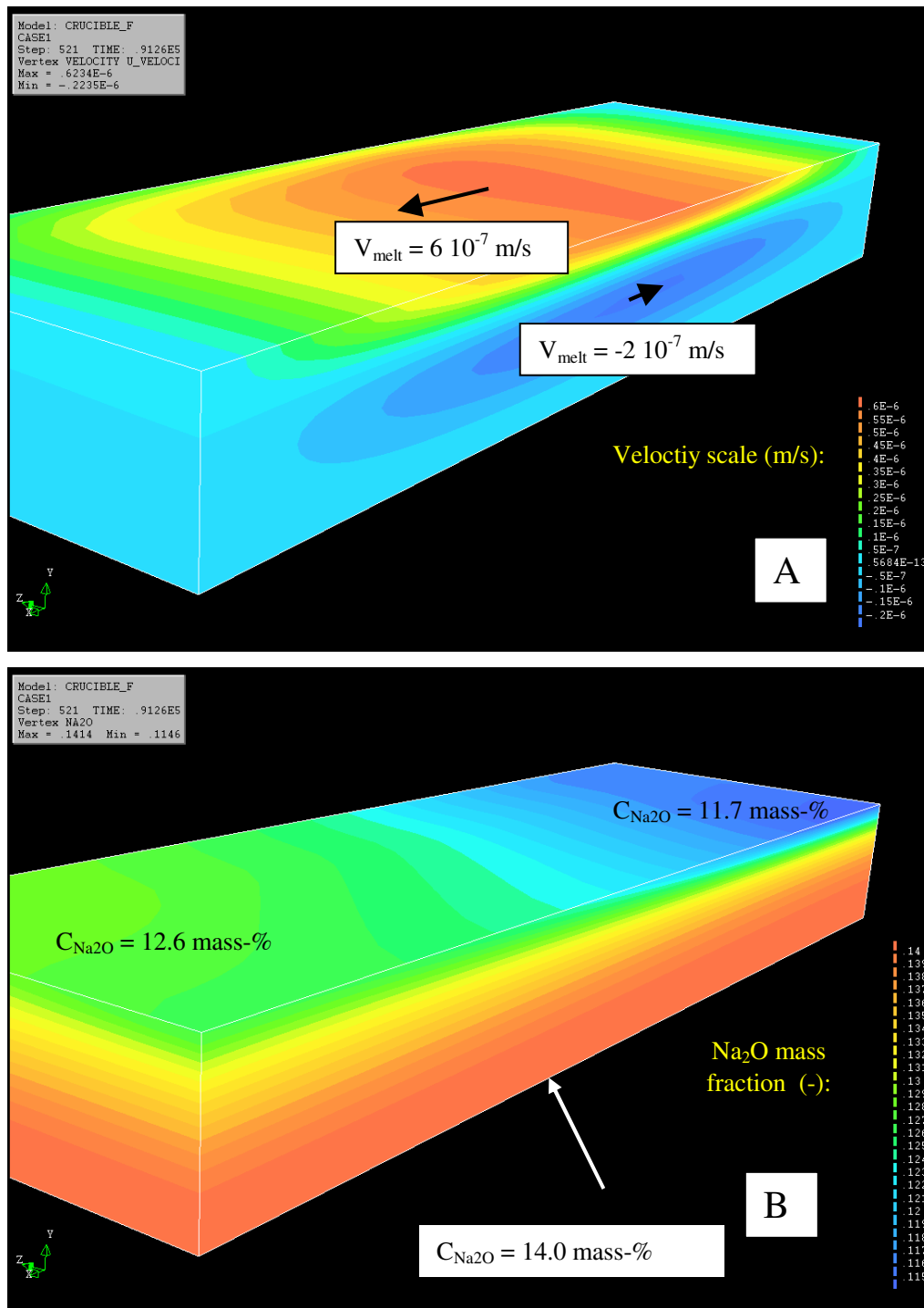


Figure 4.18: Concentrations and glass melt velocities from CFD simulations for the transpiration evaporation experiments with float glass melts without sulfate ( $T = 1504$  °C,  $p_{\text{H}_2\text{O}} = 0.33$  bar and the duration of the experiment is 520 minutes). The pictures show the glass melt in the boat/vessel. Figure A shows the calculated velocities in the melt in the x-direction, varying from  $-2 \times 10^{-7}$  m/s (blue) to  $6 \times 10^{-7}$  m/s (red). Figure B shows the Na<sub>2</sub>O mass fractions from 0.115 (blue) to 0.140 (red). Initially, the composition of the melt is not homogeneous, but Na<sub>2</sub>O and CaO depleted at the surface (see Figure 4.17). The convective flows are caused by locally different mass transfer coefficients into the gas phase.

The thickness of the Nernst boundary layer in the melt phase has been calculated from the modeled Na<sub>2</sub>O concentration gradient near the surface of the melt and equation 2.1. In the center of melt the thickness of the Nernst boundary layer is initially about 2.6 mm and after the simulated evaporation test the thickness of the Nernst boundary layer has been reduced to 1.9 mm. The calculated Na<sub>2</sub>O surface concentration at the center of the melt drops from 12.6 mass-% initially, to 12.1 mass-% after 520 minutes. With this level of convection the initially non-uniform Na<sub>2</sub>O concentration profile does not disappear.

After the evaporation experiment and cooling of the glass sample, the Na<sub>2</sub>O surface concentration measured at the centre of the glass sample, appeared to be about 12.6 mass-%. The measured thickness of the Nernst boundary layer at that position is 2.9 mm.

Both, the modeling and measuring results show that the Na<sub>2</sub>O surface concentrations as well as the Nernst boundary layer thickness in the melt hardly change during the duration of a transpiration experiment.

It is expected that due to a non-uniform sodium evaporation profile a convective loop develops in the melt, and the assumption of a fully static melt with only diffusive transport of Na<sub>2</sub>O in the vertical direction does not seem to be correct. However, the measured concentration profiles in the glass samples are mainly a result of the initial concentration gradients present in the glass samples used for the experiments.

The nearly constant sodium evaporation rate in time is mainly a result of the induced convection in the melt during the evaporation test stabilizing the local Na<sub>2</sub>O concentrations at the surface of the melt.

#### **4.5.2 Transport of boron in alkali-lean borosilicate glass melts**

In paragraph 2.2.3 the transport mechanisms of boron in borosilicate glass melts have been discussed and some suggestions of the transport processes of boron in the melt are postulated. It has been shown that the transport of B<sub>2</sub>O<sub>3</sub> in the melt can not be caused by diffusion only. As a result of non-uniform boron evaporation rates, local density and surface tension differences are expected at the glass melt surface. This will cause some convection in the melt.

In these kind of melt convection can be expected as a result of non-uniform boron evaporation rates and/or phase segregation. Equation 2.17 is used to estimate the interdiffusion coefficient of boron. For the investigated glass melts (see Table 4.3) and temperatures between 1400 °C and 1500 °C, these  $D_{B_2O_3}$  values range from  $1.0 \cdot 10^{-11}$  to

$6.6 \cdot 10^{-11} \text{ m}^2/\text{s}$ . For our evaporation tests with alkali-lean borosilicate glass melts with originally about 5 mass-%  $\text{B}_2\text{O}_3$ , this implies that the boron evaporation rates from static melts would decrease 60 to 80 % within a period of 30 till 60 minutes after the start of the evaporation test. However, our measurements show that the boron releases decrease only about 5 to 15 % within a period of 60 minutes.

For glass melt compositions with initially respectively 7.6 mass-%, 5.0 mass-% or 2.6 mass-%  $\text{B}_2\text{O}_3$ , the boron evaporation rates have been measured for different exposure times and for temperatures between 1400 °C and 1500 °C and  $p_{\text{H}_2\text{O}} = 0.32 \text{ bar}$ . From the measured boron evaporation rates, the total cumulative  $\text{B}_2\text{O}_3$  loss during the duration of the whole experiment is determined. From the total boron losses and initial content of boron oxide in the glass, the average (over the volume of the sample)  $\text{B}_2\text{O}_3$  concentrations in the melt have been calculated for different exposure times.

Figure 4.19 shows the boron evaporation rates measured during 5 different evaporation tests as a function of the average  $\text{B}_2\text{O}_3$  concentration in the melt. For  $\text{B}_2\text{O}_3$  concentrations between 4 and 5 mass-%, rather ‘smooth’ transitions has been observed between the experiments 1 and 1a at and the experiments 2 and 2a. These observations can be explained if one assumes a homogeneous glass melt composition without lower boron concentrations at the surface of the melt. However, at an average concentration of about 2.5 mass-%  $\text{B}_2\text{O}_3$  a large decrease of evaporation rate is observed comparing the experiments 2 and 3. In order to understand these results, vertical boron concentration profiles were measured in the different glass samples obtained from the evaporation tests. After an evaporation tests at 1500 °C, the  $\text{B}_2\text{O}_3$  concentration profile has been measured with SEM-WDX (this technique is described in paragraph 3.3). Based on the measured mass loss, an average  $\text{B}_2\text{O}_3$  concentration of about 3.0 mass-% is expected after the evaporation test.

Figure 4.20 shows the measured  $\text{B}_2\text{O}_3$  concentration profile from the surface to the bottom of the sample. There is hardly any vertical  $\text{B}_2\text{O}_3$  concentration gradient and the measured average  $\text{B}_2\text{O}_3$  concentration is 2.8 mass-%.

In a glass sample obtained from another evaporation test (experiment 4, using a glass sample with initially 2.6 mass-%  $\text{B}_2\text{O}_3$ ) at 1500 °C, an average  $\text{B}_2\text{O}_3$  concentration of about 1.4 mass-% is expected based on the cumulative boron losses. Again SEM-WDX has been used to measure the  $\text{B}_2\text{O}_3$  concentration profile from surface to bottom of the melt and the results are also shown in

Figure 4.20. In this particular case, the measured  $B_2O_3$  concentration at the surface is only about 0.2 mass-%, while the  $B_2O_3$  concentration at the bottom of the sample is about 1.4 mass-%.

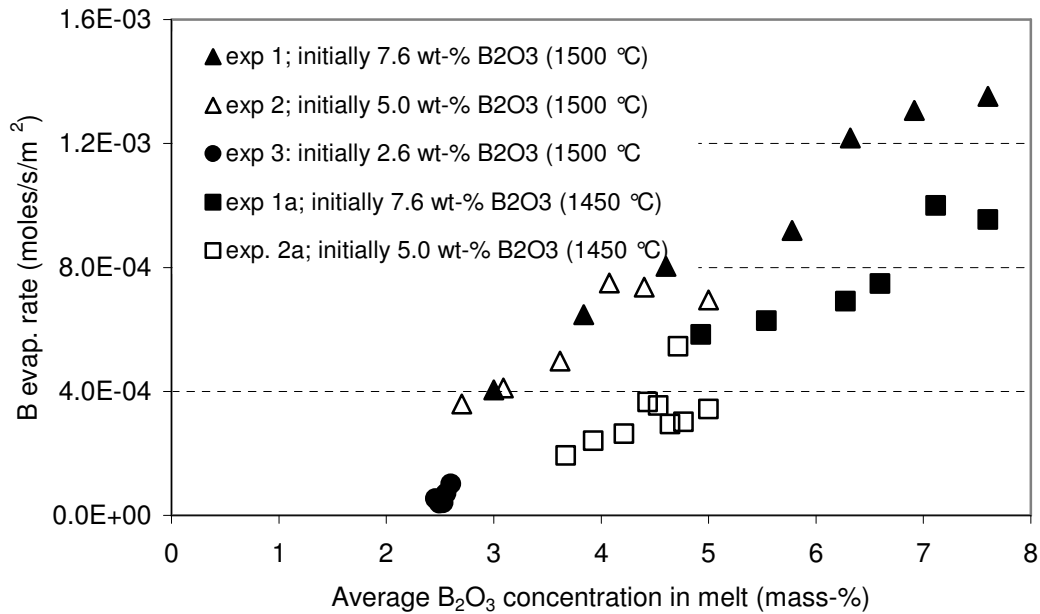


Figure 4.19: Measured boron evaporation rates as a function of the calculated average  $B_2O_3$  concentration at that time in the melt at  $T = 1450\text{ °C}$  and  $T = 1500\text{ °C}$ . The water vapor pressure in the atmosphere was about 0.32 bar.

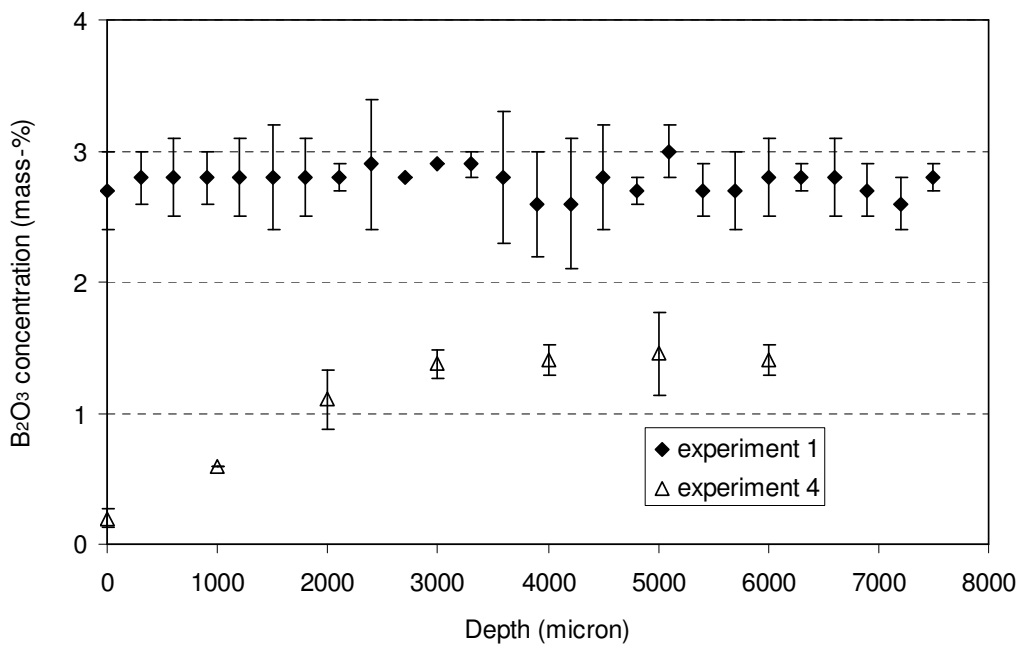


Figure 4.20: Measured vertical  $B_2O_3$  concentration profile in a glass sample obtained after the experiments 1 and 4. The measurements have been performed with SEM-WDX

The measured boron concentration profiles might be a result of phase segregation in the melt (see paragraph 2.4.2). Borosilicate melts may be considered as a mixture of a silica rich melt phase and one or more borate melt phases, such as a calcium-borate phase. The calcium-borate melt phases are probably present in the other continuous phase(s) as a very fine dispersion of small droplets (probably  $< 1 \mu\text{m}$ ) due to the relative high surface tension. In melts with low  $\text{B}_2\text{O}_3$  concentrations, more silica rich melt phases will be formed, which encapsulate the calcium-borate melt phases. In this specific situation the transport of boron ions to the surface of the melt is limited or hindered. Even the formation of a silica rich surface layer with relative low surface tension compared to calcium-borates or sodium-borates might be considered. The formation of silica rich melt phases for glass compositions with  $C_{\text{B}_2\text{O}_3} \leq 2.5 \text{ mass-}\%$  could explain the measured  $\text{B}_2\text{O}_3$  depletion in the surface layer of the melt.

#### 4.6 Measuring errors

Measured chemical activity values of  $\text{Na}_2\text{O}$ ,  $\text{K}_2\text{O}$  and  $\text{B}_2\text{O}_3$  are used to validate different thermodynamic models for different (multi-component) silicate melts. Therefore, it is necessary to quantify the error and standard deviation in the ‘measured’ chemical activities. In their paper, Van Limpt et al. [6] discussed the measuring errors in the experimentally derived chemical activities of  $\text{Na}_2\text{O}$  in silicate melts.

The possible errors in the measured chemical activities, derived from the results of the transpiration experiments, depend on a). parameters that can be measured directly like temperature, dimensions, gas flow rates, gas composition and results of chemical analysis and on b). gas or glass melt properties, such as diffusion coefficients (gas phase), viscosities, reaction equilibrium constants derived from literature or other models. Also c). the derived relations found for the gas phase mass transfer process, characterized by the Sherwood numbers may introduce some uncertainties. Since all equipment parts (mass flow controllers, gas volume meters,  $\text{O}_2$  analyzer, thermocouples) have been calibrated, errors in the first category parameters will probably lead to random deviations, but errors in the last 2 categories of parameters may lead to systematic deviations compared to the real chemical activities.

The diffusion coefficients of gaseous  $\text{NaOH}$ ,  $\text{KOH}$  and  $\text{HBO}_2$  in the furnace atmosphere or gaseous boundary layer are obtained from Chapman-Enskog relations and the maximum error for  $D$  of this estimation method is between 10 and 20 % [17]. In case that the diffusion

coefficient is the only source of error this will lead to a systematic error of about 18 – 34 % in the experimentally derived chemical activities of volatile species, such as Na<sub>2</sub>O, K<sub>2</sub>O and B<sub>2</sub>O<sub>3</sub> in the melt. The errors in the value of the dynamic viscosity of the gases, in the reaction equilibrium constant and the Sherwood number are probably lower than 2 % and have much less impact on the (indirectly) derived chemical activities.

Figure 4.21 shows the linear correlation as found between the measured and chemical activity of Na<sub>2</sub>O modeled by ASM-AS. In formula (including the standard deviation):

$$a_{\text{Na}_2\text{O}(\text{model})} = (0.98 \pm 0.04) \cdot a_{\text{Na}_2\text{O}(\text{measured})}$$

Based on the slope of the fitted linear curve (= 0.98), a large systematic error seems to be unlikely and the error in the calculated diffusion coefficient of NaOH is probably much lower than 10 %. However, the maximum errors in the separate points, as shown in Figure 4.12 are much higher than the standard deviation, but they seem to be random.

Based on the uncertainties in the parameters required for the experimental derivation of the chemical activity values of volatile glass melt species, the maximum error of each experimentally derived value for the chemical activity has been calculated [18]. The following maximum errors of the different process parameters are obtained from calibration procedures and literature data:

Temperature (T)	: ± 2 K
Water vapor pressure atmosphere (p <sub>H<sub>2</sub>O</sub> )	: ± 5·10 <sup>-3</sup> bar
Inner diameter of the furnace tube (d <sub>in</sub> )	: ± 2 %
Gas flow rate under normal conditions (ϕ <sub>n</sub> )	: ± 5 %
Measured evaporation rates (Q)	: ± 5 – 10 %
Diffusion coefficient gaseous volatile species i (D <sub>i</sub> )	: ± 10 %
Dynamic viscosity carrier gas (μ)	: ± 2 %
Sherwood number (Sh)	: ± 2 %

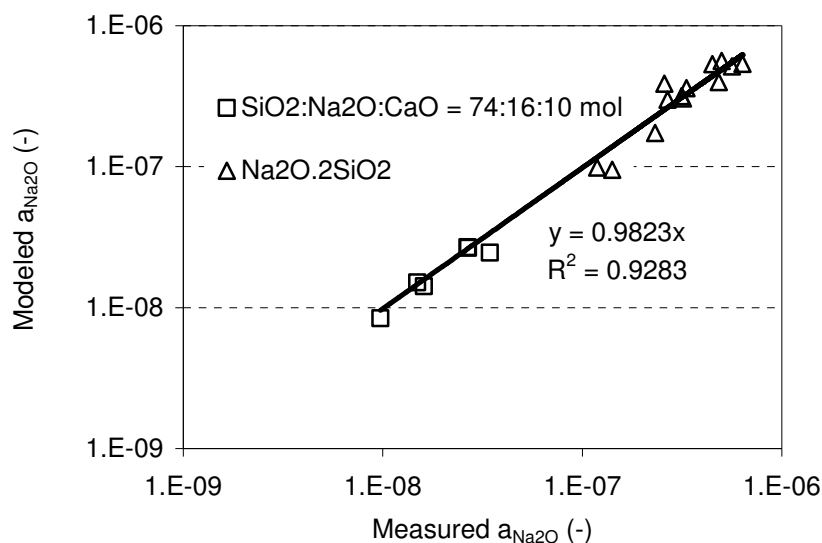


Figure 4.21: Comparison between the measured (glass melt surface) and modeled chemical activities (ASM for bulk glass) of  $\text{Na}_2\text{O}$  in a sodium-disilicate melt and a soda-lime-silica melt (initial composition  $\text{SiO}_2:\text{Na}_2\text{O}:\text{CaO} = 74:16:10$  mole-%)

For temperatures around 1300 °C, the maximum error of the measured chemical activity values of  $\text{Na}_2\text{O}$  in soda-lime-silicate melts is about 25 % but for temperatures of 1350 °C and higher, this maximum error is lower than 20 %.

For the calculation of the chemical activity of  $\text{Na}_2\text{O}$  at the surface of the sodium-silicate melt by ASM-AS, an average  $\text{Na}_2\text{O}$  mole fraction at the surface of  $0.330 \pm 0.005$  has been assumed, for the soda-lime-silicate glass the molar  $\text{Na}_2\text{O}$  fraction at the surface is assumed to be  $0.157 \pm 0.003$ .

Figure 4.12 and Figure 4.13 show all the measuring points including the error bars of the values taking into account the measuring errors as described before. The figures also contain the results of the thermochemical Associated Species Model including the error range in the calculated chemical  $\text{Na}_2\text{O}$  activity at the surface of the melt. Except for two measuring points, the measuring points and the modeling results overlap each other for both glass types.



#### 4.7 Evaporation processes of multi-component alkali-lime silicate compositions used in glass industry

In appendix II, it is shown that the presence of sulfur and chlorides in alkali-silicate melts influence the evaporation rates of sodium- and potassium-species. The measured evaporation rates of sodium species and chemical activities of  $\text{Na}_2\text{O}$  in soda-lime-silicate glass melts without sulfates and without chlorides have been presented and discussed.

In this paragraph the main results of the in appendix II described experimental and industrial investigations, are summarized. For soda-lime-silicate glass melts with sulfur in the melt,  $\text{NaOH}$  and  $\text{Na}_2\text{SO}_4$  are the main evaporating sodium species in humid and oxidized atmospheres. The evaporation rate of  $\text{Na}_2\text{SO}_4$  is proportional to the chemical activity of  $\text{Na}_2\text{SO}_4$  at the surface of the melt. But, the surface layer becomes  $\text{Na}_2\text{SO}_4$  depleted.

The effect of water vapor in the atmosphere on the extra release of sodium species from the melt is still not completely understood. Because of the lower maximum  $\text{SO}_3$  concentration in a humid atmosphere, sulfur species have to be released from the melt when being exposed to a humid atmosphere. The formation of  $\text{SO}_2$  bubbles and the formation of a dynamic, continuously refreshed foam layer at the surface of the melt may also promote the evaporation rates of volatile glass components.

For a multi-component alkali-lime-silicate melt containing  $\text{Na}_2\text{O}$ ,  $\text{K}_2\text{O}$ , sulfur and chlorine ( $\text{Na}_2\text{O} \approx 10$  mass-%,  $\text{K}_2\text{O} \approx 5$  mass-%,  $\text{SO}_3 \approx 0.1$  mass-%,  $\text{Cl} \approx 0.1$  mass-%), the evaporation rates of sodium- and potassium-species are about 40 to 60 % higher at 1500 °C compared to melts without sulfur and chlorine, but with the same basic composition concerning the other components. From these melts,  $\text{NaOH}$ ,  $\text{NaCl}$ ,  $\text{Na}_2\text{SO}_4$ ,  $\text{KOH}$ ,  $\text{KCl}$  and  $\text{K}_2\text{SO}_4$  are the main evaporating species. Linear correlations were found between the chloride evaporation rates and sulfur release rates when changing the sulfur contents in the melt or when changing the water vapor pressure in the atmosphere. This observation may be a result of the effect of sulfur on the occurrence of stronger convection in the melt. This leads to higher release rates of compounds such as  $\text{Na}_2\text{SO}_4$ ,  $\text{KCl}$  and  $\text{NaCl}$ . The formation of  $\text{SO}_2$  bubbles and the formation of a foam layer at the surface of the melt, might not only effect sulfur evaporation but will influence the release rates of chloride compounds as well.

From the observed linear correlation between the measured potassium evaporation rates and chloride evaporation rates (see Figure 4.22) it was concluded that from these melts chlorides mainly evaporate as  $\text{KCl}$  rather than  $\text{NaCl}$ .

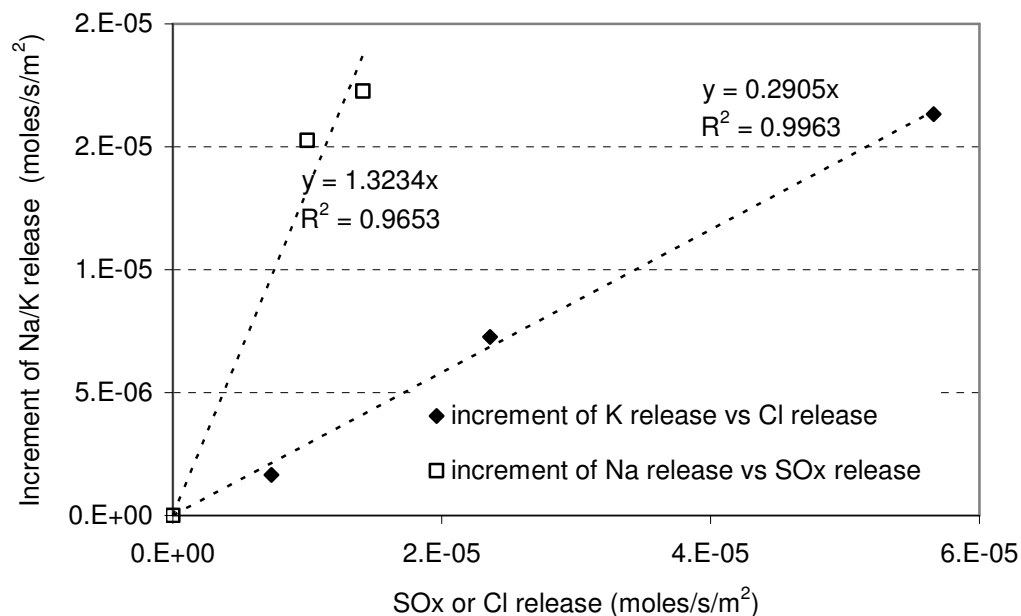


Figure 4.22: Correlation between the  $SO_x$  release and Cl release from tableware melt C (with  $SO_3$  and Cl) and the measured increase in total Na- en K-release of this melt compared to the evaporation rates from tableware melt A without  $SO_3$  and without Cl (see Table 4.2).

Obviously, sulfur and chloride species in the melt can promote the evaporation of sodium and potassium species, especially if both species together are present as fining agent in a batch of glass forming raw materials. For the special tableware glass compositions, it is not clear yet or there is no direct evidence in which form sodium and potassium species evaporate from the melt, but the most important species seem to be:  $Na_2SO_4$ , NaCl,  $K_2SO_4$  or KCl.

For alkali-lime-silicate melts, chlorides and sulfates promote the release of alkali species, such as  $Na_2SO_4$ , NaCl, KCl or possibly  $K_2SO_4$ . Due to the presence of these components, convective flows in the melt may increase and reduce the depletion rate at the glass melt surface for  $Na_2O$ ,  $K_2O$  and especially  $SO_3$  and Cl. Convection may take place as a result of non-uniform evaporation rates of volatile glass melt species along the glass melt surfaces. Because of the non-uniform evaporation rates, concentration and density differences or surface tension differences in the melt are induced. In a static melt, the evaporation rates of these species are limited by the relatively slow diffusion transport. However, temperature gradients, differences in surface tension and bubbles in the melt can strongly affect the (local) convection in the melt and the evaporation rates of these minor species. The main

evaporation species from soda-lime-silicate float glass melts and alkali-lime-silicate tableware melts are: NaOH, KOH, Na<sub>2</sub>SO<sub>4</sub>, KCl and at reducing conditions Na and K.

Compared to soda-lime float glass melts containing sulfur, the evaporation rates of sodium-sulfate from the tableware melt seems to be much lower. Due to the lower sulfur concentration in tableware glass the surface layer of the melt might be more sulfate depleted compared to float glass. In float glass the average concentration SO<sub>3</sub> is about 0.25 mass-% and in tableware glass the average concentration SO<sub>3</sub> ≈ 0.13 mass-%.

However, in float glass melts SO<sub>2</sub> bubbles might cause (some) foam production at the surface of the melt. This foam layer may explain the higher release rates of sodium species like NaOH and Na<sub>2</sub>SO<sub>4</sub>.

#### **4.8 Additional parameters influencing the evaporation during heating of melting glass forming raw materials and glass melts**

This thesis mainly focuses on the evaporation from blank glass melts. The results of evaporation modeling and experimental laboratory evaporation tests for blank silicate melts are presented in the previous paragraphs. Other parameters that also influence the evaporation of glass species during melting of glass are qualitatively and shortly described in this paragraph and demonstrated by some examples. The following aspects and processes will be discussed:

- a) Evaporation from raw material batch blankets during melting;
- b) Foam formation and evaporation.

##### **a) Evaporation from batch blankets**

During the heating of the raw materials for the production of tableware glass, the evaporation rates of sodium species, potassium species, chloride species and sulfur species have been measured. A mixture of raw materials for the production of the tableware melts has been placed in the transpiration set-up at room temperature. The raw materials are heated with a heating rate of ± 2.7 °C/minute up to a maximum temperature of about 1450 °C. The water vapor pressure in the atmosphere was 0.20 bar. The results are shown in Figure 4.23. This figure shows the measured release rates as a function of the average temperature prevailing at the sampling periods. Between 800 and 900 °C, alkali-chlorides and some alkali-sulfates are probably released from the batch.

According to thermodynamic modeling with Factsage [7] the saturation vapor pressures of pure liquid KCl and NaCl are respectively 679 Pa and 370 Pa at 900 °C. The saturation vapor pressure of HCl in an atmosphere with  $p_{\text{H}_2\text{O}} = 0.20$  bar at 900 °C is about a factor 100 lower. Pure liquid  $\text{Na}_2\text{SO}_4$  and  $\text{K}_2\text{SO}_4$  at 900 °C, in an atmosphere with a water vapor pressure of 0.20 bar will probably dissociate in gaseous NaOH or KOH,  $\text{SO}_2$  and  $\text{O}_2$ , according to these thermodynamic calculations. The saturation vapor pressures of NaOH and KOH are lower than 1 Pa. The saturation pressures of  $\text{Na}_2\text{SO}_4$  and  $\text{K}_2\text{SO}_4$  are even lower.

Thus, the presence of pure liquid KCl and NaCl in the melting raw materials seems to be an important cause of the release of sodium, potassium and chloride species from these batches. However, based on the molar ratio of the gaseous chloride species and all volatile potassium species plus sodium species ( $Q_{\text{Cl}} / [Q_{\text{K}} + Q_{\text{Na}}] = 2.4$ ), the measured chloride release can not be explained fully. As shown in paragraph 4.7.4.1 HCl will probably also be released from the first melt phases formed at temperatures below 1000 °C. Above these melt phases the vapor pressure of HCl will be higher.

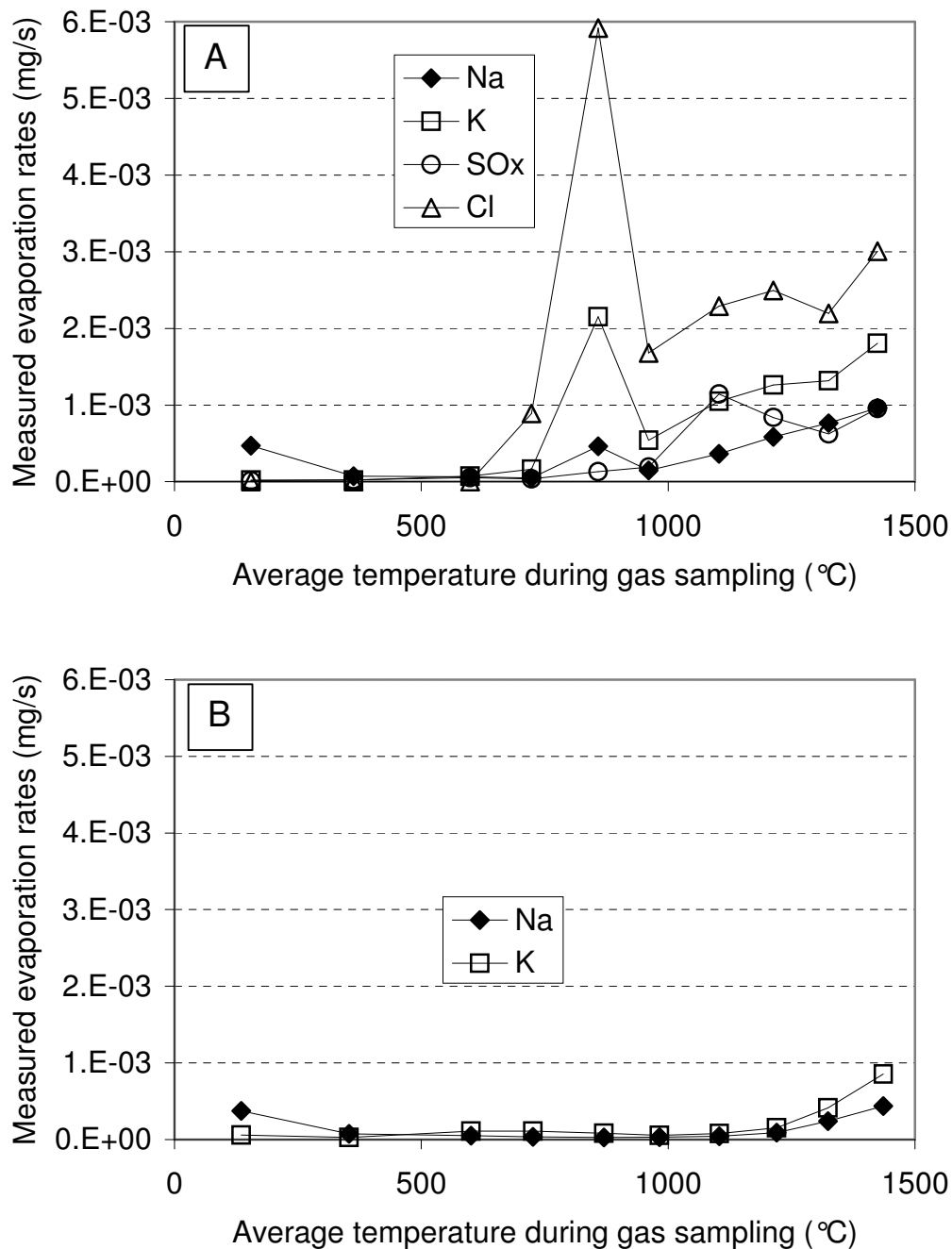


Figure 4.23: Measured evaporation rates of sodium, potassium, chloride and sulfur species during the melting of raw materials for the production of tableware glass. Figure A shows the release from tableware batch composition C containing SO<sub>3</sub> and Cl (see Table 4.2). Figure B shows the release from tableware batch composition A without SO<sub>3</sub> and Cl (see Table 4.2).

In industrial raw material / cullet mixtures for container glass production, generally fluoride contaminations are present. During heating of the melting batch blanket, fluorides are released as shown in Figure 4.24. The highest fluoride evaporation rates were observed in a humid atmosphere. According to thermodynamic simulations [7], fluorides are mainly evaporating as HF (e.g.:  $2\text{NaF (m)} + \text{H}_2\text{O (g)} \rightleftharpoons 2\text{HF (g)} + \text{Na}_2\text{O (m)}$ ) from melting glass batches exposed to humid atmospheres between 1000 and 1500 °C. The figure shows a maximum evaporation rate around 1200 °C which indicates that the fluoride mainly evaporates before complete melting. At high temperatures the surface layer of the glass melt will become fluoride depleted and the fluoride evaporation rates decrease. At dry conditions fluoride evaporates mainly as NaF from these batches/melts (see paragraph 1.2.5).

During the melting of industrial borosilicate E-glass forming raw materials, the fluoride release has been measured as a function of temperature for different partial water vapor pressures between 0 and 0.55 bar. Again the fluoride release increases with increasing  $p_{\text{H}_2\text{O}}$  as a result of HF evaporation. The maximum evaporation rates were measured around temperatures of 1100 °C (melting raw material batch blanket) and 1500 °C (fresh glass melt). HF seems to be the major volatile species, but as discussed in paragraph 1.2.5 other species like NaF,  $\text{CaF}_2$  or even  $\text{SiF}_4$  might evaporate as well.

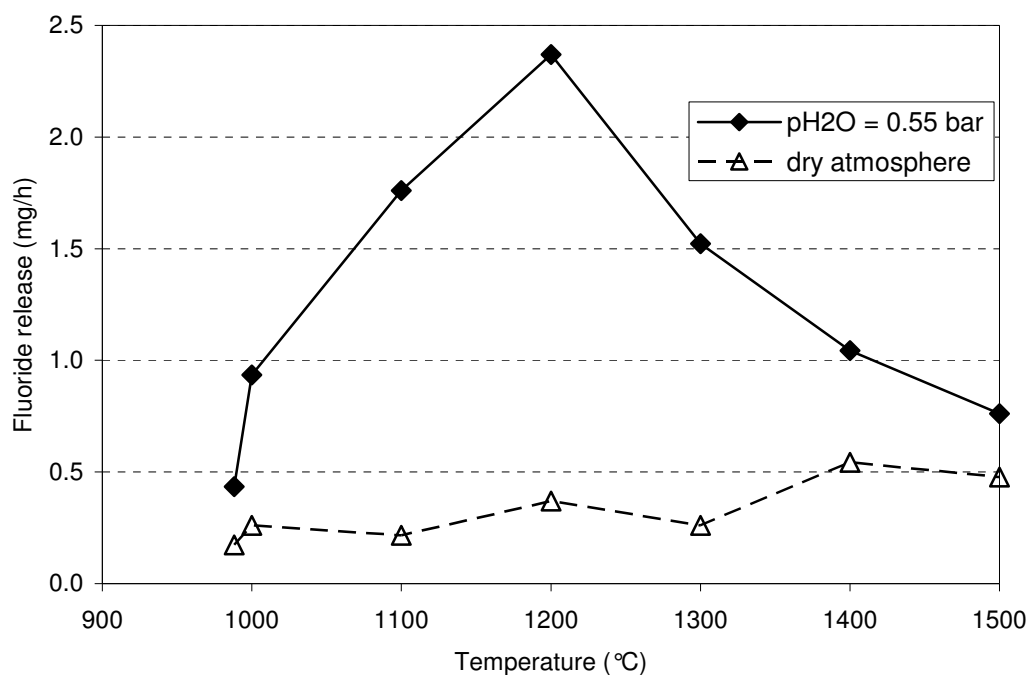


Figure 4.24: Release of fluoride species during melting of a batch for production of flint soda lime container glass as a function of temperature and water vapor concentration in the atmosphere

Besides components like fluoride and chloride, selenium might also evaporate from the melting batch blanket. Selenium is sometimes used as a de-coloring agent.

In paragraph 1.2.6 the evaporation of selenium is discussed and it was shown that selenium mainly evaporates from the melting batch blanket. Figure 4.25 shows the measured selenium evaporation rates from 4 raw material batches for the production of flint container glass, with different types of selenium raw materials. The maximum selenium evaporation rates have been observed around 1000 °C. This means that selenium indeed evaporates from the (melting) raw material batch blanket.

### **b) Foam formation and evaporation**

During the melting of sulfate rich batches or the melting of cullet (recycling glass with organic contaminations), gases like SO<sub>2</sub> might be released and foam formation can be expected [19][20]. 4 different reasons can be given to explain the changes in evaporation rates due to foaming:

- Foam acts as an insulation layer between the hot combustion gases and the glass melt. The temperature of the top surface of the foam layer can be much higher compared to the surface of a blank melt.
- The glass melt composition of the lamellae around the gas bubbles might differ from the bulk glass composition [19].
- The net surface area of a foam layer is larger than the area of a blank melt.
- The transport of volatile glass compounds in the foam layer differs from the transport of glass melt species in the bulk glass melt. Dynamic foam brings fresh bulk glass to the surface of the melt.

Figure 4.26 shows as an example, the boron and potassium evaporation rates from an industrial borosilicate E-glass melt as a function of the initial batch redox (expressed as the carbon / SO<sub>3</sub> ratio) and the measured foam height. The C/SO<sub>3</sub> ratio will influence the formation of foam on top of a glass melt. The figure shows the average foam height and total releases of boron and potassium in the temperature range from 1200 to 1500 °C. It can be seen that the average foam height decreases, as the batch/melt becomes more reducing (C/SO<sub>3</sub> ratio increases). The boron and potassium releases decrease as the C/SO<sub>3</sub> ratio increases and as the foam height decreases. Above a C/SO<sub>3</sub> ratio of 25 %, the boron and potassium evaporation starts to decrease significantly i.e. the situation of a very reduced melt without foam.

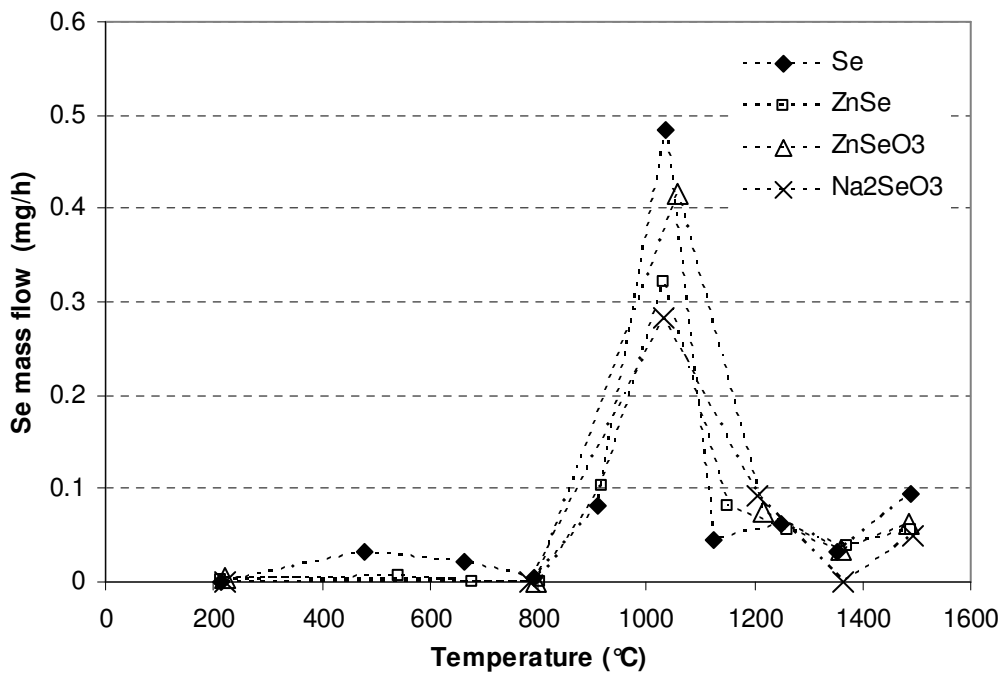


Figure 4.25: Measured selenium evaporation rates from raw material batches for production of flint container glass batches as a function of temperature. The figure shows the results of evaporation tests using 4 different selenium raw materials. The selenium input in the batch was in all cases the same (about 1 mg Se).

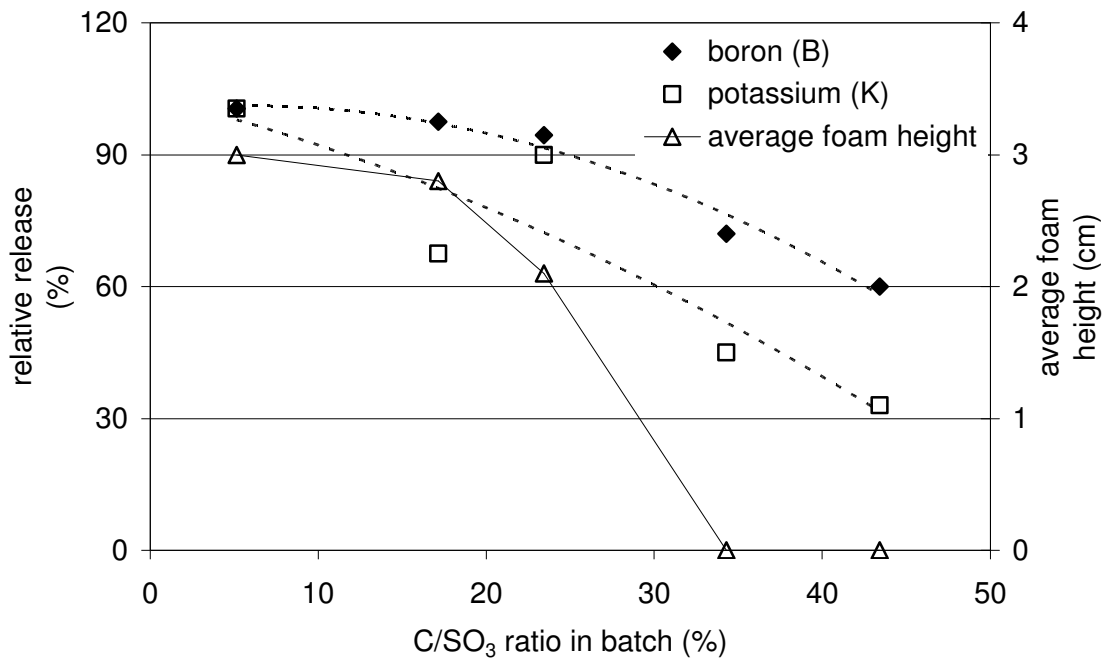


Figure 4.26: Measured foam height and evaporation rates of boron and potassium as function of the C/SO<sub>3</sub> ratio in the initial batch for melting of industrial borosilicate E-glass.



At a  $C/SO_3$  ratio of 43 % the boron release is 41 % lower and the potassium release even 68 % lower compared to a relatively oxidized batch with much more foaming ( $C/SO_3 < 10$  %). The glass melt composition of the lamella between the gas bubbles in the foam layer might deviate from the composition of the bulk melt [19]. Laimböck [20] suggested that the lamellae might contain high concentrations of surface active compounds (e.g.  $B_2O_3$  and  $K_2O$ ). Higher chemical activities of  $B_2O_3$  and  $K_2O$  in these lamellae (possibly in combination with higher surface temperatures) might be the main reason for the higher evaporation rates of boron and potassium from melts covered with foam.

#### 4.9 Concluding remarks chapter 4

The main conclusions of the experimental investigations presented in this chapter are summarized and given per item in this paragraph.

##### 4.9.1 Validation of relations for mass transfer through gas phase boundary layers in transpiration evaporation tests

For a transpiration test set-up, CFD modeling has been applied to predict the mass transport of volatile species from glass melts or model liquids into a carrier gas and to understand the fluid dynamics in the gas phase. Results of the CFD-modeling for water evaporation tests at room temperature have been validated by transpiration experiments. Excellent agreement was found between the model results and water evaporation experiments as the difference between the experimental measured evaporation rates and the CFD modeling results are less than 2 %.

The results of CFD modeling and the results of simple water transpiration evaporation experiments at room temperature are used to obtain relatively simple mass transport relations ( $Sh$  as a function of  $Re$  and  $Sc$ ) for a fixed geometry of the transpiration test set-up. These relations were shown to be applicable for other evaporating liquids and temperatures as well when using the same equipment.

##### 4.9.2 Identification of the most important evaporating species

Sodium hydroxide ( $NaOH$ ), the main evaporating species from soda-(lime)-silicate melts in a humid, oxidized atmosphere, is the result of reactive evaporation between  $Na_2O$  in the melt and water vapor in the atmosphere. The vapor pressure of  $NaOH$  is proportional to  $(p_{H_2O} \cdot a_{Na_2O})^{0.5}$ . In less oxidized atmospheres with oxygen vapor pressures of only about 100

Pa, the release of pure sodium (Na) is 25 to 50 times lower than the NaOH evaporation rates. In multi-component alkali-lime-silicate melts with  $K_2O$ , species such as KOH and K might evaporate in a similar way as sodium species for soda-(lime)-silicate melts.

In alkali-free borosilicate glass melts, boron evaporates under influence of water vapor as meta boric acid ( $HBO_2$ ). The vapor pressure of  $HBO_2$  is proportional to  $(p_{H_2O} \cdot a_{B_2O_3})^{0.5}$ .

#### 4.9.3 Derivation of chemical activities of volatile species at the surface of a glass melt

For binary sodium-silicate melts, ternary soda-lime-silicate melts, multi-component alkali-lime-silicate melts and alkali-free borosilicate glass melts (containing  $SiO_2$ ,  $Al_2O_3$ ,  $CaO$  and  $B_2O_3$ ), transpiration evaporation experiments were used to derive chemical activities of volatile components at the glass melt surface.

The indirectly measured chemical activities at the surface of the melts are compared with the results of the thermodynamic Associated Species Model. The surface composition of the melt was estimated from SEM-EDX measurements. Between the measured and modeled chemical activities a good linear correlation has been obtained for  $Na_2O$  in soda-lime-silicate and sodium-disilicate melts:  $a_{Na_2O(model)} = (0.98 \pm 0.04) \cdot a_{Na_2O(measured)}$ .

For a multi-component float glass melt, the measured activities of  $Na_2O$  are, on average, about 20 % higher than the modeled activities (Associated Species Model). For multi-component alkali-lime-silicate melts with  $K_2O$  concentrations between 5 and 8 mass-%, the measured and modeled activities of  $K_2O$  deviate less than 30 %.

These results can be regarded as fairly accurate, taking into account the experimental errors and the inaccuracy of the thermodynamic model.

For alkali-free borosilicate glass melts the experimental derived activities are used to optimize the Associated Species Model for alkali-free borosilicate melts. To improve the thermodynamic modeling of these kinds of melts, the associated species  $5CaO \cdot B_2O_3(l)$  has been introduced and thermodynamic data (Gibbs energy values) of other stoichiometric calcium-borate species were derived by fitting procedures from laboratory evaporation tests. In this adapted model, immiscibility or non-ideal mixing behavior of associated species, is not taken into account.

Both, the results of thermodynamic modeling as well as measuring results show a strong decrease in chemical activity of  $B_2O_3$  for concentrations below  $\pm 2.5$  mass-% in these borosilicate melts. This might be a result of a sudden change in the molecular structure of the melt, at  $B_2O_3$  concentrations below 2.5 mass-%.

#### **4.9.4 Description of the transport of volatile components in the melt and description of depletion phenomena**

CFD modeling shows that, besides the effect of glass melt convection due to surface tension gradients or bubbles ascending in the melt, convection may take place as a result of non-uniform evaporation rates of volatile glass melt species along the glass melt surfaces. Because of the non-uniform evaporation rates, local concentration and density differences in the melt surface layer are induced. Local convection at the surface areas of the melt promotes the transport of melt from the bulk to the surface and suppresses depletion of minor volatile compounds. In static melts, depletion of volatile glass components at the glass melt surface in progress of time, will result in decreasing evaporation rates and a surface composition that differs from the bulk composition. Thus, evaporation rates of (minor) components in the melt like chlorine, sulfur and fluorine can be influenced by occurrence of free convection of the melt.

$\text{SiO}_2\text{-CaO-Al}_2\text{O}_3\text{-B}_2\text{O}_3$  glass melts, with an average  $\text{B}_2\text{O}_3$  concentration less than 2.5 mass-%, show significant  $\text{B}_2\text{O}_3$  depletion at the surface of the melt compared to the bulk. For melts with  $\text{B}_2\text{O}_3$  concentrations higher than 2.5 mass-%, boron depletion takes place all over the glass melt volume as time proceeds and the composition of the melt appeared to be nearly uniform at all times. Possibly, borosilicate glass melts should be considered as a mixture of a silica rich melt phase and one or more borate melt phases, such as a calcium-borate phase. For melts with  $\text{B}_2\text{O}_3$  concentrations above 2.5 mass-%, the calcium-borate melt phase is probably present as a very fine dispersion of small droplets in a continuous silicate phase. In melts with low  $\text{B}_2\text{O}_3$  concentrations, more silica rich melt phases will be formed, which encapsulate the calcium-borate melt phases or which are preferably present on top of the melt. In this specific situation the transport of boron ions to the surface of the melt is limited or hindered by the silicate phase with very low  $\text{B}_2\text{O}_3$  solubility, and boron surface depletion takes place.

#### **4.9.5 Influence of minor components in the melt on the evaporation of sodium and potassium from alkali-lime-silicate melts.**

For alkali-lime-silicate melts, chlorides and sulfates promote the release of alkali species, by formation of  $\text{Na}_2\text{SO}_4$ ,  $\text{NaCl}$ ,  $\text{KCl}$  or possibly  $\text{K}_2\text{SO}_4$  vapors. In a static melt, the evaporation rates of these species are limited by the relatively slow diffusion transport from the bulk to the surface of the melt. Depletion of sulfur and chloride species at the glass melt

surface becomes more significant as the evaporation process proceeds. However, temperature gradients, local differences in surface tension and bubbles in the melt can strongly affect the (local) convection in the melt. Depletion at the surface will (partly) be eliminated and the evaporation rates of these minor species increase. Possible surface active components in a glass melt, such as  $\text{Na}_2\text{SO}_4$ ,  $\text{K}_2\text{SO}_4$ ,  $\text{NaCl}$ , and  $\text{KCl}$  might cause convective Marangoni flows. The formation of  $\text{SO}_2$  bubbles and the formation of a dynamic, continuously refreshed foam layer at the surface of the melt may also promote the evaporation rates of volatile glass components.

From the investigations, it appeared that the main evaporation species from soda-lime-silicate float glass melts and alkali-lime-silicate tableware melts are:  $\text{NaOH}$ ,  $\text{KOH}$ ,  $\text{Na}_2\text{SO}_4$ ,  $\text{KCl}$  and at reducing conditions  $\text{Na}$  and  $\text{K}$ .

#### **4.9.6 Concluding remark**

A general applicable evaporation model for a large range of glass compositions has been developed to predict the evaporation rates of the main volatile glass components. The model has been validated by laboratory evaporation experiments. The measuring results and modeling results agree well with each other.

## Appendix I Glass sample preparation for transpiration experiments

In this appendix it is shown that the homogeneity of the glass samples used for transpiration experiments depends among others on sample preparation procedure, the cullet size used for melting the sample prior to the transpiration test and the chemical composition of the used raw material mixtures. The impact of sulfates in the batch as well as the applied cullet sizes on homogeneity is discussed.

### *Sulfate free batches*

The homogeneity of the freshly prepared glass samples, molten in platinum-rhodium crucibles, is investigated by vertical concentration gradient measurements, using SEM-EDX micro-analysis.

In case of heating of a float glass raw material batch without sulfate during 1 hour at 1450 °C (in air), the SiO<sub>2</sub> concentration in the obtained glass sample dropped from 77 mass-% at the surface to 69 mass-% at the bottom, the CaO concentration increased from 5.8 mass-% at the surface to 9.1 mass-% at the bottom. The measured vertical Na<sub>2</sub>O and CaO concentration profiles for this sample are shown in Figure 4.17. The calculated density (at 20 °C) calculated from the measured composition, at the glass surface is about 80 kg/m<sup>3</sup> lower as the density at the bottom of the glass. Even after 5 hours of heating at 1450 °C in air, the vertical concentration profiles of Na<sub>2</sub>O, CaO and SiO<sub>2</sub> in the glass have hardly been changed.

Because of the concentration gradients, a net diffusive transport of Na<sub>2</sub>O and CaO from the interior of the melt to the surface of the melt is expected and finally the concentration gradients in the glass sample should disappear if this would be the only transport mechanism (e.g. no evaporation from the melt). Based on the 2<sup>nd</sup> law of Fick (equation 2.3), the boundary conditions (2.4d) and (2.4e) and  $D_{\text{Na}_2\text{O}} = 3 \cdot 10^{-11} \text{ m}^2/\text{s}$  (interdiffusion coefficient), it is expected that the Na<sub>2</sub>O surface concentration would increase about 0.5 mass-% after a period of 5 hours. However, based on the experimental results, the concentration profile does not seem to change in time anymore (i.e. horizontal stratification has been observed). Possible explanations for these stable stratification layers in the melt are:

- Very low diffusion coefficients in the melt ( $D_{\text{Na}_2\text{O}} \ll 3 \cdot 10^{-11} \text{ m}^2/\text{s}$ ),
- Micro phase segregation (with the more dense phase sinking to the bottom). In that case the melt could not be considered as one homogeneous melt, but consisting of at least 2 different (segregated) glass melt phases.

- The different phases that are formed during the melting of a not completely homogeneous batch do not mix fast enough and the less dense phases are concentrated at the top levels of the sample,

When sulfur-free, coarse cullet (5 – 10 mm) is re-melted for a period of 66 hours at 1450 °C (without evaporation) the melt is still not homogeneous and concentration gradients of CaO, Na<sub>2</sub>O and SiO<sub>2</sub> are still present. The impact of fine cullet on the homogeneity of the samples is discussed later in this appendix.

Using well-stirred homogeneous soda-lime-silicate glass samples, Schaeffer and Sanders [21] measured the concentration profiles of Na<sub>2</sub>O, CaO and SiO<sub>2</sub> as function of time during evaporation experiments. The vertical concentration profiles were measured in soda-lime-silicate glass samples (SiO<sub>2</sub> = 74 mass-%, Na<sub>2</sub>O = 16 mass-%, CaO = 10 mass-%) after transpiration evaporation tests (T=1335 °C and p<sub>H<sub>2</sub>O</sub> = 0.5 bar) of respectively 2, 13 and 25.5 hours. After these periods, the CaO surface concentration dropped from 10 mass-% to respectively 9.5 mass-%, 8 mass-% and 7 mass-%, the Na<sub>2</sub>O surface concentrations decreased from 16 mass-% to respectively 14.6 mass-%, 11.5 mass-% and 11.0 mass-%. The evaporation of NaOH explains (partly) the Na<sub>2</sub>O surface depletion, but the measured CaO concentration gradient could not be ascribed to this phenomenon. In their paper Schaeffer and Sanders [21] argue that the transport of CaO from the surface to the interior of the melt might be a result of uphill-diffusion in combination with an ion-exchange between Na and Ca ions. However, the observed CaO profiles might also be a result of other phenomena as discussed before.

Some simple melting tests were performed to study homogeneity of soda-lime-silicate melts without sulfur. Two, SiO<sub>2</sub>-CaO-Na<sub>2</sub>O-Al<sub>2</sub>O<sub>3</sub> glass samples were prepared from pure raw materials during a period of 1 hour at 1400 °C under air atmosphere. Afterwards the glass samples were quenched in water and broken into cullet. The first sample was grinded into pieces of 5 – 10 mm (coarse cullet) and the second sample was grinded into pieces of 1 – 2 mm (fine cullet). Both, the coarse cullet sample and fine cullet sample were well-mixed and re-melted at 1400 °C during a period of 30 minutes. After cooling the samples in air, SEM-EDX measurements were applied to measure the vertical concentration gradients in the samples.

The glass sample prepared from fine cullet seems to be nearly homogeneous in composition but the sample prepared from coarse cullet clearly showed vertical concentration gradients.

Compared to the CaO and Na<sub>2</sub>O concentrations at the bottom of the coarse cullet sample, the CaO and Na<sub>2</sub>O concentrations at the surface were respectively 1.6 mass-% and 0.5 mass-% lower. The SiO<sub>2</sub> and Al<sub>2</sub>O<sub>3</sub> concentrations at the surface were respectively about 1.5 mass-% and 0.5 mass-% higher.

The observed concentration gradients might be a result of the different melting phases that are formed during the heating and melting of the batch. If coarse cullet is re-melted the glass samples remain inhomogeneous, only with intensive mixing (e.g. by applying well-mixed fine cullet) homogeneous melts without concentration gradients can be prepared.

### ***Glass forming batches with sulfate***

To illustrate the impact of sulfates in the batch on the homogeneity of the obtained melt, a float glass batch with sulfates and a float glass batch without sulfates have been melted during 1 hour at 1450 °C in air atmosphere. Afterwards, the surface concentrations were measured with SEM-EDX and compared with the theoretically expected average glass composition (see Table 4.5).

*Table 4.5: Chemical composition of multi-component soda-lime silicate glass samples prepared from raw materials with and without sulfates after heating during 1 hour at 1450 °C in air atmosphere. The surface concentrations have been measured with SEM-EDX and the expected concentrations (assuming uniform compositions) have been calculated from the batch composition.*

	SEM-EDX No sulfate in batch		SEM-EDX 0.5 mass-% SO <sub>3</sub> in batch		XPS analysis
	Surface Conc. (mass-%)	Expected Conc. (mass-%)	Surface Conc. (mass-%)	Expected Conc. (mass-%)	Ratio of average concentrations measured in surface layer of both glasses (-) <sup>1)</sup>
Na <sub>2</sub> O	12.1	14.0	13.8	13.9	1.14
SiO <sub>2</sub>	77.4	71.4	72.2	71.1	0.93
CaO	5.9	8.5	7.9	8.5	1.33
MgO	3.3	5.0	4.7	5.0	1.39

<sup>1)</sup> ratio =  $C_j^{\text{surface}}(\text{glass with sulfate}) / C_j^{\text{surface}}(\text{glass without sulfate})$

The surface glass, prepared from a batch without sulfate, is very silica rich and characterized by low Na<sub>2</sub>O, CaO and MgO concentrations. The surface concentrations of the glass prepared from the batch with sulfates are much closer to the average concentrations. In the same glass samples, a surface layer of 228 nm has been analyzed with XPS. The average Na<sub>2</sub>O concentration in the surface layer of the melt with SO<sub>3</sub> was about 1.14 times higher than the average Na<sub>2</sub>O concentration at the surface of a melt, without SO<sub>3</sub> in the glass. The melts have been hardly exposed to evaporation and the lower Na<sub>2</sub>O concentration in the surface layer is probably not caused by evaporation in this case. The average SiO<sub>2</sub> content in this surface layer was 1.07 times higher in the glass without sulfate compared to sulfate containing glass (see Table 4.5).

The formed SO<sub>2</sub> bubbles during the fining process (in the melt prepared from batch with sulfates) probably contribute to a better mixing of the melt phases and therefore may result in a more homogeneous glass melt. Indeed fining bubbles in the melt were observed by video recordings during the melting of this batch [22].

As discussed in paragraph 2.2.1, Marangoni flows in the silicate melt might be a result of the formation and decay of a sulfate gall at the surface of these melts during melting of raw materials. These convective movements might also improve the homogeneity of the final glass samples.

The impact of Marangoni driven convective surface flows on the homogeneity of glass samples has been investigated by preparing float glass melts with and without sulfate (SO<sub>3</sub> input is about 0.3 mass-%) at 1400 °C. This temperature is below the fining on-set temperature and hardly any occurrence of fining bubbles are expected.

First the raw materials were well-mixed and melted at 1400 °C during 1 hour. After quenching the glass sample, the sample was broken in pieces of about 10 mm. These cullet pieces were mixed again and re-melted at 1400 °C during a half hour. Afterwards the glass samples have been cooled down in air. SEM-EDX has been applied to measure the vertical concentration profiles of the different glass components. Figure 4.27 shows as an example the measured CaO profiles and Table 4.6 shows the measured concentration differences between the surface and bottom of the glass. In the samples with SO<sub>3</sub> the measured concentration differences are a little bit smaller than the SO<sub>3</sub> free samples and probably Marangoni flows contribute to a better mixing. However, bubble evolution (between 1400 and 1450 °C) leads to even much better homogeneity.



Table 4.6: Measured concentration differences between the surface and bottom of float glass melts with and without sulfur. The glass samples were prepared from coarse cullet (10 mm) at 1400 °C.

	Glass without SO <sub>3</sub>	Glass with SO <sub>3</sub>
CaO concentration difference between surface and bottom of glass sample (mass-%)	1.5	0.8
Na <sub>2</sub> O concentration difference between surface and bottom of glass sample (mass-%)	0.5	0.1
SiO <sub>2</sub> concentration difference between surface and bottom of glass sample (mass-%)	1.5	0.7

The impact of sulfates in the glass on Marangoni convection has further been investigated with a second simple set of melting experiments. Float glass samples, with sulfate and without sulfate (composition is given in Table 4.2), have been melted in a platinum crucible at 1400 °C during 1 hour and annealed afterwards.

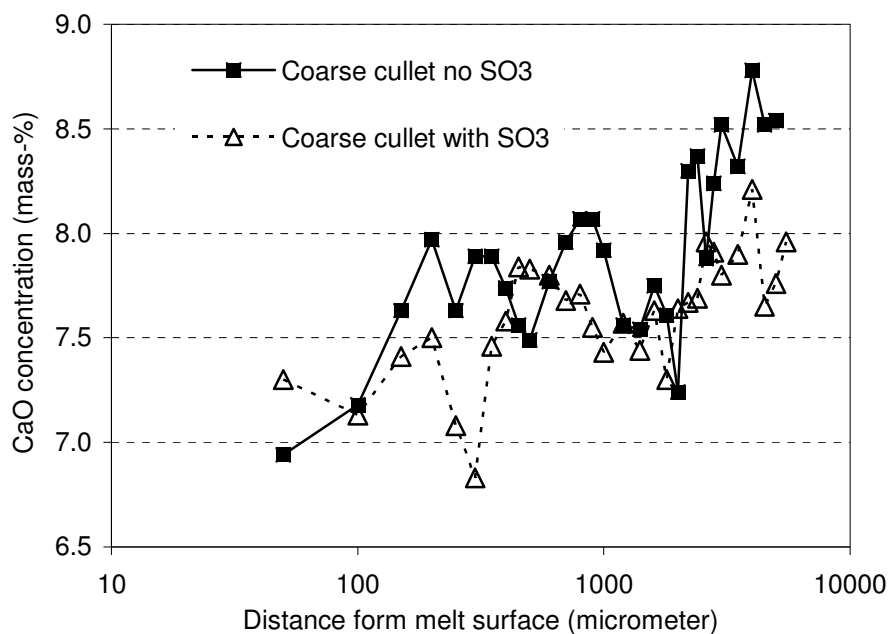


Figure 4.27: Vertical CaO concentration profiles measured by SEM-EDX in glass samples prepared from coarse cullet (10 mm) with and without sulfur. The melting temperature was 1400 °C

At the surfaces of these samples, small pieces (2x1 mm) of blue-colored, cobalt-doped, sodium-silicate glass has been placed in the centre, at the top of the glass sample. Afterwards the samples were heated again to a temperature of 1400 °C under nearly dry ambient air (to avoid NaOH evaporation). After a period of about 6 hours, the glass samples were annealed and the distribution of the blue glass over the glass surfaces was compared. In the glass melt without sulfur, one single blue dark spot is visible while for the glass with sulfur addition the bluish color is widely distributed over the surface of the melt. Since the temperature is below the fining onset temperature, hardly any fining bubbles and convection are observed [22]. The SO<sub>3</sub> contents in the glass melt with sulfate is below the concentration level at which sodium sulfate gall segregates from the melt. The distribution of the Co-doped glass is probably a result of Marangoni flows. These Marangoni flows may occur if the sulfate concentrations at the surface of the melt locally vary, due to non-uniform evaporation of Na<sub>2</sub>SO<sub>4</sub> or non-uniform decomposition at the surface of the melt.

## Appendix II Impact of sulfur and chlorides on sodium and potassium evaporation rates

As will be shown in the next paragraphs, the presence of sulfur and chlorides in alkali-silicate melts appear to influence the evaporation rates of sodium- and potassium-species. The measured evaporation rates of sodium species and chemical activities of  $\text{Na}_2\text{O}$  in soda-lime-silicate glass melts without sulfates and without chlorides have been presented and discussed in the paragraphs 4.2 and 4.3.

From alkali(-lime)-silicate melts without chloride and sulfur, exposed to a carrier gas with controlled oxygen ( $p_{\text{O}_2} \approx 0.1$  bar) and water vapor pressures ( $0.2 < p_{\text{H}_2\text{O}} < 0.3$  bar), the elements sodium and potassium evaporate mainly in the form of  $\text{NaOH}$  and  $\text{KOH}$ . The total evaporation rates of sodium and potassium appear to be proportional to  $p_{\text{H}_2\text{O}}^{1/2}$  in such cases. Thus, it is likely that Na and K evaporate mainly as  $\text{NaOH}$  respectively  $\text{KOH}$ , according reactions 1.10 and 1.18.

In appendix II.1, the impact of sodium sulfates in the raw materials batch on evaporation of sodium species in industrial float glass furnaces will be shown and discussed. In appendix II.2, the results of laboratory transpiration experiments for soda-lime-silicate glass melts, with and without sulfur are compared. Finally, the impact of chlorides on the evaporation of volatile glass species, like sodium and potassium, will be described in appendix II.3 for industrial soda-lime-silicate compositions and (commercial) multi-component tableware glass melts containing sulfur, chlorine and antimony species.

### II.1 Industrial measurements

Similar as Gebhardt's results [23], industrial investigations in this study show a linear relation between the emissions of particulate (dust) and the total amount of  $\text{SO}_x$  released from the melt plus batch (excluding the  $\text{SO}_2$  released from sulfur containing oil combustion). The results of both industrial tests (Gebhardt's results [23] and own measurements) are shown in Figure 4.28. The emitted dust contains 70 to 90 mass-%  $\text{Na}_2\text{SO}_4$ , which is mainly a reaction product of evaporated  $\text{NaOH}$  (g) and  $\text{SO}_x$ (g) formed during cooling of the flue gases [24]. It might also be partly a result of direct evaporation of  $\text{Na}_2\text{SO}_4$  from batch or glass melt. During the tests of Gebhardt, the amount of  $\text{Na}_2\text{SO}_4$  in the batch has been changed between 0.5 mass-% and 1.5 mass-%.

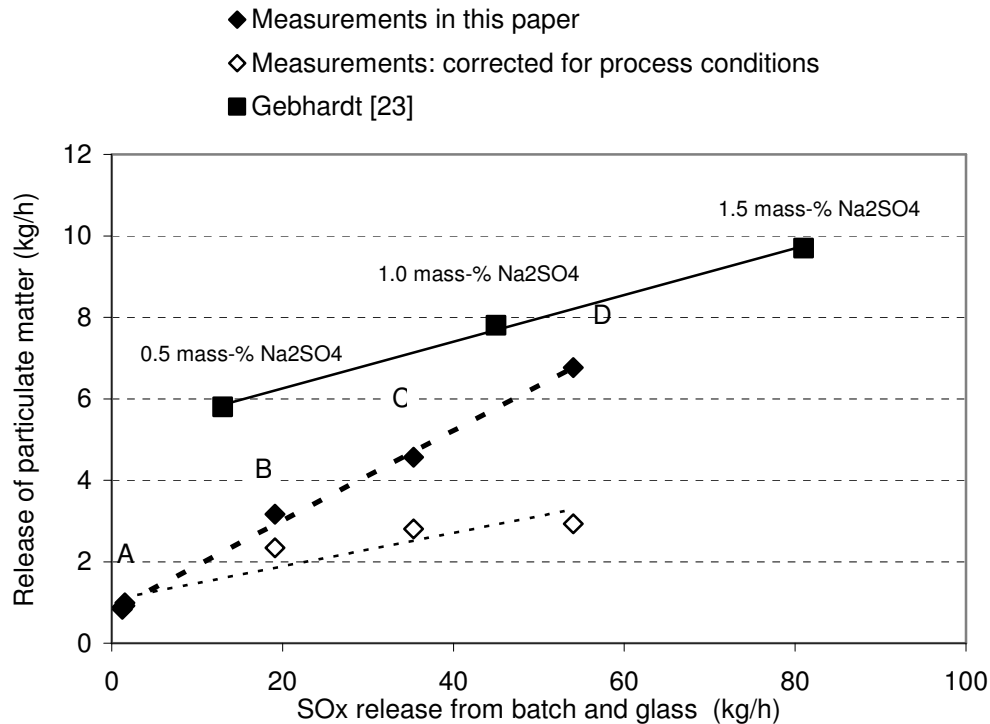


Figure 4.28: Measured particulate emissions from industrial float glass furnaces compared to the measured  $\text{SO}_2$  release from melt/batch. Gebhardt [23] varied the amount of  $\text{Na}_2\text{SO}_4$  in the batch. Here in our investigations, the cullet fraction, the type of fuel and the pull rate have been varied. The 4 different situations, indicated by the symbols A – D, and are described in paragraph 4.7.1.

The impact of the different process conditions (temperature, gas velocities, type of fuel) on the dust and  $\text{SO}_x$  emissions have been taken into account by making a normalization for temperature, water vapor pressure and gas velocities (see paragraph 4.7.1). The measured emissions of particulate matter for the situations B, C and D were ‘normalized’ to process conditions of situation A.

During our industrial tests (not normal production conditions), 3 process parameters have been changed:

1. The amount of cullet in the glass forming batch has been changed between 28 % and 100 %;
2. The pull rate has been reduced from 450 to 278 metric tons/day;
3. The type of fuel has been changed (natural gas or a mixture of natural gas and fuel-oil).

Because of these process variations, the over the length of the furnace averaged crown temperatures range from 1444 °C to 1505 °C. The relation between the emissions of particulates (dust) and the total amount of released  $\text{SO}_x$  from the batch plus melt, can only be obtained after a ‘normalization’ for process conditions like temperature, gas flows and gas composition. Equation 4.2 has been applied to ‘normalize’ for the different process

conditions. The sodium evaporation rate is assumed to be proportional to  $p_{H_2O}^{1/2}$  and  $v^{0.8}$  [25] and the temperature dependency of the sodium evaporation rate has been obtained from Figure 4.29. The semi-empirical relation 4.2 for float glass, can be applied to estimate the NaOH evaporation rate ( $Q_{NaOH}$ ) as function of water vapor pressure ( $p_{H_2O}$ ) in the atmosphere, the gas velocity ( $v$ ) just above the surface of the melt and average surface temperature ( $T$ ) of the melt.

$$Q_{NaOH} = C_5 \cdot \sqrt{p_{H_2O}} \cdot v^{0.8} \cdot e^{-23500/T} \quad (4.2)$$

For each situation, the water vapor pressure in the atmosphere ( $p_{H_2O}$ ), the average gas velocity ( $v$ ) and average temperature ( $T$ ) have been determined or estimated and the total dust release from the industrial furnace is measured. It is assumed that the dust is mainly a consequence of NaOH evaporation and a reaction with  $SO_2$  and  $O_2$  during cooling of the flue gases from 1050 °C to 700 °C [24]. Other volatile sodium species are not taken into account.

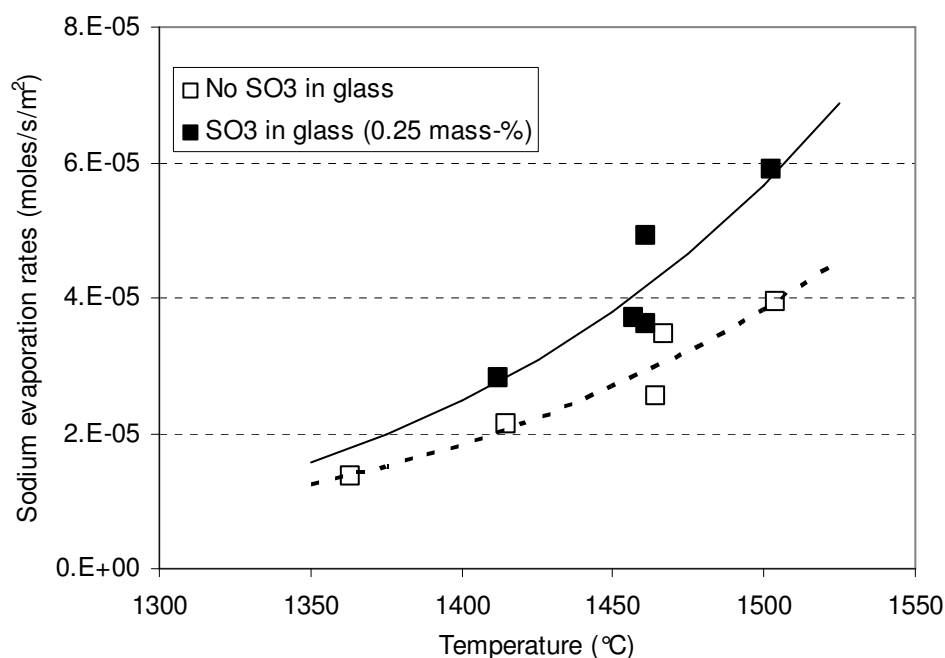


Figure 4.29: Results of laboratory transpiration experiments with float glass compositions shown in Table 4.2. The water vapor pressure was about 0.33 bar. The coarse cullet (5 – 10 mm) used for these evaporation tests has first been prepared from pure raw materials that are melted above the fining temperature. During the evaporation tests no fining (gas bubble evolution) has been observed.

During this industrial test 4 different situations can be distinguished:

- A.  $T(\text{crown})_{\text{avg}} = 1444 \text{ }^\circ\text{C}$ , amount of glass molten from cullet: 100 %, pull rate = 283 ton/day, fuel = natural gas
- B.  $T(\text{crown})_{\text{avg}} = 1462 \text{ }^\circ\text{C}$ , amount of glass molten from cullet: 39 %, pull rate = 297 ton/day, fuel = natural gas
- C.  $T(\text{crown})_{\text{avg}} = 1470 \text{ }^\circ\text{C}$ , amount of glass molten from cullet: 36 %, pull rate = 390 ton/day, fuel = natural gas + oil
- D.  $T(\text{crown})_{\text{avg}} = 1505 \text{ }^\circ\text{C}$ , amount of glass molten from cullet : 28 %, pull rate = 450 ton/day, fuel = natural gas + oil

The measured dust emissions are normalized to a situation comparable with the process conditions during situation A. These normalized dust emissions now merely depend on batch composition. As shown in Figure 4.28, there is still a difference when comparing the particulate emissions between the different cases after normalization. The differences between the normalized emissions of particulate matter between the different situations, appear to be related to the  $\text{SO}_2$  release differences.

Gebhardt's results as well as our own industrial measuring results show that for each extra kilogram released gaseous  $\text{SO}_2$  (from the batch and glass melt), the release of particulate matter increases by about 40 to 60 gram.

Laboratory transpiration evaporation tests, described in paragraph 3.2, have been used to investigate and to obtain an understanding or explanation for both of these industrial observations.

## II.2 Impact of the presence of sulfate in glass melt on the evaporation of sodium species: laboratory studies

Contrary to the results of the industrial measurements presented in the previous paragraph, Conradt and Scholze [26] found that the total sodium evaporation rates from sulfur containing soda-lime-silicate melts only slightly depend on the sulfur concentration in the glass melt (especially for  $0.07 \leq C_{\text{SO}_3} \leq 0.34 \text{ mass-\%}$ ). In all cases, the melts with sulfate show higher total sodium species evaporation rates than the melts without sulfate. At  $1400 \text{ }^\circ\text{C}$  and  $p_{\text{H}_2\text{O}} = 0.2 \text{ bar}$  the sodium evaporation rates from glass melts with  $\text{SO}_3$  are about 50 % higher than the sodium losses from glass melts without  $\text{SO}_3$ . For melts with sulfate, this probably means that the  $\text{Na}_2\text{O}$ - and  $\text{Na}_2\text{SO}_4$ -activities at the surface of the melt are about the

same in all these cases. The activities of these components seem to be nearly independent of the sulfur content. Possible explanations for the observed differences between the results of the industrial tests and the results of the laboratory evaporation tests of Conradt and Scholze are:

1. Conradt and Scholze studied only evaporation from blank melts without batch or foam. In industrial furnaces, glass components evaporate from the blank melt, foam layers and the melting raw materials.
2. Extra evaporation of sodium species as a result of a formed sodium sulfate gall ( $a_{\text{Na}_2\text{SO}_4} = 1$ ) at the surface of the melting batch in industrial glass furnaces. Directly above a sodium sulfate gall layer relatively high  $p_{\text{Na}_2\text{SO}_4}^*$  values and high  $\text{Na}_2\text{SO}_4$  evaporation rates are expected.
3. Due to the decomposition of the  $\text{Na}_2\text{SO}_4$  gall at the glass melt surface, locally a glass phase with increased  $\text{Na}_2\text{O}$  contents and  $\text{Na}_2\text{O}$  activity might be formed (see paragraph 2.2.1). From this sulfur and sodium enriched surface melt phase higher sodium evaporation rates can be expected. No  $\text{Na}_2\text{SO}_4$  gall is present during Conradt's tests and our laboratory evaporation measurements.
4. In the laboratory set-up a nearly static melt is expected and the surface layer might be seriously depleted of minor volatile components, such as  $\text{SO}_3$ .

For pure liquid  $\text{Na}_2\text{SO}_4$ , Conradt and Scholze found a nearly linear relation between the measured evaporation rate and  $p_{\text{H}_2\text{O}}^{0.5}$ . Sodium sulfate is released as pure gaseous  $\text{Na}_2\text{SO}_4$  (reaction 1.14) and reacts with water vapor to gaseous  $\text{NaOH}$  (reaction 1.16). In their transpiration experiments with sulfate containing soda-lime silicate melts, the impact of the water vapor pressure in the carrier gas on the evaporation of sodium species is fully attributed to the chemical reaction between  $\text{Na}_2\text{O}$  in the melt and  $\text{H}_2\text{O}$  in the atmosphere to form gaseous  $\text{NaOH}$  (reaction 1.10). The contribution of reaction 1.16 between  $\text{Na}_2\text{SO}_4(\text{l})$  and  $\text{H}_2\text{O}(\text{g})$  is assumed to be negligible. After all, a higher  $\text{NaOH}$  equilibrium vapor pressure would also mean a higher chemical activity of  $\text{Na}_2\text{O}$  at the surface of the melt. SEM-EDX measurements did not show higher  $\text{Na}_2\text{O}$  concentrations at the surface of the soda-lime-silicate glasses, compared to the bulk glass composition.

Sanders et al. [27] investigated the role of water vapor and sulfur compounds in sodium vaporization. They used a so-called Stirrable Transpiration Apparatus (STA) to avoid surface depletion of volatile compounds in multi-component glass melts and to improve the homogeneity of the investigated liquids or melts. In this set-up, the liquid melt is bubbled

with the carrier gas during the evaporation experiment. Contrary to the experimental results of Conrardt and Scholze, their evaporation experiments with pure liquid  $\text{Na}_2\text{SO}_4$  show a nearly independent relation between the sodium evaporation rates and the water vapor pressure in the carrier gas. However, in case small amounts of  $\text{NaOH}$  ( $< 1$  mass-%) are added to the pure liquid  $\text{Na}_2\text{SO}_4$ , the sodium vapor pressure increases with increasing water vapor pressure. Sanders et al. concluded that the evaporation of  $\text{Na}_2\text{SO}_4$  species might be limited by kinetic limitations. They suggest that  $\text{NaOH}$  acts as a catalyst. The results are questionable, since Conrardt et al. found a linear relation between the sodium evaporation rates and  $p_{\text{H}_2\text{O}}^{0.5}$  for pure  $\text{Na}_2\text{SO}_4$ .

Since Conrardt and Scholze measured the sodium evaporation rates from glass melts with and without sulfur in the glass, the equilibrium vapor pressure and chemical activities of  $\text{Na}_2\text{SO}_4$  ( $a_{\text{Na}_2\text{SO}_4}$ ) in the surface layer of the melt can be derived. For both types of melts the total sodium evaporation rates are measured under identical process conditions, i.e. the same temperatures, water vapor pressures and gas flow rates. The measured differences in total sodium evaporation rates between the two different melts, are attributed to the evaporation of  $\text{Na}_2\text{SO}_4$ . In a humid atmosphere  $\text{NaOH}$  and  $\text{Na}_2\text{SO}_4$  are assumed to be the main evaporating sodium species.

The equations 2.10 and 2.12 are used to calculate  $p_{\text{Na}_2\text{SO}_4}^*$ . The required Sherwood number or mass transfer coefficient for the gas phase has been derived from the measured  $\text{NaOH}$  evaporation rates and  $p_{\text{NaOH}}^*$  has been calculated by thermodynamic modeling (ASM-AS) for the glass composition used in their investigation. The Sherwood number (Sh) is assumed to be constant during all experiments and a difference in surface depletion of  $\text{Na}_2\text{O}$  for melts with/without sulfur has been disregarded.

The derived values of  $a_{\text{Na}_2\text{SO}_4}$  (for  $0.07$  mass-%  $< C_{\text{SO}_3} < 0.97$  mass-% independently of the sulfate content in the melt) increase from about  $0.14 \pm 0.04$  to  $0.32 \pm 0.07$  with increasing water vapor pressure from  $0.0$  to  $0.2$  bar. It seems that water vapor enhances the evaporation of  $\text{Na}_2\text{SO}_4$  or even the decomposition of  $\text{Na}_2\text{SO}_4$ .

The contents of dissolved sulfates in the glass melt after fining, generally decreases as the water content in the glass melt increases [28]. From the transpiration experiments in this study and SEM-EDX measurements afterwards, it was found that the  $\text{Na}_2\text{O}$  surface concentrations in glass melts without sulfur is maximum about  $0.7$  mass-% lower than the  $\text{Na}_2\text{O}$  surface concentration in a glass melts with sulfur. These small differences would result



in differences of only 2 till 3 % in the NaOH evaporation rates and cannot explain the observed differences of more than 50 % in total sodium evaporation rates.

Another explanation might be the formation of a (thin) foam layer at the surface of the melt. After a sudden increase of the water vapor pressure in the atmosphere, the sulfate in the melt is probably partly released as SO<sub>2</sub> bubbles. The SO<sub>2</sub> bubbles might cause (some) foam production at the surface of the melt. Compared to the blank melt, the surface area of this foam layer is larger and may cause higher evaporation rates.

### II.3 Transpiration experiments for soda-lime-silica type float glass melts

The impact of sulfur in the glass (mainly present as sulfate in oxidized glass melts [19]) on the evaporation of sodium species from the surface of alkali silicate melts is not fully understood yet and has been investigated with our transpiration set-up C for the two float glass melt compositions shown in Table 4.2. In this paragraph, the results of transpiration experiments for these soda-lime-silicate melts are discussed. Evaporation experiments for float glass melts with sulfur or without sulfur, exposed to dry as well as a humid atmosphere are performed. The evaporation rates of sodium species and sulfur species have been measured.

#### *Evaporation in dry atmosphere, effect of SO<sub>3</sub> in glass on sodium evaporation*

Experiments in a dry, oxidized atmosphere have been performed to avoid the evaporation of NaOH and pure Na (evaporating only at very reduced furnace atmosphere conditions). The objective of these experiments is the demonstration of the evaporation of Na<sub>2</sub>SO<sub>4</sub> (and even K<sub>2</sub>SO<sub>4</sub>) from these molten float glasses.

Transpiration evaporation tests have been performed for a float glass composition containing sulfur (in this oxidized molten glass the sulfur is mainly in the sulfate state), exposed to a dry atmosphere (O<sub>2</sub>/N<sub>2</sub> gas mixture, pO<sub>2</sub> = 0.11 bar) at T = 1460 °C during a period of 5 hours. Because of the oxygen in the atmosphere, the evaporation rates of pure sodium atoms and pure potassium atoms are negligible (see paragraphs 1.2 and 4.3). For 0 < t < 2 hours, the ratio between the measured total molar evaporation rates of the sodium species plus potassium species and sulfur (S): (Q<sub>Na</sub> + Q<sub>K</sub>) / Q<sub>S</sub> appears to be smaller than 2. In case of only alkali sulfate evaporation the ratio should be 2. Probably, this is a result of the

dissociation of  $\text{Na}_2\text{SO}_4$  and  $\text{K}_2\text{SO}_4$ . The reaction products  $\text{Na}_2\text{O(l)}$  and  $\text{K}_2\text{O(l)}$  dissolve in the melt and gaseous  $\text{SO}_2$  is released.

After this period of 2 hours, the molar ratio of the evaporated alkali compounds and evaporated sulfur:  $(Q_{\text{Na}} + Q_{\text{K}}) / Q_{\text{S}}$  becomes  $\pm 2$ . Thus,  $\text{Na}_2\text{SO}_4$  and  $\text{K}_2\text{SO}_4$  are probably the main volatile species at that time and the dissociation reaction of sulfate stopped. From the measured total sodium evaporation rate after 2 hours and the assumption that all sodium evaporates as  $\text{Na}_2\text{SO}_4$  in a dry atmosphere, the chemical activity of  $\text{Na}_2\text{SO}_4$  ( $a_{\text{Na}_2\text{SO}_4}$ ) in the surface layer of the melt has been calculated on a value of 0.06 for  $T = 1460$  °C and an initial  $\text{SO}_3$  concentration of 0.25 mass-%. At 1400 °C, Conradt and Scholze found under dry conditions for soda-lime-silicate melts, with initial  $\text{SO}_3$  concentration between 0.07 mass-% and 0.97 mass-%,  $a_{\text{Na}_2\text{SO}_4} = 0.14 \pm 0.04$ . These higher activities are probably a result of the different experimental conditions and different glass compositions used in their experiments.

#### ***Evaporation in humid atmosphere, effect of $\text{SO}_3$ in glass on sodium evaporation***

Additional to the previously described experiments, carried out under dry conditions, transpiration experiments with float glass melts have been performed in an oxidized and humidified atmosphere ( $p_{\text{H}_2\text{O}} \approx 0.33$  bar). The expected major volatile sodium species are now  $\text{NaOH}$  and  $\text{Na}_2\text{SO}_4$ . **Figure 4.29** shows the measured total sodium evaporation rates from float glass melts with initially 0.25 mass-%  $\text{SO}_3$  and without sulfur in the glass. Compared to glass melts without sulfur, the total sodium evaporation rates from the same glass melt compositions, but with sulfur (probably mainly present as sulfate) are about 20 to 50 % higher in the temperature range between 1400 and 1500 °C.  $\text{SO}_2$  fining bubbles in the melt are only expected if the water vapor pressure increases [28] or if the temperature of the sample exceeds the maximum temperature, achieved during sample preparation. All samples used for transpiration experiments are melted at a temperature of 1450 °C in air. Prior to the evaporation measurements, the samples are preheated in the transpiration set-up at the desired temperature for the evaporation test, during a period of 1 to 2 hours. During this period the tube is flushed with a dry  $\text{N}_2/\text{O}_2$  gas mixture. Therefore, it is expected that fining bubbles will be released only, if water vapor pressure increases.

The results of the evaporation tests are used to demonstrate that:

- a) sodium depletion at the surface of the melt and
- b) extra  $\text{NaOH}$  evaporation as a result of the reaction between  $\text{Na}_2\text{SO}_4$  in the melt and water vapor,

do not explain the increased sodium evaporation rates from melts containing  $\text{SO}_3$ .

***a) Sodium depletion at surface of the melt***

From the differences between the sodium evaporation rates of melts with sulfur and melts without sulfur, the chemical activity of  $\text{Na}_2\text{SO}_4$  at the surface of float glass samples has been determined for  $1400 < T < 1500$  °C and  $p_{\text{H}_2\text{O}} = 0.33$  bar. For this calculation the procedure described in paragraph 4.7.2 has been used.

The data are obtained from results of 5 transpiration experiments, which results are shown in Figure 4.29. The chemical activity  $a_{\text{Na}_2\text{SO}_4}$ , decreases from about 0.20 at 1400 °C to about 0.13 between 1450 and 1500 °C. Because of the higher  $\text{Na}_2\text{SO}_4$  evaporation rates at 1500 °C, the sulfur retention becomes lower, especially at the glass melt surface. The activities of  $\text{Na}_2\text{SO}_4$  in a humid atmosphere ( $p_{\text{H}_2\text{O}} = 0.33$  bar) seem to be at least 2 times higher than the  $a_{\text{Na}_2\text{SO}_4}$  values derived in our approach at dry evaporation conditions ( $a_{\text{Na}_2\text{SO}_4} \approx 0.06$ ). The trends showed by these results agree rather well with the results of Conradt and Scholze, as discussed in paragraph 4.7.2.

Chemical analysis of glass samples were used to investigate the assumed  $\text{SO}_3$  depletion at the surface of the melt. A float glass sample directly obtained after a transpiration experiment at 1460 °C ( $p_{\text{H}_2\text{O}} = 0.33$  bar), has been divided in different horizontal layers which are grinded, dissolved in HF and analyzed by ICP-ES. The total average thickness of the sample was 8 mm. The measured  $\text{SO}_3$  concentration in the surface layer with a thickness of about 1 to 1.5 mm is 0.14 mass-%. The  $\text{SO}_3$  concentration increases with depth from values between 0.20 mass-% and 0.30 mass-% for  $1 < y < 6$  mm to  $\text{SO}_3 = 0.43$  mass-% for  $6 < y < 8$  mm ( $y$  is distance from surface). The average sulfur concentration (expressed as  $\text{SO}_3$ ) in the sample after the evaporation test has been measured with XRF: 0.30 mass-%.

Based on the measured  $\text{Na}_2\text{SO}_4$  evaporation rates and the assumption made in literature [26] that the activity of  $\text{Na}_2\text{SO}_4$  is about the same as the  $\text{SO}_3$  concentration in the soda-lime-silica glass melts expressed in mass-%. The measured  $\text{SO}_3$  surface concentration of 0.14 mass-% corresponds well with the calculated chemical activity of  $\text{Na}_2\text{SO}_4$  in this surface layer:  $a_{\text{Na}_2\text{SO}_4} = 0.13$ .

Based on the results of transpiration experiments for float glass melts (with and without sulfate addition) at  $1460 \pm 5$  °C, the chemical activities of  $\text{Na}_2\text{O}$  at the surface of the melt were derived from the measured NaOH evaporation rates. From the melt containing sulfate,

it is assumed that NaOH and Na<sub>2</sub>SO<sub>4</sub> are the only volatile sodium species and that all the measured sulfur release evaporates as Na<sub>2</sub>SO<sub>4</sub>. Furthermore, the Associated Species Model has been used to calculate the chemical activity of Na<sub>2</sub>O for the bulk composition of the melt. All the derived chemical activities for Na<sub>2</sub>O determined in this way are about similar:

- $a_{\text{Na}_2\text{O}}$  measured for surface of this float glass melt without SO<sub>3</sub>:  $1.4 \cdot 10^{-8}$
- $a_{\text{Na}_2\text{O}}$  measured for float glass melt surface with SO<sub>3</sub> (assuming all sulfur evaporates as Na<sub>2</sub>SO<sub>4</sub>) :  $1.5 \cdot 10^{-8}$  to  $2.0 \cdot 10^{-8}$
- $a_{\text{Na}_2\text{O}}$  derived from Associated Species Model (assuming no depletion at surface) :  $1.7 \cdot 10^{-8}$

Sodium depletion at the surface of the melt cannot explain the differences in sodium evaporation.

The chemical activity of Na<sub>2</sub>O is determined by assuming that all sodium evaporates as NaOH (no Na<sub>2</sub>SO<sub>4</sub> evaporation). The calculated activity values for  $a_{\text{Na}_2\text{O}}$  in glass compositions with SO<sub>3</sub> are much higher in this case:  $2.9 \cdot 10^{-8} < a_{\text{Na}_2\text{O}} < 4.6 \cdot 10^{-8}$ . According to calculations with ASM-AS these activities correspond with Na<sub>2</sub>O surface concentrations between 16 and 19 mass-%. SEM-EDX profile measurements in float glass samples containing sulfur, after transpiration experiments however, do not show these high concentrations near the surface of the melt.

### ***b) Role of water vapor on evaporation of sodium species***

The role of water vapor on the evaporation of sodium species from soda-lime-silicate melts containing SO<sub>3</sub> will be discussed in more detail. The release of sulfur-species from the melt depends also on the sulfate concentration in the melt. The maximum sulfate content of the oxidized melt depends on the redox state, composition of the melt [28], the water content in the melt [19] and the maximum temperature of the melt. As the water vapor pressure in the atmosphere increases, the water content in the melt increases and the residual contents of SO<sub>3</sub> generally decreases [19]. According to Papadopoulos [28], the calculated maximum concentration dissolved SO<sub>3</sub> in a float glass type of melt exposed to air, is about 0.42 mass-% at T = 1460 °C, but for  $p_{\text{H}_2\text{O}} = 0.33$  bar the calculated maximum concentration is only about 0.23 mass-%. At T = 1500 °C, the maximum amount of dissolved sulfate decreases from 0.24 mass-% SO<sub>3</sub> to 0.13 mass-% SO<sub>3</sub> after increasing  $p_{\text{H}_2\text{O}}$  from 0 to 0.33 bar. At the beginning of an evaporation test (t = 0), the water vapor injection is turned on and the water vapor

pressure increases rapidly from 0 to 0.33 bar. At  $t = 0$  the  $\text{SO}_3$  concentration is assumed to be 0.24 mass-%. Because of the lower maximum  $\text{SO}_3$  concentration in a humid atmosphere, sulfur species have to be released from the melt when being exposed to a humid atmosphere. As already discussed in paragraph 4.7.2 the  $\text{SO}_2$  bubbles might cause (some) foam production at the surface of the melt. Compared to the blank melt, the surface area of this foam layer is larger and may cause higher evaporation rates.

Thus, for soda-lime-silicate glass melts with sulfur in the melt,  $\text{NaOH}$  and  $\text{Na}_2\text{SO}_4$  are the main evaporating sodium species in humid and oxidized atmospheres. The evaporation rate of  $\text{Na}_2\text{SO}_4$  is proportional to the chemical activity of  $\text{Na}_2\text{SO}_4$  at the surface of the melt. But, the surface layer becomes  $\text{Na}_2\text{SO}_4$  depleted. The effect of water vapor in the atmosphere on the increased release of sodium species from  $\text{Na}_2\text{SO}_4$  in the melt is still not completely understood.

#### II.4 Sodium and potassium evaporation from industrial glass melt compositions containing chlorides and sulfur

The vapor pressures  $p_{\text{NaCl}}^*$ ,  $p_{\text{KCl}}^*$  and  $p_{\text{HCl}}^*$  were obtained from thermodynamic calculations for pure  $\text{NaCl}$  and pure  $\text{KCl}$  in a humid atmosphere ( $p_{\text{H}_2\text{O}} = 0.20$  bar) and temperatures between 500 and 1000 °C. In all cases, the calculated vapor pressures of  $\text{NaCl}$  and  $\text{KCl}$  are 10 to 100 times higher than the vapor pressure of  $\text{HCl}$ .

As discussed in paragraph 1.2.3, thermodynamic properties of chlorides in silicate glass melts can be estimated with the thermodynamic Factsage model [7]. FactSage has been used also to calculate the vapor pressures of  $\text{NaCl}$  and  $\text{HCl}$  in equilibrium with a soda-lime-silica melt containing chloride ( $\text{SiO}_2 = 74$  mol-%,  $\text{Na}_2\text{O} = 16$  mol-%,  $\text{CaO} = 10$  mol-% and  $\text{NaCl} = 0.1$  mol-%) for temperatures between 1000 and 1500 °C. For all these calculations, the water vapor pressure was kept constant:  $p_{\text{H}_2\text{O}} = 0.20$  bar. According to these thermodynamic equilibrium calculations at  $T = 1500$  °C, about 83 % of all gaseous chloride species is present as  $\text{NaCl}$ , the rest is  $\text{HCl}$ . At  $T = 1000$  °C, the fraction  $\text{NaCl}$  is only 27 %. At 1500 °C, the total vapor pressure of the chloride species together for this melt exposed to  $p_{\text{H}_2\text{O}} = 0.20$  bar is about 7 times higher than at  $T = 1000$  °C.

In case that 2 mol-%  $\text{Na}_2\text{O}$  is replaced in this glass composition by an equal amount  $\text{K}_2\text{O}$ , the total vapor pressure of all chloride species ( $\text{NaCl}$ ,  $\text{KCl}$  and  $\text{HCl}$ ) increases about 25 – 30 % according to the thermodynamic modeling. Despite the much lower  $\text{K}_2\text{O}$  concentration (2 mole-%) in the melt compared to the  $\text{Na}_2\text{O}$  concentration (14 mole-%), the calculated vapor

pressure levels of NaCl and KCl deviate less than 20 % from each other for  $1300 < T < 1500$  °C.

For carrying out these thermodynamic calculations, the composition of the melt has been assumed homogeneous. However, as a result of chloride evaporation, the surface layer of the melt can be chloride depleted. Laboratory evaporation tests have been performed to investigate this phenomenon. A crucible filled with raw materials for industrial flint container glass, has been placed directly in a hot tube furnace flushed with a gas flow. The chloride release was measured as a function of time. The experiments have been performed at temperatures of 1200 °C and 1500 °C at dry and humid atmospheres ( $p_{\text{H}_2\text{O}} = 0$  bar and  $p_{\text{H}_2\text{O}} = 0.55$  bar). The results presented in Figure 4.30 show that the initial chloride release is almost independent of the furnace temperature. Compared to the dry atmosphere, the chloride release was about 5 to 6 times higher under humid conditions during the first hour (batch melting-in period) after placing the batches in the hot furnace. After this period the measured chloride releases decrease rapidly. Almost directly after the batch is placed in the hot furnace, melting phases are formed and this melt is further heated to the set-point temperature of the furnace.

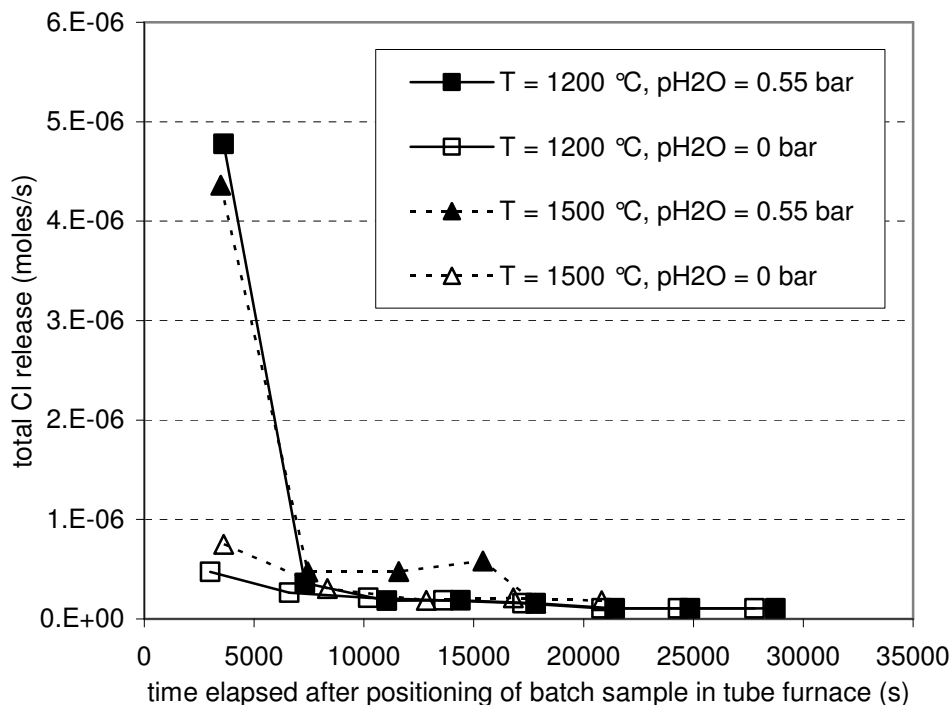


Figure 4.30: Measured total chloride releases from typical industrial raw material batches for flint glass that have been placed directly in a preheated furnace with a temperature of respectively 1200 and 1500 °C. The water vapor pressures ( $p_{\text{H}_2\text{O}}$ ) in the atmosphere were respectively 0 and 0.55 bar

According to thermodynamic calculation results, HCl will be released from the salts or melt phases at relative low temperatures (< 1200 °C), at higher temperatures the evaporation of NaCl will dominate. The sudden drop of the measured chloride release after about 1 hour and the limited temperature dependency can be explained if chloride depletion at the surface layer of the melt is assumed.

#### II.4.1 Chloride evaporation from industrial produced multi-component tableware glass compositions; thermodynamic modeling

Other investigated commercial glasses, like the tableware glass compositions A, B and C shown Table 4.2, contain other fining agents such as antimony-oxide, NaCl or a mixture of the 3 fining compounds. These glasses also contain about 5 mass-% K<sub>2</sub>O. Thus, in addition to sodium- and sulfur-species, several other species such as K-, Cl- and Sb-compounds, might evaporate from these tableware glass melts. For evaporation of chloride species, the reactions and reaction equilibria 1.20 till 1.29 are postulated, based on thermodynamic modeling (see paragraph 1.2.3). The values for the different equilibrium constants have been obtained from the application of thermodynamic databases for pure substances given by Factsage [7]. Because of the known chemical activities of K<sub>2</sub>O and Na<sub>2</sub>O in the melt (paragraph 4.4) (assuming that sulfur and chloride does not change these Na<sub>2</sub>O and K<sub>2</sub>O activities), the ratio between  $(p_{NaCl}^*)^2$  and  $(p_{KCl}^*)^2$  can be calculated by combining equation 1.25 with equation 1.27:

$$\frac{K_{HCl,1}}{K_{HCl,2}} = \frac{a_{Na_2O}}{a_{K_2O}} \cdot \frac{(p_{KCl}^*)^2}{(p_{NaCl}^*)^2} \quad (4.3)$$

The saturation pressures  $p_{NaCl}^*$ ,  $p_{KCl}^*$  and  $p_{HCl}^*$  can be estimated from the equations 1.21, 1.23, 2.10 and 4.3. For these calculations the chloride mass balance as well as the measured evaporation rate  $Q_{Cl-total}$  are required. NaCl, KCl and HCl are assumed to be the only volatile chloride species. This procedure is only permitted in the case that all Cl-species evaporate from the surface of the melt (no KCl or NaCl fining bubbles). Based on these assumptions, it is calculated that for tableware glass melts B and C at  $T = 1500$  °C and  $p_{H_2O} = 0.2$  bar, about 20 % of all released Cl evaporates as HCl.

From the measured chemical activities of Na<sub>2</sub>O and K<sub>2</sub>O of this glass at T = 1500 °C [1], the ratio  $Q_{\text{NaCl}} / Q_{\text{KCl}} \approx p^*_{\text{NaCl}}/p^*_{\text{KCl}}$  would be 1.2 (assuming the same mass transfer coefficient in the gas phase). Thermodynamic calculations with Factsage [7] predict for tableware glass composition B (see Table 4.2), with a theoretical chloride concentration of 0.4 mass-%, nearly identical chemical activities of NaCl and KCl at 1500 °C:  $a_{\text{KCl}} \approx a_{\text{NaCl}} \approx 0.4$ . However, during the melting of the raw materials 60 to 80 % of all chloride might be released. For a glass melt with  $a_{\text{NaCl}} = a_{\text{KCl}} = 0.1$ , the saturation vapor pressures of NaCl and KCl at 1500 °C would be about 0.1 bar. This would mean that the evaporation rates of NaCl and KCl are about 100 times higher than the NaOH and KOH evaporation rates. Probably the surface of the glass melt is strongly chloride depleted.

#### II.4.2 Chloride evaporation during melting of raw materials

During the melting of the tableware raw material batches B and C and during the first heating stages of these glass samples in the tube furnace chloride species are released. From the measured chloride evaporation rates and the measured chloride contents in the glass sample after the evaporation test (Cl ≈ 0.03 mass-%), it was calculated that about 70 to 75 % of all chlorides are released already before the gas sampling (evaporation measurements) started. For the tableware samples B and C, the chloride concentration in the melt after heating up, but just before the start of the evaporation experiment has been calculated to be about 0.12 mass-%.

The chloride evaporation rates during the preparation of glass samples before the transpiration evaporation experiments are about 3 to 4 times higher than the measured chloride evaporation rates from the obtained glass melt at a higher constant temperature.

#### II.4.3 Laboratory experiments

The release of volatile glass components can be affected by ascending fining bubbles, which often contain gases such as SO<sub>2</sub>, oxygen and/or chloride species/vapors. These fining bubbles may not only contain glass melt vapors or evaporation products, but will also cause convective mixing of the melt. Convection will result in less depletion of volatile components at the surface layer and consequently this causes higher evaporation rates. To control whether fining bubbles can be expected during the transpiration evaporation tests, the fining process of tableware glass samples (composition C) has been visualized by using this fining test facility [18]. The fining test facility is described in paragraph 3.4.



During the melting of tableware cullet in transparent vitreous silica crucibles (composition C, Table 4.2) video recordings were used to visualize the melting and fining process. The composition of the released gases has been measured by applying an oxygen analyzer and a Fourier Transform Infra-Red analyzer (FTIR) able to measure the H<sub>2</sub>O, HCl and SO<sub>2</sub> concentrations in the carrier gas after being exposed to the molten glass. Extractive gas sampling via gas wash bottles in combination with ion-chromatography has been used to measure the total release of chloride species. The results are shown in Table 4.7.

The tableware cullet, used for this test, has been prepared by melting this glass from pure raw materials, first heated at 1400 °C (temperature lower than fining onset) during a period of 1½ hour. After this period, the fresh glass melt was quenched and broken and used for this fining experiment.

In a dry atmosphere, the tableware cullet with size of about 5 – 10 mm, has been heated from room temperature to 1250 °C applying a heating rate of 10 °C/minute, afterwards the sample has been heated up to 1520 °C at a heating rate of 2 °C/minute. During a period of about 4 hours, the furnace temperature has been kept constant at 1520 °C. During this period of 4 hours, the crucible was flushed initially with a mixture of N<sub>2</sub> and O<sub>2</sub> (p<sub>O2</sub> = 0.1 bar). After a period of 1 hour water vapor (p<sub>H2O</sub> = 0.20 bar) has been added to the gas-mixture. The process parameters during the experiment and the measured releases of HCl (Q<sub>HCl</sub>) and total chloride species (Q<sub>Cl-total</sub>) are shown in Table 4.7.

Table 4.7: Measured HCl and total chloride release from tableware melt C (see Table 4.2) before and during fining. The melt has been prepared from tableware cullet.

Time interval (minutes)	Temperature (°C)	Water vapor pressure (bar)	Total <u>average</u> Cl release rate (mg/s)	Average HCl release (mg/s)	Q <sub>HCl</sub> / Q <sub>Cl-total</sub> ratio (-)
0 -120	20 – 1250	0	1.0 10 <sup>-5</sup>	0	0
120 - 135	1250 -1520	0	2.0 10 <sup>-4</sup>	0	0
135 - 195	1520	0	2.2 10 <sup>-4</sup>	0	0
195 - 255	1520	0.20	2.4 10 <sup>-4</sup> *	1.6 10 <sup>-4</sup>	0.65
255 - 375	1520	0.20	1.0 10 <sup>-5</sup>	0	0

\* A peak concentration of 2.4 10<sup>-3</sup> mg/s has been measured.

Directly after water vapor ( $p_{\text{H}_2\text{O}} = 0.2$  bar) has been added to the furnace atmosphere, the HCl release increased within 2 minutes to a peak level of  $2.4 \cdot 10^{-3}$  mg/s (given as Cl), 10 minutes later the HCl release dropped to almost 0 mg/s. Except for this short period, most evolved chloride during this experiment is probably released in the form of KCl or NaCl vapors.

During a period of about 15 minutes, between 1440 and 1470 °C (dry atmosphere), some fining bubbles have been observed in the melt and the measured  $\text{SO}_2$  release increased from about  $0.7 \cdot 10^{-3}$  to  $1.7 \cdot 10^{-3}$  mg/s. Above 1470 °C hardly any bubbles have been observed anymore.

Thus, during evaporation tests with tableware melts at 1400 °C (below fining temperature) and 1500 °C (above fining temperature), no fining bubble evolution takes place and the measured releases of volatile species are merely a result of evaporation from the surface of the melt. For glass samples heated above the fining temperature, the residual  $\text{SO}_3$  and chloride concentrations are lower than glass samples heated at temperatures below the fining temperature.

The impact of  $\text{SO}_3$  and Cl in the melt on the evaporation of K- and Na-species has been investigated with 4 different transpiration evaporation experiments using tableware glasses A, B and C. The compositions of these glasses are given in Table 4.2. For the evaporation tests 1 to 3, pre-melted glass samples are used. The sample preparation procedure is described in paragraph 4.2. In the fourth evaporation test, a boat with raw materials is placed directly in the tube furnace at room temperature. The raw materials were heated in the transpiration set-up with a gradient of 2 °C/minute. The following tests and conditions have been applied:

1. Evaporation test 1, with tableware glass melt A and melt B at  $T = 1500$  °C and  $p_{\text{H}_2\text{O}} = 0.18 \pm 0.02$  bar (oxidizing furnace atmosphere conditions). The impact of chloride in the glass melt on the sodium and potassium species evaporation has been investigated for tableware compositions without sulfur.
2. Evaporation test 2, with tableware glass melt A and melt C at  $T = 1500$  °C exposed to a dry atmosphere. The impact of chlorides plus sulfur in the melt on the sodium and potassium species evaporation has been investigated under dry, oxidizing atmosphere conditions.
3. Evaporation test 3, with tableware glass melt A and melt C at  $T = 1500$  °C and  $p_{\text{H}_2\text{O}} \approx 0.2$  bar. The impact of chlorides and sulfur in the glass melt on sodium and potassium

species evaporation has been investigated for a water vapor containing oxidized atmosphere.

4. Evaporation test 4, with fresh tableware melts A and C, directly heated and melted from chemical pure raw materials with an average temperature of 1425 °C and  $p_{\text{H}_2\text{O}} \approx 0.2$  bar. The impact of chlorides and sulfur on sodium and potassium species evaporation from a fresh melt with still active fining agents (evolution of  $\text{SO}_2$  and NaCl vapor bubbles) has been investigated for a water vapor containing oxidized atmosphere.

***1) Evaporation test 1: Effect of chlorides on the evaporation of Na and K species from tableware melts***

The tableware melts A and B contain hardly sulfur. In melt A, antimony-oxide has been used as a fining agent, while in melt B sodium chloride has been used for aiding bubble removal during melting of the glass. The Na, K and Cl evaporation rates of these melts have been measured at 1500 °C. Based on the results of the previous fining test, fining bubbles are not expected during the evaporation test. The expected volatile species from melt A are: NaOH, KOH and Sb-species. From melt B, apart from NaOH and KOH, NaCl, KCl and HCl species might evaporate, but no antimony-species.

For identical process conditions, the differences between the measured total sodium evaporation rates from melt A and melt B (with Cl) are less than 1 %, the measured total K evaporation rate from melt B is about 10 % higher than the total K release from melt A. When assuming that all gaseous chloride species from melt B are released as KCl and NaCl, it is calculated that about 15 % of the evaporated alkali species ( $Q_{\text{Na}} + Q_{\text{K}}$ ) are released as alkali-chlorides.

Based on the procedure described in paragraph 4.7.4.1 the chemical activities of NaCl and KCl in the surface layer of the melt have been estimated. The activities of NaCl and KCl are in the range between  $2 \cdot 10^{-5}$  and  $4 \cdot 10^{-5}$ . These experimentally derived chemical activities (relative to pure non-mixed liquid compounds at the same temperature) are about 10000 times lower than the modeled activities (Factsage) of KCl and NaCl for these glass melts. The low chemical activities of NaCl and KCl are probably a result of a chloride depleted surface layer of the melt. These results confirm the results of the previously described evaporation experiment shown in Figure 4.30. This figure shows the time dependent chloride release from

soda-lime-silicate melts and suggests depletion and decrease of chloride evaporation as time proceeds.

As described by Köpsel [29] the Cl-species can also be released through fining bubbles. For high chloride concentrations in the melt and high temperatures, these bubbles might contain Cl-species. The fining test, described before, shows that for the applied test conditions here, this is not the case during the evaporation tests, performed at temperatures at which fining bubble evolution does not take place.

Thus, the effect of chlorides in an almost static melt on the evaporation of sodium and potassium is relatively small. The surface layer of the melts become probably chloride depleted soon after the start of the evaporation test.

## ***2) Evaporation test 2: Effect of chloride and sulfur in glass melts on sodium and potassium release rates at dry furnace atmosphere conditions***

The evaporation rates of Na-, K-, S- and Cl-species from tableware melt C, containing SO<sub>3</sub>, Cl and Sb, have been measured in a dry, oxidizing atmosphere ( $p_{O_2} = 0.11$  bar) at 1500 °C. Therefore, only NaCl, KCl, Na<sub>2</sub>SO<sub>4</sub> and/or K<sub>2</sub>SO<sub>4</sub> evaporation is expected and no evaporation of NaOH and K. Figure 4.31 shows the total measured evaporation rates of Na, K, S and Cl species as a function of time. Up to 150 minutes after starting the evaporation test, the average molar evaporation rate of chloride and the total average molar evaporation rate of sodium plus potassium differ only 10 %. Probably sodium and potassium evaporate as NaCl and KCl. About 63 % of the evaporated chlorides is released as KCl and 37 % as NaCl. Between 150 and 300 minutes after the start of the experiment all the measured evaporation rates decrease due to depletion of the surface layer of the melt. Between 300 and 450 minutes the measured evaporation rates are about constant. In this period 50 to 75 % of all evolving chlorides is released as KCl.

Compared to the previous evaporation test 1, with glass type B at  $T = 1500$  °C and  $p_{H_2O} = 0.17$  bar, and no sulfur, the average total Cl release from glass C appeared to be about 80 % higher. In a dry atmosphere, chlorides in these melts mainly evaporate as potassium chlorides. The presence of sulfates in the melt seems to promote the chloride release, comparing the calculated NaCl and KCl releases from glass melt C with glass melt B (with about the same Cl-content). Figure 4.32 shows an almost linear relation between the measured total chloride evaporation rates and the total sulfur release rates (expressed as SO<sub>x</sub>). Possibly

the chloride release as well as the sulfur release are strongly affected by the transport of volatile species in the melt.

### 3) Evaporation test 3: Effect of chloride plus sulfur in the glass melt on sodium and potassium release rates in a water vapor containing atmosphere

Figure 4.33 shows the measured total sodium and total potassium evaporation rates as a function of time from a melt at 1510 °C exposed to an atmosphere with  $p_{\text{H}_2\text{O}} = 0.20$  bar for tableware glass compositions A and C (see Table 4.2). Compared to tableware melt A (melt without  $\text{SO}_3$  and without Cl), the total potassium evaporation rates from melt C are about 1.4 times higher and the sodium evaporation rates are about twice as high. The total Cl evaporation rates as well as the sulfur release rates from melt C in this water vapor containing atmosphere are about 2 till 3 times higher than the evaporation rates of these species from the same melt C at dry atmosphere conditions.

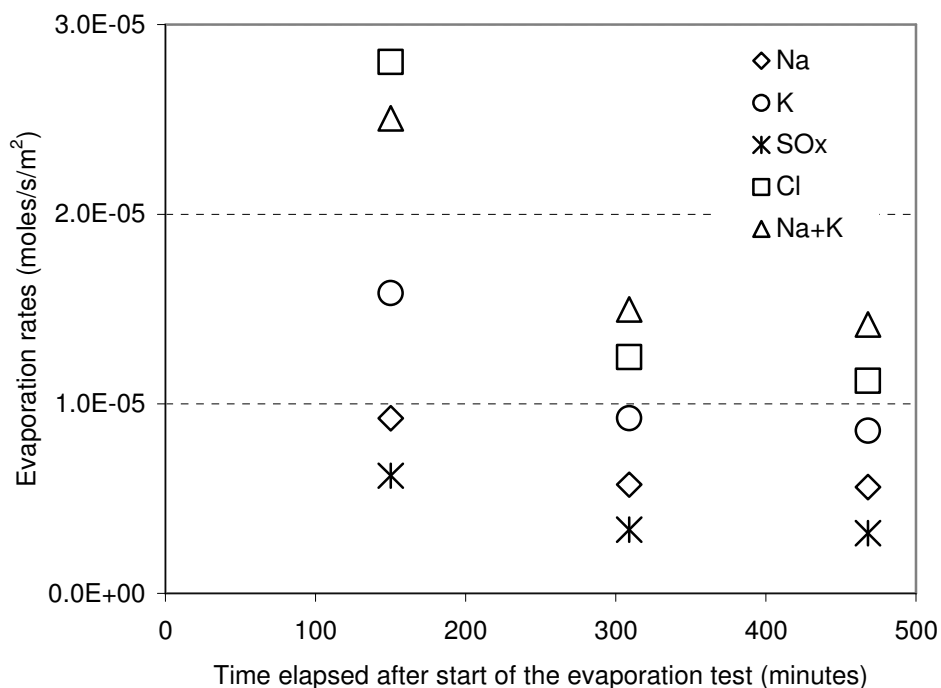


Figure 4.31: Measured total evaporation rates of Na, K, Cl and  $\text{SO}_x$  as a function of time from tableware melt C (see Table 4.2). During the measurements a dry oxidized ( $p_{\text{O}_2} = 0.11$  bar) carrier gas was applied and the temperature was 1500 °C. The glass melt at the start of the experiment is already fined (no bubble formation during evaporation test).

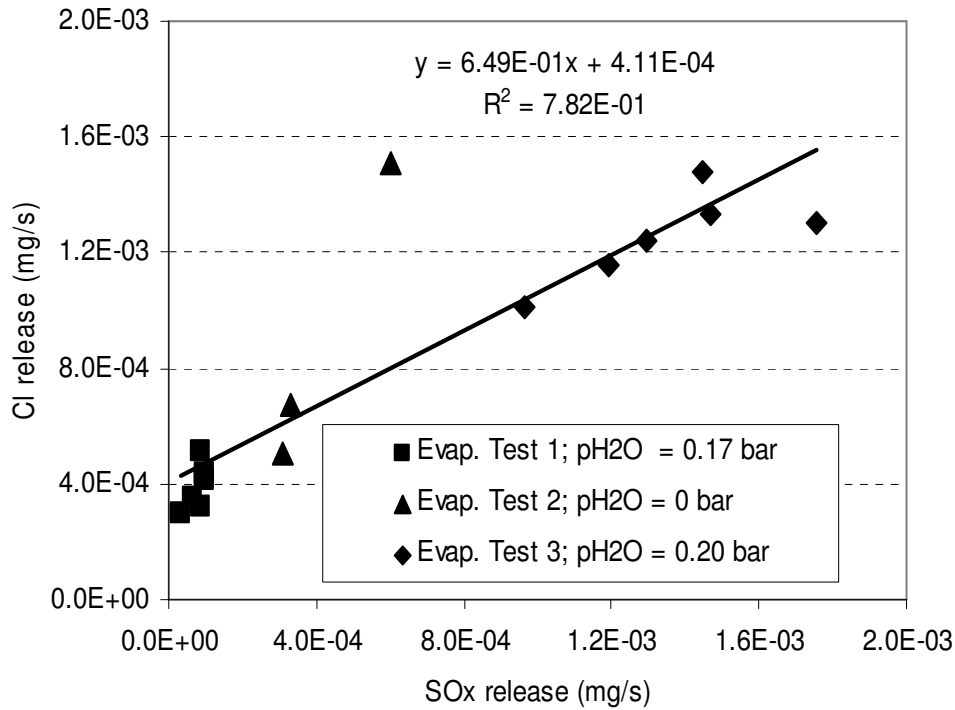


Figure 4.32: Measured Cl evaporation rates as function of the measured SO<sub>x</sub> release rates for 3 different evaporation tests with tableware melt C at 1500 °C. The evaporation tests are described in paragraph 4.7.3.

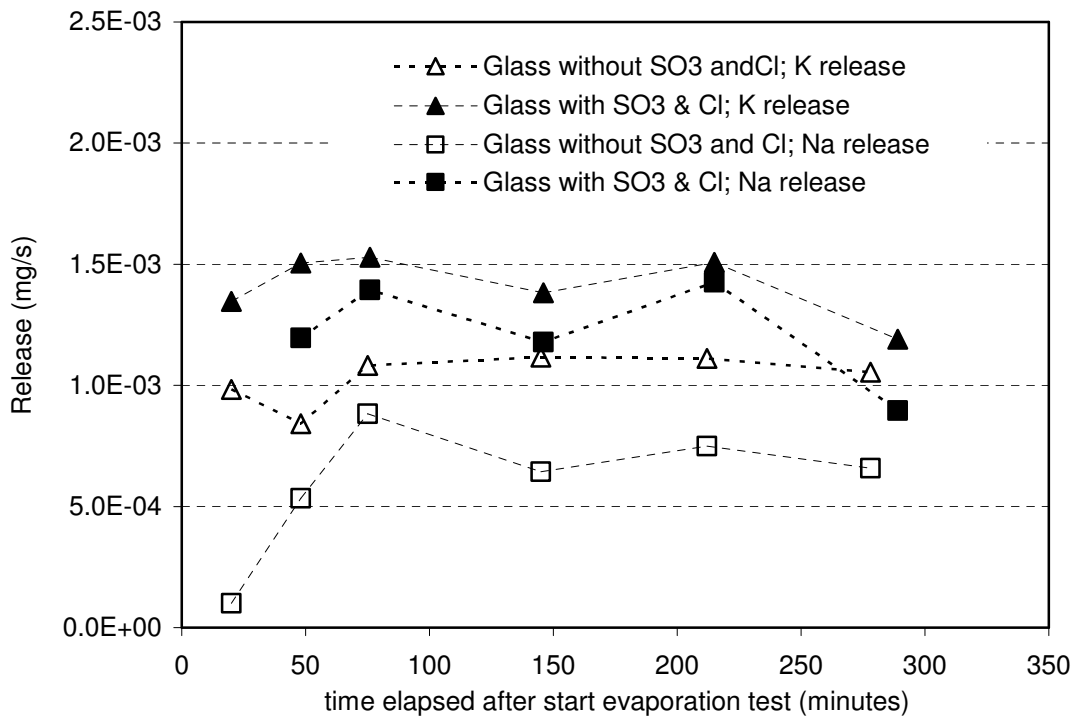


Figure 4.33: Results of laboratory transpiration experiments for tableware glass compositions A and C (see Table 4.2) The total sodium and potassium evaporation rates were measured as a function of time from glass melts with and without SO<sub>3</sub> at 1510 °C.

The total releases of Na- and K-species seem to be increased for melt C compared to melt A, due to the release of alkali-chlorides and maybe alkali-sulfates. Later in this paragraph the results of these tests will be discussed in more detail.

***4) Evaporation test 4: Effect of chloride and sulfur in the glass melt on the sodium and potassium release rates from a fresh melt with active fining agents***

During the heating of a 'fresh' tableware melt C (with SO<sub>3</sub> and Cl), the sodium, potassium, chloride and sulfur release rates have been measured at an average temperatures of about 1425 °C. The heating rate was about 2.7 °C/minute, the water vapor pressure is constant: p<sub>H2O</sub> = 0.2 bar.

Compared to the previous experiment with the same glass type C at a higher, but constant temperature of 1510 °C and p<sub>H2O</sub> = 0.2 bar, the measured evaporation rates of Na, K, S and Cl are equal or higher during this evaporation test.

Despite the lower temperatures, the chloride release is more than 2 times higher and the potassium release is about 40 % higher compared to the previous evaporation test, but the measured SO<sub>x</sub> and Na release rates for are about the same.

For this evaporation test at 1425 °C, the chloride release rate, Q<sub>Cl</sub>, is about the same as the alkali evaporation rate, Q<sub>Na+K</sub>. This indicates that sodium and potassium are mainly released as NaCl and KCl vapors, during this test. This test also shows that the chloride release strongly depends on the transport of chloride species in the melt.

## References

- [1] H.A. Schaeffer, D.M. Sanders, 'Verdampfungsvorgänge an einem Na<sub>2</sub>O-CaO-SiO<sub>2</sub>-Glas, Dampfdruck- und Konzentrationsprofilmessungen', *Glastech. Ber.*, **49** [5], 95-102 (1976)
- [2] D.M. Sanders, H.A. Schaeffer, 'Reactive Vaporization of Soda-Lime-Silica Glass Melts', *J.Am.Ceram.Soc.*, **59** [3-4], 96 -101 (1976)
- [3] H. van Limpt, R. Beerkens, A. Lankhorst, A. Habraken, 'Mass transfer relations for transpiration evaporation experiments', *Int. J. of Heat and Mass Transfer* **48**, 4265-4281 (2005)
- [4] O. Verheijen, 'Thermal and chemical behavior of glass forming batches', Thesis Eindhoven University of Technology, The Netherlands (2003)
- [5] H. van Limpt, R. Beerkens, O. Verheijen, 'Models and experiments for sodium evaporation from sodium containing silicate melts', *J.Am.Ceram.Soc.* **89** [11], 3446-3455 (2006)
- [6] R.G.C. Beerkens, J.A.C. van Limpt, 'Evaporation in industrial glass melt furnaces', *Journal of Glass Science and Technology* **74** [(9), 245-257 (2001)
- [7] C.W. Bale, P. Chartrand, S.A. Degterov, G. Eriksson, K. Hack, 'FactSage Thermochemical Software and Databases', *Calphad*, Vol. **26** [2], 189-228 (2002)
- [8] H. Franz, H. Scholze, 'Die Löslichkeit von H<sub>2</sub>O-Dampf in Glasschmelzen verschiedener Basizität', *Glastechn. Ber.* **36** [9], 347-355 (1963)
- [9] F. Geotti-Bianchini, L. De Riu, 'Infrared spectroscopic analysis of water incorporated in the structure of industrial soda lime glass', *Glastechn. Ber.* **68** [7], 228-240 (1995)
- [10] H. van Limpt, R. Beerkens, 'Evaporation experiments and modelling for glass melts', to be published in *Glass Technol.: Eur. J. Glass. Sci. Technol. A* **48** [3], (2007)
- [11] A.J. Faber, R. Koch, O.S. Verheijen, 'Influence of oxy-fuel atmosphere on water concentration in glass and the effects of the oxy-fuel atmosphere on the glass melting', TNO report HAM-RPT-97-266, July (1997)
- [12] Verein Deutscher Eisenhüttenleute, *VDEh Slag Atlas*, 2nd edition. Verlag Stahleisen GmbH, Düsseldorf, ISBN 3-514-00457-9 (1995)
- [13] R. Conradt, 'A Simplified Procedure to Estimate Thermodynamic Activities in Multicomponent Oxide Melts', *Molten Salt Chemistry and Technology* ed. by H. Wendt, Trans Tech Publication Zürich, Switzerland, **5-6**, 155-162 (1998)
- [14] A. Steiner, 'Foam glass production from vitrified municipal waste fly ashes' thesis University of Eindhoven (2006)



- [15] R.G.C. Beerkens, 'Sulphate decomposition and sodium activity in soda-lime-silicate melts', *J. Am. Ceram. Soc.* **86** [11], 1893 – 1899 (2003)
- [16] D.M. Sanders, H.A. Schaeffer, 'Reactive Vaporization of Soda-Lime-Silica Glass Melts', *J.Am.Ceram.Soc.* **59** [3-4], 96 -101 (1976)
- [17] R.C. Reid, J.M. Prausnitz, B.E. Poling, 'The Properties of Gases and Liquids', Fourth ed., McGraw-Hill Book Company, New York, ISBN 0-07-051799-1 (1987)
- [18] G.L. Squires, 'Practical Physics', McGraw-Hill Publishing Company Ltd., London (1968)
- [19] P. Laimböck, 'Foaming of glass melts' Thesis Eindhoven University of Technology, The Netherlands (1998)
- [20] R. G. C. Beerkens, J. van der Schaaf, 'Gas Release and Foam Formation During Melting and Fining of Glass' *J. Am. Ceram. Soc.*, **89** [1], 24–35 (2006)
- [21] H.A. Schaeffer, D.M. Sanders, 'Verdampfungsvorgänge an einem Na<sub>2</sub>O-CaO-SiO<sub>2</sub>-Glas, Dampfdruck- und Konzentrationsprofilmessungen', *Glastech. Ber.* **49** [5], 95-102 (1976)
- [22] M. Rongen, A.J. Faber, R. Beerkens, R. Breeuwer, 'Physical fining techniques of glass melts', ESG-Conference, Sunderland, UK, September 10th - 14th (2006)
- [23] F. Gebhardt, 'Emissionen von Glasschmelzwannen und deren Minderung durch schmelztechnische Maßnahmen', *Glastech. Ber.* **59** [12], 344-349 (1986)
- [24] R.G.C. Beerkens, 'Deposits and condensation from flue gases in glass furnaces', Thesis Technical University Eindhoven (1986)
- [25] R.G.C. Beerkens, J.A.C. van Limpt, 'Evaporation in industrial glass melt furnaces', *Journal of Glass Science and Technology* **74** [9], 245-257 (2001)
- [26] R. Conradt, H. Scholze, 'Zur Verdampfung aus Glasschmelzen', *Glastech. Ber.* **59** [2], 34-52 (1986)
- [27] D.M. Sanders, M.E. Wilke, S. Hurwitz, W.K. Haller, 'Role of water vapor and sulfur compounds in sodium vaporization during glass melting', *J.Am.Ceram. Soc.* **64** [7], 399-404 (1981)
- [28] K. Papadopoulos, 'Reply to the comments by T.J. Harper and S. Holmquist on "The solubility of SO<sub>3</sub> in soda-lime-silicate melts', *Phys. Chem. Glasses* **18** [4], 77-78 (1977)
- [29] D. Köpsel, 'Solubility and Vaporization of Halogenides', *Glass Sci. Technol.* **73** C2, 43-50 (2000)

## 5. Evaporation modeling for industrial glass furnaces

In this study a modeling approach to estimate the kinetics of glass melt volatilization processes has been developed. In chapter 4, the application of the developed evaporation model is demonstrated for the evaporation experiments with multi-component silicate melts in a laboratory transpiration set-up. In this chapter, basically the same evaporation model will be applied to calculate (local) evaporation rates from glass melts in different types of fossil-fuel fired glass melt furnaces.

The evaporation rates in industrial glass melt furnaces depend on the process conditions, such as:

- Glass melt composition (at the surface);
- Temperature of the glass melt surface;
- Composition of the atmosphere. Especially the partial water vapor pressure level (air-fuel firing versus oxy-fuel firing) and the carbon monoxide partial vapor pressures just above the melt are important;
- Exposure time of a flowing glass melt volume to the combustion atmosphere;
- Local gas velocities and gas phase turbulence intensity just above the glass melt surface.

Application of the developed evaporation model in combination with CFD modeling of gas flows and glass melts, offers the possibility to optimize the process conditions and furnace design concerning limited evaporation rates in industrial glass melt furnaces. The combination of models, for instance can be used to find the optimum process parameters or furnace designs with respect to heat transfer, energy consumption and evaporation from the melt. Calculations by CFD models provide, local gas or glass melt velocities, temperatures and distribution of species in the different domains of the glass furnace.

The developed evaporation model in this study applied for industrial glass melting furnaces is validated for a few cases by comparing the model calculations with results of industrial evaporation measurements. For several industrial glass furnaces the average and local evaporation rates have been determined and compared to results of evaporation modeling.

Phenomena like foaming and melting of raw materials will influence the total evaporation rates of different species in industrial furnaces. In paragraph 4.8, the impact of these parameters and phenomena is discussed qualitatively. However, the developed evaporation

model describes only the evaporation kinetics from a blank melt without a foam layer and without a batch blanket of not completely molten raw materials.

The measured and modeled local concentrations of volatile species in the combustion chambers of industrial glass furnaces are compared and will show the accuracy of the evaporation model in practice and the deficiencies of the modeling approaches. This comparison will show possibilities to improve the evaporation model.

In this chapter, 3 examples show some applications of the evaporation model, developed and validated for different glass melts. The most important technological application is the prediction of rates of volatilization of different evaporating species from blank glass melts in industrial furnaces. The first example, given in paragraph 5.1, shows the calculated local thicknesses of the Nernst boundary layers for NaOH in the gas phase for an oxygen-natural gas fired glass furnace and for a cross-fired (air-natural gas) regenerative glass melting furnace.

For the oxygen-gas fired soda-lime-silicate glass furnace, the calculated distribution of the evaporated NaOH species in the combustion chamber is shown. The calculated NaOH concentrations at different positions in the combustion chamber are compared with measured total sodium concentrations.

Paragraph 5.2 shows results for an example of sodium evaporation from the melt in an industrial glass melting furnace and the impact of this volatilization on corrosion of the silica refractory materials applied in the crown of an oxygen-fired soda-lime silicate furnace. Sodium hydroxide reacts with silica, forming sodium silicate melts at certain conditions.

In paragraph 5.3, different thermodynamic models have been compared for the calculation of the boron species evaporation rates from industrial E-glass furnaces.

**Nomenclature**

$C_6$	constant in equation 5.5 [ $m^{0.2} \cdot s^{-0.2}$ ]
$h$	mass transfer coefficient [ $m \cdot s^{-1}$ ]
$m$	stoichiometry factor in equilibrium reaction [-]
$n$	stoichiometry factor in equilibrium reaction [-]
$q$	stoichiometry factor in equilibrium reaction [-]
$p$	vapor pressure (Pa)
$Q$	molar flux density [ $mole \cdot m^{-2} \cdot s^{-1}$ ]
$R$	gas constant [ $8.31432 \text{ J} \cdot mole^{-1} \cdot K^{-1}$ ]
$Sc$	Schmidt number ( $=\mu/\{\rho \cdot D\}$ ) [-]
$T$	absolute temperature [K]
$v$	velocity of gas or melt [ $m \cdot s^{-1}$ ]

Subscripts and superscripts

*	saturated gaseous atmosphere
bulk	parent glass or main gas stream
refractory	near refractory surface
g	gas phase
i	component i in gas phase
j	(evaporating) component in melt
m	melt phase

Greek and other symbols

$\delta_N$	=	Nernst boundary layer thickness [m]
------------	---	-------------------------------------

## 5.1 Sodium evaporation in industrial fossil-fuel fired glass furnaces

CFD calculations have been applied to calculate the temperatures and flows (velocities of gases in the combustion space) and turbulence in the combustion space of a glass furnace. From these results, mass transfer coefficients of volatile species in the gas phase ( $h_{g,i}$ ) have been estimated [1]. The local mass transfer boundary layer thickness or the Nernst boundary layer thickness ( $\delta_N$ ) of the gas boundary layer at the glass melt surface can be determined from the gas velocities and the Schmidt number ( $Sc$ ). The local mass transfer coefficients were obtained from the calculated Nernst boundary layer as described in paragraph 2.3.3. CFD models for combustion space and glass melt domain are applied to calculate the glass melt surface temperature. The thermodynamic Associated Species Model can be used to calculate the chemical activities of volatile glass compounds on top of the glass melt. Depletion of volatile glass components at the surface of the melt is neglected. From equation 2.3 the saturation pressures of the evaporation products are calculated. The local evaporation rates are obtained from equation 2.10. From the local NaOH evaporation rates, the distribution of NaOH in the combustion chamber can be determined using CFD modeling. Throughout the gas phase domain within the combustion chamber, a mesh or grid of volume cells has been constructed. For each of these volume cells, the in chapter 2 (appendix I) defined set of differential equations has been discretized. Three velocity components, pressure and the concentration of the volatile species are calculated in each cell. Figure 5.1 shows the calculated thickness of the Nernst boundary layer at the glass surface of one section of a cross-fired regenerative furnace between two burner ports. The calculated boundary layer thickness varies between 0.5 and 1 cm. Figure 5.2 shows as an example the calculated NaOH vapor concentrations in the combustion chamber of a soda-lime-silicate oxy-fuel furnace. In an oxygen-gas fired furnace the local gas velocities above the melt are 3 to 4 times lower and consequently the Nernst boundary layer is thicker. The average calculated boundary layer thickness is  $2.7 \pm 0.5$  cm. In case of the cross-fired regenerative furnace, the mass transport coefficient for an evaporated species such as NaOH, is about 3.4 times higher compared to the case of this oxygen-gas fired furnace. For the modeled furnaces, the NaOH evaporation rates were not measured but Figure 5.3 shows measured sodium concentrations at different positions in the combustion chamber of a typical oxygen-gas fired, soda-lime-silicate glass furnace. It is assumed that all sodium evaporates as NaOH because of an oxidized atmosphere.

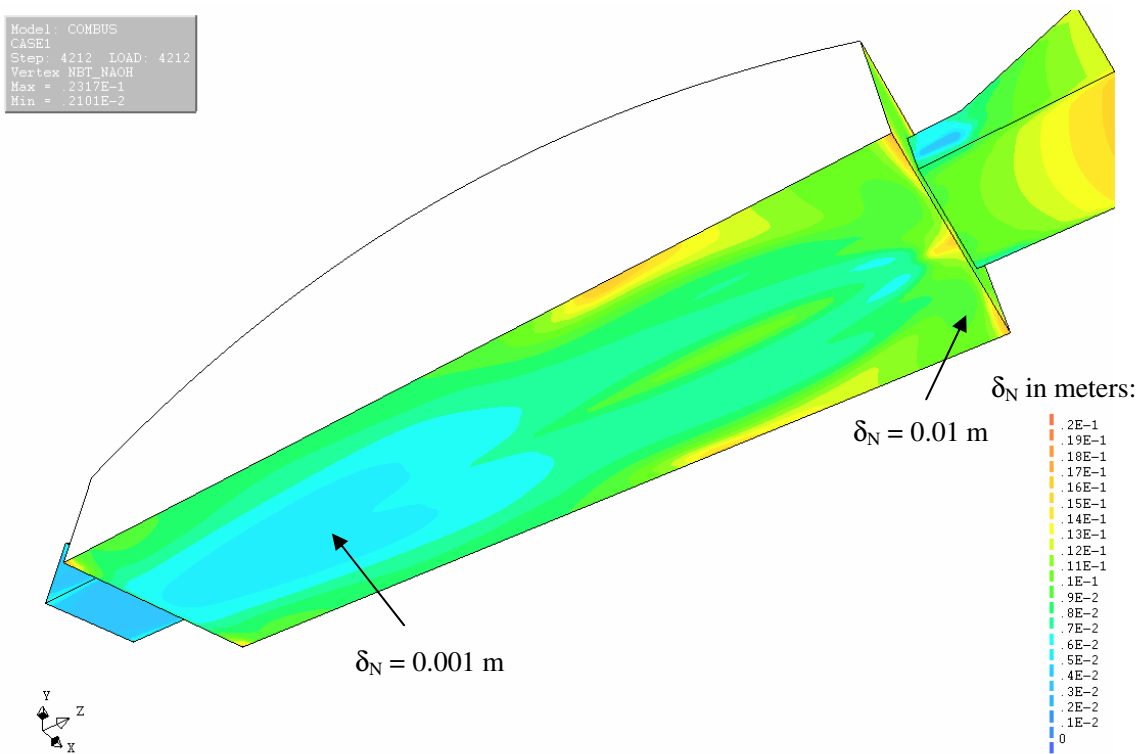


Figure 5.1: Calculated contours of the Nernst boundary layer thickness (in meters) for NaOH evaporation from the glass melt surface. The figure shows one combustion chamber section of a regenerative cross-fired furnace with burner ports at both sides. The scale range for  $\delta_N$ : 0 to 0.02 m.

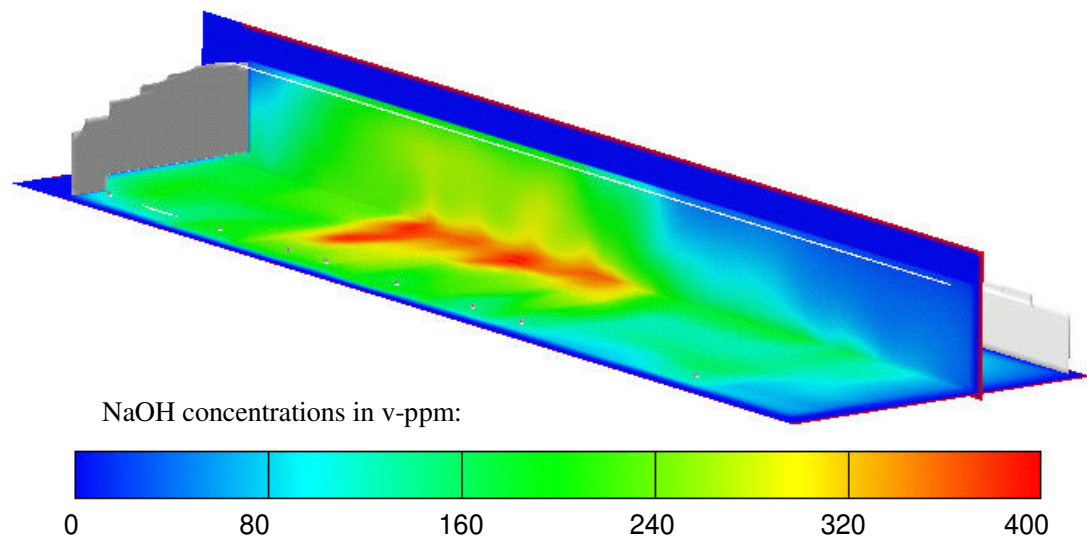


Figure 5.2: From CFD calculations obtained NaOH concentrations in the combustion chamber of a soda-lime-silicate oxy-fuel furnace. The NaOH concentrations vary between 0 and 400 v-ppm.

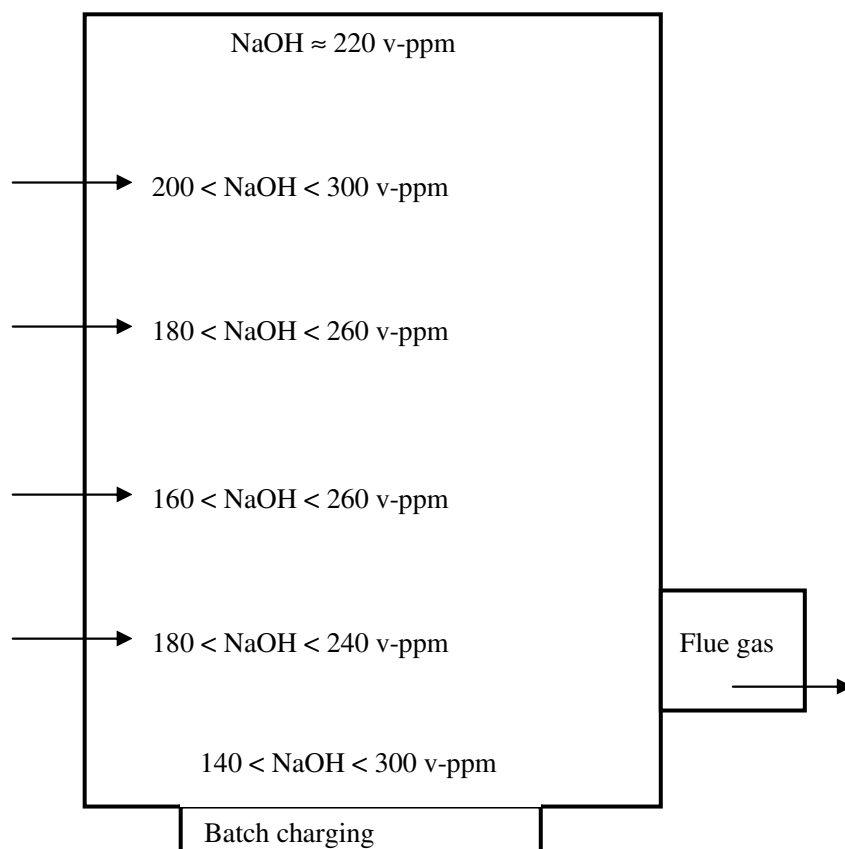


Figure 5.3: Schematic horizontal cross section of the combustion chamber of a soda-lime-silicate oxygen-gas fired glass furnace. The figure shows the measured NaOH concentrations in v-ppm at different positions. For the sampling of the hot combustion gases water-cooled probes have been used.

The local gas compositions, were determined by extractive gas sampling via water-cooled probes and gas wash bottles as shown in Figure 5.4. After each sampling period, the probe is carefully rinsed. Both the solutions, the solution from the gas wash bottles and the rinsing liquid are collected in one bottle and then chemically analyzed with ICP-ES.

Halfway the length-direction of the combustion chamber, close to the side-wall and above a nearly blank glass melt, the measured sodium concentrations vary between 160 and 260 v-ppm ( $=10^{-6} \text{ m}^3/\text{m}^3$ ). The modeling results show in the same area of the combustion chamber nearly the same NaOH concentrations (160 to 240 v-ppm). In the center of the furnace near the crown (hot-spot) the measured sodium concentrations lie between 240 and 320 v-ppm, the modeled NaOH concentrations lie between 240 and 300 v-ppm.

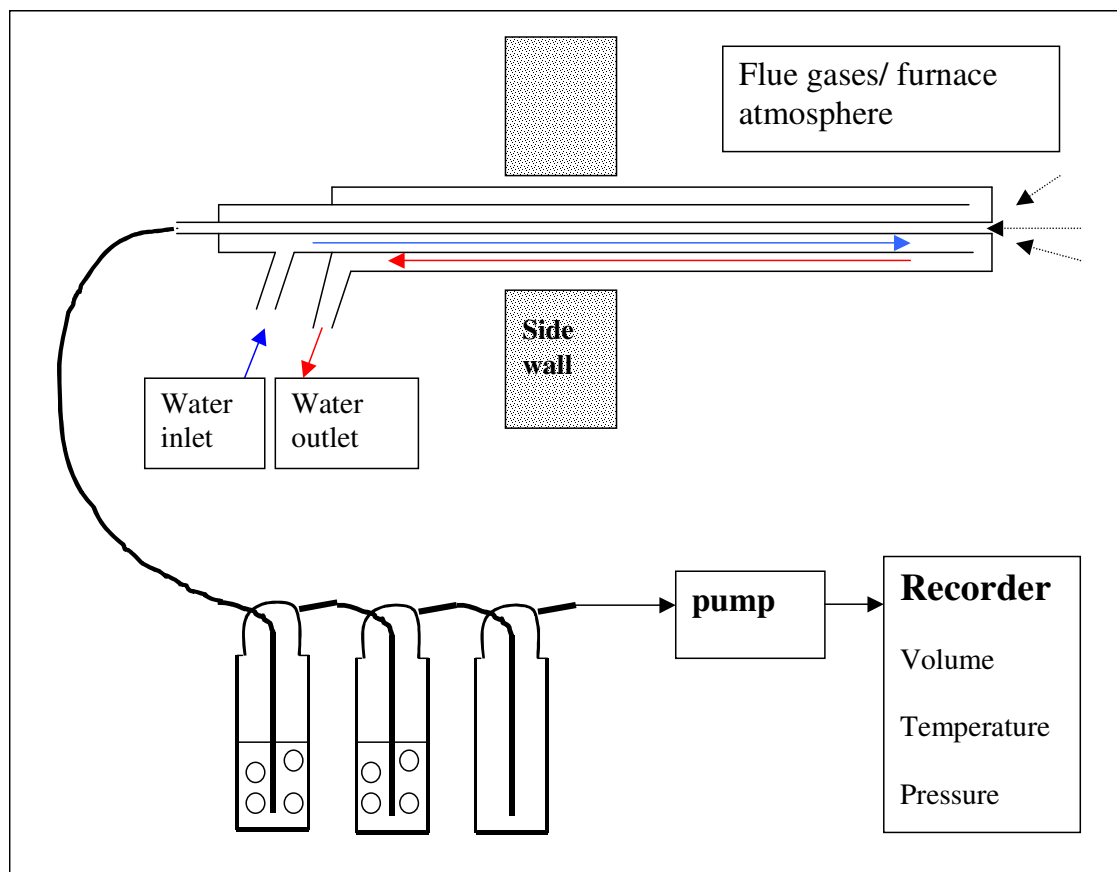


Figure 5.4: Schematic presentation of the gas sampling probe, used for the extractive sampling of hot combustion gases from combustion spaces of glass furnaces.

The sodium evaporation rates depend on the process conditions in the furnace, such as: a) temperatures in the furnace, b) the local gas velocities near the surface of the melt, c) oxidation state of the atmosphere (reducing flames promote the evaporation of elemental sodium) or d) foam formation. The process conditions might be slightly different in various glass furnaces. The modeled and measured NaOH concentrations are in the same range. The evaporation models can be used to find process conditions and furnace design parameters to minimize sodium evaporation and silica corrosion (see paragraph 5.2) in glass furnaces.

## 5.2 Reduction of superstructure corrosion and emissions

Evaporation from the glass melt surface is one of the main causes of dust emissions, but the evaporation of glass melt components may also lead to the formation of aggressive vapors (alkali or lead vapors), reacting with the superstructure refractory materials [2][3]. The condensation products, formed during the cooling of the combustion gases, may also foul and block regenerator passages [4]. Process variables and parameters in glass furnaces like



temperature, water vapor pressure of the combustion gases, gas velocities and glass composition all influence the evaporation rates of volatile components from the melt as described in chapter 1.

Problems with corrosion of silica type refractories in the combustion chamber have been observed due to these evaporation processes from the melt, especially in oxygen-fired furnaces. The alkali evaporation process governs the alkali vapor concentrations in the furnace atmosphere and consequently the reactions between these aggressive vapors and silica refractory materials in the superstructure (crown) [3].

Alkali and lead vapors appear to be aggressive towards silica refractory materials. Experiences with oxygen-fired soda-lime-silica furnaces equipped with silica crowns showed in some cases strong attack of silica [5][6] and formation of low viscous silicate phases at the refractory surface. Silica refractory type (quality) and design of the furnace are important aspects for the crown performance and lifetime.

The chemical attack of silica crowns by these alkali vapors depend mainly on temperature, gas velocities and sodium vapor pressures [2][3][7][8][9][10][11].

This paragraph, shows the results of evaporation modeling for industrial glass melt processes. Furthermore, the reaction mechanisms and thermodynamics of silica attack by sodium vapors will be discussed and modeling results for the kinetics of silica attack by sodium hydroxide, evaporating from the melt are shown.

### **5.2.1 Modeling of evaporation of sodium species from soda-lime-silicate glass melts in industrial furnaces**

The evaporation model, described in chapter 2, is applied to calculate the saturation vapor pressures of NaOH ( $p_{\text{NaOH}}^*$ ) above the soda-lime-silicate melts. The evaporated species diffusing through the gaseous boundary layer above the melt into the main combustion gas stream are distributed by the turbulent gas flows in the combustion space. As discussed in paragraph 5.1 the distribution of the vapors in the furnace atmosphere depends on the flame patterns, burner types, burner positions, design of combustion chamber and position and size of the exhaust port. As described in paragraph 5.1, CFD modeling can be applied to estimate the three velocity components, pressure and the concentration of the volatile species in each cell of the gas phase domain. The CFD modeling is used to calculate the distribution of the vapors and to estimate the concentration levels close to the silica crown [12]. The

concentration levels of evaporated NaOH at positions in the combustion space close to the crown are important for the attack of silica by these vapors [13].

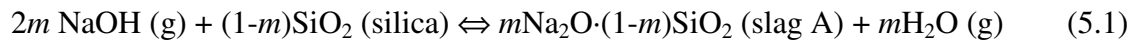
Wu et al [12] showed examples of CFD calculations and modeling results for NaOH distribution in combustion spaces of oxygen-fired soda-lime-silica glass furnaces using evaporation models as described in references [14][15]. He showed that the height of the combustion chamber and position of the exhaust port of the furnace have an important effect on the evaporation rate from the melt and distribution of the glass melt vapors (NaOH in this case) in the combustion space. An increase of the crown height in combination with increased burner distance from glass melt surface and a lower vertical exhaust port position will lower the sodium species vapor pressures at the crown. For a shallow crown (normal crown) the NaOH vapor pressure is typically 65-80 % of the NaOH vapor pressure 5-10 cm above the glass melt surface (just above the boundary layer). For taller crowns with a 50 up to 100 % increased height, the NaOH concentrations close to the crown surface is typically less than 50 % of the partial vapor pressure level of NaOH, at about 5-10 cm above the melt.

In this study, vapor pressures of sodium species in combustion spaces of a few industrial soda-lime-silica glass melting furnaces have been measured. Typical levels of the total vapor pressure of sodium species in these oxygen-natural gas fired furnaces, at positions close to the silica crown are 18-25 Pa (close to values calculated by Wu [12]), but locally higher levels have been found. In the case of very shallow crowns much higher  $p_{\text{NaOH}}$  values can be expected. Thus, the ratio of the partial sodium vapor pressure at positions a few cm from the crown to the partial sodium vapor hydroxide pressure above the melt generally decreases by increasing the height (distance between crown and glass melt) of the glass furnace combustion chamber.

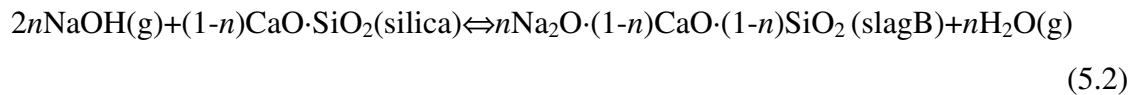
### 5.2.2 Reactions between silica and sodium vapors

Experimental refractory corrosion studies on laboratory scale [3][7], simulating glass furnace atmospheres, showed that the absorption of sodium in silica refractory materials during exposure of silica to sodium hydroxide vapors depends strongly on gas velocity. This observation indicates that the mass transfer of sodium species in the gas phase towards the surface of the silica refractory, for instance the surface of the silica crown, strongly determines the kinetics of sodium absorption and sodium silicate formation and loss of silica refractory material by this process.

Silica can react directly with sodium vapors transferred to the silica surface:

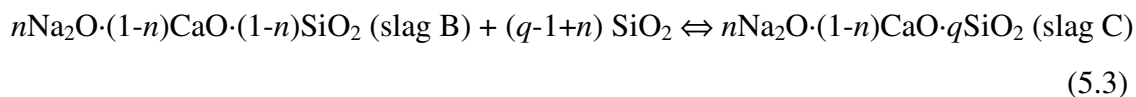


However, most silica types contain about 5 mass-% calcium silicate. Calcium silicate is a binding phase between the pure silica (tridymite or cristobalite) phases. According to the CaO-Na<sub>2</sub>O-SiO<sub>2</sub> ternary phase diagram [16] this phase absorbs sodium species from the vapor phase:



This reaction product B, the non-reacted silica and the calcium silicate phase are in equilibrium with each other until all calcium silicate has reacted. Then this reaction product (slag B) will absorb more sodium from the vapor phase and will dissolve silica, changing the composition of the slag (slag becomes sodium and silica richer and the lime content in the slag will decrease) and leading to increased silica loss. The rate of these reactions is determined by the mass transfer of NaOH to the silica refractory surface and the sodium infiltration in the formed silicate phases. Due to diffusion of sodium species in the silica material, in progress of time the Na<sub>2</sub>O-infiltration and silicate slag reaction proceeds into interior layers of the crown.

The composition of the silicate phase (Na<sub>2</sub>O-CaO-SiO<sub>2</sub> phase) at the silica surface determines the NaOH saturation vapor pressure in equilibrium with the prevalent water vapor pressure in the combustion/furnace atmosphere and this phase. This silicate phase composition depends on time and will change due to absorption of sodium from the atmosphere (reaction equation 5.2) and the dissolution of silica in this slag B and due to the diffusion of sodium oxide into the interior layers. The loss of silica by dissolution in the formed sodium calcium silicate slag is given by the reaction:



Slag C can further absorb sodium oxide (from the gas phase) and silicon oxide (from the non-reacted part of the silica), following the liquidus compositions (at prevalent temperature) given in the ternary phase diagram [16].

### 5.2.3 Kinetics of silica attack by alkali vapors

Beerkens et al. [2][3] developed a kinetic model, based on the mass transfer process in the gas phase. Mass transfer is dependent on gas velocity, shape of crown, vapor pressure of NaOH in furnace atmosphere, NaOH equilibrium pressure (equilibrium of NaOH in gas phase with the Na<sub>2</sub>O in silicate surface slag) and on the diffusion mass transfer in the silicate phases. The model assumes local chemical equilibrium between all involved phases: the NaOH vapor pressure at the silica surface, the local silicate composition (reaction product) and the non-reacted silica.

Results of these models are the sodium concentration profiles in the glassy phase of the refractory, depending on exposure time. The fraction of dissolved silica (compared to original silica) in the refractory at different depths and times can be determined.

The parameters that determine the total conversion of the original silica into low viscous silicate slags (slag C) are:

- Temperature of the silica surface; at lower temperatures the silica or calcium silicate phase will absorb more sodium (higher concentrations) from the vapor phases compared to high temperatures;
- The gas velocity along the crown; the mass transfer coefficient ( $h_g = D_{\text{NaOH}}/\delta_N$ ), or Nernst boundary layer thickness for NaOH, depends on the gas velocity. The gas phase mass transfer of NaOH caused by the driving force: ( $p_{\text{NaOH}}^{\text{crown,bulk}} - p_{\text{NaOH}}^{\text{refractory}*}$ ) and mass transfer coefficient  $h_g$  ( $\text{m}\cdot\text{s}^{-1}$ ) leads to flux  $Q_{\text{NaOH}}$  ( $\text{mol}\cdot\text{m}^{-2}\cdot\text{s}^{-1}$ ):

$$Q_{\text{NaOH}} = h_g \cdot \left( \frac{p_{\text{NaOH}}^{\text{crown,bulk}} - p_{\text{NaOH}}^{\text{refractory}*}}{R \cdot T} \right) \quad (5.4)$$

$p_{\text{NaOH}}^{\text{refractory}*}$  = local partial pressure of NaOH in equilibrium with water vapor pressure and composition of the silicate layer at the surface of the silica crown (Pa)

The value of  $h_g$  depends on gas velocity, distance from the leading edge of the gas flow along the refractory surface, gas properties (density, viscosity), and geometrical properties of the crown. For turbulent flow conditions in the gas phase,  $h_g$  is generally proportional to the gas velocity along the crown to the power 0.8 [17][18] (for laminar flow to the power 0.5).

$$h_g = C_6 \cdot v_g^{0.8} \quad (5.5)$$

The value of  $C_6$  can be derived from Sherwood or Nusselt relations given in literature [14][17][18] for different flow characteristics.

- c. The NaOH vapor pressure  $p_{NaOH}^{crown,bulk}$  (see equation 5.4) in the furnace atmosphere close to the crown.

A high evaporation rate and strong mixing conditions in the combustion space leads to high values of  $p_{NaOH}^{crown,bulk}$  at the vicinity of the crown.

- d. The calcium content.

This concentration in the silica refractory determines the volume of material (initially  $CaO \cdot SiO_2$ ) directly reacting with sodium (equation 5.2), forming a sodium calcium silicate slag. A large concentration of calcium silicate will form a large volume of slag in which the silica can dissolve before complete silica saturation in this slag. Thus increasing CaO concentration will increase the reactive volume of silicate slag B in the silica after exposure to a furnace atmosphere.

Figure 5.5 shows the non-dissolved fraction of silica relative to the original pure  $SiO_2$  grains in the silica refractory at equilibrium conditions for different temperatures and 2 silica types (0.5 mol and 2.5 mol-% CaO) as a function of NaOH vapor pressure. This figure has been derived from thermodynamic calculations, using the ASM approach. Increasing  $p_{NaOH}$  levels and decreasing temperatures lead to a lower fraction of non-dissolved silica at equilibrium conditions or with other words will cause more silica being finally dissolved in the silicate slag phases.

High evaporation rates of alkali species (e.g. NaOH) from the glass melt surface and low volume flows (such as in oxygen-fired furnaces) in the combustion process will lead to high NaOH concentration levels due to limited dilution of the aggressive glass melt vapors.

Thus,  $p_{NaOH}^{bulk}$  values will become higher as combustion gas volume decrease. From *Figure 5.5* we can observe that at values of  $p_{NaOH}^{bulk} > 20$  Pa and temperatures below 1400-1450 °C, silica strongly tends to reacts with NaOH (undissolved silica fraction approaches a value 0). The rate of silica attack depends on the mass transfer process in the gas phase (equation 5.4).

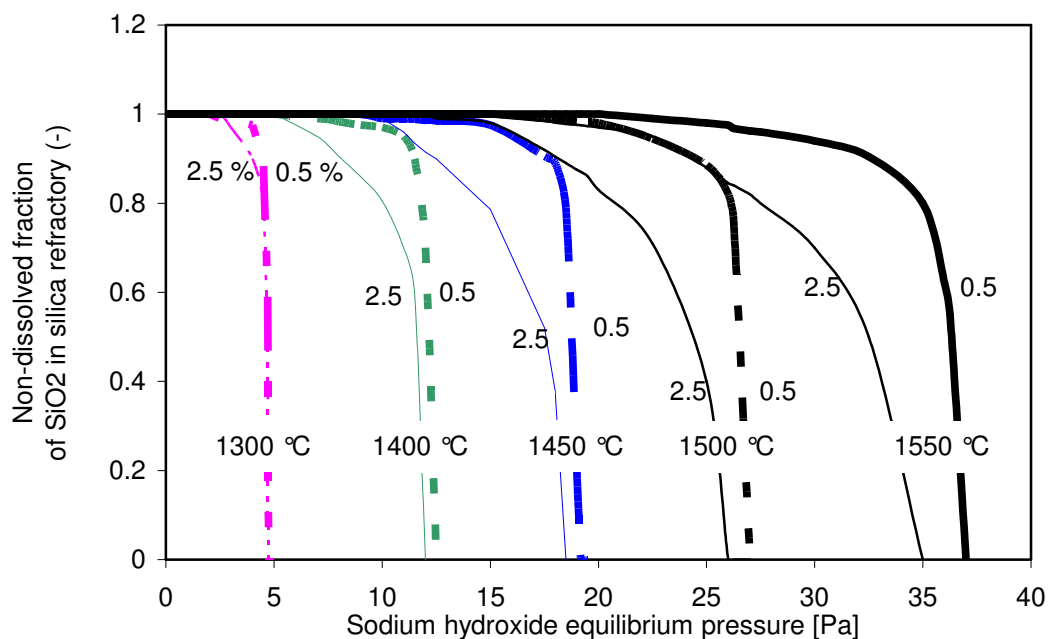


Figure 5.5: Non-dissolved  $\text{SiO}_2$  in silica refractory in equilibrium with  $\text{NaOH}$  vapor pressure (X-axis) at different temperatures for 2 silica types (with 0.5 mole-% and 2.5 mole-%  $\text{CaO}$ ). Below a certain temperature almost all silica will finally dissolve when exceeding a certain  $p\text{NaOH}$ -level [2].

On one hand side increased furnace temperatures will enhance the evaporation of glass melt volatiles, but increased crown temperatures are less sensitive for alkali attack than lower temperatures.

#### 5.2.4 Modeling results of evaporation kinetics for sodium evaporation from soda-lime-silicate glass melt in industrial glass furnaces

The evaporation loss and volatilization rates depend on the following parameters:

- Glass melt composition. Components with high chemical activity ( $\text{Na}_2\text{O}$ ,  $\text{B}_2\text{O}_3$ ,  $\text{PbO}$  etcetera) show high rates of reaction, forming volatile reaction products. The chemical activity level can be determined by thermodynamic models similar to associated species models [1][9] or models described by Pelton et al. [19], Shakhmatkin et al. [20] and Conradt [21].

- b. Temperature at glass melt surface. Especially at temperatures above 1400-1500 °C, the saturation vapor pressures of the evaporation products become significant and increase progressively with temperature.
- c. Gas flow conditions. Turbulent gas flows with high gas velocities (high Reynolds number) lead to thin gas phase boundary layers adjacent to the glass melt surface, steep concentration gradients of the evaporating components in the gas phase, and high mass transfer rates.
- d. Composition of furnace atmosphere. Increased water vapor concentration cause strong NaOH evaporation, carbon monoxide will lead to extra formation of sodium vapor (elemental Na).
- e. Depletion of volatile components at the glass melt surface. Lower evaporation rates are expected as a result of the lower chemical activities of volatile components at the glass melt surface. Convection in the glass melt may counteract this depletion of volatile species at the glass melt surface.

#### Validation of industrial evaporation model

For a few oxygen-natural gas fired industrial soda-lime-silica glass melting furnaces, total sodium evaporation rates have been estimated by evaporation modeling. The sodium evaporation rates have also been measured to be able to validate the evaporation model. All the furnaces show about the same designs. In all these furnaces the same type of glass is produced. But the burner settings were different. Table 5.1 shows some process data of these furnaces. Based on results of CFD modeling the actual gas velocity a few centimeters above the melt (outside the boundary layer) is estimated on 0.5-0.7 m/s.

The measured specific particulate (per ton molten glass) and sodium emissions are distinctly different for the different furnace situations and burner settings. The evaporation model results show that the burner settings (mainly influencing gas velocity above the melt and local CO concentration) and the reducing/oxidizing combustion conditions greatly effect the evaporation level of sodium species. The quantitative effect of temperature, gas velocity, water vapor pressure and partial CO pressure on the sodium evaporation rate in these furnaces is estimated by a sensitivity analysis. For this sensitivity analysis the empirical relation 5.6 has been applied [22]. With this equation the total evaporation rates of sodium species can be estimated as a function of temperature (T), gas velocity (v), water vapor pressure ( $p_{H_2O}$ ) and the CO vapor pressure ( $p_{CO}$ ).

Table 5.1: Operational conditions of oxygen-gas fired soda-lime-silica glass furnaces and measured particulate emissions. Differences between the 5 tests are mainly burner type and temperature levels. Three different furnaces are used for these tests.

Test number (burner settings & furnace)	1	2	3	4	5
Average glass melt surface temperature in °C estimated from coupled crown temperatures	1494	1494	1511	1511	1453
Surface area in m <sup>2</sup>	39	39	39	39	60
Na <sub>2</sub> O content of glass in mass%	16.5	16.5	16.5	16.5	16.5
Water vapor pressure in furnace atmosphere in 10 <sup>5</sup> Pa	0.6	0.6	0.6	0.6	0.6
Burner type	tube-in-tube	sheet flame	sheet flame	sheet flame	staged
Low Momentum/high momentum burner	high	high	high	high	low
Estimated oxygen pressure above melt in 10 <sup>5</sup> Pa	0.03	0	0	0	0.005
CO-pressure above melt in 10 <sup>5</sup> Pa	0.001	0.065	0.065	0.013	< 0.001
Burner horizontal or directed to glass melt surface	horizontal	7° directed	7° directed	7° directed	horizontal
Measured dust emission in kg/t glass	0.276	0.398	0.559	0.485	0.189
Measured Na <sub>2</sub> O emission in kg/t glass	0.096	0.190	0.315	0.262	0.087
Measured NaOH concentration in furnace atmosphere in Pa	21.8	26.0	36.0	38.5	9.9

$$Q_{Na-total} = C_5 \cdot \sqrt{P_{H_2O}} \cdot v^{0.8} \cdot e^{-23500/T} + C_6 \cdot \sqrt{\frac{P_{CO}}{P_{CO_2}}} \cdot v^{0.8} \cdot e^{-20500/T} \quad (5.6)$$

The different relevant process parameters in this analysis have been varied between:

- glass surface temperature (T) : 1420 – 1520 °C
- water vapor pressure (pH<sub>2</sub>O) : 0.5 – 0.65 bar
- gas velocity above glass surface (v) : 0.5 – 0.9 m/s
- CO levels in atmosphere : 0 – 7 vol.-%, dry

Figure 5.6 shows the effect of reducing flames on the sodium evaporation. In case of 3.5 % CO in the combustion space just above the melt, the total sodium evaporation rate (Na + NaOH) is doubled compared to an atmosphere without CO (NaOH). The effects of temperature, gas velocity and water vapor pressure are given in Figure 5.7. The influence of temperature variations in these ranges seems to be of major importance. A temperature increase from 1470 to 1520 °C results in a doubling of the sodium evaporation rate, an increase of the gas velocity from 0.7 till 0.9 m/s shows a 25 % higher sodium evaporation



rate. Variations in water vapor pressure between 0.5 and 0.65 bar hardly influences the total sodium evaporation.

Figure 5.8 shows the results of the industrial measurements: obviously changes in the position and type of burner and the oxygen-natural gas ratio (determining  $p_{O_2}$  and  $p_{CO}$  vapor pressures) will cause large differences in dust emissions and sodium evaporation. The gas velocities and glass melt surface temperatures in these examined furnaces are calculated with a CFD model [23]. Table 5.1 shows also data for the estimated gas velocity values and average glass melt surface temperatures. The modeling results for NaOH and Na evaporation rates (only Na and NaOH evaporation is taken into account) and consequently the total  $Na_2O$  losses from the melt show the same trend as the measurements, see Figure 5.8. The model shows that the hot spot area at the glass melt surface, occupying about 30 % of the total glass melt surface is responsible for 60-80 % of the total amount of released sodium species from the melt.

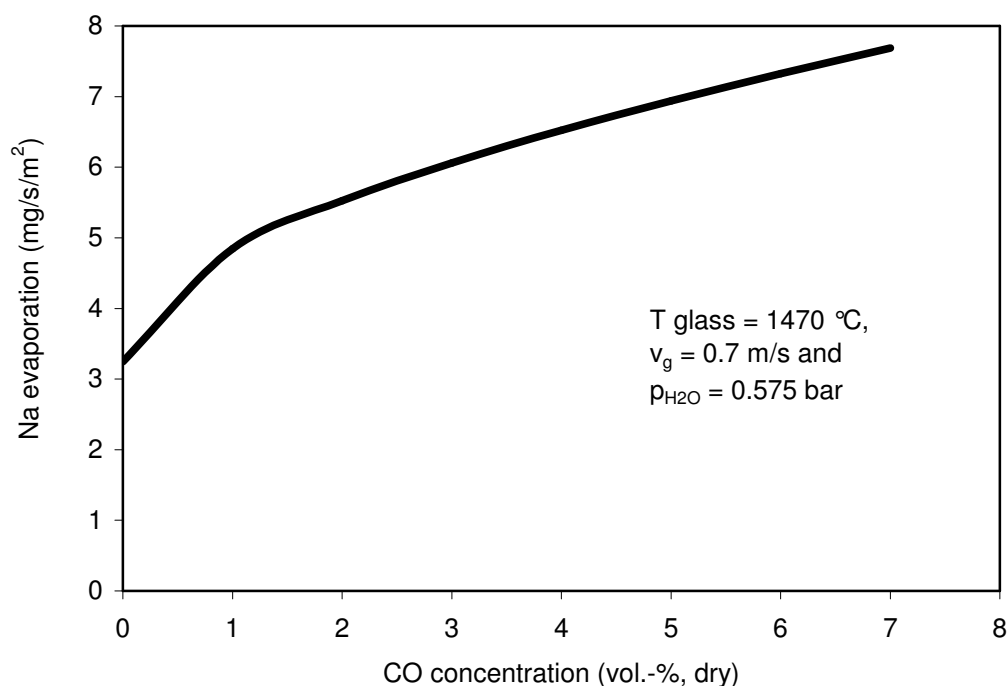


Figure 5.6: Modeling result for sodium evaporation in oxy-fuel fired soda-lime-silica glass furnaces. Influence of CO (combustion chamber) on the sodium evaporation.

### Burner elevation

Figure 5.9 shows the estimated effect of the burner position above the glass melt surface on evaporation and dust emissions. CFD models for the combustion chamber have been used to estimate the gas velocities above the glass melt surface. An increase of the distance between the burner and glass melt surface leads to a significant lower gas velocity above the melt, lower evaporation rate and this lowers the concentrations of glass melt vapors in the furnace atmosphere.

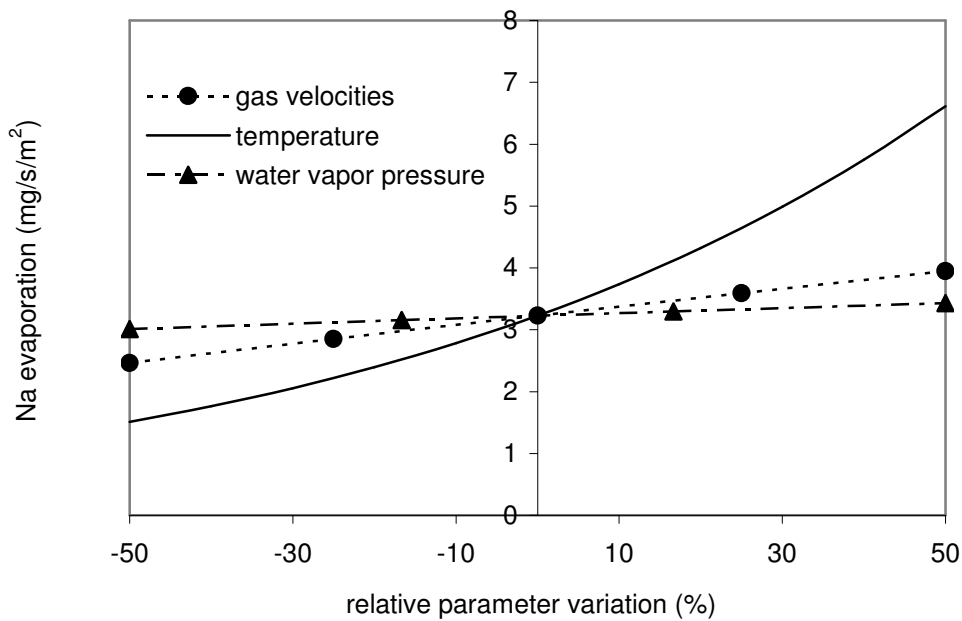


Figure 5.7: Sodium evaporation rate in oxygen-natural gas fired soda-lime-silica glass furnaces. Sensitivity analysis by modeling the total sodium evaporation, dependent on the most relevant process parameters within given ranges

Water vapor pressure range:	0.5 bar (-50 %) and 0.65 bar (+50 %).
Temperature range:	1420 till 1520 °C (y = 0: 1470 °C)
Gas velocity range:	0.5 - 0.9 m/s (y = 0: 0.7 m/s)

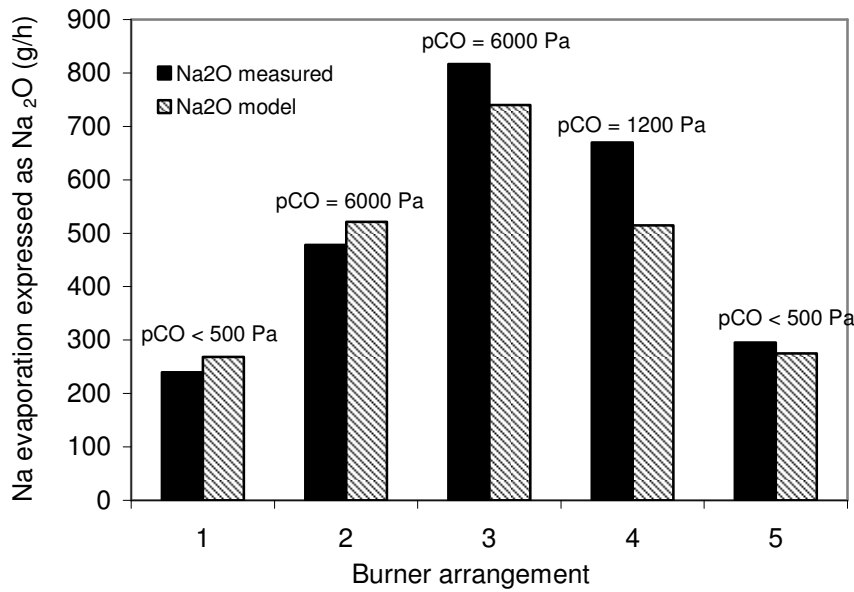


Figure 5.8: Na<sub>2</sub>O evaporation losses (by Na and NaOH evaporation) for 5 different situations (process conditions) in oxy-gas fired soda-lime glass furnaces. Results of measurements and evaporation model. The dust emissions are about proportional to Na<sub>2</sub>O loss

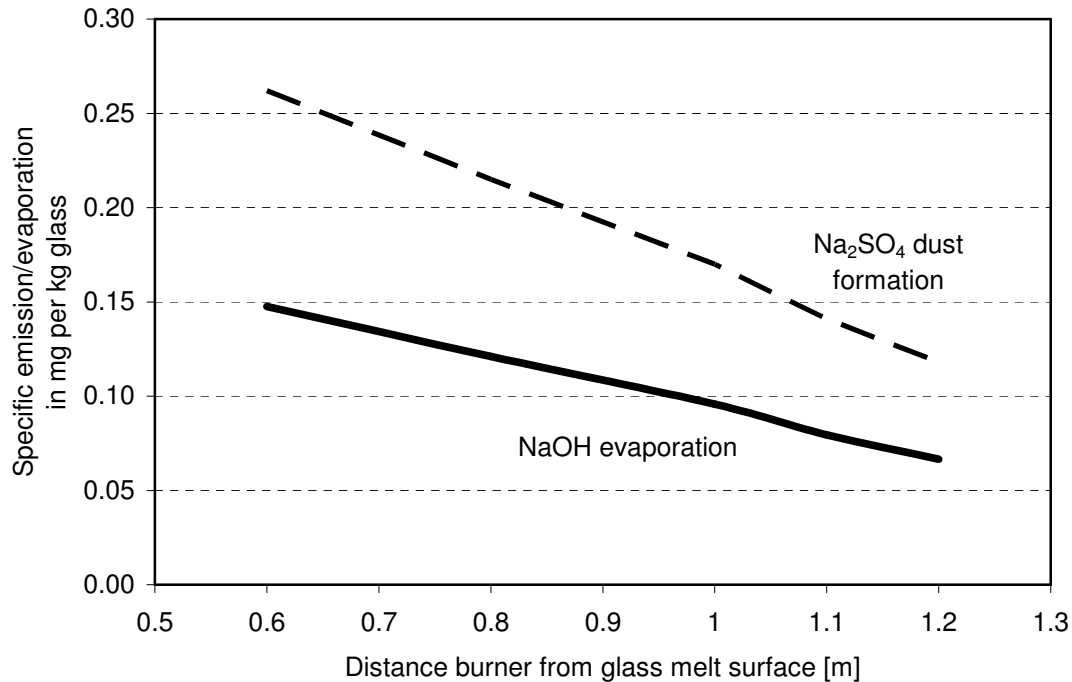


Figure 5.9: Effect of vertical burner position from melt on sodium hydroxide evaporation from soda-lime-silica glass melt and consequently sodium sulfate dust emissions

### 5.2.5 Modeling results of silica attack

Observations in this study from industrial oxygen-natural gas fired soda-lime-silica glass furnaces, show typical NaOH vapor pressures in the furnace atmosphere of 15 to more than 20 Pa and severe corrosion when silica surface temperatures decrease below 1450 °C at  $p_{\text{NaOH}} > 18$  Pa. The modeling results shown in Figure 5.5 predict the same behavior. For  $p_{\text{NaOH}}$  levels below 20 Pa and temperatures above 1500 °C only a limited part of the silica will be converted into a slag in case silica with low or no CaO contents is applied.

The rate at which the silica reacts can be determined by calculation of the sodium transfer to the silica surface and subsequently infiltration of sodium species into the refractory by diffusion. For these calculations mass transfer equations are used and the diffusion equation of Fick (equation 2.4) is solved. Furthermore, a local equilibrium between the residual SiO<sub>2</sub> phases and the sodium calcium silicate slag in the refractory interior is assumed.

From the average slag composition and temperature, the slag viscosity is derived. For Na<sub>2</sub>O, Hermans [24] derived a correlation between viscosity and sodium oxide interdiffusivity (equation 2.17). The sodium inter-diffusion coefficient in the silica is estimated to be  $1 \cdot 10^{-10}$  to  $2 \cdot 10^{-10}$  m<sup>2</sup>/s at respectively 1350 °C and 1600 °C.

The silica refractory -NaOH interaction modeling steps are:

1. Determination of the NaOH equilibrium pressure at the silica surface (NaOH in equilibrium with water vapor pressure and silicate composition at surface);
2. Flux of NaOH to surface determined by equation 5.4. The local vapor pressure of NaOH in the combustion space can be measured or derived by CFD modeling in combination with evaporation models [3];
3. Penetration of NaOH into refractory by diffusion;
4. Dissolution of silica in silicate phase as a function of distance from the surface, assuming local chemical equilibrium between the silica and the sodium enriched silicate slag in the refractory;
5. Calculation of the fraction of dissolved silica (function of position);
6. Next time-step and determination of change in surface composition;
7. Step 1 again.

Figure 5.10 shows at 1400 °C the silica loss at different time intervals for a NaOH vapor pressure of 20 Pa and a gas velocity of 2.5 m/s.

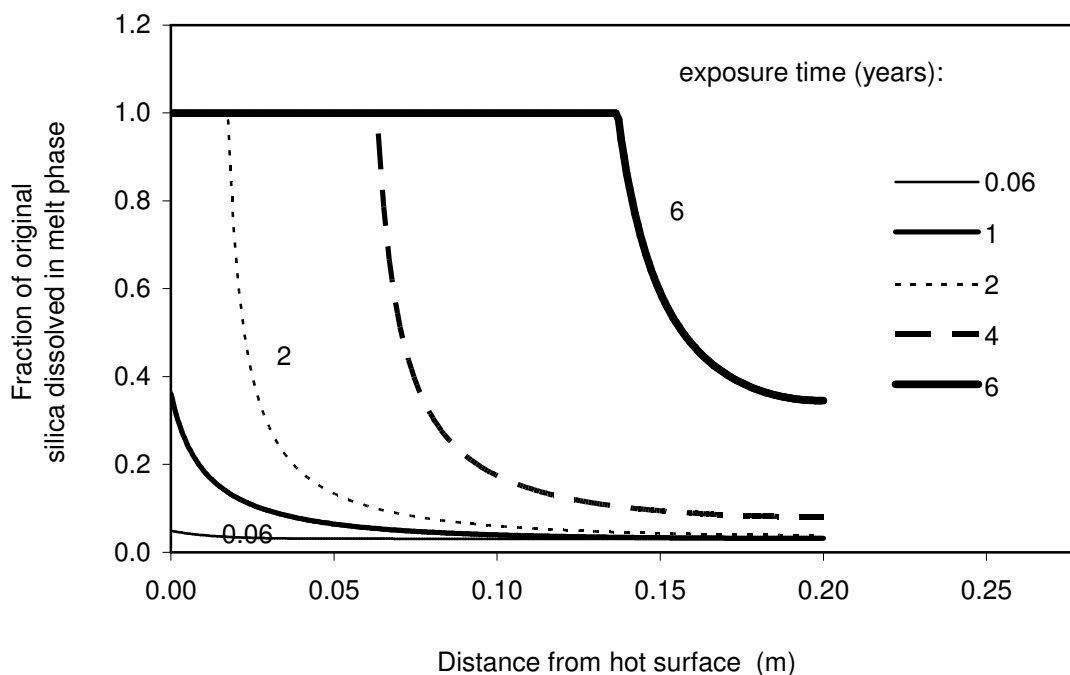


Figure 5.10: Loss of silica after 0.06 to 6 years exposure to oxygen-gas fired furnace atmosphere at 1400 °C and  $p_{\text{NaOH}} = 20 \text{ Pa}$  for a local gas velocity of 2.5 m/s for silica with 2.5 mass-% CaO, 2 m downstream the leading edge.

After 6 years about 12 cm of silica is completely dissolved and lost. Typical slag compositions: 7-12 mass %  $\text{Na}_2\text{O}$  about 10-15 % CaO and about 80 mass %  $\text{SiO}_2$ .

Figure 5.11 shows for almost the same conditions, but for 100 °C higher temperature, the silica loss at different depths in the refractory. The increased temperature lowers the silica loss considerably and this agrees very well with industrial observations. In case of very high NaOH vapor pressures (> 25 Pa) the refractory can also be attacked above 1500 °C. Model calculations show less than 10 % silica loss in the refractory, even at the surface after 6 years for  $p_{\text{NaOH}} = 20 \text{ Pa}$ , and at temperature levels of 1550 °C.

Increasing the crown heights may keep the NaOH vapor pressures below 15-18 Pa and in that case hardly any silica attack is expected for temperatures above 1470 °C when using silica with low CaO contents.

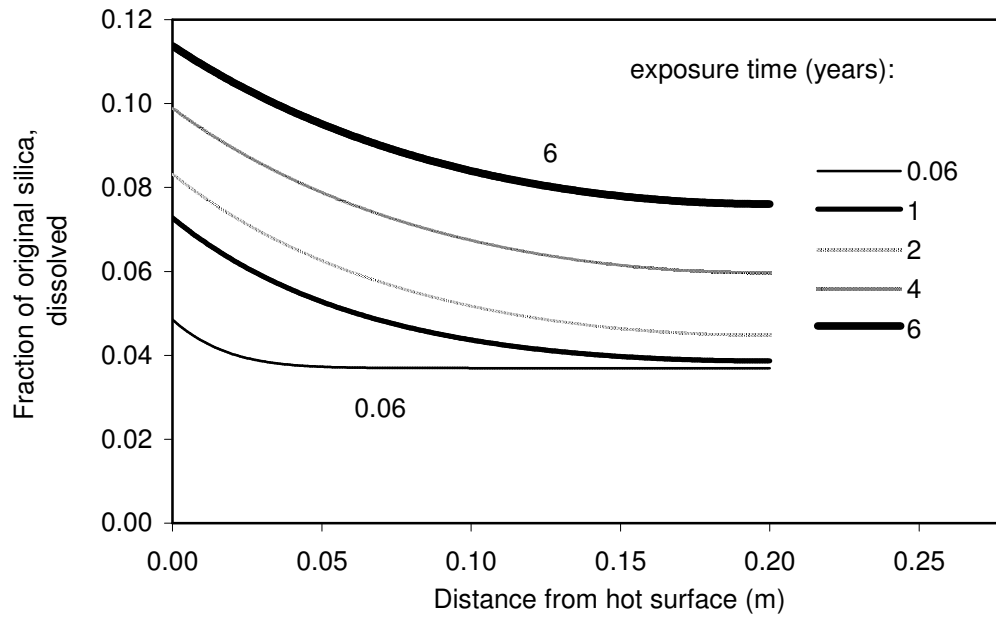


Figure 5.11: Loss of silica after 0.06 to 6 years exposure to oxygen-gas fired furnace atmosphere at 1500 °C and  $p_{\text{NaOH}} = 20 \text{ Pa}$  for gas velocity of 2.5 m/s for silica with 2.5 mass-% CaO, 2 m downstream leading edge. Note the small amount of dissolved  $\text{SiO}_2$  (< 12 %) even after 6 years.

In order to avoid these critical conditions, the distance between the glass melt surface and burners should be increased (lowering evaporation rates and NaOH pressures), the combustion space height may be increased (the tall crown concept) [25] and CFD models can be used to optimize design and position of the exhaust port. Application of silica refractory qualities with low CaO content is preferred.

### 5.3 Boron evaporation from industrial E-glass melts

Boron evaporation rates are predicted for an oxygen-gas fired alkali-lean (total alkali-oxides < 1 mass-%) borosilicate E-glass furnace. CFD modeling has been applied to calculate gas velocity profiles in the combustion chamber and to predict the Nernst boundary layer thickness (see chapter 2.3.3). Figure 5.12 shows such a gas velocity profile for a cross section with oxygen-gas burner in the furnace [26]. The TNO Glass Tank Model has been used to calculate the glass melt surface temperatures [23][26]. The glass composition is about the same as the composition of 'glass 2' shown in chapter 4, table 4.2 and contains about 5 mass-% B<sub>2</sub>O<sub>3</sub>. The melt is assumed to be homogeneous (no surface depletion) and the impact of foam and melting raw material batch on the boron evaporation is neglected.

In this E-glass furnace, boron mainly evaporates under influence of water to form gaseous meta-boric acid, i.e. HBO<sub>2</sub> (equations 1.30 and 1.31). The evaporation rates of NaBO<sub>2</sub> and KBO<sub>2</sub> are expected to be much lower. The required chemical activities values of B<sub>2</sub>O<sub>3</sub> in the melt were derived from the Associated Species Model for borosilicate glass melts (see paragraph 2.5.3). Furthermore, the local boron concentrations in the combustion chamber have been measured by using the equipment shown in Figure 5.4. From the natural gas consumption per burner, the composition of the natural gas and the measured local CO<sub>2</sub> concentrations, the local flue gas volume flows were calculated from the CO<sub>2</sub> balance. From the measured boron concentration in the combustion gases and the local flue gas volume flows the boron evaporation rates have been estimated.

Figure 5.13 shows the calculated HBO<sub>2</sub> evaporation rate and glass surface temperature over the length axis in the centre of the furnace. For these calculations, the thermodynamic modified Associated Species Model was used, which is described in paragraph 2.5.3. Over the length axis the Nernst boundary layer thickness is about constant: 2.65 cm. It can be seen that the boron evaporation rate is strongly affected by the glass surface temperature. The maximum HBO<sub>2</sub> evaporation rate is  $3.0 \cdot 10^{-3}$  moles/s/m<sup>2</sup>. The measured boron evaporation rates, shown in Figure 5.14, also show this strong temperature dependency. The measured maximum HBO<sub>2</sub> evaporation rate is  $3.8 \cdot 10^{-3}$  moles/s/m<sup>2</sup>. Finally the total B<sub>2</sub>O<sub>3</sub> losses are modeled and measured. The total boron species concentrations were measured in the hot flue gases directly leaving the combustion chamber. For the modeling results two different thermodynamic models were applied: 1) the Associated Species Model for borosilicate glass melts described in paragraph 2.5.3 and 2) Factsage [19]. The measuring and modeling results

are shown in Figure 5.15. By applying the modified Associated Species Model the measured and modeled boron evaporation rates differ maximum 25 %.

When using the derived chemical activities of  $B_2O_3$  from Factsage, the modeled boron evaporation rates are about 4 times higher than the measured boron evaporation rates.

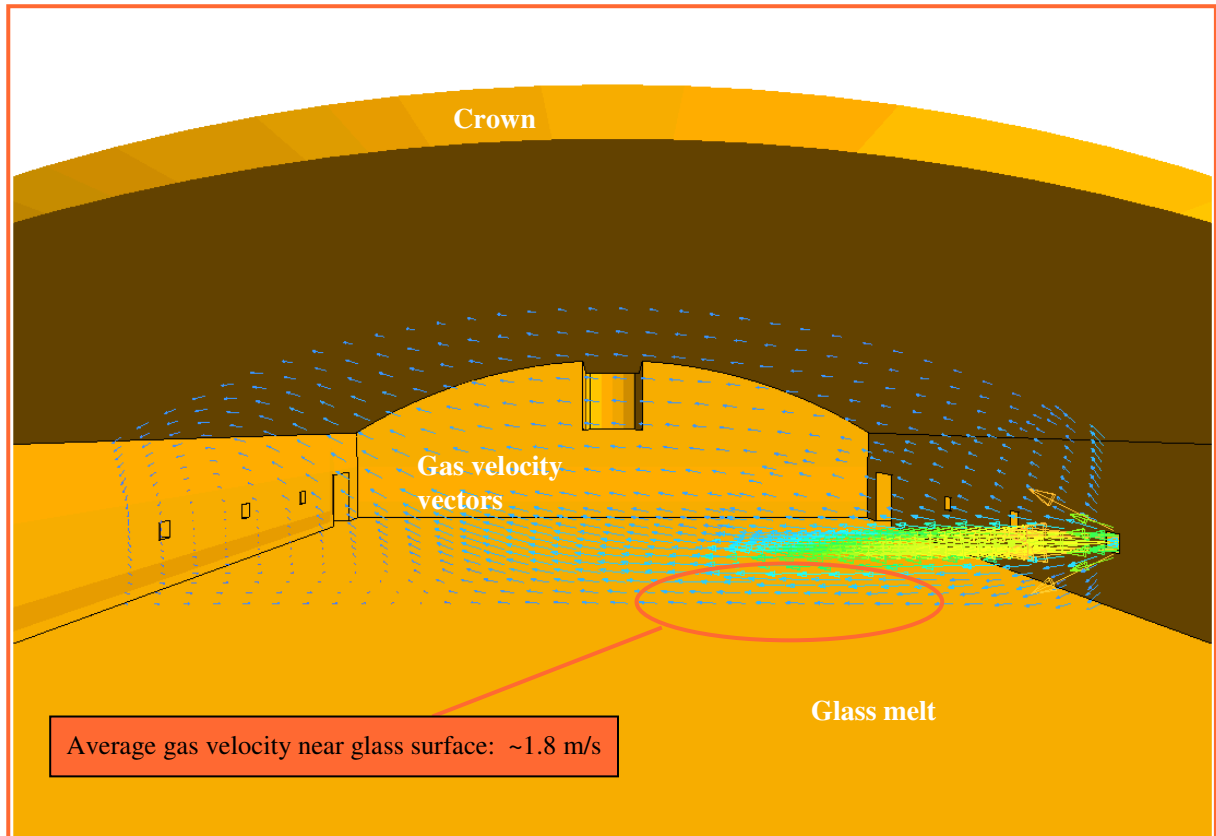


Figure 5.12: Calculated gas velocity profile at a vertical cross section of an oxygen-gas fired E-glass furnace, including one burner [26]. The gas velocity profiles were used to derive the Nernst boundary layer thickness near the glass surface.



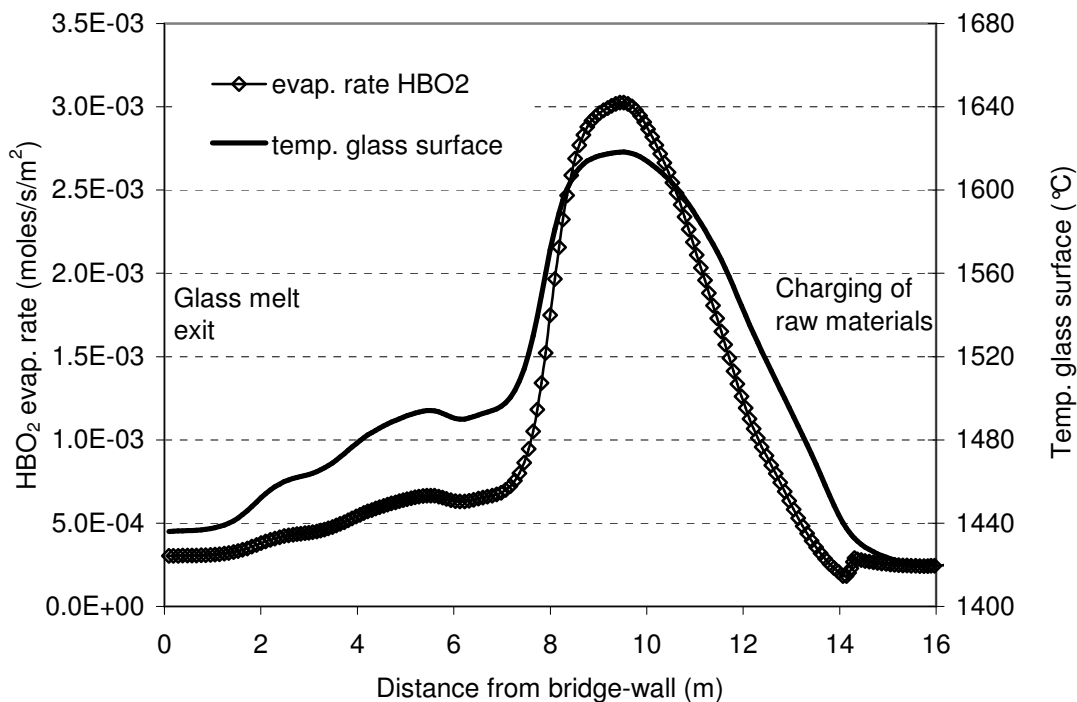


Figure 5.13: Calculated evaporation rate profile of HBO<sub>2</sub> and temperature profile over the length axis of an oxygen-gas fired E-glass furnace. The modeling results have been obtained from CFD calculations in combination with the modified thermodynamic Associated Species Model described in paragraph 2.5.3.

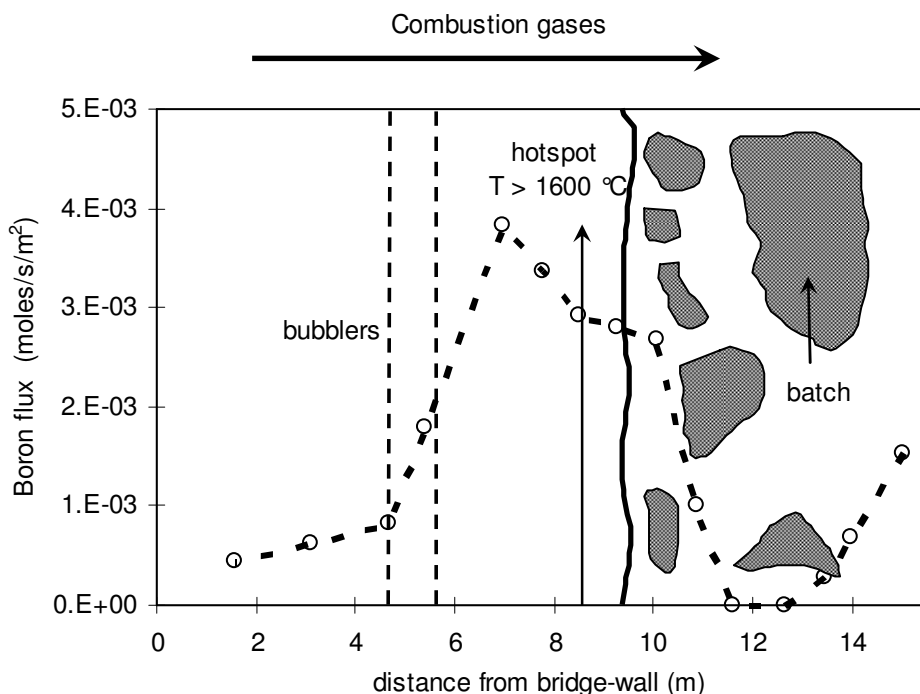


Figure 5.14: Measured boron evaporation rates in an industrial E-glass furnace. In the figure the position of the hot-spot, batch blanket and bubbler rows are shown.

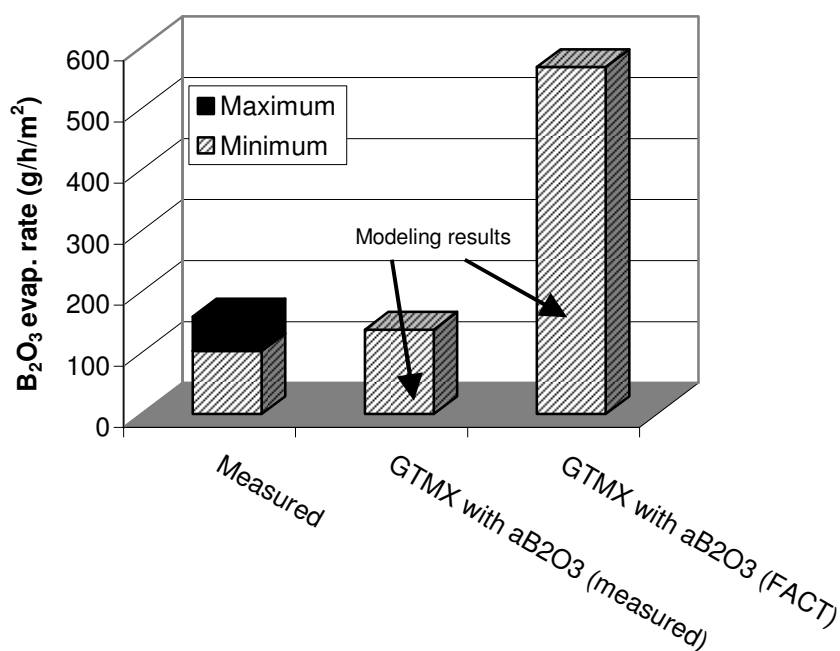


Figure 5.15: Total average  $B_2O_3$  losses of an industrial oxygen-gas fired E-glass furnace. The total  $B_2O_3$  losses were measured in the hot flue gases directly leaving the combustion chamber. For the modeling results two different thermodynamic models were applied: 1) the modified Associated Species Model described in paragraph 2.5.3 and 2) Factsage [19]

#### 5.4 Conclusions chapter 5

The developed universal evaporation model, is applied to predict the evaporation rates of different volatile glass compounds from blank melts in industrial fossil-fuel fired glass furnaces. The model has been used to predict the evaporation rates of sodium species (NaOH, and Na) and boron species ( $HBO_2$ ), from glass melts in industrial glass furnaces. The measured and modeled local concentrations of volatile species in the combustion chambers of industrial glass furnaces are compared.

For an industrial oxygen-gas fired E-glass borosilicate glass furnace, the experimentally determined local boron species evaporation rates at different locations in the combustion chamber have been compared with the modeled local  $HBO_2$  evaporation rates. The measured maximum boron species evaporation rate was about 27 % higher than the modeled maximum boron evaporation rate (taking only  $HBO_2$  formation into account). Since industrial E-glass melts contains small amounts of alkali-oxides (0.5 - 1 mass-%), the difference between modeling results and measured values is probably caused by additional evaporation of other boron compounds such as  $KBO_2$  and  $NaBO_2$ .

For an oxygen-gas fired glass furnace, producing a multi-component soda-lime-silicate glass, the NaOH vapor pressures in the combustion chambers have been modeled. In several other comparable oxygen-gas fired glass furnaces, the total sodium concentrations were measured at different positions in the combustion chamber. At different positions in the combustion chamber above a nearly blank melt, the measured and modeled sodium concentrations deviate 10 to 20 %. Near the side wall of the combustion chamber, both the measured and modeled sodium concentrations lie between 160 and 260 v-ppm, near the crown the average sodium concentration was about 280 v-ppm.

In a third case, models have been used to estimate the kinetics of evaporation of sodium species from soda-lime-silicate glass melts in combination with a separate model (from literature) for silica refractory attack by sodium vapors. By combining these models the rate of corrosion of the silica refractory materials applied in the crown of the combustion chamber can be estimated. These models show the same trends as the recent observations in industrial practice of oxygen-fired glass furnaces: severe corrosion of silica by NaOH vapors in low temperature areas of the crown for  $p_{\text{NaOH}} > 15 \text{ Pa}$ .

For the evaporation modeling in industrial glass melt furnaces, the surface of the melt is assumed to be blank. However, in industrial glass melt furnaces the surface of the melt will partly be covered with a melting batch blanket of raw materials. Sometimes the surface of the melt is also partly covered with a foam layer.

The contribution of direct volatilization of raw material components from the surface of the batch blanket (i.e. mixture of glass forming raw materials) is probably low. Vapor pressures of these components are rather low up to 1200 °C, and above 1000 °C, the single components have reacted to form silicates and therefore the vapor pressures of most batch components above the reacting batch blankets will be relatively low.

Foaming may lead to higher evaporation rates of volatile glass components. In E-glass furnaces it is estimated that the evaporation rates of boron might probably increase 10 – 30 % as a result of foaming. The sodium evaporation rates in multi-component soda-lime-silicate glass furnaces, might increase 10 to 15 % as a result of foaming.

## References

- [1] H. van Limpt, R. Beerkens, O. Verheijen, 'Models and experiments for sodium evaporation from sodium containing silicate melts', *J. Am. Ceram. Soc.* **89** [11], 3446-3455 (2006)
- [2] J.A.C. van Limpt, R.G.C. Beerkens, 'Reduction of superstructure corrosion and emissions by modern glass furnace design and optimized operation', paper presented at XX ATIV conference, Parma, Italy, 14 – 16 September (2005)
- [3] R.G.C. Beerkens, O.S. Verheijen, 'Reactions of alkali vapours with silica based refractory in glass furnaces, thermodynamics and mass transfer', *Phys. Chem. Glasses* **46** [6], 583-594 (2005)
- [4] R.G.C. Beerkens, 'Deposits and condensation from flue gases in glass furnaces', PhD thesis Eindhoven University of Technology (Technische Hogeschool Eindhoven) December (1986)
- [5] H.T. Godard, L.H. Kotacska, J.F. Wosinski, S.M. Winder, A. Gupta, K.R. Selkregg, S. Gould, 'Refractory Corrosion Behaviour under Air-Fuel and Oxy-Fuel Environments', *Ceram. Eng. Sci. Proc.* **17** [1], 180-207 (1996)
- [6] A.J. Faber, O.S. Verheijen, 'Refractory corrosion under oxy-fuel firing conditions', *Ceram. Eng. Sci. Proc.* **18** [1], 109-119 (1997)
- [7] A.J. Faber, R.G.C. Beerkens, 'Reduction of Refractory Corrosion in Oxy-Fuel Glass Furnaces', Proceedings of the 18<sup>th</sup> International Congress on Glass San Francisco. Edited by the American Ceramic Society, Westerville Ohio, USA 1998 ICG 467 – 006, July (1998)
- [8] R.H. Nilson, S.K. Griffiths, N. Yang, P.M. Walsh, M.D. Allendorf, B. Bugeat, O. Marin, K.E. Spear, G. Pecoraro, 'Analytical models for high-temperature corrosion of silica refractories in glass-melting furnaces', *Glass Sci. Technol.* **76** [3], 136-151 (2003)
- [9] M.D. Allendorf, K.E. Spear, 'Thermodynamic Analysis of Silica Refractory Corrosion in Glass-Melting Furnaces'. *J. Electrochemical Soc.* **148** [2], B59-B67 (2001)
- [10] M.D. Allendorf, R.H. Nilson, B. Bugeat, M.U. Ghani, O. Marin, A. Gupta, G.A. Pecoraro, K.E. Spear, P.M. Walsh, H.E. Wolfe, 'Analytical models for high-temperature corrosion of silica refractories in glass-melting furnaces', *Advances in Fusion and Processing of Glass III. The American Ceramic Society, Westerville, OH. Ed. J.R. Varner, T.P. Seward III, H.A. Schaeffer, Ceram. Trans.* **141**, 163-178 (2003)
- [11] J. Kynik, S.M. Winder, K.R. Selkregg, 'Superstructure Refractory Selection for Oxyfuel melting of Lead-Alkali-Silicate Glass', *Advances in Fusion and Processing of Glass II. The*

American Ceramic Society, Westerville, OH. Ed. A.G. Clare & L.E. Jones, *Ceramic Trans.* **82**, 413 – 419 (1998)

[12] K.T. Wu, H. Kobayashi, 'Three-dimensional modelling of alkali volatilization/crown corrosion in oxy-fired glass furnaces', *Corrosion of materials by molten glass*. The American Ceramic Society Westerville OH. Ed. Pecoraro G.A. et al., **78**, 205-216 (1996)

[13] R.G.C. Beerkens, 'Angriff des Silikagewölbes durch Verdampfungsprodukte der Glasschmelze', *Kurzreferate German Glass Society* (editor Deutsche Glastechnische Gesellschaft e.V.), Annual Meeting Würzburg, 23.-25. May (2005)

[14] R.G.C. Beerkens, 'Modelling the kinetics of Volatilization from Glass Melts', *J. Am. Ceram. Soc.* **84** [9], 1952-1960 (2001)

[15] R.G.C. Beerkens, J.A.C. van Limpt, 'Evaporation in industrial glass melt furnaces', *Glastech. Ber. Sci. Technol.* **74** [9], 245 – 257 (2001)

[16] G.W. Morey, N.L. Bowen, 'High SiO<sub>2</sub> corner of system Na<sub>2</sub>O-CaO-SiO<sub>2</sub>', *J. Soc. Glass Technol.* **9**, 232-233 (1925)

[17] R.B. Bird, W.E. Stewart, E.N. Lightfoot, 'Transport Phenomena', John Wiley, New York (1960)

[18] V. Gnielinski, 'Wärmeübertragung bei erzwungener einphasiger Strömung', *VDI Wärmeatlas 6*. Edition VDI Verlag GmbH Düsseldorf, Ga1-Ga5 (1991)

[19] A.D. Pelton, G. Eriksson, M. Blander, 'A thermodynamic Database Computing System for Multi-component Glasses', *Proceedings of the 1<sup>st</sup> International Conference on Advances in the Fusion of Glass I*, Alfred NY. The American Ceramic Society, Westerville. Ed. by D.F. Bickford, E.N. Boulos, F. Olix, W.E. Horsfall, J.N. Lingscheit, W.C. LaCourse, F.E. Woolley, F. Harding, L.D. Pye, 27.1-27.11 (1988)

[20] B.A. Shakhmatkin, N.M. Vedishcheva, M.M. Shultz, A.C. Wright, 'The thermodynamic properties of oxide glasses and glass-forming liquids and their chemical structure', *J. Non-Crystalline Solids* **177**, 249-256 (1994)

[21] R. Conradt, 'A Simplified Procedure to Estimate Thermodynamic Activities in Multicomponent Oxide Melts', *Molten Salt Chemistry and Technology* ed. by H. Wendt, Trans Tech Publication Zürich, Switzerland **5-6**, 155-162 (1998)

[22] J.A.C. van Limpt, A.J. Faber, 'Reduction of emissions by decreasing volatilization in glass furnaces, phase 2; Experimental simulation tests on volatilization in glass furnaces', TNO report HAM-RPT-98-408, TNO Institute of Applied Physics, Eindhoven (1998)

- [23] A.M. Lankhorst, H.P.H Muijsenberg, M.J.P. Sanders, 'Coupled combustion modelling and glass tank modelling in oxy- and air-fired glass-melting furnaces', Proceedings International Symposium on Glass Problems ICG Annual Meeting September 4-6 (1996) Edited by Şişecam, Istanbul, Turkey, **1**, 378-384 (1996)
- [24] J. Hermans, 'Diffusion in Multicomponent Silicate Melts', PhD thesis Rheinisch-Westfälischen Technische Hochschule Aachen Germany (2004)
- [25] H. Kobayashi, 'Tall Crown Glass Furnace Technology for Oxy-Fuel Fired Glassmelting', 65<sup>th</sup> Conference on Glass Problems 19. – 20. October 2004. Columbus Ohio (USA), Cer. Eng. Sci. Proc. **26** [1] (2005)
- [26] A.M. Lankhorst, A.F.J.A. Habraken, O.M.G.C. Op den Camp, O.S. Verheijen, 'Simulation Of The Impact Of Different Combustion Systems On The Flow And Temperature Distribution In Glass Melting Furnaces' Presented at the HVG/NCNG Colloquium on Operation and Modelling of Glass Melting Furnaces, RWTH Aachen, Germany, November 8 (2005)



## 6. Conclusions and outlook

The main goal of our study was the development of a generic model to predict the kinetics of volatilization processes from glass melts in glass furnaces. The evaporation modeling approach that has been developed in this investigation, is applicable for all types of fossil fuel fired glass furnaces and can be applied universally to describe kinetics of evaporation processes from different multi-component glass compositions in laboratory transpiration experiments. Laboratory-scale transpiration evaporation experiments have been used to identify the most important evaporating glass melt species and to validate the evaporation modeling results. Evaporation kinetics of sodium-silicate melts, multi-component alkali-lime-silicate melts and alkali-free borosilicate melts have been studied by this equipment. Finally, the developed evaporation model has been applied to predict the evaporation rates in industrial glass melt furnaces.

The main conclusions of this study and the outlook are presented in this chapter.

### 6.1 Identification of volatile species and evaporation reactions

Sodium species are the main evaporating species from sodium-silicate melts and alkali-lime-silicate melts, but from the latter type of melt potassium species are released as well. Boron compounds are the most volatile species from alkali-lean borosilicate glass melts. In a humid, oxidized atmosphere, volatile glass melt compounds are released under influence of water vapor by the formation of volatile reaction products such as NaOH, KOH and HBO<sub>2</sub>. It has been shown that the evaporation rates of these species are proportional to the square root of the applied partial water vapor pressure ( $p_{\text{H}_2\text{O}}^{1/2}$ ). In a reduced atmosphere also elemental sodium and potassium evaporate.

From alkali-lime-silicate melts containing sulfur and chlorine, the species: Na<sub>2</sub>SO<sub>4</sub>, K<sub>2</sub>SO<sub>4</sub>, NaCl, KCl and HCl can be released, besides the main evaporating species which are hydroxide vapors and alkali atoms (K, Na). The evaporation rates of the sulfate and chloride compounds might be limited by the slow transport of sulfur and chloride to the surface of the static glass melts, as time progresses.

### 6.2 Mass transport relations for the gas phase (boundary layer approach)

For the experimental laboratory transpiration set-up as well as industrial glass furnaces, a modeling approach for the determination of the mass transport of evaporating



species into the gas phase has been developed. It has been shown for most cases, that mass transfer in the gas phase boundary layer is the main step governing evaporation kinetics.

For a complex geometrical configuration of a transpiration test set-up, CFD modeling has been applied to predict the mass transport of volatile species from glass melts or model liquids into a carrier gas and to understand the fluid dynamics in the gas phase. CFD models are applied to calculate the distribution of volatile species in this phase. Results of the CFD-modeling for water evaporation tests at room temperature have been validated by transpiration experiments. Excellent agreement was found between the model results and water evaporation experiments as the difference between the experimental measured evaporation rates and the CFD modeling results are less than 2 %.

The results of CFD modeling and the results of simple water transpiration evaporation experiments at room temperature are used to obtain relatively simple mass transport relations ( $Sh$  as a function of  $Re$  and  $Sc$ ) for a fixed geometry of the transpiration test set-up. These relations were shown to be applicable for other evaporating liquids and temperatures as well when using the same equipment.

### **6.3 Chemical activities of volatile glass compounds in multi-component silicate melts**

The thermodynamic Associated Species Model (ASM) has been applied and improved to derive chemical activities of volatile glass components like  $Na_2O$ ,  $K_2O$  and  $B_2O_3$ . The  $Na_2O$  activity values, calculated by the ASM model, are compared with experimental data derived from literature references. For ternary  $SiO_2$ - $Na_2O$ - $CaO$  melts at 1400 °C, the deviations between the modeled and experimentally derived activities are less than 30 %.

Three different thermodynamic models (including ASM) were used to derive chemical activities of sodium oxide in multi-component soda-lime-silicate based melts, between 1200 °C and 1600 °C. The maximum deviations, comparing the different models, decrease with increasing temperature from a factor 5 at 1300 °C to a factor 1.5 at 1600 °C.

In most cases the accuracy of the Associated Species Model appears to be sufficient to estimate evaporation rates from most glass melts as shown in this thesis. However, this level of inaccuracy can also explain a large part of the differences found between modeled and measured evaporation rates for these type of glass melts.

The chemical activities of  $Na_2O$  in binary sodium-silicate melts and ternary soda-lime-silicate melts, have been determined experimentally by laboratory evaporation tests, using the

transpiration set-up. From evaporation rates and known mass transfer relations, equilibrium vapor pressures and chemical activities of volatile glass melt species at the glass melt surface can be determined. On the other hand these activities have also been derived from the applied thermodynamic model in this study (ASM). The indirectly measured chemical activities are compared with the results of the thermodynamic Associated Species Model. A very good linear correlation has been obtained for the measured and modeled chemical activities of Na<sub>2</sub>O in ternary soda-lime-silicate and binary sodium-disilicate melts:

$$a_{\text{Na}_2\text{O}(\text{model})} = (0.98 \pm 0.04) \cdot a_{\text{Na}_2\text{O}(\text{measured})}$$

Furthermore, the chemical activities of Na<sub>2</sub>O and other species in more complex multi-component float glass melt surface compositions have been measured also. For this multi-component glass melt, the measured activities of Na<sub>2</sub>O in the surface layer of a float glass melts are, on average, about 20 % higher than the activities determined by the model (Associated Species Model).

The chemical activities of K<sub>2</sub>O at the surfaces of several types of multi-component alkali-silicate melts, have been determined from the measured KOH evaporation rates and compared with the results of the thermodynamic Associated Species Model assuming bulk glass compositions. The measured activities of K<sub>2</sub>O deviate less than 30 % from the modeled values.

Deviations might be caused by measuring errors, surface depletion of volatile compounds and/or incomplete databases for all relevant associated species used in the applied thermodynamic Associated Species Model. The maximum error in the measured chemical activities is estimated to be 20 – 25 %.

#### ***Extension of the thermodynamic model (ASM) for alkali-lean borosilicate glass melts***

The measured chemical activities of B<sub>2</sub>O<sub>3</sub> ( $a_{\text{B}_2\text{O}_3}$ ) of alkali-lean borosilicate types of glass melts used for the production of E-glass fibers, deviate 1 to 3 decades from results of existing thermodynamic models such as the Associated Species Model or the commercially available thermodynamic software package Factsage. This deviation is probably caused by: A) lack of accurate thermodynamic data (especially for stoichiometric calcium-borate compounds with a molar ratios CaO/B<sub>2</sub>O<sub>3</sub> > 3) of associated species in these glass compositions, B) absence of

important associated species in the model or C) to other phenomena such as non-ideal mixing of the chosen associated species.

In this study, the existing Associated Species Model is optimized for  $\text{SiO}_2\text{-CaO-Al}_2\text{O}_3\text{-B}_2\text{O}_3$  glass melt compositions. To improve the thermodynamic modeling of these kinds of melts, the associated species  $5\text{CaO}\cdot\text{B}_2\text{O}_3(\text{l})$  has been introduced and thermodynamic data (Gibbs energy values) of other stoichiometric calcium-borate species were derived by fitting procedures, using results of  $a_{\text{B}_2\text{O}_3}$  from laboratory evaporation tests. In this adapted model, immiscibility is not taken into account.

Both, the results of thermodynamic modeling as well as measuring results show a strong decrease in chemical activity of  $\text{B}_2\text{O}_3$  for concentrations below  $\pm 2.5$  mass-% in these borosilicate melts. This might be a result of a sudden change in the molecular structure of the melt below 2.5 mass-%  $\text{B}_2\text{O}_3$ .

#### **6.4 Transport of volatile compounds in the melt**

It is demonstrated by CFD modeling that, besides the effect of glass melt convection due to surface tension gradients or bubbles ascending in the melt, convection may take place as a result of non-uniform evaporation rates of volatile glass melt species along the glass melt surfaces. Because of the non-uniform evaporation rates, local concentration and density differences in the melt surface layer are induced. Local convection at the surface areas of the melt promotes the transport of melt from the bulk to the surface and suppress depletion of minor volatile compounds. However, temperature gradients, differences in surface tension and bubbles in the melt can strongly affect the (local) convection in the melt and the evaporation rates of minor species, such as chlorine, sulfur and fluorine.

The transport of boron in a  $\text{SiO}_2\text{-CaO-Al}_2\text{O}_3\text{-B}_2\text{O}_3$  melt during transpiration experiments, can not be described by one-dimensional diffusion process in a static melt. Only, the investigated glass melts with an average concentration less than 2.5 mass-%  $\text{B}_2\text{O}_3$  show significant  $\text{B}_2\text{O}_3$  depletion at the surface of the melt compared to the bulk. For the melts investigated here and  $\text{B}_2\text{O}_3$  concentrations higher than 2.5 mass-%, boron depletion takes place all over the glass melt volume as time proceeds and the composition of the melt was nearly uniform at all times. Possibly, borosilicate glass melts should be considered as a mixture of a silica rich melt phase and one or more borate melt phases, such as a calcium-borate phase. For melts with  $\text{B}_2\text{O}_3$  concentrations above 2.5 mass-%, the calcium-borate melt phases are probably

present in the other continuous phase(s) as a very fine dispersion of small droplets (probably  $< 1 \mu\text{m}$ ) due to the relative high surface tension. In melts with low  $\text{B}_2\text{O}_3$  concentrations, more silica rich melt phases will be formed, which encapsulate the calcium-borate melt phases or is preferably present on top of the melt. In this specific situation the transport of boron ions to the surface of the melt is limited or hindered by the silicate phase with very low  $\text{B}_2\text{O}_3$  solubility.

### **6.5 Evaporation tests for industrially produced alkali-lime silicate glasses**

For alkali-lime-silicate melts, chlorides and sulfates promote the release of alkali species, such as  $\text{Na}_2\text{SO}_4$ ,  $\text{NaCl}$ ,  $\text{KCl}$  or possibly  $\text{K}_2\text{SO}_4$ . In a static melt, the evaporation rates of these species are limited by the relatively slow diffusion transport in the melt. Depletion of sulfur and chloride species at the glass melt surface increases as the evaporation process proceeds. Temperature gradients, differences in surface tension and bubbles in the melt can strongly affect the (local) convection in the melt and the evaporation rates of these minor species. The formation of  $\text{SO}_2$  bubbles and the formation of a dynamic, continuously refreshed foam layer at the surface of the melt may also promote the evaporation rates of volatile glass components.

From the investigation, it appeared that the main evaporation species from soda-lime-silicate float glass melts and alkali-lime-silicate tableware melts are:  $\text{NaOH}$ ,  $\text{KOH}$ ,  $\text{Na}_2\text{SO}_4$ ,  $\text{KCl}$  and at reducing conditions  $\text{Na}$  and  $\text{K}$ .

### **6.6 Evaporation modeling for industrial glass furnaces**

The evaporation model developed in this study has been used to estimate the evaporation rates of volatile sodium and boron species from blank glass melts in industrial glass furnaces. The modeling results were compared with the results of industrial evaporation measurements.

To model evaporation processes in industrial glass melt furnaces, first a combustion modeling procedure is required to calculate the mass transport of volatile species from glass melts into combustion chambers of industrial glass furnaces. In the combustion chamber of an industrial glass furnace, gas flows are predominantly turbulent. The gas flow patterns in case of turbulent conditions are modeled by the standard 'k- $\epsilon$  turbulence model' in CFD (Computational Fluid Dynamics) calculation schemes. However, the applied k- $\epsilon$  model is only valid for fully turbulent flows. In order to correctly calculate momentum-, mass- and

energy fluxes near the (melt) surfaces without the necessity to use very fine grids, empirical relations, derived from literature, are applied. Velocities, temperatures and mass fractions as function of the distance from the glass melt surface, are derived. For the descriptions of these so-called ‘wall functions’ for heat transport and mass transport, analogies with momentum transport are used.

For an industrial oxygen-gas fired E-glass borosilicate melting furnace, the experimentally determined local boron species evaporation rates at different locations in the combustion chamber have been compared with the modeled local evaporation rates of  $\text{HBO}_2$ , assuming this species as being the main boron vapor. The measured maximum boron species evaporation rate was about 27 % higher than the modeled maximum boron evaporation rate (taking only  $\text{HBO}_2$  formation into account). Since industrial E-glass melts contains small amounts of alkali-oxides (0.5 to 1 mass-%), the difference between modeling results and measured values is probably caused by additional evaporation of other boron compounds such as  $\text{KBO}_2$  and  $\text{NaBO}_2$ . Laboratory evaporation tests showed about 10 to 30 % higher boron evaporation rates for industrial E-glass types, containing less than 1 mass-% alkali-oxides, compared to alkali free borosilicate glass melts with nearly the same composition and the same  $\text{B}_2\text{O}_3$  contents.

For an oxygen-gas fired glass furnace, producing a multi-component soda-lime-silicate glass, the  $\text{NaOH}$  vapor pressures in the combustion chambers have been modeled and measured. Above a nearly blank melt, the measured and modeled sodium concentrations deviate only 10 to 20 % from each other.

In a third case, models have been used to estimate the kinetics of evaporation of sodium species from soda-lime-silicate glass melts in combination with a separate model (from literature) for silica refractory attack by sodium vapors. By combining these models the rate of corrosion of the silica refractory materials applied in the crown of the combustion chamber can be estimated. These models show the same trends as the recent observations in industrial practice of oxygen-fired glass furnaces: severe corrosion of silica by  $\text{NaOH}$  vapors in low temperature areas of the crown for  $p_{\text{NaOH}} > 15 \text{ Pa}$ .

## 6.7 Concluding remarks and outlook

A general applicable evaporation model for a large range of glass compositions has been developed to predict the evaporation rates of the main volatile glass components. The model has been validated by laboratory evaporation experiments as well as industrial

evaporation rate measurements. The results agree well with the beforehand defined objectives of this study.

The developed evaporation model is mainly applied to predict the evaporation rates of volatile sodium, potassium and boron species of sodium-silicate melts, alkali-lime silicate melts and alkali-lean borosilicate glass melts. But, the existing evaporation model can be applied for a wider range of glass compositions, such as lead glass or LCD glass, and other volatile species (e.g. Pb, Sb, Cl, F). For the extended use of the evaporation model, the thermodynamic Associated Species Model has to be tested and if necessary to be modified or optimized for these new glass compositions. This adaptation can be done in two different ways:

1. In the thermodynamic Associated Species Model, the thermodynamic data of additional associated species have to be included to be able to describe the complete system;
2. In some glass melts, phase segregation occurs or associated species do not ideally mix. For these systems the Associated Species Model approach has to be modified to account for positive excess Gibbs free energy of mixing. Borosilicate and glass-ceramics compositions are suspected as not ideally mixed melts.

Validation of these models for new applications or glass compositions by transpiration evaporation measurements, as described in this thesis, is strongly recommended.

The thermodynamic Associated Species Model cannot only be used to predict chemical activities as such, but can also be applied in combination or as part of a refractory corrosion model, or to calculate solubilities of certain components in the multi-component silicate melts or even to model crystallization processes during cooling of the melt.

Besides the adaptations in the thermodynamic modeling, modifications in the mathematical mass transport models might be required. The evaporation rates from silicate melts of minor components present at low concentration levels (e.g. F, Cl, Se or Sb), are often limited by the slow transport of these species to the surface of the melt, leading to distinct surface depletion of these elements. At the surface of the melt the concentrations of these volatile compounds might eventually decrease to zero. CFD (Computational Fluid Dynamics) modeling, taking into account the convection at surface near areas is a powerful tool to describe the transport of these minor compounds in the melt phase in case of non static melts. Phenomena like Marangoni flows and ascending fining bubbles seem to be important for convection in several industrial glass melting processes and the refreshment of the top melt layers.



## Samenvatting

In de meeste glasovens worden fossiele brandstoffen verbrand om met behulp van stralingswarmte glasgrondstoffen te smelten en de glassmelt te verwarmen. Tijdens het smeltproces bij hoge temperaturen zullen glas componenten zoals natrium, kalium, boor en lood verdampen vanuit de glassmelt.

Er zijn drie belangrijke redenen om verdampingsprocessen in glas ovens te bestuderen. Ten eerste is de verdamping van vluchtige glascomponenten vanuit de oppervlakte laag van de smelt één van de belangrijkste oorzaken voor de emissies van stof en zware metalen. Ten tweede kan de incongruente verdamping van glas componenten in de smelt leiden tot verarming van deze vluchtige componenten in de oppervlakte laag van de smelt. Ten gevolge van deze verarming kunnen glasfouten en in-homogeniteiten in het uiteindelijke glasproduct ontstaan. Ten derde kunnen er ten gevolge van de verdamping van glascomponenten agressieve dampen gevormd worden, zoals alkali en lood dampen, die kunnen reageren met vuurvaste materialen toegepast in de bovenbouw (verbrandingskamer) van een glasoven of met vuurvaste materialen toegepast in de rookgaskanalen.

De verdampingssnelheden hangen af van de proces omstandigheden in een glasoven, zoals:

- Samenstelling van de glassmelt (aan het oppervlak);
- Temperatuur van het glassmelt oppervlak;
- Samenstelling van de atmosfeer. Met name de waterdamp en de koolmonoxide concentraties net boven het glassmelt oppervlak zijn van belang;
- De tijdsduur dat een glassmelt volume-element wordt blootgesteld aan de atmosfeer;
- Lokale gassnelheden en turbulentie intensiteit net boven het glassmelt oppervlak.

Voor verschillende glassoorten zijn zowel de interactie tussen de ovenatmosfeer en het glassmelt oppervlak, alsmede de verschillende verdampingsreacties door diverse onderzoekers kwalitatief beschreven en bediscussieerd. Een universeel mathematisch verdampingsmodel om de verdampingssnelheden van vluchtige glascomponenten te voorspellen in industriële glasovens en laboratorium ovens, was tot op heden niet beschikbaar.

### **Doelstelling**

De belangrijkste doelstelling van dit project is de ontwikkeling van een algemeen toepasbaar verdampingsmodel, bruikbaar voor verschillende soorten glasovens en verschillende glassamenstellingen. Het model zal bestaan uit gevalideerde massa transport relaties en



gesimuleerde thermodynamische eigenschappen van multi-component silicaat glassmelten. Met dit verdampingsmodel kunnen de verdampingsnelheden van vluchtige componenten vanuit diverse glassmelten berekend worden. Het model kan worden toegepast om de invloed van procesparameters op de verdampingsnelheden van diverse vluchtige componenten te bepalen en om de verarming van vluchtige componenten aan het smeltoppervlak te voorspellen. Dit onderzoek richt zich primair op de verdamping vanuit multi-component silicaat glassmelten voor de industriële productie van glasproducten.

### **Aanpak**

Tijdens deze studie is een verdampingsmodel ontwikkeld en gevalideerd met behulp van laboratorium verdampingsproeven. Om het ontwikkelde verdampingsmodel toe te kunnen passen zijn 5 verschillende stappen nodig:

- I. Identificatie van de vluchtige componenten en de belangrijkste verdampingsreacties onder de heersende condities voor de onderzochte glassmelt.
- II. Modelleren van het massa transport van vluchtige glascomponenten in de smelt. Het diffusieve transport van vluchtige glascomponenten wordt beschreven met behulp van de tweede wet van Fick en een bekende inter-diffusiecoëfficiënt (afkomstig van literatuur, experimenten of modellen). Met behulp van Computational Fluid Dynamics (CFD) modellen, wordt zowel het convectieve als diffusieve transport van vluchtige componenten van de bulk naar het oppervlak van een glassmelt beschreven.
- III. Modelleren van massa transport in de gas fase. Het transport van vluchtige gasvormige componenten van het smeltoppervlak in de atmosfeer wordt beschreven voor laminaire en turbulente gasstromen.
- IV. Het zogenaamde thermodynamische Associated Species Model (ASM) wordt toegepast om de chemische activiteiten van vluchtige componenten in de glassmelt te berekenen.
- V. Berekening van de verdampingsnelheden. Aan de hand van de verdampingsreactie, de bijbehorende evenwichtsconstante en de chemische activiteit van de vluchtige glascomponent in glassmelt oppervlakte laag kan de verzadigingsdampdruk van het gasvormige reactieproduct bepaald worden. De lokale verdampingsnelheid van de diverse gasvormige componenten wordt bepaald uit de lokale massa transportcoëfficiënt (of Nernst grenslaag dikte in de gas fase), de lokale verzadigingsdampdruk van de vluchtige component en de dampdruk van deze component in de bulk gasstroom. De lokale dikte van de Nernst grenslaag in de gas fase boven de smelt kan

bepaald worden uit het gas snelheidsprofiel, berekend met behulp van CFD modellen.

De CFD modellen zijn toepasbaar voor zowel laminaire als turbulente gasstromen.

Laboratorium transpiratie experimenten zijn gebruikt om: A) de gemodelleerde verdampingssnelheden te valideren en B) om de verdampingskinetiek te bestuderen voor natriumsilicaat smelten, multi-component alkali-kalk-silicaat smelten en alkalivrije borosilicaat smelten. In de transpiratie opstelling kunnen de samenstelling van de atmosfeer, de temperatuur en de gassnelheid ingesteld worden. De verdampingssnelheden van natrium, kalium, boor, chloride en zwavel componenten zijn bepaald voor verschillende glassmelten met bekende chemische samenstelling.

Zoals later beschreven in deze samenvatting, is er een procedure ontwikkeld om chemische activiteiten te bepalen aan de hand van de gemeten verdampingssnelheden tijdens laboratorium transpiratie experimenten. De validatie van het verdampingsmodel bestaat uit een vergelijking van de experimentele en de gemodelleerde chemische activiteiten. Voor de thermodynamische berekeningen is gebruik gemaakt van het Associated Species Model (ASM).

### **Massa transport relaties voor de gas fase**

Om het transport van gasvormige vluchtige componenten vanuit vloeistoffen en smelten in de gas fase te kunnen beschrijven zijn massa transport relaties afgeleid. Deze massa transport relaties zijn ontwikkeld voor zowel de laboratorium transpiratie experimenten als voor industriële glasovens. CFD modellen bleken uitermate geschikt om de massatransport van vluchtige componenten in een draaggas te beschrijven voor een complexe geometrie van een transpiratie opstelling. Deze CFD modellen zijn toegepast om de verdeling van vluchtige componenten in de gas fase te beschrijven en om de fluidum dynamica in de gas fase te begrijpen. Water is gebruikt als modelvloeistof om massatransport processen in transpiratie experimenten te onderzoeken. De resultaten van CFD-modelleringen voor transpiratie experimenten met water bij kamertemperatuur zijn gevalideerd met behulp van transpiratie experimenten. De gemodelleerde en experimentele resultaten kwamen uitstekend overeen, aangezien de verschillen tussen de gemeten en gemodelleerde verdampingssnelheden minder dan 2 % waren. De resultaten van de CFD modellering en de resultaten van de water verdampingsproeven zijn gebruikt om eenvoudige massa transport, of Sherwood relaties, af te leiden voor de geometrie van een transpiratie opstelling. In deze studie is aangetoond dat deze empirische Sherwood relatie toegepast kan worden voor andere vloeistoffen of smelten en andere temperaturen zolang dezelfde opstelling wordt gebruikt.

## **Chemische activiteiten van vluchtige glas componenten in multi-component silicaat smelten**

Voor het ontwikkelde verdampingsmodel zijn de chemische activiteiten van vluchtige componenten aan het smeltoppervlak nodig. Er zijn echter nauwelijks experimentele technieken beschikbaar om verzadigingsdampdrukken en chemische activiteiten te kunnen meten bij hoge temperaturen. Aangetoond is dat de verzadigingsdampdrukken en chemische activiteiten bepaald kunnen worden met behulp van de massa transport relaties voor de transpiratie opstelling en de gemeten verdampingssnelheden van vluchtige componenten. De ontwikkelde methode biedt nieuwe mogelijkheden om de chemische activiteiten van vluchtige componenten, zoals  $\text{Na}_2\text{O}$ ,  $\text{K}_2\text{O}$  and  $\text{B}_2\text{O}_3$ , te meten met een maximale meetfout tussen 10 en 30 %.

De experimenteel bepaalde thermodynamische eigenschappen van de diverse glas componenten zijn gebruikt om het thermodynamische model te valideren en te optimaliseren voor multi-component silicaat smelten. Vanwege de verschillen in moleculaire structuur tussen natron-kalk-silicaat glassmelten en borosilicaat glassmelten, moet het toegepaste thermodynamische model voor beide glassoorten op een verschillende manier aangepast worden.

De chemische activiteiten van  $\text{Na}_2\text{O}$  in een binaire natriumsilicaat smelt en een ternaire natron-kalk-silicaat smelt zijn experimenteel bepaald met behulp van laboratorium verdampingsproeven in de transpiratie opstelling en zijn berekend met behulp van het thermodynamische Associated Species Model voor multi-component glassmelten. Tussen de gemeten en gemodelleerde chemische activiteiten van  $\text{Na}_2\text{O}$  bestaat een goede lineaire correlatie voor binaire natriumsilicaat smelten en ternaire natron-kalk-silicaat smelten:

$$a_{\text{Na}_2\text{O}(\text{model})} = (0.98 \pm 0.04) \cdot a_{\text{Na}_2\text{O}(\text{gemeten})}$$

De transpiratie verdampingsexperimenten zijn ook gebruikt om de chemische activiteiten te meten van  $\text{Na}_2\text{O}$  en  $\text{K}_2\text{O}$  in multi-component alkali-kalk-silicaat glassamenstellingen. Voor deze glassamenstellingen is het verschil tussen de gemeten en gemodelleerde chemische activiteiten maximaal circa 30 %.

De laboratorium transpiratie opstelling is tevens gebruikt om de verdampingssnelheden van boor te meten vanuit alkali vrije borosilicaat glazen. De verdampingssnelheden van boor zijn gebruikt om de chemische activiteiten van boor aan het oppervlak van de smelt te bepalen. De gemeten chemische activiteiten van  $\text{B}_2\text{O}_3$  in alkalivrije borosilicaat glassmelten wijken 1 tot 3 decades af van de resultaten van bestaande thermodynamische modellen. Deze afwijkingen zijn waarschijnlijk het gevolg van een tekort aan nauwkeurige

thermodynamische data voor stoichiometrische calciumboraat componenten met een molaire ratio  $\text{CaO/B}_2\text{O}_3 > 3$  of het ontbreken van andere belangrijke stoichiometrische componenten in het thermodynamische model.

Een methodiek om het bestaande thermodynamische Associated Species Model (ASM) te verbeteren voor borosilicaat glassamenstellingen is gepresenteerd en gedemonstreerd voor een selectie van alkalivrije borosilicaat glassmelten, bestaande uit  $\text{SiO}_2$ ,  $\text{CaO}$ ,  $\text{Al}_2\text{O}_3$  en  $\text{B}_2\text{O}_3$ . In dit aangepaste model wordt ontmenging van smelt fasen niet meegenomen.

Zowel de resultaten van de thermodynamische modellering als de meetresultaten voor deze borosilicaat glassmelten, tonen een sterke afname in chemische activiteit voor borosilicaat glassamenstellingen met  $\text{B}_2\text{O}_3$  concentraties lager dan ongeveer 2.5 massa-%. Dit is mogelijk een gevolg van een verandering in de moleculaire structuur van de smelt.

Om het bestaande universele verdampingsmodel uit te kunnen breiden voor een groter aantal glassoorten, zoals bijvoorbeeld lood-glas en LCD glas, en andere vluchtige componenten (bv.  $\text{Pb}$ ,  $\text{Sb}$ ,  $\text{Cl}$ ,  $\text{F}$ ), zou het thermodynamische Associated Species Model geoptimaliseerd moeten worden voor deze glassamenstellingen en glascomponenten. Deze optimalisatie zou op twee verschillende gerealiseerd kunnen worden:

1. In het thermodynamische Associated Species Model, zouden de thermodynamische data van nieuwe stoichiometrische componenten (associated species) toegevoegd moeten worden om het volledige glassysteem te kunnen beschrijven;
2. In sommige glassmelten treedt fasescheiding op of mengen de stoichiometrische componenten niet ideaal. Voor zulke systemen moet de aannames van het Associated Species Model aangepast worden om de zogenaamde positieve exces Gibbs vrije energie van mengen te kunnen verdisconteren. Borosilicaat en glaskeramiek glassamenstellingen mengen mogelijk niet ideaal.

Het wordt sterk aanbevolen om het aangepaste verdampingsmodel te valideren met behulp van transpiratie verdampingsexperimenten, zoals beschreven in dit proefschrift.

Het thermodynamische Associated Species Model kan niet alleen toegepast worden om chemische activiteiten te voorspellen, maar kan ook toegepast worden in corrosiemodellen waarmee de aantasting van vuurvaste materialen beschreven kan worden. Tevens kan het thermodynamische model toegepast worden om de oplosbaarheid van bepaalde componenten in een multi-component silicaat smelt te bepalen of om kristallisatie processen te beschrijven tijdens het afkoelen van een smelt.

### **Transport van vluchtige componenten in een smelt**

Ten gevolge van oppervlakte verarming van vluchtige glascomponenten, wijkt de samenstelling van het smeltoppervlak soms af van de bulk samenstelling van de smelt. Met behulp van de resultaten van experimenteel onderzoek zijn de fenomenen zoals oppervlakte verarming en vrije convectie in de smelt kwalitatief beschreven. Deze fenomenen worden beïnvloed door lokale verschillen in verdampingssnelheid en de aanwezigheid van oppervlakte actieve stoffen (gradiënten in oppervlaktetenspanning of belvorming). Met behulp van CFD modelleringen is aangetoond dat, naast convectie ten gevolge van oppervlaktetenspanningsgradiënten of opstijgende gasbellen, niet uniforme verdampingssnelheden tevens tot convectie in de smelt kunnen leiden. Vanwege de niet uniforme verdamping van vluchtige glascomponenten, ontstaan er concentratie en dichtheidsverschillen in de smelt. Ten gevolge van convectie in de smelt wordt het materiaaltransport van de bulk naar het oppervlak van de smelt bevorderd, waardoor de verdampingssnelheden van glascomponenten zoals chloor, zwavel en fluor (aanwezig in lage concentraties) stabiliseren. In statische smelten zal er oppervlakteverarming plaatsvinden van deze componenten naarmate de tijd verstrijkt.

Aan het oppervlak van de smelt kunnen gradiënten in oppervlaktetenspanning ontstaan als het gevolg van concentratie verschillen aan het oppervlak. Deze gradiënten in oppervlaktetenspanning kunnen convectieve Marangoni stromingen veroorzaken. Ten gevolgen van Marangoni stromingen in de smelt neemt het transport van vluchtige glascomponenten toe in vergelijking met het diffusieve transport in een statische smelt. Mogelijkerwijs ontstaan er Marangoni stromingen ten gevolge van oppervlakte actieve stoffen in de smelt zoals  $\text{Na}_2\text{SO}_4$ ,  $\text{K}_2\text{SO}_4$ ,  $\text{NaCl}$ ,  $\text{KCl}$  en  $\text{B}_2\text{O}_3$ .

### **Verdampingsexperimenten met industrieel geproduceerde alkali-kalk-silicaat glazen**

De verdampingssnelheden van alkali componenten, zoals natrium en kalium, vanuit multi-component alkali-kalk-silicaat smelten neemt toe door de aanwezigheid van chloriden en zwavel in de smelt. De verdamping van componenten zoals  $\text{Na}_2\text{SO}_4$ ,  $\text{NaCl}$ ,  $\text{KCl}$  en mogelijkerwijs  $\text{K}_2\text{SO}_4$  vanuit deze smelten wordt bevorderd. In een statische smelt zullen de verdampingssnelheden van deze componenten afnemen als functie van de tijd. Echter, ten gevolge van temperatuur gradiënten, verschillen in oppervlakte spanning of gasbellen in de smelt, kunnen de lokale stromingen in de smelt en verdampingssnelheden van deze componenten sterk toenemen. Dit onderzoek toont aan dat de belangrijkste vluchtige componenten vanuit natron-kalk-silicaat vlakglas smelten en alkali-kalk-silicaat tafelglas

smelten NaOH, KOH, Na<sub>2</sub>SO<sub>4</sub> en KCl zijn. Onder reducerende omstandigheden zullen tevens Na en K verdampen.

De verdamping van componenten, aanwezig in lage concentraties, is vaak gelimiteerd door het langzame transport van vluchtige componenten naar het oppervlak van de smelt. Dit leidt tot een duidelijke oppervlakte verarming van deze elementen. Aan het oppervlak kunnen de concentraties van deze componenten zelfs verminderen tot nul. Wellicht kunnen CFD modellen toegepast worden om het convectieve transport van deze componenten in de smelt te beschrijven. Bij het modelleren zal de convectie in de oppervlakte lagen van de smelt meegenomen moeten worden. Fenomenen zoals Marangoni stromingen en opstijgende louter bellen lijken van groot belang voor de convectie in diverse industriële glassmelt processen.

### **Modelleren van verdamping in industriële glasovens**

Het in deze studie ontwikkelde verdampingsmodel is toegepast om de verdampingssnelheden van natrium en boor componenten in industriële glasovens te simuleren. De model resultaten en de resultaten van industriële verdampingsmetingen zijn met elkaar vergeleken. Om de verdampingsprocessen in industriële ovens te kunnen modelleren, is het noodzakelijk een verbrandingsmodel te gebruiken waarmee de massa transport van vluchtige componenten in de verbrandingskamer van een industriële glasoven beschreven kan worden. In de verbrandingskamer van een industriële glasoven zijn de gasstromen turbulent. Om deze turbulente stromingen te kunnen modelleren is het standaard 'k-ε turbulentie model' toegepast in de gebruikte CFD simulaties. Dit k-ε model is echter alleen geldig in het geval van volledige turbulentie. Om het transport van impuls, massa en energie nauwkeurig en correct te kunnen berekenen zonder gebruik te hoeven maken van een zeer fijne gridcel structuur, zijn empirische relaties gebruikt die de snelheden, temperaturen en massa fracties als functie van de afstand tot het glassmelt oppervlak beschrijven. Deze methodiek is toegepast om de verdamping van natrium en boor in industriële glasovens te berekenen.

### **Slotopmerking**

In deze studie is een algemeen toepasbaar verdampingsmodel ontwikkeld voor een brede reeks van glassamenstellingen, waarmee de verdampingssnelheden van vluchtige componenten voorspeld kan worden. Het model is zowel gevalideerd met laboratorium

## Samenvatting

verdampingsexperimenten als met industriële verdampingssnelheidsmetingen. De resultaten van deze studie stemmen goed overeen met de vooraf geformuleerde doelstellingen.

## Dankwoord

Ruim 12 jaar na afronding van mijn HTS-studie (technische natuurkunde) en na meerdere jaren praktisch onderzoek aan emissies van glasovens, ben ik begonnen aan mijn promotiestudie bij de Glass Group van TNO Industrie en Techniek (destijds TPD). Deze periode van 12 jaar heeft mijn promotor Ruud Beerkens ongeveer nodig gehad om mij er van te overtuigen deze uitdaging aan te gaan. Mede gedreven door mijn weetgierigheid over de herkomst van de emissies van glasovens ben ik uiteindelijk in 2002 met deze studie begonnen. Terugkijkend op deze promotie periode kan ik alleen maar zeggen: Ruud hartelijk dank voor deze stimulans, het vertrouwen en de adviezen waarmee je me van dienst bent geweest. Frank Simonis en André Verweij ben ik zeer erkentelijk voor het feit dat ik deze studie heb mogen uitvoeren bij TNO en hun hulp bij het verkrijgen van financiële middelen voor deze studie.

This PhD-study was one of the first 'Glass Trend' projects, financially supported by four industrial partners: Rio Tinto (Borax), AGC Flat Glass Europe (Glaverbel), PPG Fibre Glass and Rona. I very much appreciate the discussions and recommendations from Benoît Cherdon, Bruno Symoens, Jaap van der Woude, Jan Boogaardt, John Simon, Pierre Carleer, Peter Vrabel and Wibo Roolvink. Their suggestions very much supported this PhD study.

Tevens wil ik een woord van dank richten aan de Nederlandse glasindustrie, vertegenwoordigd in de NCNG. Dankzij de vele NCNG studies en de vele procesmetingen bij hun glasovens, heb ik veel praktische kennis opgedaan op het gebied van verdamping, emissies en energie. Deze praktische kennis heeft sterk bijgedragen in het kunnen uitvoeren van mijn promotie studie.

Tijdens deze studie ben ik me in toenemende mate bewust geworden van de kennis en expertise die aanwezig is bij TNO. Vele collega's hebben me gedurende mijn promotieonderzoek bijgestaan op diverse vlakken. Zo wil ik vooral Edwin van Steen, maar zeker ook Marco van Kersbergen, Tiny Sanders en Ester de Vrees bedanken voor hun experimentele ondersteuning tijdens mijn promotie. Ook wil ik de HTS-afstudeerders Harold Philipsen, Geert van de Oetelaar en Bart Verkoeijen bedanken voor hun bijdrage aan mijn promotie studie. De hulp van Adriaan Lankhorst, Andries Habraken en Luuk Thielen bij het mathematisch modelleren van verdampingsprocessen in glasovens voelde als een verfrissend turbulent windje tijdens mijn onderzoek, waarvoor ik hen graag wil danken. Ook Oscar Verheijen verdient alle lof voor het feit dat hij de moed heeft gehad om een natuurkundige



wegwijs te maken op het gebied van chemie. Anne-Jans Faber wil ik graag bedanken voor zijn steun als vraagbaken en zijn hulp bij het initiëren van dit project. Mijn kamergenoot Mathi Rongen dank ik hartelijk voor zijn mentale steun en zijn functie als toehoorder en discussiepartner.

Ook mijn 2<sup>e</sup> promotor Jaap Schouten ben ik zeer erkentelijk voor zijn steun in het volbrengen van de promotiestudie.

Het feit dat de laatste maanden van deze studie mijn werkweek van 40 uur ruimschoots werd overschreden ging ten koste van mijn rol als vader van mijn gezin. Het feit dat mijn vrouw José en mijn drie kinderen Renée, Anne en Bram me deze kans gegeven, maar vooral gegund hebben, en het begrip dat zij getoond hebben voor mijn beperkte aandacht aan het gezin, is voor mij van onschatbare waarde geweest.

I would like to thank all these persons for their contributions to my PhD-study.

Hans van Limpt

## **Curriculum Vitae**

Hans van Limpt was born on February 10, 1966 in Reusel, the Netherlands. He studied Applied Technical Physics and graduated at the Polytechnic school Eindhoven (HTS) in 1989. After his military national service he started to work as research engineer in the Glass Group of TNO. His specialisation was research into environmental problems and saving of energy in the glass industry. His professional experiences are focused on evaporation processes, NO<sub>x</sub> reduction, emission measurements and energy balances of industrial glass furnaces. In the period 1990 – 2002 he was project leader in the TNO Glass Group. Since 2000 Hans van Limpt is a member of the Technical Committee 13, 'Environment', of the International Commission on Glass (ICG). In 2002 he started his PhD study: 'Modeling of emissions' at TNO, resulting in this thesis.

## Publications

- [1] H. van Limpt, R. Beerkens, O. Verheijen, 'Models and experiments for sodium evaporation from sodium containing silicate melts', *J.Am.Ceram.Soc.* **89** [11], 3446-3455 (2006)
- [2] B. Scalet, S. Slade, A. Kasper, G. Van Marcke de Lummen, K. Gitzhofer, H. van Limpt, 'Selenium emissions from glass melting furnaces: formation, sampling and analysis. A position paper by the Technical Committee 13, 'Environment', of the International Commission on Glass (ICG)', *Glass Technology – European Journal of Glass Science and Technology Part A* **47** [2], 29-38 (2006)
- [3] H. van Limpt, R. Beerkens, 'Evaporation experiments and modeling for glass melts', proceedings *Advances in Fusion and Processing of Glass*, Dresden Germany (2006)
- [4] R. Beerkens, H. van Limpt, 'Analysis of energy consumption and energy saving measures for glass furnaces', *Proceedings 80. Glastechnische Tagung der DGG*, Dresden (2006)
- [5] J.A.C. van Limpt, R.G.C. Beerkens, 'Reduction of superstructure corrosion and emissions by modern furnace design and optimized operation', *XX. ATIV Conference Modern Technologies and Techniques for Glass Manufacturing*, Parma Italy, 14-16 September (2005)
- [6] R. Beerkens, H. van Limpt, 'Chemistry of boron in flue gases of glass furnaces & emission reduction', *Glass Trend workshop: Borosilicate glasses and raw materials in the glass industry*, Castellón, Spain (2005)
- [7] H. van Limpt, R. Beerkens, A. Lankhorst, A. Habraken, 'Mass transfer relations for transpiration evaporation experiments', *Int. J. of Heat and Mass Transfer* **48** 4265-4281 (2005)
- [8] A.J. Faber, H. van Limpt, 'Evaporation of volatile components from glass melts', *XVII. Technical Exchange Conference of International Crystal Federation*, Telfsbuchen, Austria (2005)
- [9] R. Beerkens, H. van Limpt, 'Modeling of evaporation processes' *HVG/NCNG Colloquium on operation of glass melting furnaces*, Aachen, Germany (2005)
- [10] H. van Limpt, 'Evaporation modelling', *Glass International*, **27** [3], 12 (2004)

- [11] R.G.C. Beerkens, G. Jacobs, J.A.C. van Limpt, 'Energy efficiency benchmarking of glass furnaces', *Glass Science and Technology*, **77** [2], (2004)
- [12] G. Jacobs, H. van Limpt, 'Energy benchmarking of glass furnaces', *Glass*, 81 [4], 108 (2004)
- [13] H. van Limpt, R. Beerkens, O. Verheijen, 'Mass transport of volatile species from glass melts into gas atmospheres', proceedings Annual meeting of the International Commission on Glass, Campos do Jordão, Brasil (2003)
- [14] H. van Limpt, 'Process controlled reduction of evaporation in glass furnaces', Proceedings 6<sup>th</sup> ESG Conference, Montpellier, France (2002)
- [15] H. van Limpt, 'Benchmarking energy-efficient glass production', *Glass International* **25** [6], 11-12, (2002)
- [16] R.G.C. Beerkens, J.A.C. van Limpt, 'Evaporation in industrial glass melt furnaces', *Journal of Glass Science and Technology*, **74** [(9)] 245-257 (2001)
- [17] R. Beerkens, J. van Limpt, 'Energy efficiency benchmarking of glass furnaces', proceedings 62<sup>nd</sup> Conference on Glass Problems, University of Illinois, Urbana-Champaign, USA (2001)
- [18] R. Beerkens, J. van Limpt, 'Impact of glass furnace operation on evaporation from glass melts', *Ceramic Engineering and Science Proceedings* **22** part 1, 175-204 (2001)
- [19] R.G.C. Beerkens, H. van Limpt, 'Influence of glass furnace operational conditions on the evaporation from soda-lime and borosilicate glass melts', *Int. Glass Journal* (2000)
- [20] H.J. Koch, J.A.C. van Limpt, A.J. Faber, 'Combustion control by CO/NO<sub>x</sub> sensing and prediction of volatilization and for the reduction of NO<sub>x</sub> emissions and Na-volatilization in-situ', proceedings Advances in Combustion Technologies for Glass Processing, Pittsburgh USA (2000)
- [21] R.A. Bauer, A.M. Lankhorst, J.A.C. van Limpt, 'Using computer simulation tools to reduce emissions in glass furnaces', *Int. Glass Journal* **99** [6] 28 -32 (1999)
- [22] G. de Leede, H. van Limpt, 'Energy savings and energy monitoring in the Dutch glass industry', *Klei, Glas en Keramiek* 11 (1999)
- [23] R. Beerkens, H. van Limpt, U. Kircher, B. Scalet, A. Kasper, G. van Marcke, G. Tackels, G. Delhopytal, C. Masy, 'SO<sub>2</sub> emissions and sulphur balances of soda lime

glass melting furnaces: Report of the International Commission on Glass (ICG)  
Technical Committee 13 Environment', Glass sci. technol. **72** [10], 303-314 (1999)